# Characterization of HIV-1 host interactions by advanced fluorescence microscopy

Lehmann, Martin

UNIVERSITÉ DE GENÈVE

Section de chimie et biochimie
Département de biochimie

FACULTÉ DES SCIENCES
Professeur J. Gruenberg

Département de Microbiologie et
Médecine Moléculaire

FACULTÉ DE MÉDECINE
Professeur V. Piguet

# Characterization of HIV-1 Host Interactions by Advanced Fluorescence Microscopy

THÈSE

présentée à la Faculté des sciences de l'Université de Genève
pour obtenir le grade de Docteur ès sciences, mention biochimie

par

**Martin Lehmann**

de

Alt Zauche-Wuβwerk (Allemagne)

Thèse N$^{o}$ 4407

GENÈVE

Nom de l'Atelier d'Impression: Uni Print Center Uni-Mail

2012

UNIVERSITÉ
DE GENÈVE

FACULTÉ DES SCIENCES

***Doctorat ès sciences***
***Mention biochimie***

Thèse de *Monsieur Martin LEHMANN*

intitulée :

**" Characterization of HIV-1 Host Interactions by Advanced Fluorescence Microscopy "**

La Faculté des sciences, sur le préavis de Messieurs V. PIGUET, privat docent et directeur de thèse (Facutlé de médecine, Département de microbiologie et médecine moléculaire et Welsh Institute of Dermatology, Cardiff University, Wales, United Kingdom), J. GRUENBERG, professeur ordinaire et codirecteur de thèse (Département de biochimie) et U. GREBER, professeur (Institute of Molecular Life Science, University of Zurich, Switzerland), autorise l'impression de la présente thèse, sans exprimer d'opinion sur les propositions qui y sont énoncées.

Genève, le 24 février 2012

**Thèse - 4407 -**

**Le Doyen**, Jean-Marc TRISCONE

N.B.- La thèse doit porter la déclaration précédente et remplir les conditions énumérées dans les "Informations relatives aux thèses de doctorat à l'Université de Genève".

## Résumé en français

La cause de l'épidémie actuelle du syndrome d'immunodéficience acquise (SIDA), qui jusqu'à 2011 avait causé la mort de plus de 30 million d'humains, est le virus de l'immunodéficience humaine (VIH). Malgré une stabilisation du nombre de personnes infectées et une diminution de nouvelles infections, le SIDA demeure un problème de santé et d'économie majeur, notamment dans les pays en voie de développement en Afrique.

La majorité des infections VIH sont transmises par voie sexuelle et par les muqueuses. Dans le tissu des muqueuses, les virions du VIH s'attachent aux cellules dendritiques par le récepteur de surface DC-SIGN, un lectine de type C. La plupart des virions sont dégradés et leurs antigènes sont présentés aux cellules T. Les virions intacts restants sont transférés entre cellules dendritiques et cellules T par contact cellulaire appelé synapses infectieuses. La signalisation du VIH via DC-SIGN et des protrusions membranaires riches en actine sont impliquées dans la transmission du VIH. Malgré une relevance physiologique importante, leurs rôles spécifiques dans les synapses infectieuses entre cellules dendritiques et cellules T primaire restent inconnus.

La réplication du VIH dans les cellules T $CD4^+$ et dans les macrophages mène à une activation générale du système immunitaire, à la mort des cellules T et à une défaillance du système immunitaire. Au contraire, la plupart des infections des virus d'immunodéficience simiens (VIS) sont dans leurs hôtes naturels non-pathogènes. Les différences de pathogénicité entre VIH et VIS peuvent être expliquées par l'adaptation du virus à son hôte et par les activités différentes de la protéine Nef de ces lentivirus. Les Nefs des lentivirus de primates dérèglent la communication entre des cellules T et les cellules présentatrices d'antigènes en modulant le niveau de certains récepteurs impliqués dans la formation de la synapse immunologique.

L'interaction des virions VIH avec des protéines hôtes, pendant l'entrée et l'assemblage, se passe sur une échelle se situant en dessous de la limite de diffraction de ~200nm. Des techniques de microscopie de super-résolution basées sur la détection de fluorescence des molécules individuelles permettent de visualiser des structures cellulaires avec quelques nanomètres de résolution. La tetherin interagie avec des VIH et inhibe la libération des virions de la membrane plasmique cellulaire. Le mécanisme moléculaire de ce facteur antiviral reste partiellement inconnu.

Un microscope de super-résolution a été mis en place afin de visualiser des virions, des sites d'assemblage viral et l'organisation cellulaire de tetherin pendant la restriction de VIH. Avec ce microscope et des nouveaux outils d'analyse d'images nous a permis de déterminer la taille des clusters de tetherin, le nombre des molécules de tetherin au site d'assemblage viral. De plus, nous avons testé différents modèles de recrutement de tetherin au site d'assemblage du VIH.

A l'aide de la microscopie des cellules vivantes, la microscopie électronique et des approches génétiques et pharmacologiques, nous avons pu établir un rôle important de Cdc42 et des extensions de membranes dans le transfert du VIH. Le VIH active Cdc42 par une voie de signalisation de DC-SIGN dans les cellules dendritiques afin d'augmenter le nombre des extensions membranaires et favoriser le transfert VIH aux cellules T. Finalement nous avons caractérisé l'effet des allèles Nef de différents lentivirus des primates sur la formation des synapses immunologiques entre cellules T infectées et cellules présentatrices d'antigènes primaires par microscopie à fluorescence confocale. Le VIH et son précurseur, contrairement à la plupart des VIS sont incapables d'empêcher la formation des synapses immunologiques et la signalisation précoce des cellules T infectées, ce qui peut expliquer en partie leurs différents effets pathologiques.

Dans cette thèse la microscopie super-résolution et la microscopie confocale ont permis de mieux caractériser le mécanisme de restriction de tetherin et l'effet de HIV sur les synapses infectieuses et immunologiques qui jouent un rôle important dans la transmission et la pathogenèse du VIH.

**The present thesis resulted in the publication of the following peer-reviewed articles:**

Lehmann, M., Rocha, S., Mangeat, B., Blanchet, F., Uji, I.H., Hofkens, J., and Piguet, V. (2011). Quantitative Multicolor Super-Resolution Microscopy Reveals Tetherin HIV-1 Interaction. PLoS Pathog *7*, e1002456.

Lehmann, M., Nikolic, D.S., and Piguet, V. (2011a). How HIV-1 Takes Advantage of the Cytoskeleton during Replication and Cell-to-Cell Transmission. Viruses *3*, 1757-1776.

Nikolic, D.S., Lehmann, M., Felts, R., Garcia, E., Blanchet, F.P., Subramaniam, S., and Piguet, V. (2011). HIV-1 activates Cdc42 and induces membrane extensions in immature dendritic cells to facilitate cell-to-cell virus propagation. Blood *118*, 4841-4852.

Arhel, N., Lehmann, M., Clauss, K., Nienhaus, G.U., Piguet, V., and Kirchhoff, F. (2009). The inability to disrupt the immunological synapse between infected human T cells and APCs distinguishes HIV-1 from most other primate lentiviruses. J Clin Invest *119*, 2965-2975.

# Contents

## Abstract

HIV-1 is responsible for the current AIDS epidemic that caused 30 million dead so far. Albeit an overall stabilization of incidence rates and declining new infections, AIDS represents a major health and economic problem to some developing countries.

HIV-1 infection mainly occurs through unprotected sexual intercourse and subsequent mucosal transmission. In mucosal tissue dendritic cells (DC) can capture HIV-1 through cell surface receptors (e.g. the C-type lectin DC-SIGN), degrade virions and present viral antigens to T-cells. Remaining intact virions are transferred to $CD4^+$ T-cells at cell-to-cell contacts, called infectious synapses. Both DC-SIGN signaling and actin-containing cellular protrusions are implicated in HIV-1 cell-to-cell transfer, but their definitive role in highly relevant immature DC T-cell transfer remains unclear.

HIV-1 replication in $CD4^+$ T-cells and macrophages leads to general immune activation, T-cell depletion and final failure of the immune system. In contrast, most SIV infections in their natural hosts are nonpathogenic. Primate lentiviruses use their Nef proteins to manipulate the communication of T cells with antigen-presenting cells (APC) through cell-contacts named immunological synapses.

The interaction of individual HIV-1 virions with cellular proteins during entry and assembly occurs at scales below the diffraction limit of light that is ~200nm. Novel super-resolution microscopy techniques achieve nanometer resolution of fluorescently labeled molecules in intact cells. The cellular factor tetherin directly interacts with budding HIV-1 virions and inhibits their release. The restriction mechanism at the molecular scale remains largely unclear.

Establishment of quantitative multicolor super-resolution microscopy enabled the visualization of HIV-1 virions, assembly sites and the cellular organization and restriction mechanism of tetherin. New quantitative tools were established to determine sizes of tetherin clusters, number of tetherin molecules and to test models for tetherin recruitment to HIV-1 budding sites.

Live-cell fluorescence and electron microscopy together with genetic and pharmacological approaches were used to show that HIV-1 activates Cdc42 via DC-SIGN signalling to induces membrane extensions in immature dendritic that play important roles in cells to cell-to-cell transfer.

The effect of primate Nef proteins on immunological synapses between infected primary T-cells and APCs was characterized by immunofluorescence and high resolution confocal laser scanning microscopy. The inability to disrupt the immunological synapse between infected human T cells and APCs distinguishes HIV-1 from most other primate lentiviruses and could explain important differences in lentiviral pathogenesis.

In this thesis, super-resolution and confocal fluorescence microscopy allowed a detailed characterization of HIV-1 tetherin interaction, infectious and immunological synapses that play important roles in HIV-1 transmission and pathogenesis.

# Introduction

## HIV pathogenesis and AIDS

In 1983 the group of Luc Montagnier isolated a virus from a lymph-node-biopsy from an patient with early symptoms for the acquired immunodeficiency syndrome (AIDS) [1]. This virus was later named Human Immunodeficiency Virus 1 (HIV-1). Repeated isolation of HIV-1 from AIDS patients and culture in T-cell lines enabled development of antibodies for blood testing, cloning, sequencing and molecular characterization of the viral genome, which led to the development of antiviral therapies[2-5]. In 1986 a related virus named HIV-2 was isolated from AIDS patients from West Africa[6].

Since its first description in 1981, more than 30 million people died of AIDS. According to estimations from UNAIDS 33.3 million people lived with AIDS in 2010. Notably 68% of the global HIV cases are found in Sub-Saharan Africa with incidence rates as high as 26% for Swaziland (Figure 1). While incidence rates in many sub-Saharan countries decline, HIV-1 rates are still increasing in Europe and Central Asia, mainly due to sex work, drug use and men having sex with men. Albeit an overall stabilization of the AIDS epidemic, the high incidence rates and mortality in sub-Saharan African countries bring major problems to those fragile economies and deficient health systems.

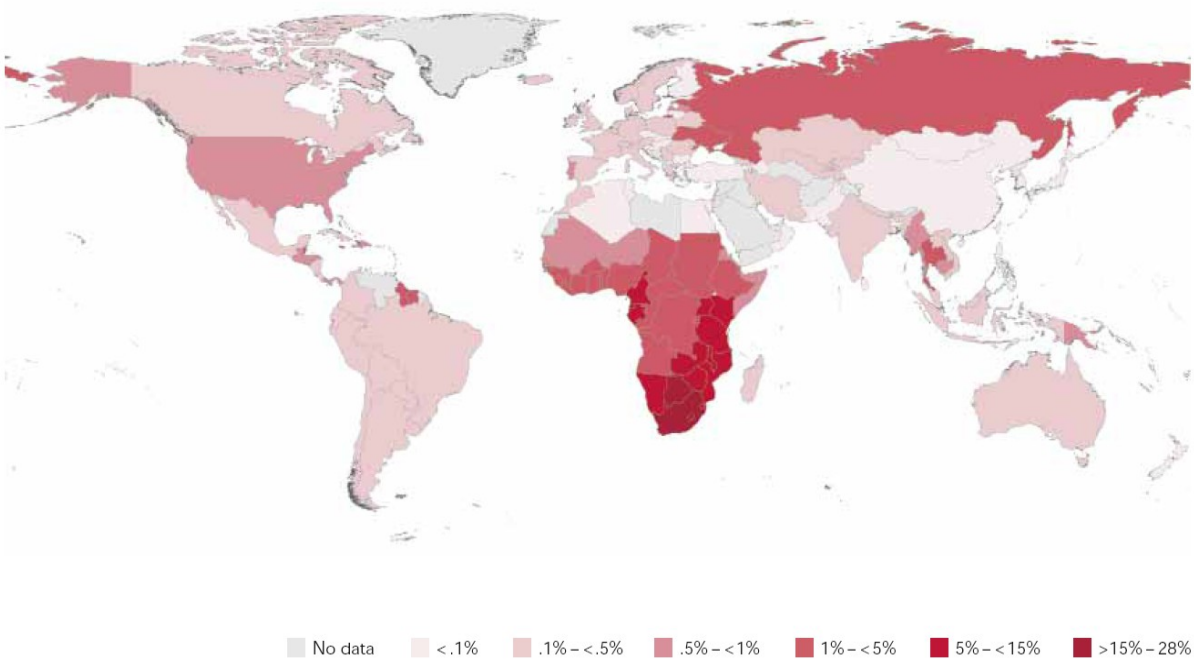


**Figure 1. Global prevalence of HIV in 2009 (UNAIDS)**

Approximately 1.8 million people died of AIDS in 2009 that are significantly less than in 2004 (2.1 million). The number of new infection, 2.6 million in 2009 also declined compared to 3.1 million in 1999 (www.unaids.org). The overall decrease of mortality and new infections can be explained by facilitated access to antiretroviral treatment, changes in sexual behavior, increased condom use and male circumcision. In addition, mother-to-child transmissions are declining and could be virtually eliminated by granting universal access of HIV-1 positive pregnant women to anti-viral treatment (www.unaids.org). Similarly, large-scale testing and antiviral treatment of infected people can drastically reduce AIDS transmissions. All approaches including male circumcision must face compliance, social and economic concerns and must be combined into strategies meanwhile research for an effective vaccine is enforced [7].

HIV transmission occurs through unprotected sexual intercourse, mother to child transmission during delivery and breastfeeding, multiple uses of drug injection equipment and untested blood transfusions. Semen and vaginal fluids containing HIV-1 can initiate infection through unprotected sex with a probability of 0.1-0.5% while blood transfusion from HIV-1 positive donors results in about 90% of infection[8].

The acute phase generally follows few weeks after an HIV-1 infection and is characterized by high viral replication in activated $CD4^+$ T-cells, notably in gut associated lymphoid tissue[8, 9]. High viral titers are associated with a sharp decline in $CD4^+$ T-cells, flu-like symptoms and increase levels of interferon, commonly found as an innate immune response to viral infections [8, 10]. Subsequently adaptive immune responses decrease viral titers to low levels and allow $CD4^+$ T-cell numbers to rebound to pre-infection levels (Figure 2). HIV-1 specific cytotoxic $CD8^+$ cell responses remove most infected cells at the end of the acute phase. First HIV-1 specific antibodies appear during seroconversion[11]. The overall effectiveness of the immune response is reflected by the viral titer at the end of the acute phase. This so-called virological set point is a general predictor for future disease progression[12]. Ongoing low viral replication, normal $CD4^+$ T-cell numbers and effective adaptive immune responses characterize an asymptomatic period or clinical latency that can last for years (Figure 2). Nevertheless general immune activation, viral cytopathicity and killing of infected cells by cytotoxic $CD8^+$ T-cells lead to a slow decrease of total $CD4^+$ T-cells. Further virus specific adaptive immune responses are impaired through preferential infection and elimination of HIV-1 specific $CD4^+$ T-cells[13]. Clinically AIDS is diagnosed when $CD4^+$ T cell numbers drop below 200 per microliter, that is often associated with the appearance of opportunistic

infections of otherwise non-pathogenic bacteria (*Mycobacterium tuberculosis*), fungi (*Pneumocystis jiroveci*) and malignancies from earlier viral infections, for example human herpes virus 8 [8]. Untreated AIDS patients mainly die within few years after infection from pneumonias, lymphomas or other infections (Figure 2). Failure of the immune system to clear and control HIV-1 infection is attributed to viral immune escape, HIV-1-mediated killing of $CD4^+$ T cells, general immune activation and alteration of the lymphoid tissue organization [14, 15].

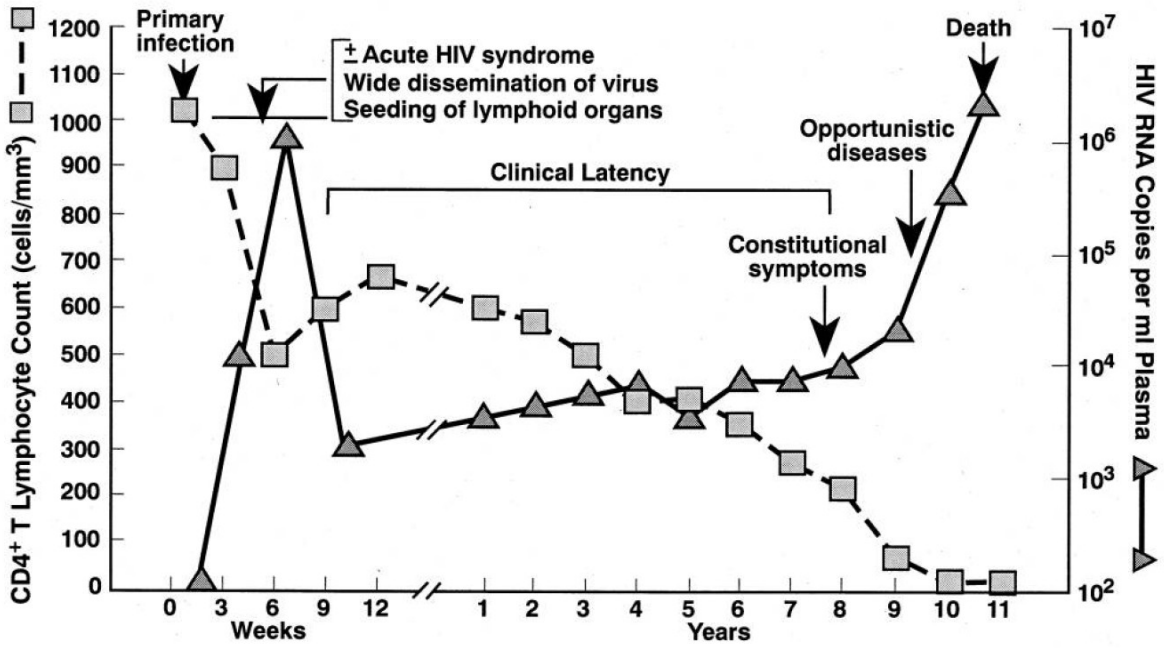


**Figure 2. Course of HIV-1 infection in untreated patient (Cohen & Fauci, 2001).**

The first HIV-1 inhibitor azidothymidine (AZT) efficiently blocked reverse transcription but proved inefficient in clinical trials because of rapid emergence of drug-resistant mutants.

The introduction of highly active anti-retroviral therapies (HAART), a combination of three antiviral drugs, considerably decreased AIDS associated morbidity, mortality and new HIV-1 infections. HAART are available as a standard treatment for 5 million people mostly in industrialized countries but cannot completely clear HIV-1 infection. Failure to cure HIV-1 with antiretroviral therapies has so far been attributed to infected resting $CD4^+$ T-cells, that have a very long life span and therefore act as viral reservoirs[15, 16]. The need for long-term treatment and relatively high costs further limit large-scale application of HAART in the mostly affected countries with low income. Additionally all available retroviral drugs produce severe side effects, such as diarrhea, nausea, peripheral neuropathy, rash, hyperbilirubinemia

and body fat redistribution [8]. Similar to single-drug resistance the inaccurate replication of the HIV-1 genome can produce multi-drug resistant strains[17].

Recent advances in basic research and vaccine development show promising results to prevent and cure AIDS. A HIV-1 specific recombinase can excise the integrated viral genomes from infected cell DNA[18], but faces major delivery problems in-vivo. A recent HIV-1 vaccine and several microbicide trials offered modest protection[7, 19]. Therefore, the search for new and cheaper drugs showing fewer side effects as well as the identification of new potential targets for AIDS therapy and prevention remain a high priority.

## HIV-1 phylogeny

As part of the retrovirus genus HIV-1 posses a RNA genome that upon entry into the cytoplasm becomes reverse transcribed into DNA and integrated into the host genome. Simple retroviruses like murine leukemia virus (MLV) code for Gag, Envelope, reverse transcriptase (RT), integrase (IN) and protease (PR). Lentiviruses like HIV-1 and simian immunodeficiency virus (SIV) acquired and evolved multiple regulatory proteins to optimize replication and modulate adaptive immune responses[20]. Those regulatory proteins allow lentiviruses to infect non-dividing cells, evade immune control and trigger slow progression towards disease. Because of ancient retroviral infection of cells within the germline, vertebrate genomes contain thousands of endogenous retroviruses that mostly lost their replicative potential. Since endogenous retroviruses and related retrotransposons can integrate into host genes, they constitute a major driving force for the evolution of vertebrate genomes.

Both HIV-1 and HIV-2 arose from zoonotic transmissions of SIVs that are found in chimpanzees (SIVcpz) and sooty mangabeys SIV (SIVsm), respectively. Three independent transmissions of SIVcpz gave rise to the HIV-1 groups M, N and O [21-23], of which HIV-1 M became the pandemic strain. Recent sequence analysis dated the zoonosis of HIV-1 M back to the end of the 19$^{th}$ century (1884-1924) in Kinshasa (Congo). The authors propose that the spread of HIV-1 group M was favored by development of colonial cities with crowding and prostitution increasing the probabilities of HIV-1 transmissions[24]. Contrary to HIV-1, that causes a global pandemic HIV-2 is less infectious and restricted to West Africa[23].

Several primates are infected by lentiviruses, but except in humans, chimpanzees and rhesus macaques, currently described SIV infections do not produce AIDS-like symptoms in their

natural hosts[1, 23, 25]. Similar to HIV-1 both SIVcpz and SIVmac originated from recent zoonotic transmissions to chimpanzees and rhesus macaques, respectively. Therefore, prolonged co-evolution of primate lentiviruses seems to result in non-pathogenic infections, while recent zoonotic transmissions cause AIDS-like symptoms. Alternatively the negative factor (Nef), an accessory protein common to all primate lentiviruses, has evolved different strategies in simian hosts to control immune activation and AIDS in humans in the case of HIV-1 infections[26, 27]. Therefore, a better understanding of immune responses of non-human primates to adapted and "foreign" SIV and the molecular dissection of Nef functions could provide important new insight into HIV-1 pathogenesis.

## HIV-1 virion structure

HIV-1 virions are spherical particles of 100-150 nm diameter that are surrounded by a lipid membrane[28] as depicted in Figure 3 and 4. The viral membrane contains trimeric spikes of HIV-1 envelope glycoprotein (Env), which is synthesized as the polyprotein precursor gp160. Proteolytic cleavage of gp160 by cellular proteases produces the transmembrane part gp41 and the mature surface glycoprotein part gp120 that form a non-covalent dimer[29]. Below the viral membrane Matrix (MA) forms an incomplete shell [30]. The central core structure is composed of a hexagonal lattice of capsid (CA) proteins that encapsulate two copies of the nucleocapsid-coated genomic RNA together with the enzymes required for early replication, namely reverse transcriptase (RT) and Integrase (IN). Except for the viral protein R (Vpr), that associates with the viral capsid, the exact localization of the non-structural proteins protease (PR), p6, Nef, IN and RT is not known (Figure 4).

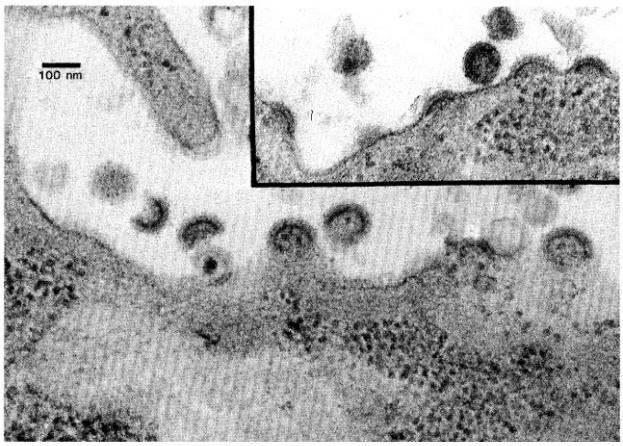


**Figure 3. Electron microscopy image of HIV-1 producing lymphocytes**. *Various stages of particle budding are visible (from Barré-Sanoussi 1983)*

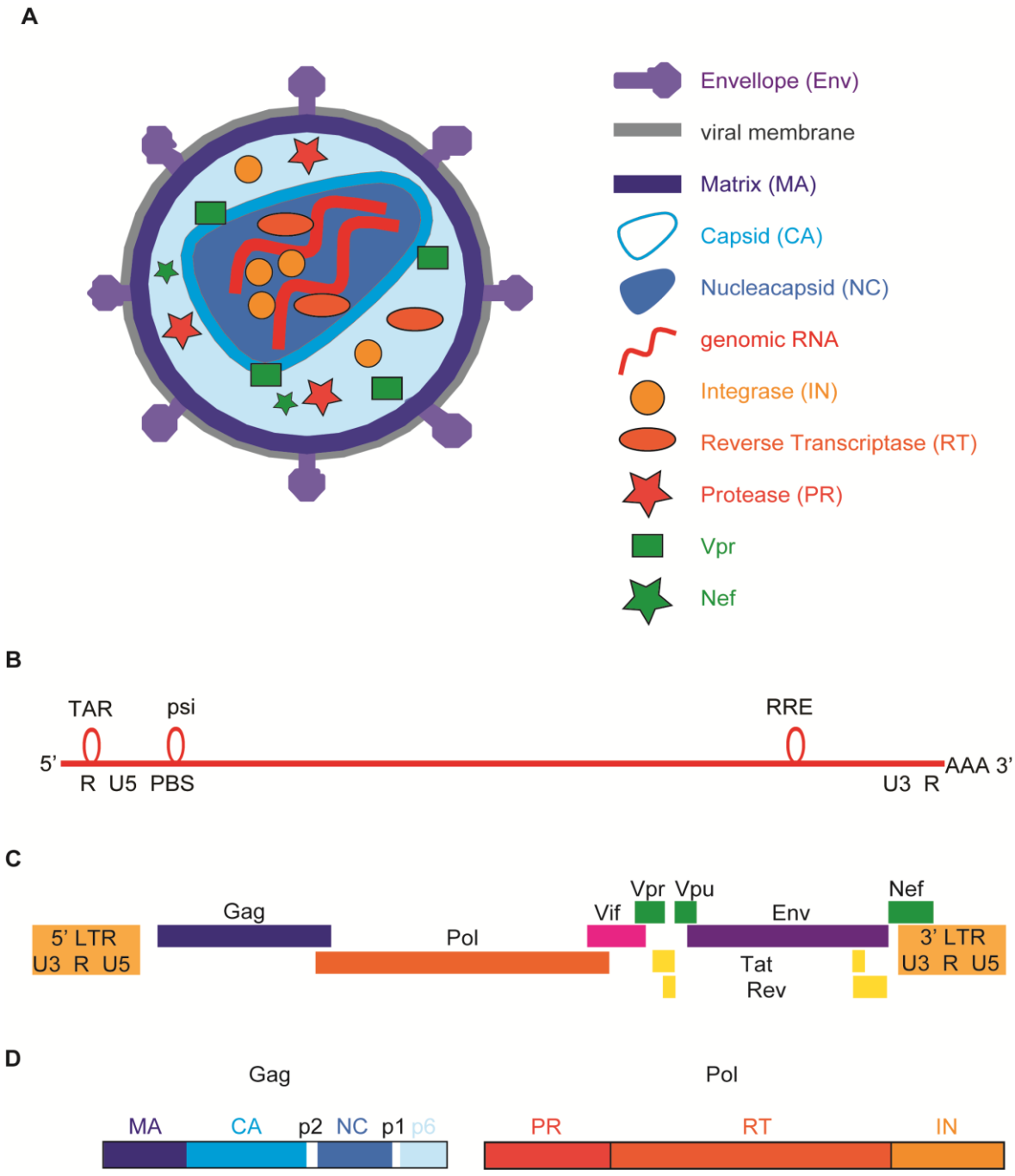


**Figure 4. HIV-1 virion and genome structure.**

*(A) Representation of the structure of the mature HIV-1 virion. While Env is composed of heterotrimers of gp41 and gp120 it is depicted here as a unique structure for simplicity reasons. Note that the exact position of non-structural proteins is not clear.*

*(B) Genomic RNA structure with primer binding site (PBS), TAR, packaging signal (psi) and Rev response elements (RRE) as described in the text.*

*(C) Genomic organization of HIV-1 proviral DNA with indicated protein coding regions*

*(D) HIV-1 structural precursor proteins Gag and Pol are cleaved into the indicated mature products*

The complete HIV-1 infection cycle as depicted in Figure 5 takes about 24hours and consists of the following steps: attachment, fusion, cytoplasmic transport/uncoating/reverse transcription, nuclear import, integration, transcription and translation of viral proteins, assembly, budding and release.

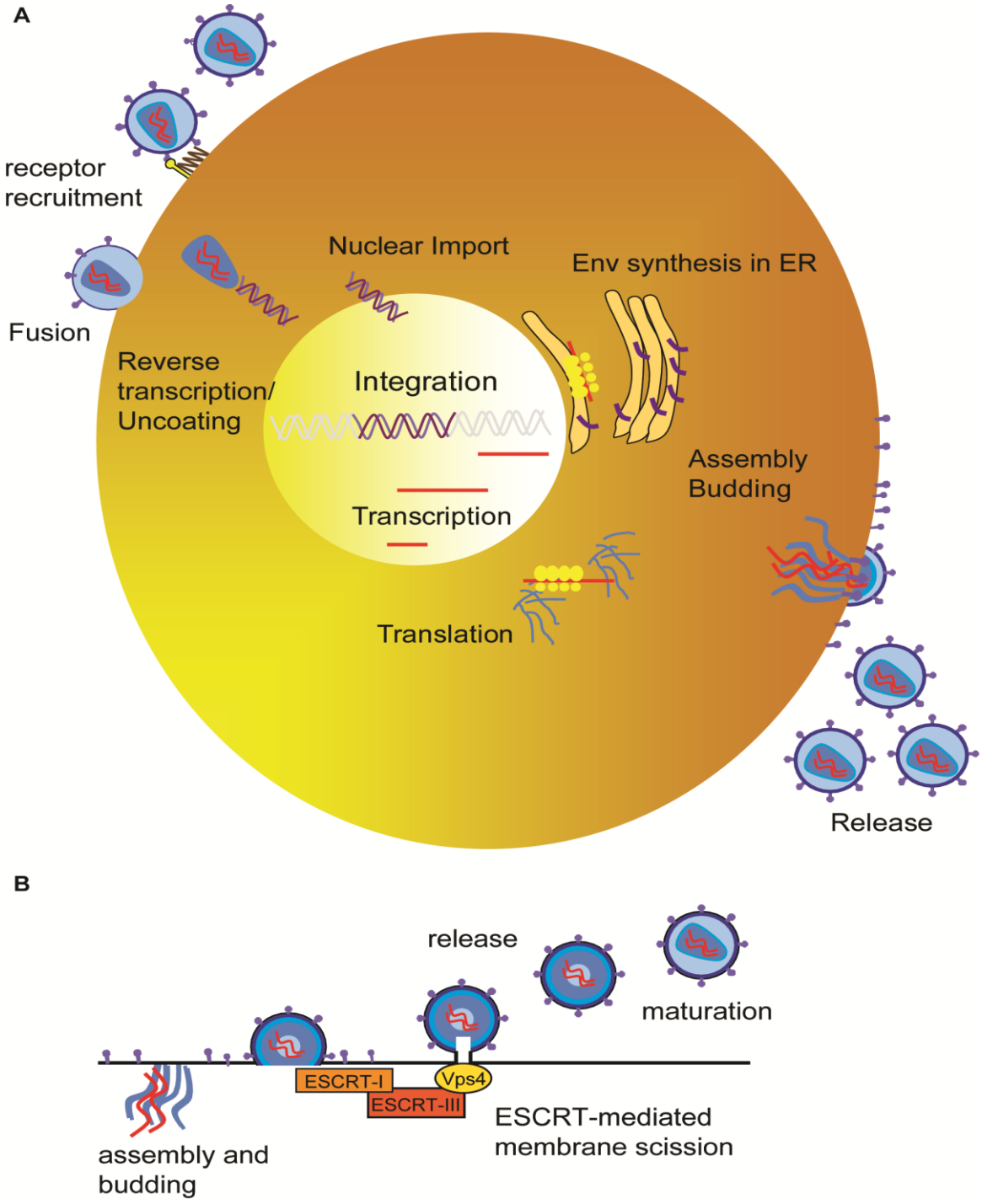


**Figure 5. Schematic representation of the HIV-1 life cycle.**

*(A) Simplified HIV-1 life cycle as described in the text.*

*(B) Gag assembly, budding and ESCRT-mediated scission leads to HIV-1 particle release.*

## HIV-1 infection cycle: early events

HIV-1 particles that enter genital tissue during unprotected sexual intercourse through lesions or transcytosis can infect T-cells or be taken up by dendritic cells (DC) via Env interaction with the C-type lectin DC-SIGN [31, 32]. HIV-1 captured by DC can be transferred to T-cells and results in vigorous replication[33-35]. This scenario could take place after DC have migrated to proximal lymph nodes and contact T-cells to initiate immune responses[36]. HIV-1 infection can be initiated by cell-associated and cell-free virions. Possible target cells expressing the receptor CD4 are resting and activated $CD4^+$ T-cells, macrophages and immature dendritic cells. Env interacts sequentially with the primary receptor CD4 and coreceptor CXCR4 or CCR5, which leads to the exposure of a hydrophobic peptide in gp41 that mediates membrane fusion [29]. Viruses that use CCR5 as coreceptor to infect T-cells, macrophages and DC are called R5 or macrophage –tropic and are found at the initial stage of infection. Later when replication mainly occurs in activated $CD4^+$ T-cells X4 or T-cell tropic Env emerge that use the CXCR4 coreceptor[29].

Additionally to fusion, binding of HIV-1 Env to CD4 induces actin-dependent clustering of CD4, CXCR4 and CCR5 as well as signaling leading to membrane recruitment of actin via the ERM complex, activation of actin crosslinker Filamin A, Rho GTPases and actin depolymerization factor cofilin[37, 38]. Env temporally controls actin-dynamics to recruit receptor /coreceptor recruitment and to remove the cortical cytoskeleton barrier and allow fusion pore enlargement[38, 39]. Early studies indicated that Env mediated membrane fusion occurs at neutral pH at the plasma membrane. Whether membrane fusion occurs at the plasma membrane or from endosomes is still under debate and depends on the subtype of HIV-1 Env and the cell type used[40]. Membrane fusion and matrix shedding liberates the viral capsid into the cytoplasm where reverse transcription, uncoating and formation of the preintegration complex (PIC) occur. Reverse transcription of the genomic RNA starts at a cellular tRNALys and produces a linear double stranded DNA copy flanked by long terminal repeats (LTR)[29]. Frequent alterations between the two genomic RNAs from a different strains and the high error rate of the HIV-1 RT of $10^{-5}$/base pair result in considerable genetic variability. While reverse transcription and uncoating occurs, the PIC is actively transported on actin and microtubules towards the nucleus[39, 41-43]. The exact timing and the spatial coordination of reverse transcription, uncoating and nuclear import remain incompletely characterized mainly due to the transient, unstable and low abundant nature of the PIC [44]. Nevertheless through biochemical isolation of PICs several cellular and viral proteins were found associated with

the PIC, namely IN, RT, Vpr but also low amounts of MA[45, 46]. Since HIV-1 can infect non-dividing cells, the PIC has to cross the nuclear envelope. The viral proteins Vpr, IN, MA, and central DNA flap structure were proposed to mediate nuclear import through mechanisms involving nuclear localization signals of interactions with nuclear pore complexes. Specifically recent genome wide small interfering RNA (siRNA) screens identified the karypherin TNPO3 and several components of nuclear pore complexes as important host factors for HIV-1 replication[47, 48].

Following nuclear import of the PIC the viral dsDNA is preferentially integrated into transcriptional active regions of the host genome and becomes a provirus[49] . Therefore the chromatin structure affects the localization of proviral DNA and later its transcriptional activity[50].

## HIV-1 infection cycle: late events

Initial transcription of the HIV-1 provirus through cellular RNA polymerase II that acts on the U3 promoter region occurs at very low level but becomes activated by cellular transcription factors like NF-κB and NFAT. NF-κB and NFAT are found in activated $CD4^+$ T-cells. That explains high HIV-1 replication in activated $CD4^+$ T-cells[15]. Low amounts of the viral transactivator protein Tat that is produced from early low abundant viral transcripts, increases proviral transcription to normal levels.

The 9kbp viral transcript can produce unspliced (Gag/ GagPol and genomic RNA), partially spliced (Vif, Vpr, Vpu and Env) or fully spliced (Tat, Rev and Nef) mRNAs [15]. Similar to Tat that regulates transcription via binding to the TAR element, Rev binds the Rev-response element (RRE) in fully and partially spliced HIV-1 mRNAs and allows their CRM-1 dependent nuclear export, despite the presence of introns. Therefore, HIV-1 can produce multiple mRNAs through alternative splicing in a time and activation dependent manner.

Once in the cytoplasm the different viral mRNA species are translated into viral proteins.

The Env precursor gp160 is translated into the ER and transported through the secretory pathway to the plasma membrane. During passage through the Golgi apparatus gp160 becomes glycosylated and gets cleaved into its subunits gp41 and gp120,that assemble into trimers [51].

The structural protein Gag and the enzyme coding protein GagPol are produced from the unspliced genomic RNA (9kbp) through ribosomal frame shift in a ratio of 20:1. Gag and

GagPol precursor proteins are myristolated at their N-termini and targeted for assembly to the plasma membrane[52]. HIV-1 Gag consists of four structural domains matrix (MA), capsid (CA), nucleocapsid (NC) and p6, separated by spacer peptides SP1 and SP2. Gag associates with the inner leaflet of the plasma membrane specifically with phospholipids $PI(4,5)P_2$ through highly basic residues in MA and its N-terminal myristate moiety. Through a myristoyl-switch, that is sequestration and exposure of the myristate moiety in a hydrophobic pocket in MA, membrane binding is coupled to Gag multimerisation[29, 53, 54].

Gag multimerization occurs both through CA-CA and NC-gRNA interactions. Low order Gag multimers form first in the cytoplasm through interaction of NC with a packaging signal in the genomic RNA, which leads to myristate exposure and membrane recruitment (Figure 5B). High order Gag multimerisation and assembly at the plasma membrane depend on cholesterol and sphingomyelin, that are found in nanometer-sized lipid raft domains and become enriched in the viral membrane[55, 56]. Cold detergent extraction of cellular membranes and antibody patching of raft proteins leads to cofractionation and colocalisation of raft lipids, respectively with typical raft associated proteins and HIV-1 Gag and Env proteins[53]. HIV-1 proteins have a partial affinity for lipid raft domains and lipids play an important role in viral budding.

Env becomes incorporated into the viral membrane by interaction of the cytoplasmic tail of gp41 with MA. Additionally, viral particles incorporate a large numbers of cellular proteins like ICAM-1, HLA I and II and LFA-1 that can influence subsequent binding to target cells[57].

Also HIV-1 assembly was observed at tetraspanin-rich microdomains (TEM) containing CD63, CD81 and CD9 [58]. Multimerisation of 1500-2000 Gag molecules drives membrane curvature, membrane domain coalescence and budding[54].

The final step of membrane scission is catalyzed by components of the endosomal sorting complexes required for transport (ESCRT). In detail, the PTAP motive within p6 interacts with the tumor suppressor gene 1 (Tsg101) that subsequently recruits components of the ESCRT machinery to the Gag assembly site (Figure 5B). ESCRT-mediated membrane scission occurs in topologically similar processes like budding of vesicles into multivesicular body (MVB) and during cytokinesis, which is the final step of membrane scission after meiosis.

Since the ESCRT machinery is also present at the late endosomes/MVB and budding structures were observed at intracellular compartments in macrophages and dendritic cells, endosomal membranes were proposed to act as alternative budding sites for HIV-1 [53, 59, 60]. Internal virions could be released after fusion of MVBs with the plasma membrane and would

allow HIV-1 to escape neutralizing antibodies, constitute a long-term viral reservoir and eventually become transferred to T-cells by cell-to-cell transfer[59, 61].

Recently those internal compartments were shown to be invaginations of the plasma membrane[59, 62]. Those virus filled compartments in HIV-1 infected macrophages and DCs depend on the actin cytoskeleton and remain connected with the cell surface via thin channels[63, 64].

Assembly, budding and membrane scission proceed over 10-15 minutes resulting in immature particles, that are released from the cell surface[65, 66]. The viral PR cleaves Gag into MA, CA, NC and p6 leading to the characteristic viral ultrastructure described above. The processes of assembly, budding, scission and maturation are depicted in Figure 5B.

## Accessory lentiviral proteins: Vpr,Vif, Nef and Vpu

In contrast to simple retroviruses like MLV HIV-1 aquired several accessory proteins, namely Vpr, Vif, Nef and Vpu that are often dispensable for HIV-1 replication in cell culture. In contrast these proteins are required for efficient in vivo replication and reflect the adaptation of HIV-1 to innate and adaptive immune responses[20, 67].

### Vpr

The viral protein R (Vpr) interacts with the p6 domain of Gag and therefore becomes incorporated into virions[68] . Vpr remains associated with capsid/PIC in newly infected cells[42]. Its nucleocytoplasmic localization suggest that Vpr plays a role in nuclear import of the PIC [67]. Additionally Vpr plays a role in viral gene transcription through induction of cell-cycle arrest in the G2 phase. As Vpr interacts with the E3-ligase DDB1 it potentially induces the degradation of cellular factors that negatively affect HIV-1 replication[69, 70].

Vpr-deficient HIV-1 shows significantly attenuated replication in macrophages, but is dispensable in peripheral blood mononuclear cells (PBMC) and T-cell lines[71]. Both Vpr-deficient HIV-1 and SIVs are significantly less pathogenic in vivo[72]. Recently Vpx, a related protein found in HIV-2 and several SIVs, induce degradation of macrophage and dendritic cell specific factor SAMHD1 and increased infection in this cell types[73]. Overall, the exact contribution of the different mechanism of Vpr and Vpx action to in vivo pathology remain unclear.

**Vif**

The viral infectivity factor (vif) is crucial for HIV and SIV replication in vivo. Vif mediates proteasomal degradation of APOBEC3G ( apolipoprotein B mRNA-editing enzyme catalytic polypeptide-like 3G) and thereby impairs APOBEC3G incorporation into viral particles [74]. Viral particle-associated APOBEC3G, a DNA cytidine deaminase induces G-to-A hypermutations during reverse transcription that drastically reduce the infectivity of newly produced virus [75, 76].

**Nef**

The negative factor (Nef) is important for HIV and SIV replication in vivo and significantly associated with pathogenesis in humans and rhesus macaques[26, 77].

Nef affects (i) cell surface levels of various proteins implicated in viral replication and immune responses, (ii) intracellular signaling and cytoskeleton dynamics and (iii) viral infectivity.

Nef is myristolated and found both at the cytoplamic leaflet of internal and plasma membrane. It downregulates CD4, CD28, MHC-I and MHC-II from the surface of the cell[27, 78]. Downregulation of CD4 prevents interaction with the Env and is achieved through increased endocytosis and lysosomal degradation in the presence of Nef. In the absence of Nef viral particles incorporate less Env and remain attached to the cell surface via ENV CD4 interactions[79, 80]. MHC-I downmodulation from the cell surface of infected cells to can prevent their recognition and killing by cytotoxic CD8 T-cells [81]. Cell surface removal of MHC-II and CD28 in infected antigen-presenting cells (APC) and T-cells, respectively can impair activation $CD4^+$ T-cells and HIV-1 specific adaptive immune responses[82].

Nef impairs intracellular signaling and cytoskeleton remodeling through interaction with the cellular protein PAC2 [38] leading to membrane extensions on infected macrophages and T-cells[83, 84].

Nef interacts with dynamin-2 and clathrin and thereby increases viral infectivity at an early post-fusion steps that possibly involves the cortical actin cytoskeleton or a host factor from virions that limits fusion pore enlargement and passage of the viral core through the cortical actin cytoskeleton [85, 86].

**Vpu**

The viral protein U (Vpu) enhances HIV-1 replication by two independent mechanisms. First Vpu mediates proteasomal degradation CD4 in the ER through a βTrCP-dependent

mechanism, completing the effect of the previously described of Nef on CD4 [20]. Second Vpu enhances viral release by counteracting the late acting restriction factor tetherin[87]. The earlier proposed ion-channel activity of Vpu seems not to be implicated in the tetherin counteraction[88]. The main part of this thesis will focus on HIV-1 tetherin interaction.

## Structure and subcellular localization of tetherin

Tetherin, alternatively named bone marrow stromal antigen 2 (BST-2), HM1.24 antigen or cluster of differentiation 317 (CD317) was initially identified as a surface marker of terminally differentiated B-cells of patients with multiple myeloma and several B-cell lines[89]. Antibodies against tetherin can be used as immunotherapy against multiple myeloma[90-92].

Tetherin is a specific marker of murine plasmacytoid dendritic cells (pDC) [93, 94], but is low or absent on freshly isolated human pDC [95]. Furthermore tetherin expression in vitro and in vivo can be upregulated by type I and II interferons (IFN) and viral infections, that induce an IFN response[10, 87, 93, 94, 96]. Various human tissues express tetherin constitutively, notably hepatocytes, pneumocytes, ducts of major salivary glands, pancreas and kidney, Paneth cells, epithelia, Leydig cells, plasma cells, bone marrow stromal cells, monocytes and vascular endothelium[95, 97]. Similarly, different rat tissues showed expression of tetherin[98].

The human *tetherin* gene is located on Chromosome 19 p13.2 and codes for a highly glycosylated protein of 180 amino acids, that migrates at 30-36 kDa in SDS-PAGE[99].
Human tetherin is a type II transmembrane protein (Figure 6) composed of a short N-terminal cytoplasmic tail (aa 1-20), a transmembrane (TMD, aa 21-48) and an extracellular domain (aa 49-161). Most of the extracellular domain forms an extended coiled coil (aa 68-152) and contains a C-terminal glycophosphatidylinositol (GPI) at Serine 161 as derived from structure predictions (www.uniprot.org/uniprot/Q10589).
Rat tetherin was shown to contain the predicted transmembrane domain as well as the C-terminal GPI-anchor[98]. Tetherins from human, rat and mouse show only 36 and 41% sequence homology[100] (Figure 6B), but topological features appear well conserved in structure predictions (www.uniprot.org/uniprot/Q811A2; www.uniprot.org/uniprot/Q8R2Q8).
The GPI anchor of human and rat tetherin is necessary for its localization to detergent resistant membranes (DRM), indicating possible lipid raft association of tetherin[98, 101, 102].

Notably lipid raft association was abolished after treatment with phosphatidyl-inositol-specific phospholipase C (PI-PLC) [98, 102]. Further evidence for the presence of a C-terminal GPI anchor came from retention of tetherin in the ER of cells lacking peptide-N-glycosidase F, an ER-resident enzyme required for GPI modifications[103]. Nevertheless direct GPI modification of tetherin could not be demonstrated directly and remains to be validated by mass spectroscopy[104].

The extracellular domain of human tetherin contains two N-Linked glycosylation sites (N65 and N92), that are modified with high-mannose sugars and complex sugars in the ER and Golgi, respectively[103, 105]. Therefore endogenous tetherin appears mainly as the complex-glycosylated form of 30-36kDa, whereas overexpressed tetherin contains high mannose modifications and runs at 28kDa in reducing SDS-Page[99,101].

Three cysteine residues (C53, C63 and C91) form intermolecular disulfide bonds [99,101,106]. Both the relative positions of N-linked glycosylation sites and three cysteine residues are well conserved between human, rhesus macaque, rat and mouse tetherins (Figure 6A).

Three independent crystal structures of the oxidized form of the extracellular domain of human tetherin show a parallel dimer. The extended coiled coils are linked through intermolecular disulfide-bonds C53-C53, C63-C63 and C91-C91[107-109]. The interplay between stabilizing disulfide bonds and disturbed coiled coil interactions within tetherin dimers results in a rather flexible extracellular structure[107].

This flexible structure could act as a molecular ruler of 17 nm, that connects both of tetherin's membrane anchors and permits dynamic disassembly and reassembly of the coiled coil domains[110].

Of note, the extracellular domain can form tetramers under reducing conditions that were found in crystal structures, analytical ultracentrifugation and electron microscopy. But these tetrameric structures reorganized into parallel dimers under physiological relevant reducing conditions[108, 109]. All three structural studies noted increased flexibility at the N-terminus, indicated by generally lower resolved crystals, presence of destabilizing coiled coil residues and preferential proteolytic cleavage.

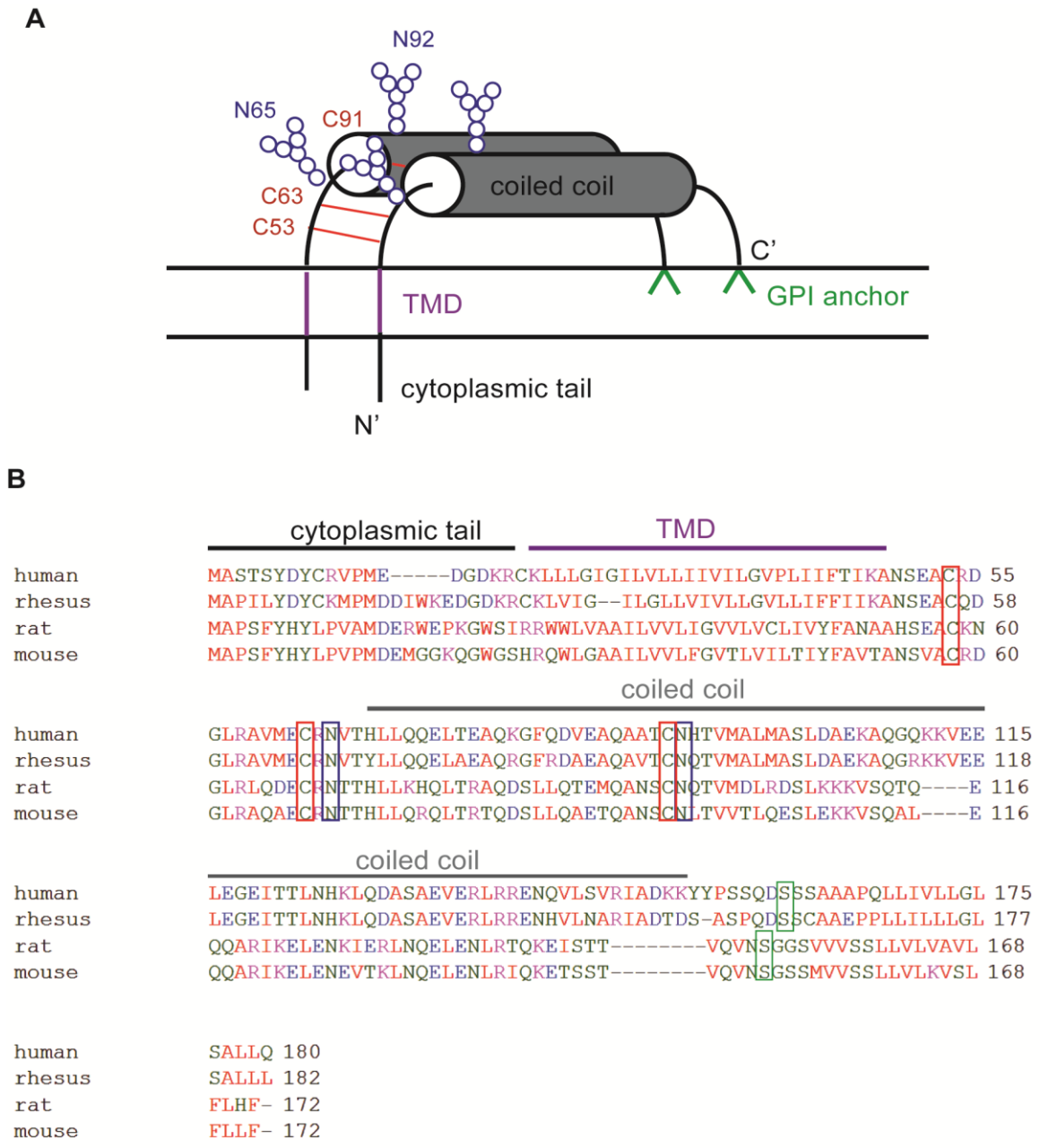


**Figure 6. Tetherin structure and sequence alignment.**

*(A) Schematic representation of the human tetherin dimer indicating the N-terminal cytoplasmic tail, transmembrane (TMD, mangenta) and coiled coil (gray) domains as well as intermolecular disulfide bonds at C51, C63 and C91 (red), sugar modifications at N65 and N92 (blue) and the C-terminal glycophosphatidylinositol anchor (GPI, green).*

*(B) Sequence alignment of tetherin of human, rhesus macaque, rat and mouse using ClustalW2[111], Individual amino acids are depicted as red (small and hydrophobic), blue (acidic), magenta (basic) or Hydroxyl/Amine/Basic (green). Structural features are depicted based on human tetherin secondary structure predictions and conserved cysteines (red box), asparagines (blue box) and GPI-modified serines (green box) are highlighted.*

As a type II transmembrane protein, tetherin is synthesized in the rough ER and follows the secretory pathway. The TMD is predicted to act as a signal anchor (www.uniprot.org/uniprot/Q10589). In the lumen of the ER tetherin folds, disulfide bond form, high-mannose glycosylation and GPI-modification take place[99,101]. Complex sugar modifications occur subsequently in the Golgi-apparatus [105].

Tetherin then localizes to the plasma membrane and is reinternalized into the Trans Golgi Network (TGN) and recycling endosomes[98, 102]. Clathrin-mediated endocytosis of tetherin from the plasma membrane occurs through a dual tyrosine motif in the N-terminal cytoplasmic tail and involves clathrin adapter protein 2 (AP2), dynamin and the GPI-modification of tetherin [101, 102, 112]. Notably the relative distribution of tetherin between ER, TGN and plasma membrane is strongly dependent on the cell type and expression system. In polarized cells rat and human tetherin localize specifically to the apical plasma membrane[98, 113]

## Cellular functions of tetherin

Tetherin has been implicated in monocyte adhesion to human endothelial cells[114], consistent with its expression in vascular endothelium[95]. Additionally tetherin was identified as a ligand of the orphan receptor immunoglubin-like transcript 7 (ILT7) present on human pDCs (Figure 7A). Interaction of tetherin and ILT7 control toll-like receptor (TLR) dependent IFN synthesis and was proposed to act as a negative feedback regulator for IFN production in human pDC [115, 116].

Due to the unusual topology of its two membrane anchors tetherin was initially proposed to link adjacent lipid rafts[98] and to connect lipid rafts to the cortical actin cytoskeleton to maintain apical microvilli in polarized cells[113] (Figure 7B).

Tetherin is upregulated by interferon and acts as a broad antiviral factor (Figure 7C).

Tetherin inhibits the release of enveloped viruses like HIV-1[87, 96], SIVs and different other retroviruses [117, 118], prototypic foamy virus[119], filoviruses like Lassa, Ebola and Marburg virus [117, 120, 121], the rhabdovirus vesicular stomatis virus (VSV)[122], Kaposi's Sarcoma associated herpes virus (KSHV)[123] and orthomyxovirus influenza A [124]. Notably replication of viruses that do not bud from the plasma membrane like the poxvirus Vaccinia virus and hepatitis C virus (HCV) are not restricted by tetherin [125, 126].

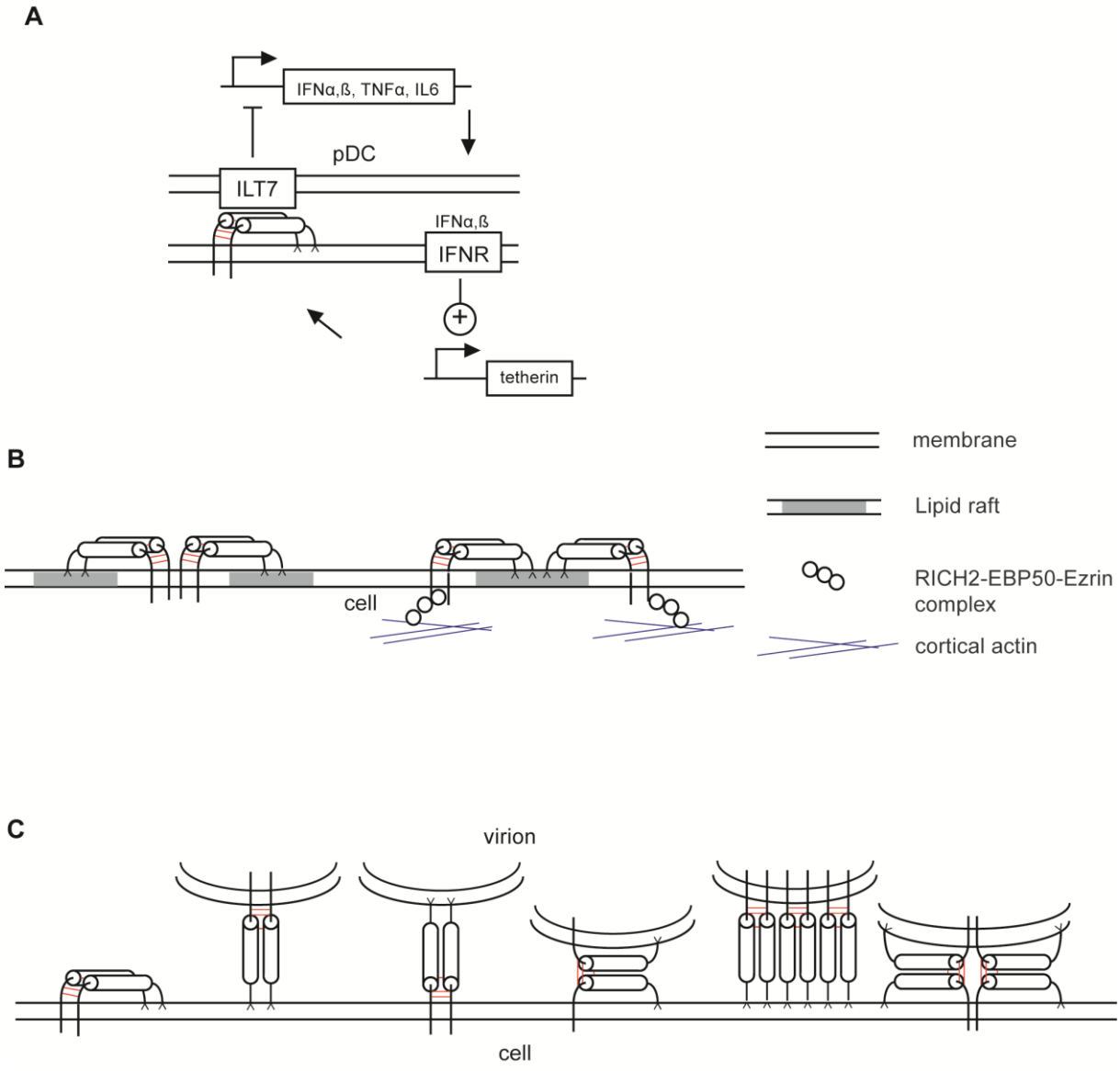


**Figure 7. Proposed cellular and antiviral functions of tetherin.**

*(A) Interaction of tetherin with the immunoglubin-like transcript 7 (ILT7) on human plasmacytoid dendritic cells (pDC) blocks toll-like receptor induced cytokine production (IFNα,β, TNFα and IL6) from pDCs. IFNα,β upregulates tetherin levels via IFN signaling.*

*(B) Based on different raft association of TMD and GPI anchor tetherin was proposed to link adjacent lipid rafts (left). Via the association of the cytoplasmic tail with RICH2-EBP50-ezrin complex tetherin could link lipid rafts to the apical cortical actin cytoskeleton in polarized cells (right).*

*(C) Tetherin acts as an antiviral factor against diverse viruses by bridging the viral and cellular plasma membrane and thus restricting their release. Of note the exact orientation and number of tetherin molecules involved in tethering viral particles is not clear.*

The antiviral activity of tetherin is reflected by positive selection during primate evolution that is characteristic of adaptation of tetherin to specific viral antagonist[127, 128].
Recently tetherin was shown to restrict retroviral replication in-vivo in an interferon-dependent manner [94]. The tetherin knock-out mice used in this study diplayed no developmental and immunological deficiencies, that could be expected if tetherin plays an important role in cellular organization and immune responses [94]. Nevertheless tetherin could have different functions in human and mice. Human pDCs for example do not express tetherin, while murine pDC express high levels of this protein [93, 94, 115].

The antiviral activity of tetherin is best studied for HIV-1. Tetherin restricts HIV-1 release directly by incorporating one of its membrane anchors into the viral membrane during budding[87, 103]. The presence of tetherin at budding sites was demonstrated by immuno-electron and immunofluorescence microscopy by several groups [82,96,99,129-131]. The tethering process does not require additional factors to be present in the cellular or viral membrane, since tetherin activity can be observed in various cell lines from different species [132]. Rather tetherin topology which is characterized by two pairs of membrane anchors linked by a flexible coiled coil seems important for virus restriction, since an art-tetherin molecule composed of heterologous proteins domains in a tetherin topology potently restricted HIV-1 release [103]. The exact orientation of tetherin during HIV-1 tethering was one subject of this thesis and will be discussed later.
HIV-1 particles that remain attached to the cell surface through tetherin are subsequently endocytosed [87] through interactions with BCA2/Rabring7 [133].

## Viral countermeasures against tetherin

Tetherin is an important anti-viral factor, so several viruses developed different strategies to counteract tetherin (Figure 8).

HIV-1 Vpu counteracts tetherin activity[87, 96]. Vpu specifically interacts with human and chimpanzee tetherin through its TMD[87, 128, 134]. Difference of tetherin antagonism between group M, N, O and P Vpus are strongly correlated to TMD interactions with tetherin[135].

Tetherin counteraction is finally achieved through cell surface removal[96, 128], that partly correlates with intracellular degradation[127, 136]. The cytoplasmic tail of Vpu contains a beta transducin repeat-containing protein (βTrCP) interaction motif that is implicated in CD4 and tetherin degradation. Specifically βTrCP-dependent degradation of tetherin can occur via the proteasome in 293T cells and macrophages [100, 137, 138] or late endosomes/lysosomes in HeLa cells and T-cell lines [112, 139]. In HeLa cells Vpu additionally retains tetherin in TGN/recycling endosomes[140] without affecting overall tetherin endocytosis rates. Alternatively it was proposed that Vpu can counteract tetherin in the absence of surface downmodulation and degradation through an yet undefined mechanism[141]. Mechanistic and cell-types specific differences in the Vpu-mediated tetherin counteraction might be due to differences in tetherin expression, subcellular distribution, trafficking and biosynthesis or endocytosis rates.

HIV-2, Ebola and SIVtan counteract tetherin restriction via their Env proteins[142, 143 144]. SIVs that infect old world monkeys overcome their natural host's tetherin through Nef, but are efficiently restricted by human tetherin. Human tetherin has a five amino acid deletion in its cytoplasmic tail that impairs Nef binding[118, 145]. SIV Nefs recruit AP2 to old world monkey tetherin cytoplasmic tail and increase tetherin endocytosis[146]. Interestingly Nef-deficient SIV develops compensatory changes in the cytoplasmic tail of gp41 to counteract tetherin in rhesus macaques[147]. Therefore the overall importance of tetherin restriction of primate lentiviruses is illustrated by positive selection of tetherin residues in the cytoplasmic tail and TMD as well as rapid adaptation of new tetherin agonists like Vpu and gp41 [82].

KSHV K5 induces ubiquitination of cytoplasmic lysines of human tetherin leading to its proteasomal degradation[123, 136].

Viruses like VSV and Influenza A inhibit IFN responses and therefore impair tetherin upregulation during viral infections[148]. Similarly, in vivo Moloney MLV infection did not induce interferon and was therefore not affected by tetherin. In vitro tetherin potently restricts MLV release[87, 94]. Therefore, MLV had no need to evolve a specific tetherin antagonist since

it avoids an interferon response in their natural hosts. Overall several different viruses developed strong tetherin antagonists illustrating the importance and broad anti-viral action of this interferon-stimulated factor.

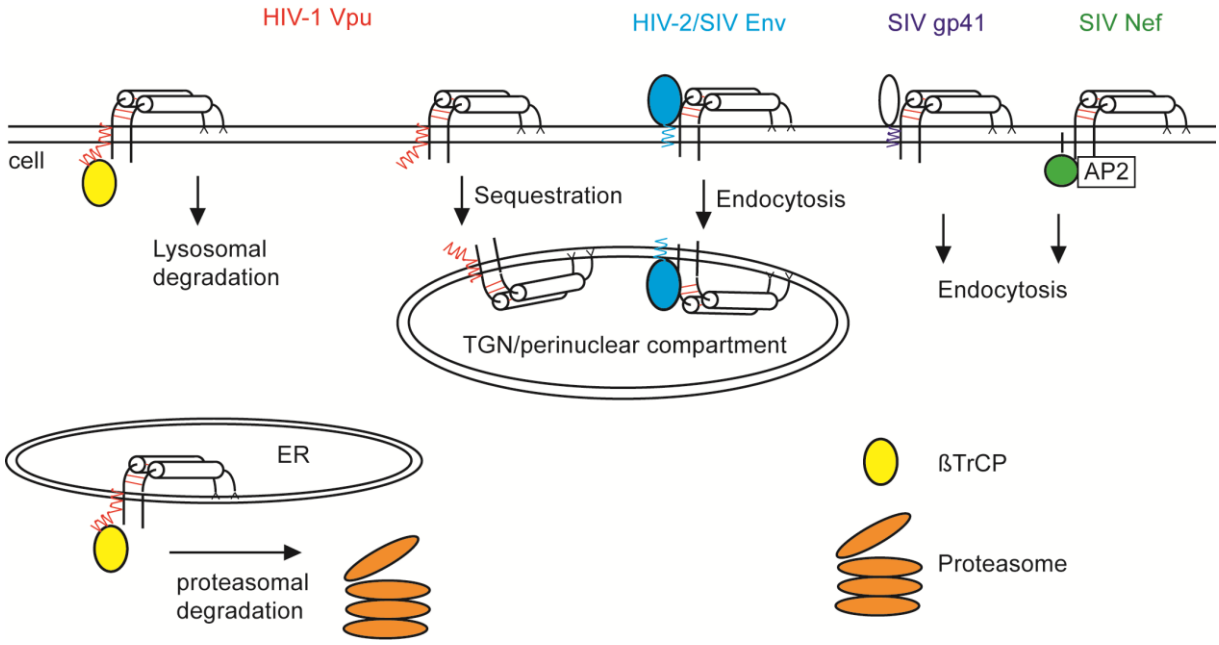


**Figure 8. Viral countermeasures against tetherin.**

*HIV-1 Vpu (red) interacts with the tetherin transmembrane domain (TMD) and induces βTrCP-dependent proteasomal and lysosomal degradation as well as βTrCP-independent intracellular sequestration. HIV-2 and SIV Env (light blue) interact with the tetherin extracellular domain and induces endocytosis and intracellular sequestration of tetherin. SIV gp41 (dark blue) interacts with tetherin and induces its endocytosis. SIV Nefs (green) interact with the cytoplasmic tail of tetherin, recruits adapter protein 2 (AP2) leading to tetherin endocytosis.*

## Introduction to fluorescence light microscopy

Fluorescence microscopy has become a widespread tool to investigate biological molecules, organelles and processes in living cells, tissues and even whole animals . Electron microscopy (EM) provides the highest resolution of cellular structures and isolated biological complexes with nm resolution. EM requires highly invasive sample preparation techniques and labeling of specific molecular species at high densities remains challenging.

The main advantage of fluorescence microscopy is specific labeling of multiple biological structures with fluorescent molecules in intact or even living cells. Unfortunately, the resolution of conventional fluorescence microscopy is limited to ~200nm that is the size of many cellular organelles and viruses like HIV-1. Recently developed super-resolution techniques achieve resolutions of down to 10 nm approaching the resolution offered by electron microscopy. The temporal and spatial resolutions of important biological imaging techniques are summarized in Figure 9.

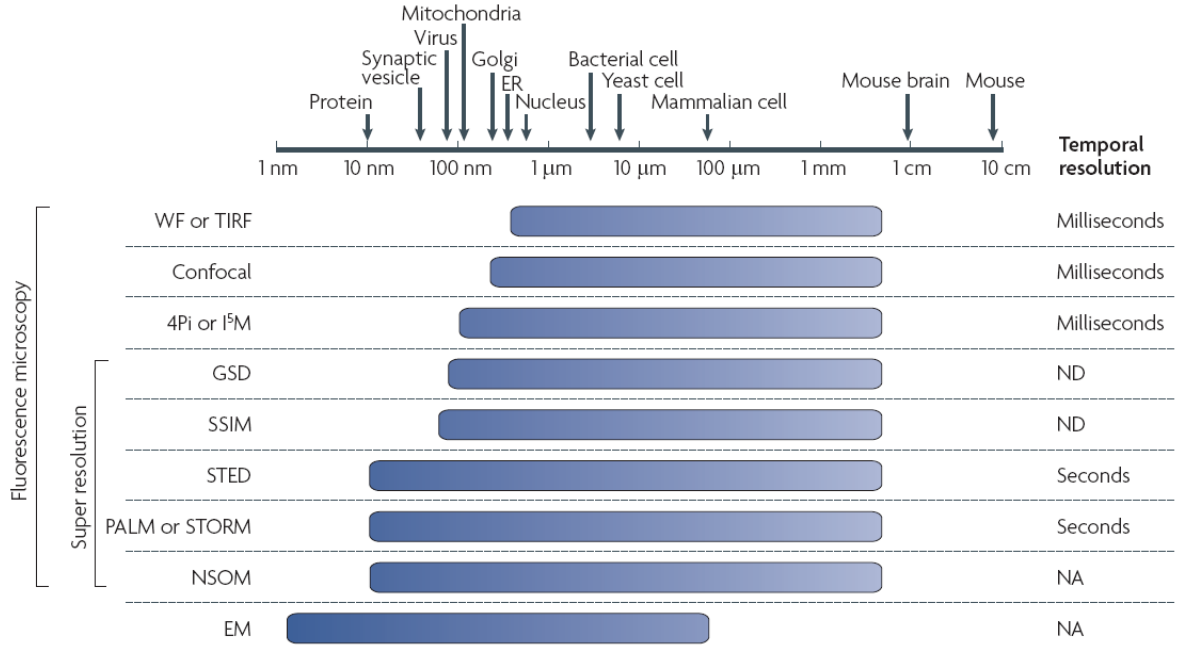


**Figure 9. Spatial and temporal resolution of fluorescence imaging techniques**

*Average sizes of biological features displayed on a logarithmic scale. Wide-field (WF) and total internal reflection fluorescence (TIRF) microscopy are diffraction limited. Confocal, 4Pi and I5M increase lateral and axial resolution. Ground state depletion (GSD), saturated structured illumination microscopy (SSIM), stimulated emission depletion (STED), photoactivation localization microscopy (PALM), stochastic optical reconstruction*

*microscopy (STORM) and near-field scanning optical microscopy (NSOM) are super-resolution methods. Electron microscopy (EM), NA not applicable (adapted from [149]).*

In 1873, Ernst Abbe found that optical resolution of lenses is limited by the diffraction of light. Optical resolution is defined as the minimal distance between two point light sources that can be resolved. Resolution of an objective depends on the wavelength of collected light λ and the numerical aperture of the objective lens (n sinα) defined by the refractive index of the immersion medium (n) and the opening angle of the objective lens (α) .

$$lateral\ resolution = \Delta x, \Delta y = \frac{\lambda}{2\ n \sin \alpha}$$

$$axial\ resolution = \Delta z = \frac{2\lambda}{n \sin^2 \alpha}$$

A light source that is smaller than the resolution of the optical system, for example a single fluorescent molecule, appears as a blurred spot when imaged with a microscope. The intensity profile of this spot, the so-called Airy pattern can be described by a point-spread function (PSF) with significantly stretched z-dimensions. In practice on can measure the full-width at half maximum (FWHM) of this PSF and derive the effective resolution of the optical microscope.

Light microscopes collect transmitted or reflected light from a sample by objective lenses to create a magnified image of the sample. Images are projected into an eyepiece or captured by film or digital cameras.

Standard wide-field light microscopes use absorbance, scattering and phase to create sample contrast to visualize cells and many intracellular structures like the nucleus or lipid droplets. The specific localization of molecular species is limited by diffraction and out-of-focus light further reduces image clarity. Since many cellular structures have little or no contrast, the introduction of specific fluorescence labeling and highly sensitive imaging enabled widespread structural characterization of cells and tissues.

In 1852, Stokes discovered fluorescence as a property of certain substances to absorb light of a certain wavelength and emit light of a longer wavelength (Figure 10A). The difference of absorbance and emission maxima, called Stokes shift enables highly specific detection of fluorophors by carefully selecting excitation light and emission filters (Figure 10B).

Biological materials exhibit autofluorescence, notably at the lower end of the visible spectrum. Specific labeling of biological structures can be achieved with small organic molecules, fluorescent proteins and inorganic quantum dots. Very bright small organic dyes and quantum dots can be conjugated to antibodies and used in standard immunostaining protocols. Peptides or Proteins that react with small fluorescent molecules as well as fluorescent proteins, like green fluorescent protein (GFP) can be genetically tagged to proteins of interests. Fluorescent molecules, proteins and quantum dots cover a wide spectral range and allow imaging of multiple molecular species at the same time.

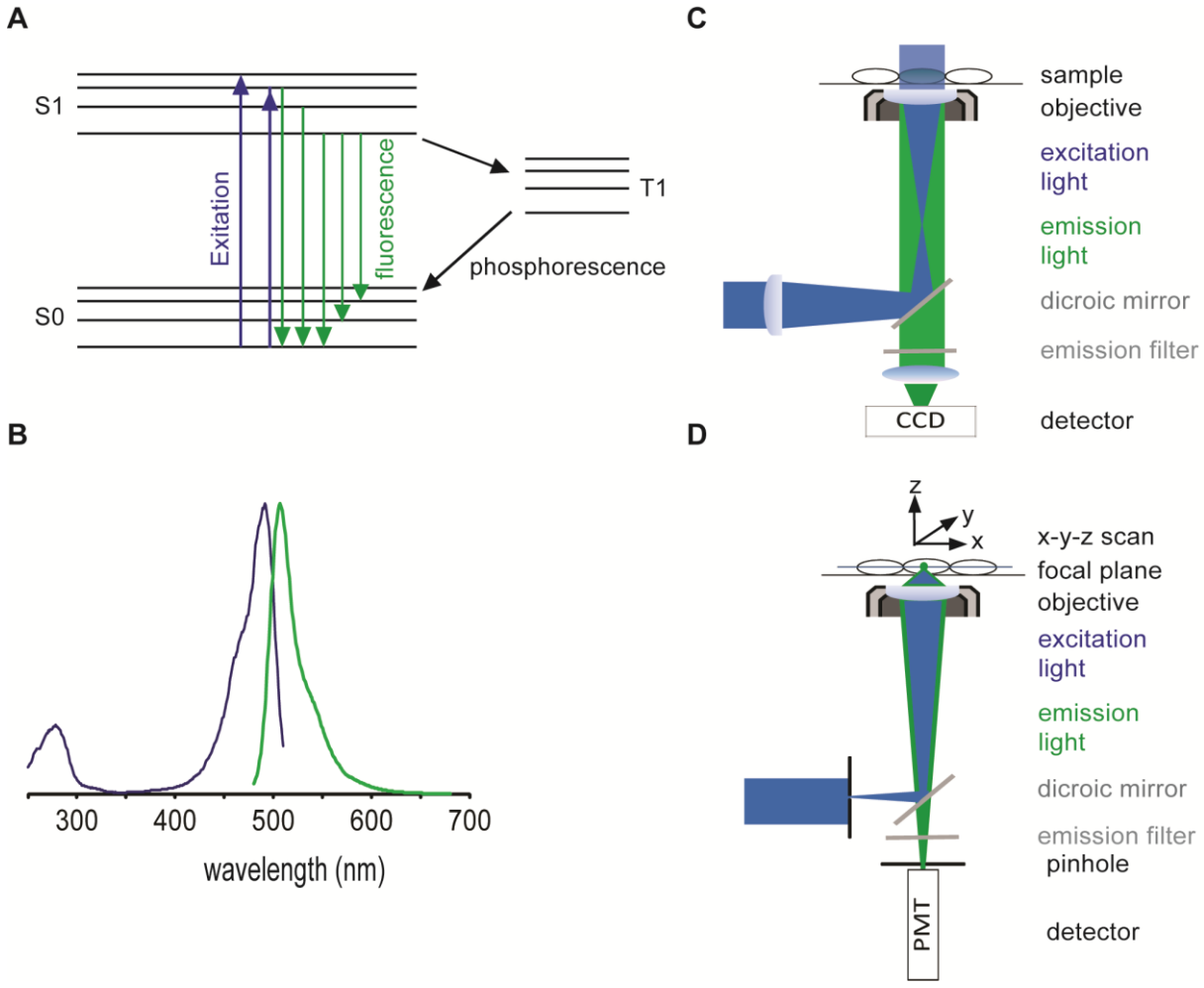


**Figure 10. Principle of fluorescence microscopy**

*(A) Jablonski diagram of a fluorophore displaying ground states (S0), excited states (S1) and triplet states (T1). Excited molecules in the S1 state can return to the S0 state within nanoseconds by emitting fluorescence light. Alternatively, molecules in the S1 state undergo transitions into triplet states and eventually emit phosphorescence within microseconds before returning to the S0 state.*

*(B) Absorbance (blue) and fluorescence emission spectra (green) of the green form of Dendra2 reflect the multitude of transitions between different energy levels within S0 and S1 as shown in panel A.*
*(C) In wide-field fluorescence microscopy blue excitation light is reflected by a dicroic mirror into the objective lens and excites a wide-field within the sample. Green emission light is collected by the same objective, passed through the dicroic mirror and emission filters and focused on a detector, for example a charge-coupled device (CCD). The combination of excitation light, dicroic mirrors and emission filters must eventually be optimized for each individual fluorophor.*
*(D) In confocal laser scanning microscopy excitation light is provided by a laser source that is focused into the sample by the objective to form a detection spot with dimensions of the microscope PSF. Emitted light is collected by the same objective and out-of-focus light is blocked by a pinhole in front of a photomultiplier tube. The confocal detection spot is scanned over the sample in x-y-z direction and can therefore produce optical sectioning.*

## Increasing resolution of fluorescence microscopy

Current wide-field fluorescence microscopes usually achieve resolutions of ~200 nm in lateral and ~500 nm in axial direction by using shortest wavelengths tolerated by cells (>400 nm) and high NA objectives of 1.5 (Figure 10C). Images appear significantly blurred due to fluorescence emission collected from out of focus planes.
Introduction of confocal and two-photon microscopy enabled optical sectioning and deep tissue imaging (Figure 10D). Adding pinholes to the excitation and emission light path or using absorption of two photons in confocal and two-photon microscopy, respectively, allow excitation and detection of fluorescence from a single focal plane. In both techniques, powerful laser light is required to pass enough light through pinhole onto the detector or to enable two-photon absorbance. Images are subsequently acquired by scanning the excitation/detection spot over the sample. High laser power and point-wise detection in scanning confocal microscopy can significantly damage living cells and tissues. Optical sectioning without point-scanning can be achieved by spinning disc confocal microscopy that limits light exposure and allows long terms live imaging with high temporal resolution. Another fast optical sectioning technique is single plane illumination microscopy (SPIM)[150]. In SPIM sheets of excitation light are scanned through thick specimens and emission light is

collected by wide-field optics. Although confocal, two photon and single plane illumination microscopy enabled optical sectioning and 3D imaging none of these techniques significantly increases the lateral or axial resolution beyond the diffraction limit.

Combining two opposing objectives in 4Pi and $I^5M$ microscopy increased the effective numerical aperture and improved lateral resolution. Both lateral and axial resolution could be significantly improved to about 100 nm[151, 152] but require technical challenging alignment of two objectives.
Another concept to break the diffraction limit is near-field scanning optical microscopy (NSOM) that was already proposed in 1928. First images of biological samples by NSOM were just obtained in 1992[153]. In NSOM light is guided directly to the sample through nanometer-sized aperture that is scanned over the sample surface. Whereas lateral resolution is determined by the size of the tip and is in the range of 20-120 nm, sample and probe preparation and restriction to surface imaging limited widespread biological application of NSOM.

In far-field microscopy resolution below the diffraction limit was finally achieved by spatially or temporally controlled transitions between different fluorescent states[149].
Spatially patterning of excitation and emission light is used in structured illumination and stimulated emission depletion (STED) microscopy, respectively.

## Structured illumination microscopy

3D Structured illumination microscopy (3D-SIM) can increase axial and lateral resolution of a wide-field microscope by a factor of two and provides at the same time optical sectioning[154]. Interference patterns formed between samples structures and spatially modulated excitation light contain higher resolution information that can be extracted by deconvolution. SIM can visualize multiple standard fluorophores in fixed cells and fluorescent proteins in live cells[155, 156]. Saturated SIM (SSIM) uses extremely high laser powers to achieve 50 nm resolution of cellular structures labeled with a photoswitchable protein[157]. Of note SSIM samples need to be densely labeled with stable fluorophores to achieve super-resolution below 100nm, since high laser power and repeated imaging significantly degrade the fluorescence signal.

## Stimulated emission depletion (STED) microscopy

In STED microscopy two pulsed laser beams with different wavelengths and shapes illuminate the sample in a confocal scanning mode. The first excitation laser pulse is immediately followed by a red shifted depletion laser pulse that transfers excited fluorophores back to the ground state by stimulated emission (Figure 11A-C). The superposition of the focused excitation pulse and the donut-shaped depletion pulse creates a spatially reduced effective PSF. The remaining fluorescence emitted from the center of the two superposed pulses is registered by a sensitive photo-multiplier tube at each scanned point of the image. The resolution achieved by STED microscopy depends on the maximal intensity of the depletion laser $I^{max}$ and the fluorophor-specific intensity of the depletion laser to deplete 50% of the fluorescence signal $I^{sat}$ and is obtained by extending Abbe's law[152]:

$$spatial\ resolution = \Delta x = \frac{\lambda}{2\ n\ sin\alpha\ \sqrt[2]{\frac{I^{max}}{I^{sat}}}}$$

λ emission wavelength

NA numerical aperture of the objective

As $I^{sat}$ is a characteristic of the fluorophor not all fluorophors are well suited for STED microscopy. Using an optimal fluorophor ATTO 532 with a custom made STED set-up achieved 15-20 nm lateral resolution [158, 159], that was extended to 50-70 nm in all three dimensions in biological samples. Despite the requirement of multiple high power laser lines STED microscopy was successfully extended to two-color and live cell imaging[160-162].

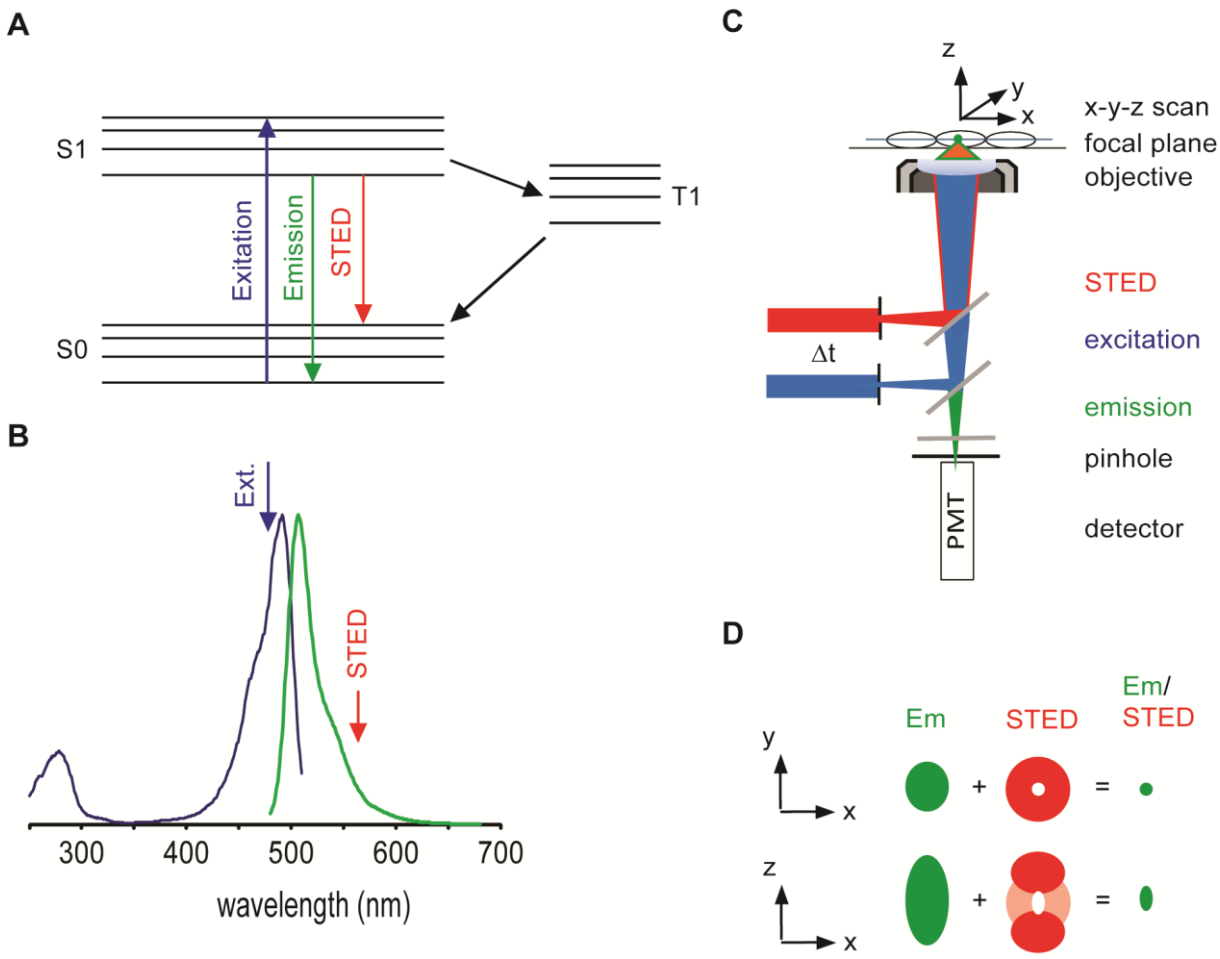


**Figure 11. Principle of stimulated emission depletion (STED) microscopy**

*(A) Jablonski diagram of a fluorophore displaying ground states (S0), excited states (S1) and triplet states (T1). Excited molecules in the S1 state can return to the S0 state within nanoseconds by emitting fluorescence light. Alternatively, a red-shifted STED laser pulse depletes excited molecules from the S1 state without causing fluorescence emission. (B) Absorbance (blue) and fluorescence emission spectra (green) with excitation and STED wavelengths indicated. (C) STED is realized in the context of a confocal laser scanning microscopy as depicted in this scheme. Excitation and STED laser pulses are time-shifted and focused into the sample by a lens in a way that they have different shapes as shown in (D). Overlaying the emission point-spread function with the donut-shaped STED spot that features a naught at its center results in a subdiffraction spot. The STED detection spot is scanned over the sample with a step size of half the desired resolution. STED can produce resolution of 20 nm in x-y and 50 70nm in z direction under optimal conditions. This figure was inspired by* [152].

## Single molecule localization microscopy

Single molecule localization (Figure 12) is used in similar approaches termed photoactivation localization microscopy (PALM)[163], fluorescent PALM (fPALM)[164], stochastic optical reconstruction microscopy (STORM)[165], direct STORM (dSTORM)[166] and ground-state depletion followed by single molecule return (GS-DIM)[167]. Single molecules can be localized with a lateral precision (Δx, Δy) that depends on the excitation wavelength, numerical aperture of the objective and pixel size included in $c_1$ and $c_2$, the number of collected photons (N) and the background noise per pixel (b)[149].

$$lateral\ resolution = \Delta x, \Delta y \approx \frac{c_1}{\sqrt[2]{N}} + \frac{c_2\ b}{N}$$

Importantly the resolution of single molecule localization microscopy critically depends on background level and the number of photons emitted by single molecules.

Fluorescent proteins and bright fluorescent organic dyes usually give 400 and 10 000 photons, respectively that results in ~20 nm and ~2 nm localization precision assuming the absence of background. Therefore, the brighter the fluorescent probe the better the localization precision and effective resolution. Cellular autofluorescence, fluorescence from impurities and background from non-activated molecules limit the resolution, but can be minimized by careful cleaning, sample preparation, choice of fluorophors with non-fluorescent dark states. Lower background can also be achieved by imaging single molecules in total internal reflection fluorescence (TIRF) mode[163].

Effective resolution in single molecule based microscopy is determined by localization precision but also by the number of localizations according to the Nyquist criterion[168]. Nyquist resolution is twice the average distance between neighboring localizations. For example in order to achieve 20nm effective resolution the average distance between localized fluorophors should be less than 10nm.

Therefore the number of emitted photons, the number of single molecule localizations and the photobleaching rate of fluorescent probes determine their suitability for live-cell PALM and STORM[168, 169]. Live PALM microscopy of adhesion complexes and STORM of clathrin-mediated endocytosis achieved imaging rates of 25-60s and 30s, respectively. Even when live cell PALM analysis of HIV-1 Gag and an viral envelope glycoprotein did not full-fill the Nyquist criterion important insights into dynamic membrane organizing principles could be obtained from single particles tracking at temporal resolutions of 50-100ms [170, 171].

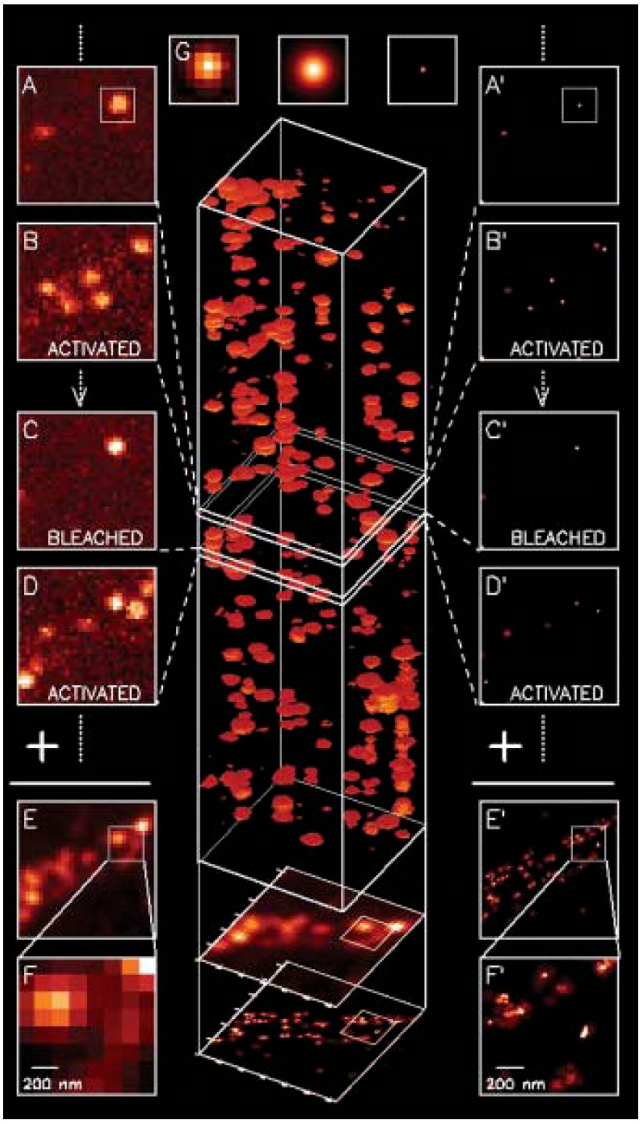


**Figure 12. Principle of photoactivation localization microscopy**

*A sparse set of photoactivatable proteins fused to the protein of interest is activated by a brief pulse of 405 nm light (A, B) and imaged until most fluorophors are bleached (C). Single molecule positions are determined by Gaussian fitting of intensity distributions (G) with a precision* $\Delta x,y \approx \sigma_{x,y}/N^{1/2}$ *,where* $\sigma_{x,y}$ *denotes the standard deviation of the Gaussian function and N the number of collected photons. Repeated activation (G), imaging, localization and finally summing up single molecule positions from all frames results in a super-resolution image (E', F'). Other single molecule localization techniques are based on the same principle. Taken from*[163].

## Probes for single molecule localization microscopy

Importantly in order to control the density of single molecules within the imaging frame that is critical to localization, two concepts were introduced:

As depicted in Figure 13 the fluorescent dyes Alexa Flour 647 (Alexa 647, Invitrogen,) can be transferred to a triplet state by applying high laser powers of 657 nm at 15 kW/cm$^2$ [169, 172]. In a reducing and oxygen free environment reactivation of Alexa 647 from the dark state is achieved by exciting a nearby activator fluorophor, for example Cy2 with 457nm light [172] or by illuminating the sample directly with 514 nm[166]. Combinations of activator and reporter fluorophores coupled to the same secondary antibody molecule enable multicolor STORM [173]. Several fluorophores were found to have light induced dark states and reactivation properties in defined chemical environments and inside cells similar to Alexa 647 [169, 174, 175]. Organic fluorescent dyes are mostly targeted to biological structures by immunodetection, that has limited access to live cells.

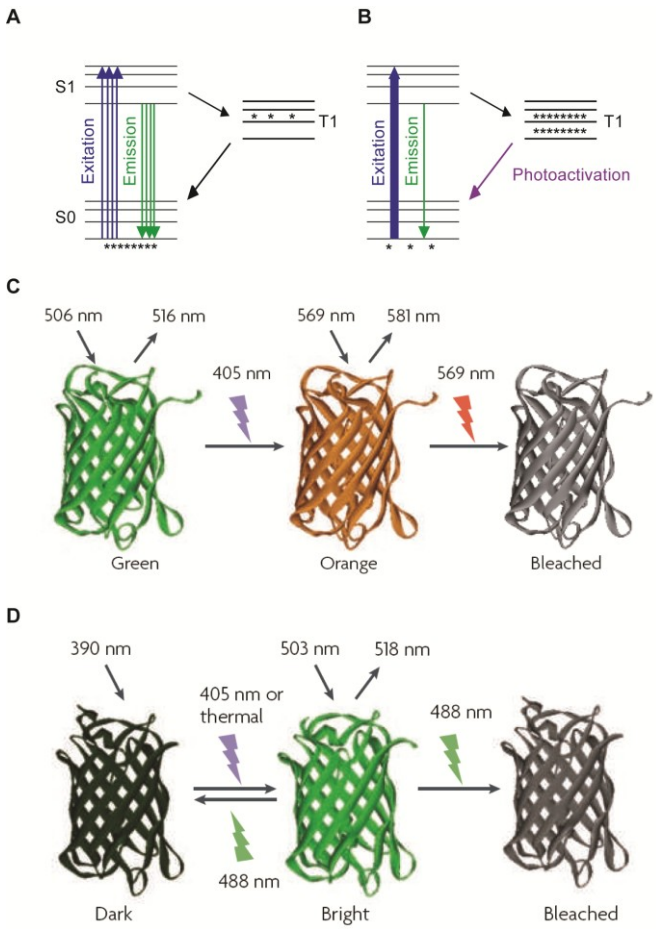


**Figure 13. Fluorescent transitions of organic dyes and fluorescent proteins**

*(A) At low laser power multiple molecules within a field undergo excitation and emit fluorescence*

*(B) At high laser power most molecules are transferred to dark states (triplet states). Few molecules spontaneously or through photoactivation return to the S0 state and can be imaged individually.*

*(C) Irreversible photoshifting of mEosFP between a green and a orange form*

*(D) Reversible photoactivation of Dronpa between dark and green state*

Numbers indicate wavelengths.

Panels C and D were taken from [149]

Other probes used for fluorescent single molecule localization are photoactivatable and photoswitchable fluorescent proteins (Figure 13C,D), that change their spectral properties upon exposure to light with specific wavelengths[149]. Similar to organic dyes high localization precision for fluorescent proteins will depend on their extinction coefficients ($\varepsilon_{abs}$), fluorescence quantum yield ($\eta_{fl}$), contrast between unactivated and activated forms and activation rate. As for most cell biology applications monomeric fluorescent proteins are preferred as they usually minimally interfere with fusion protein functions.

Photoactivatable fluorescent proteins (PAFP) can convert irreversibly from a dark to a fluorescent form. Examples are commonly used PA-GFP [164, 176] and PA-mCherry1[177], that were combined into two-color PALM[177]. Alternatively, PAFP are irreversibly shifted from one fluorescent to another fluorescent form that differ both in excitation and emission maxima. Popular examples are green-to-red photoconverters are mEosFP[178], mKikGr[179] and Dendra2[180], but also blue-to-green PS-CFP2[180] and orange-to-far-red photoswitcher PS-mOrange[181] are available.

The highest localization precisions in lateral and axial directions have been obtained with recently optimized form of mEosFP that is mEos2[182] in interferometric PALM[183] of fixed cells and living cells[169]. tdEos was use in single particle tracking PALM (sptPALM) and allowed tracking of HIV-1 Gag with 50ms temporal resolution[171].

Reversible photoswitchable fluorescent proteins can be converted multiple times between dark and fluorescent states, like for example Dronpa[184]. Dronpa is repeatedly converted from dark to a green fluorescent state by 405 nm light and returns back to the dark state upon excitation with 488nm used for imaging the green form, that limits its photon yield[149]. Padron, a Dronpa variant with positive switching characteristics allowed monochromatic multilabel PALM in combination with Dronpa[185]. Similarly red fluorescent rsCherry and rsCherryRev were engineered and could be used in monochromatic multilabel PALM[186]. Initially for multicolor PALM imaging tdEos was used in combination with Dronpa or PS-CFP2[187]. Recently of three PAFP could imaged simultaneously as their emission separated spectrally[188].

Alternative labels for localization microscopy are photocaged fluorophores and quantum dots. Caged O rhodamine and carboxyfluoresceine were used in initial PALM studies[163]. Alternatively labeling strategies known as CLIP and SNAP can be used to label fusion proteins with bright organic dyes for live-cell dSTORM [169, 175]. Both strategies still require fusion of circa 180 aa to the protein of interest that may interfere with protein functions.

Consequently, small molecule labeling techniques are needed that require only a short peptide sequence like in case of the tetracysteine Tag (6-10 aa, Invitrogen).

Quantum dots are extremely bright and photo-stable semiconductor nanocrystals with sharp but size dependent emission peaks. Importantly QD can be attached to antibodies or streptavidin. Recently QD were reported to show light induced blue shifts of emission due to shrinking of the nanocrystal. This "blueing" effect was used to perform localization microscopy with 20 nm resolution using a simple camera, commonly found in webcams[189].

## The single molecule localization microscope

Single molecule super-resolution microscopy is generally performed with a TIRF-capable microscope equipped with powerful lasers, appropriate filters, high NA wide-field objectives and very sensitive EMCCD cameras as exemplified in Figure 14.

High numerical aperture TIRF objectives allow collecting emitted photons efficiently and increasing contrast through selective excitation of up to 200 nm slices from the coverslip. Oil-immersion objectives provide higher NA (NA $\geq$ 1.4) than water immersion objectives (NA $\geq$ 1.2), but produce higher spherical aberrations[190]. Combined magnification from the objective and tube lenses should be adjusted in such a way that the signal from a single molecule signal occupies at least 2 pixels in order to avoid localization errors[190]. The effective resolution can be obtained from photon counts per single molecule or by imaging isolated single molecules [172]. Powerful readout lasers are required to maximize photon counts from individual emitting fluorophors and to bring most of the organic dyes to the dark state. Readout laser wavelengths should be as close as possible to excitation maxima of the fluorophors. Dicroic mirrors and bandpass filters should be optimized to eliminate all excitation light from the detection channel, allow distinction of emission from different fluorophors and maximize the collection of emitted light from single molecules. The camera frame rates should reflect a compromise between maximizing photon counts and minimizing exposure times to limit errors due to stage drift and movement of living cells. Usually 405 nm activation light is applied as pulses or continuously, depending on the fluorophor properties. For PAFP the intensity of activation light or the length of activation pulses can be gradually increased over the course of the experiment since less and less PAFP are available for imaging. The density of activated molecules should not exceed one molecule/$\mu m^2$ to avoid localization errors due to overlapping single molecule images.

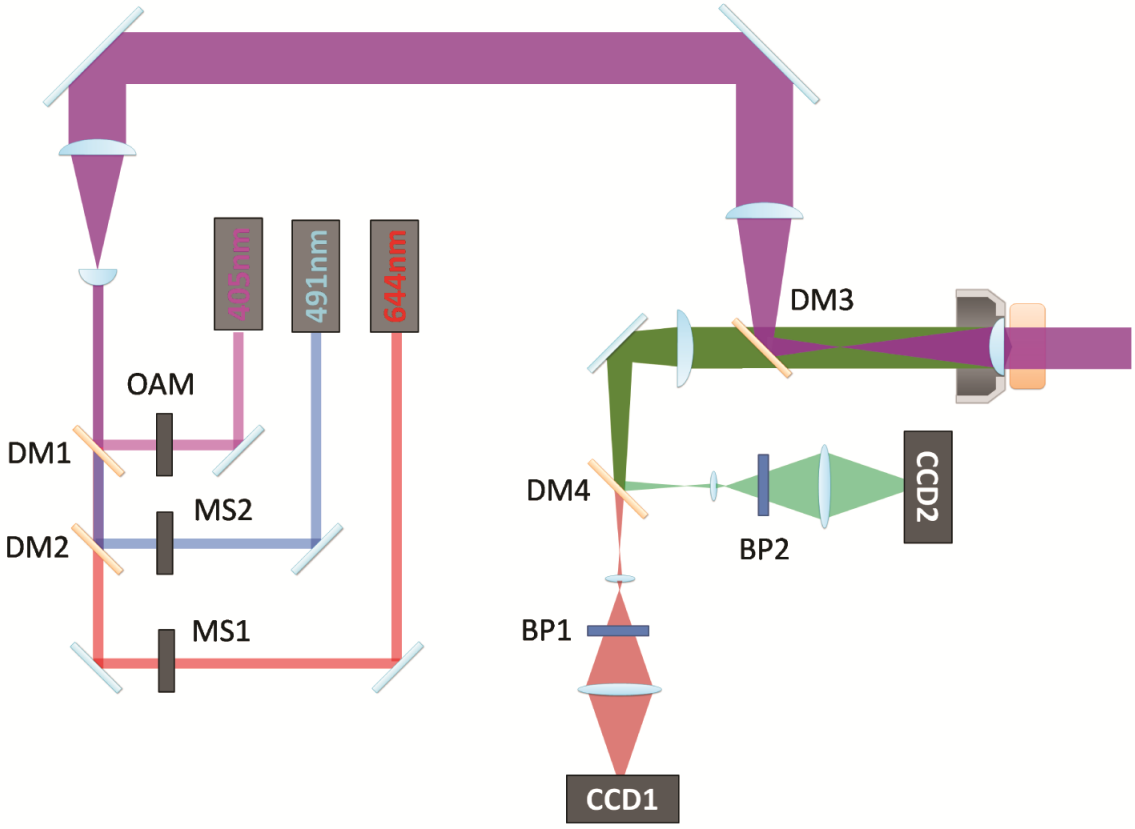


**Figure 14. Scheme of two-color single molecule super-resolution set-up used to detect Dronpa and Alexa 647**

*The activation laser (405nm) and the excitation lasers 491nm and 644nm are expanded, collinearly aligned and directed to the microscope stand via dichroic mirrors (DM1 and DM2) and controlled by mechanical shutters (MS1 and MS2). Lasers are subsequently focused on the back focal plane of a high numerical aperture TIRF objective and directed into the sample in TIRF mode. Fluorescence is collected by the same objective from the 100-200nm TIRF plane immediately above the coverslip. The intensity of activation laser light is adjusted by an acoustic optic modulator (OAM) and determines the density of activated molecules. Fluorescence is separated from excitation light by DM3 and separated by DM4 into two detection channels containing Dronpa and Alexa 647 specific filters ((BP1 and BP2). Tube lenses in each detection channel are used to further magnify images that are finally detected on EMCCD cameras (CCD1 and CCD2). See Material and Methods and Figure S2 of [191] for details.*

# Results and Discussion

## Paper 1: Quantitative Multicolor Super-Resolution Microscopy Reveals Tetherin HIV-1 Interaction

HIV-1 assembly and interaction with host-cell proteins occur at length scales below the diffraction limit of visible light, which is typically below 250 nm. Widely used electron microscopy techniques provide detailed pictures of viral and cellular structures, but specific and high density labeling of proteins is challenging. Novel single molecule based super-resolution microscopy techniques achieve nanometer resolution of cellular and viral proteins under minimally invasive conditions. We were particularly interested in the interaction of HIV-1 with the cellular restriction factor tetherin that inhibits HIV-1 release through direct incorporation into viral membranes. Tetherin plasma membrane distribution, virus-tetherin interaction and orientation of tetherin molecules across host cell and viral membrane are not yet fully understood.

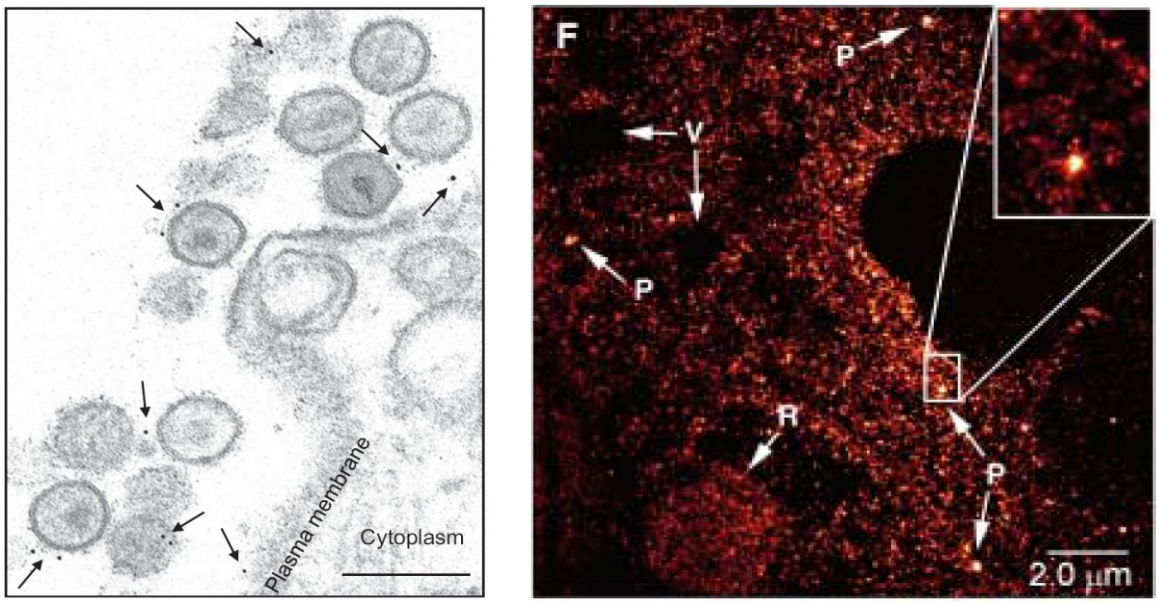


**Figure 15. Examples of Immunoelectron microscopy and PALM of HIV particles**

*(A) Transmission electron microscopy analysis of HT1080 that stably express tetherin-HA cells that were infected with vpu-deficient HIV-1 and stained with anti-HA antibodies and IgG gold particles, scale bar 200nm (from Perez-Caballero 2009) (B) PALM image of a fixed COS-7 cell expressing HIV-1 Gag tagged with tdEos showing voids (V), high density regions (R) and particles (P) of 100-150nm in the inset*[163] *(from Betzig et al (2006)*

Previous immune-electron microscopy analysis found tetherin at budding sites but low density labeling allowed no quantitative analysis of tetherin distribution (Figure 15).

Here for the first time, we set-up and applied multicolor super-resolution microscopy based on single molecule localization to analyze HIV-host interactions. First, we established labeling of the HIV-1 structural protein Gag and tetherin with monomeric photoactivatable proteins, that minimally affected both proteins functions (Figure 1-2 and S1). HIV-1 labeling was best achieved by Gag and Vpr fused to Dronpa and mEosFP. A two-color super-resolution microscope was build and calibrated using fluorescent beads. We then labeled viral particles with PAFP fusions and antibodies to reveal known and unknown viral protein localization by super-resolution microscopy (Figure 1 and S2-3). We could resolve Matrix and Capsid structures within individual HIV-1 particles and found Integrase colocalized with Capsid as well as a clustered Env distribution at the viral membrane (Figure 1C, D). Overall, we established three fluorescent labels with different spectral characteristics that can be used on transfected and immunostained cells. At the plasma membrane of fixed cells we visualized tetherin alone and at HIV-1 budding sites. We found tetherin within single clusters of 70-90nm both in the absence and presence of HIV-1 (Figure 2-3). Through a combination of enzymatic removal or surface-tethered virions and super-resolution analysis we could establish that tetherin incorporates its TMD into budding virions and restricts particles release as an extended dimer (Figure 4 and 5). Careful photo-physical characterization of purified single molecules of mEosFP and optimization of imaging and analysis conditions allowed the subsequent determination of tetherin molecule numbers at budding sites (Figure 7).

OPEN ACCESS Freely available online

PLoS PATHOGENS

# Quantitative Multicolor Super-Resolution Microscopy Reveals Tetherin HIV-1 Interaction

**Martin Lehmann[1], Susana Rocha[2], Bastien Mangeat[1,3], Fabien Blanchet[3], Hiroshi Uji-i[2], Johan Hofkens[2], Vincent Piguet[1,3]***

**1** Departments of Microbiology and Molecular Medicine, Dermatology and Venereology, University Hospital and Medical School of Geneva, Geneva, Switzerland, **2** Laboratory for Photochemistry and Spectroscopy, Department of Chemistry, Katholieke Universiteit Leuven, Heverlee, Belgium, **3** Department of Dermatology and Wound Healing, Cardiff University School of Medicine and University Hospital of Wales, Cardiff, Wales, United Kingdom

## Abstract

Virus assembly and interaction with host-cell proteins occur at length scales below the diffraction limit of visible light. Novel super-resolution microscopy techniques achieve nanometer resolution of fluorescently labeled molecules. The cellular restriction factor tetherin (also known as CD317, BST-2 or HM1.24) inhibits the release of human immunodeficiency virus 1 (HIV-1) through direct incorporation into viral membranes and is counteracted by the HIV-1 protein Vpu. For super-resolution analysis of HIV-1 and tetherin interactions, we established fluorescence labeling of HIV-1 proteins and tetherin that preserved HIV-1 particle formation and Vpu-dependent restriction, respectively. Multicolor super-resolution microscopy revealed important structural features of individual HIV-1 virions, virus assembly sites and their interaction with tetherin at the plasma membrane. Tetherin localization to micro-domains was dependent on both tetherin membrane anchors. Tetherin clusters containing on average 4 to 7 tetherin dimers were visualized at HIV-1 assembly sites. Combined biochemical and super-resolution analysis revealed that extended tetherin dimers incorporate both N-termini into assembling virus particles and restrict HIV-1 release. Neither tetherin domains nor HIV-1 assembly sites showed enrichment of the raft marker GM1. Together, our super-resolution microscopy analysis of HIV-1 interactions with tetherin provides new insights into the mechanism of tetherin-mediated HIV-1 restriction and paves the way for future studies of virus-host interactions.

**Citation:** Lehmann M, Rocha S, Mangeat B, Blanchet F, Uji-i H, et al. (2011) Quantitative Multicolor Super-Resolution Microscopy Reveals Tetherin HIV-1 Interaction. PLoS Pathog 7(12): e1002456. doi:10.1371/journal.ppat.1002456

**Editor:** Hans-Georg Krausslich, Universitätsklinikum Heidelberg, Germany

**Received** May 17, 2011; **Accepted** November 9, 2011; **Published** December 15, 2011



**Funding:** VP was supported by the Human Science Frontier Program and Swiss National Science Foundation. SR was supported by Portuguese Foundation for Science and Technology (FCT) PhD grant SFRH/BD/27265/2006. JH was supported by the long-term structural funding program "Methusalem" by the Flemish government, the K.U. Leuven research fund (GOA 2006/2, CREA2007), Fonds voor Wetenschappelijk Onderzoek Vlaanderen (FWO grant G.0402.09) and the Herculesstichting. The funders had no role in study design, data collection and analysis, decision to publish, or preparation of the manuscript.

**Competing Interests:** The authors have declared that no competing interests exist.

* E-mail: piguetv@cardiff.ac.uk

## Introduction

Although viruses heavily depend on the host cell machinery for their replication, they also face numerous blockades imposed by cellular proteins at several distinct steps in their life cycle. Recently, tetherin, an interferon-induced transmembrane protein has been shown to restrict the release of HIV-1 [1,2] and other enveloped viruses [3–5]. Viruses also possess several anti-tetherin activities encoded by proteins such as HIV-1 Vpu [2,6], SIV Nefs and Envelope (ENV) [7–9], HIV-2 ENV[10] and Karposi's sarcoma-associated herpesvirus K5 [5].

Tetherin possesses two membrane anchors in an unusual topology, namely a N-terminal transmembrane (TM) domain and a C-terminal glycophosphatidylinositol (GPI) lipid anchor, proposed to mediate lipid raft interaction [11]. The extracellular domains of two tetherin molecules form parallel cysteine-linked coiled-coil domains [12,13]. Perez-Caballero *et al.* used tetherin mutants and artificial tetherin composed of fragments of heterologous proteins in a tetherin-like topology to demonstrate that tetherin inhibits HIV-1 release through direct tethering of virions to cells [13]. Direct incorporation of tetherin into HIV-1 virions was also confirmed by biochemical analysis and electron microscopy [13–15]. HIV-1 Vpu interacts with the tetherin transmembrane domain [6,16] and counteracts tetherin by degradation and removal from the cell surface [2,17–19]. Through these combined activities, Vpu impairs incorporation of tetherin into virions and restriction [13]. Detailed analysis of tetherin distribution in the plasma membrane, of the role of lipid rafts in HIV-1 tetherin interactions and of the orientation and number of tetherin molecules involved in restriction is still lacking.

HIV-1 assembly into virions of 100–150 nm diameter at the plasma membrane of infected cells involves an extensive range of host cell factors [20]. Widely used electron microscopy techniques provide detailed pictures of viral and cellular structures, but high density labeling of viral and cellular proteins as well as quantitative image analysis remain challenging. Novel single-molecule super-resolution imaging by photoactivated localization microscopy (PALM) [21], fluorescence PALM (fPALM) [22], stochastic optical reconstruction microscopy (STORM) [23] and direct STORM (dSTORM) [24] exploit photoswitching properties of photoactivatable fluorescent proteins (PAFP) and organic dyes to localize them with nanometer resolution. Multicolor super-resolution microscopy [25,26] can resolve distances of 20–200 nm that are relevant for virus-host interactions and bridge the gap between

## Author Summary

Human immunodeficiency virus 1 (HIV-1) assembles and interacts with cellular proteins at the plasma membrane of infected cells. Here, we analyzed individual HIV-1 virions, viral assembly sites and the mechanism of tetherin restriction by multicolor super-resolution microscopy using fully functional fluorescently labeled tetherin and viral proteins. Viral proteins within virions were visualized with nanometer resolution yielding new insight into the structure of the HIV-1. Our super-resolution analysis was extended to tetherin, a cellular restriction factor that inhibits the release of several enveloped viruses. Tetherin was localized in clusters of 70–90 nm at the plasma membrane that contain 5–11 dimers. In contrast tetherin clusters found at HIV-1 assembly sites contained on average 4–7 tetherin dimers. Clustering of tetherin was dependent on both tetherin membrane anchors. The transmembrane domain of tetherin associated with budding virions independently of GM1 lipid raft domains. Our data indicated that extended dimers tether HIV-1 virions directly to the cell. Overall, we provide for the first time super-resolution analysis of authentic virions, virus budding sites and HIV-1 interactions with the anti-viral factor tetherin. Our data offer novel insights into the mechanisms of tetherin restriction.


Fluorescence Resonance Energy transfer (FRET) and conventional diffraction limited fluorescence microscopy [27].

Previous super-resolution imaging revealed single molecule dynamics and assembly of tandem-EosFP tagged HIV-1 Gag into virus-like particles of 100–200 nm [21,28].

Here, we set up labeling of HIV-1 and tetherin with monomeric PAFP and antibody staining for multicolor super-resolution microscopy in cells. We visualized precise localization of HIV-1 proteins in virions and at budding sites at the plasma membrane of cells. Super-resolution analysis showed that tetherin formed clusters, whose integrity depended on both membrane anchors. Importantly, tetherin clusters closely associated with HIV-1 budding sites. Through a combination of biochemical analysis and super-resolution microscopy of tetherin mutants, we showed that tetherin restricts virion release as extended dimers and that the transmembrane domain of tetherin possesses affinity for HIV-1 assembly sites.

## Results

In order to perform single-molecule super-resolution microscopy of HIV-1, we fused different PAFP to HIV-1 Gag, the major structural protein of virions, yielding: Gag-Dronpa, Gag-PS-CFP2, Gag-Dendra2, Gag-mKikGR, Gag-mEosFP and Gag-PAmCherry (Figure S1A). The monomeric PAFP are expected to minimally interfere with HIV-1 particle formation [29,30], a potential caveat of the Gag fused to tandem-EosFP. The different constructs were expressed together with full-length HIV-1 in 293T cells and analyzed for incorporation into HIV-1 particles, effect on viral infectivity and performance in single-color super-resolution imaging [31]. We selected Gag-Dronpa and Gag-mEosFP for super-resolution imaging of HIV-1 virions, due to their expression as full length fusion proteins, minimal impact on infectivity and superior signal-to-noise ratios (Figure S1B–D).

To visualize HIV-1 and cellular proteins labeled with PAFP or Alexa Fluor 647 labeled antibodies, we setup a two-color super-resolution microscope with widefield illumination in total internal reflection (TIR) mode. Fluorescence emission of Dronpa, mEosFP and Alexa Fluor 647 were detected simultaneously by two Electron Multiplying CCD cameras using specific filter sets and synchronized photoactivation/excitation/detection schemes as depicted in Figure S2. Notably, differences in alignment of both cameras and chromatic aberrations were corrected using a high resolution mapping procedure (Figure S3) based on local weighted mean transformation [32]. Colocalization precision of $\sim$17 nm throughout the total field of view was routinely achieved (Figure S3F). Our two-color super-resolution microscope therefore enabled colocalization analysis of proteins labeled with PAFP or antibodies in the range of 20–200 nm which covers scales relevant to HIV-1 host interactions.

### HIV-1 virion structure and assembly sites

To determine the localization of HIV-1 proteins within virions, we performed super-resolution microscopy on double-labeled HIV-1 particles.

HIV-1 virions specifically incorporated Dronpa-labeled Vpr, a HIV-1 protein associated with viral cores, Gag-Dronpa and Gag-mEosFP, but not Dronpa alone (Figure 1A and Figure S4A). Notably, labeling HIV-1 virions with the monomeric PAFP fusions minimally affected infectivity and therefore likely preserves virion structure (Figure 1B).

HIV-1 virions that contained HA-tagged integrase (INHA) and Dronpa-Vpr were fixed on coverslips, permeabilized and further labeled by indirect immunofluorescence against Integrase (IN), capsid (CA), matrix (MA) or gp120 envelope (ENV) followed by Alexa Fluor 647-coupled secondary antibodies (Figure 1C–E). Super-resolution microscopy of double labeled virus particles showed an important increase in resolution when compared to diffraction-limited confocal laser scanning or total internal reflection fluorescence (TIRF) microscopy (Figure 1C and Figure S1D). The high degree of colocalization in super-resolution images of the two HIV-1 proteins Dronpa-Vpr and CA (Figure 1C) demonstrated the performance of the calibration procedure in a biological context. The sizes of HIV-1 structures were determined through cluster analysis of single molecule localizations as described in Materials and Methods after testing on simulated clusters (Figure S5). We found similar average sizes for Dronpa-Vpr (94$\pm$17 nm), Gag-Dronpa (108$\pm$39 nm) and Gag-mEosFP (94$\pm$37 nm, mean$\pm$StD) consistent with their localization inside HIV-1 virions (Figure S4B).

In contrast, IN, CA, MA and ENV showed more variable sizes: 75$\pm$20 nm for IN, 112$\pm$31 nm for CA, 117$\pm$45 nm for MA and 127$\pm$45 nm for ENV (mean$\pm$StD, Figure 1D and Figure S4C). Notably, IN colocalized with Dronpa–Vpr cores as a discrete structure with narrow size distributions, likely due to their common presence in the viral core. Similar sizes observed for CA and MA structures could result from proximity of the C-terminal epitope of mature MA and the epitope recognized by the CA antibody. In contrast, HIV-1 ENV was found in 1-2 discrete peripheral clusters per Dronpa-Vpr containing virion (Figure 1E).

Next, we used super-resolution microscopy to visualize HIV-1 in a cellular context. We analyzed HIV-1 protein distribution at the plasma membrane of non-permeabilized HeLa cells transfected with HIV-1 and Gag-mEosFP and stained for ENV. We observed distinct clusters of Gag-mEosFP surrounded by antibody labeled ENV clusters (Figure 1F) that represent HIV-1 assembly sites [21,28,29]. Altogether, our data demonstrates that super-resolution microscopy allows precise localization of HIV-1 proteins in infectious virions and budding structures, which previously could only be observed by electron microscopy [33–35].

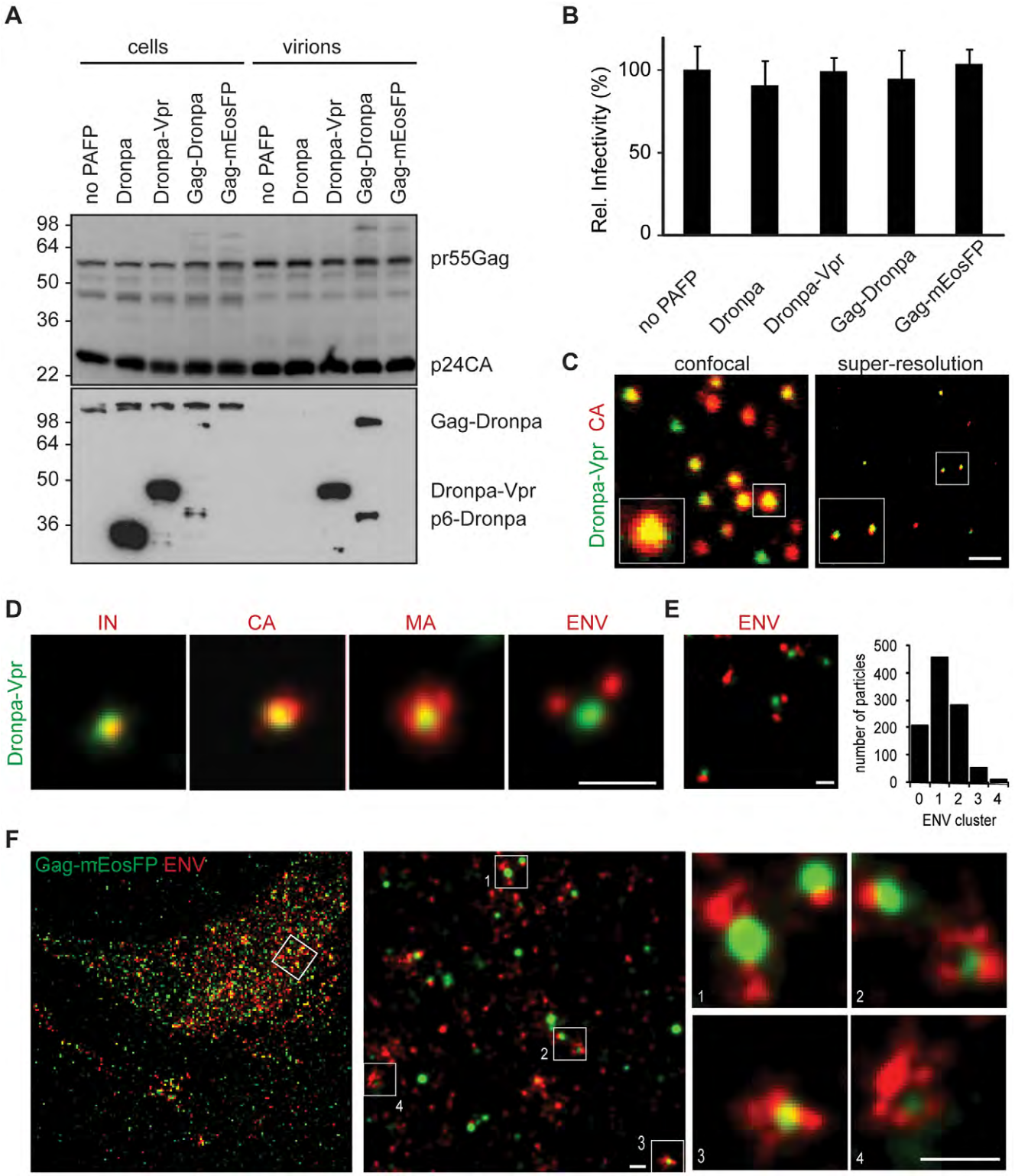


**Figure 1. Structural features of single HIV-1 virions and assembly sites are revealed by multicolor super-resolution microscopy.** (A) Western blot analysis (anti-p24CA upper, anti-Dronpa bottom) of cellular lysates and purified virions from 293T cells transfected with HIV-1 INHA and indicated photoactivatable fluorescent protein (PAFP). Sizes of molecular weight markers are shown in kilodaltons. (B) Relative infectivity of virions from (A). Error bars represent standard deviation of triplicate titrations. One representative experiment out of two is shown for panel A and B. (C) Virions labeled with Dronpa-Vpr and primary anti-CA and Alexa Fluor 647 secondary antibodies were analyzed by confocal laser scanning (left) or super-resolution microscopy (right). (D) Virions containing Dronpa-Vpr (green) were labeled by indirect immunofluorescence with primary antibodies against HA (IN), HIV-1 capsid (CA), matrix (MA) or gp120 (ENV) and Alexa Fluor 647 secondary antibodies (red). Representative super-resolution images from two virus preparations are shown. (E) Super-resolution image (left) of ENV (red) on Dronpa-Vpr particles (green). Quantification (right) was performed by counting the number of ENV clusters on 1000 HIV-1 particles in 4 images of two independent virus preparation. (F) HeLa cells

expressing HIV-1 Δvpu and Gag-mEosFP (green) were labeled by indirect immunofluorescence with primary anti-gp120 (ENV) and Alexa Fluor 647 secondary antibodies (red), conventional resolution (left) and super-resolution image (right), scale bars 1 μm (c) and 200 nm (d–f).
doi:10.1371/journal.ppat.1002456.g001

## Tetherin distribution and orientation

We next set out to visualize HIV-1 tetherin interactions at the plasma membrane using this technique. First, the plasma membrane distribution of endogenous and overexpressed tetherin was analyzed by super-resolution microscopy in cells. Tetherin constructs containing N-terminal mEosFP or epitope-tags (HA or Flag) inserted after the extracellular coiled-coil domain (Figure 2A) efficiently restricted the release of vpu-deficient HIV-1 (HIV-1 Δvpu) and are counteracted by Vpu in transfected 293T cells (Figure 2B and Figure S6A). Notably the cellular levels of mEosFP-tetherin, tetherin-Flag and tetherin-HA were reduced in presence of HIV-1 Vpu (Figure 2C and Figure S6B), indicating efficient Vpu-mediated degradation of these constructs. The N-terminal fusion of mEosFP to tetherin does not interfere with HIV-1 assembly (Figure S6C) and no cleavage of the fusion protein was observed (Figure 2C and Figure S6C). Overall, labeling tetherin with PAFP and epitope-tags minimally affects restriction activity and preserves Vpu-sensitivity.

In HeLa cells we found endogenous and overexpressed tetherin in homogenously distributed clusters of 70–90 nm using labeling with mEosFP or antibody staining followed by super-resolution microscopy (Figure 2D). Ripley's L function was previously used to characterize extent of clustering of influenza hemagglutinin (HA) and T cell receptor complexes [36,37] and was tested on simulated clusters of 50–400 nm (Figure S5). Ripley's L function indicated clustering of endogenous tetherin and all tetherin constructs tested (Figure 2E). In contrast tetherin mutants lacking the transmembrane domain (delTM) or GPI anchor (delGPI) showed decreased clustering (Figure 2F), which was confirmed by decreased peaks of Ripley's L function that shifted to larger distances compared to wild-type tetherin (Figure 2G). Overall, labeling of tetherin for super-resolution microscopy preserved restriction activity, Vpu-sensitivity and revealed a clustered distribution, which depends on both tetherin's membrane anchors.

## Distribution of tetherin molecules at HIV-1 assembly sites

Since super-resolution microscopy enabled us to resolve structural features of viral particles and the distribution of tetherin (Figures 1 and 2), we next determined where tetherin localizes with respect to HIV-1 assembly sites. HeLa cells were cotransfected with HIV-1 Δvpu and Gag-mEosFP and tetherin-HA or tetherin-Flag and analyzed by indirect immunofluorescence and super-resolution microscopy. Gag-mEosFP-containing budding structures at the plasma membrane were mostly found in close proximity with a single cluster of tetherin-HA or tetherin-Flag (Figure 3A and B). Similarly, mEosFP-tetherin clusters were found close to groups of HIV-1 ENV clusters at HIV-1 assembly sites (Figure 3C). Close examination of 500 individual tetherin-positive budding sites revealed that 80% contained a single cluster of mEosFP-tetherin (Figure S6D). Finally bivariant Ripley's L function confirmed coclustering of different tetherin constructs with either Gag-mEosFP or HIV-1 ENV at HIV-1 budding sites (Figure 3D). We conclude that tetherin in single clusters closely associates with HIV-1 budding sites.

## Tetherin restriction mechanism

As both tetherin membrane anchors are essential for restricting HIV-1 release [13], different orientations of tetherin dimers across the cell and viral membrane are possible. Two models must be considered: (i) the "extended model" in which pairs of membrane anchors are incorporated into the cell membrane and the viral membrane, and an extended coiled-coil domain spans the gap between both membranes or (ii) the "parallel model" where one tetherin monomer is incorporated into the cell membrane and the other monomer into the viral membrane (Figure 4A). The apparent distances of circa 17 nm found between tethered virions by electron microscopy [6] and the structure of the tetherin ectodomain [12] favor the extended model but definitive proof is missing.

Tetherin-restricted virions are efficiently released from the cell surface by treatment with subtilisin A, a protease with relatively low specificity [1,6,14,15]. If virions are retained following the parallel model, subtilisin A treatment should leave monomeric low molecular weight N-termini inside stripped particles.

293T cells expressing HIV-1 Δvpu and N-terminal HA-tagged tetherin were treated with subtilisin A, cell lysates and released virions were then analyzed by Western blot. Analysis of cellular extracts showed constant pr55Gag content, whereas the majority of glycosylated tetherin at 36 and 60 kDa, as well as virions containing p24CA were efficiently removed by subtilisin A treatment (Figure 4B). Only a HA fragment of ~26 kDa was found inside stripped virions by non-reducing SDS-PAGE/Western blot analysis (Figure 4B). Under reducing SDS-PAGE a single band migrated at ~13 kDa, consistent with a previously proposed cleavage site at RNVT/H68 [13,14]. Altogether, we found dimeric N-termini associated with subtilisin A stripped virions, which is not compatible with the parallel model of tetherin orientation.

If tetherin retains viruses via the extended model, cleavage of the tetherin GPI anchor by phosphatidyl-inositol-specific phospholipase C (PI-PLC) should release tethered virions. To test this hypothesis, 293T cells transfected with HIV-1 Δvpu and tetherin-HA, HA-tetherin or the inactive mutant tetherin-HA delTM (Figure S6A and [13]) were treated with PI-PLC or subtilisin A. Stripped virions were pelleted through sucrose and analyzed by Western blot. Both PI-PLC and subtilisin A treatment released virions retained by tetherin (Figure 4C). Quantification from several experiments revealed that PI-PLC treatment (1 U/ML) released 20% of virions compared to the maximal release by 5 μg/ML subtilisin A (Figure 4D). To compare PIPLC and subtilisin A activities on tetherin we used wt tetherin HA and the mutant delTM, that is attached to the cell only via a GPI anchor. Fluorescence-activated cell sorting (FACS) analysis revealed that PI-PLC specifically reduced cell-surface levels of tetherin-HA delTM, whereas increased signal from tetherin-HA could result from increased access of antibodies to the internal HA tag after tetherin GPI cleavage (Figure 4E). Subtilisin A treatment removed the majority of tetherins from the cell surface, indicating that lower release of tetherin restricted virions by PI-PLC can be explained by its lower activity in cleaving the tetherin GPI anchor when compared to proteolysis cleavage by subtilisin A.

Finally, virions released by PI-PLC treatment contained nearly full length dimeric tetherin (Figure 4F). Therefore, since both PI-PLC and subtilisin A treatments removed tethered virions, which respectively contained dimeric tetherin and dimeric N-terminal tetherin fragments we conclude that tetherin restricts HIV-1 release as an extended dimer.

To characterize further the orientation of tetherin upon incorporation into the membrane of assembling virions, we

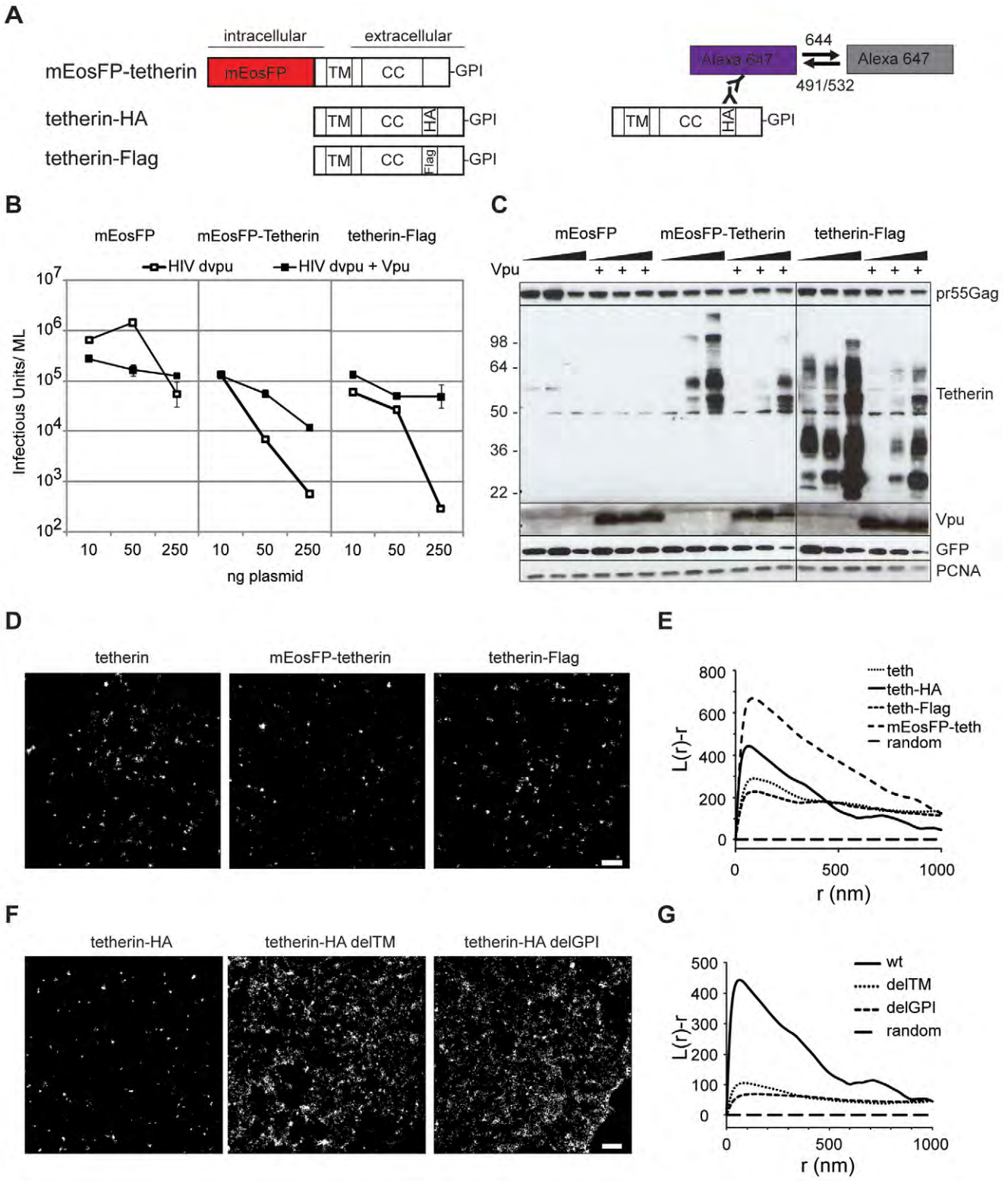


**Figure 2. Tetherin localization to micro-domains depends on both membrane anchors.** (A) Schematic presentation of tetherin constructs used and labeling/photoswitching scheme of fluorescent Alexa Fluor 647 (violet) and dark state (grey), tetherin structural features are: transmembrane domain (TM), coiled-coil domain (CC) and Glycosylphosphatidylinositol (GPI) anchor. HA or Flag are internal HA or Flag tags. (B) 293T cells were transfected with HIV-1 Δvpu and either mEosFP, mEosFP-tetherin or tetherin-Flag without or with Vpu as indicated and infectious output was determined on HeLa indicator cells. Error bars represent range of duplicate titrations. (C) Western blot analysis of cell lysates from B) was performed for pr55Gag, tetherin, Vpu, GFP as transfection control and PCNA as loading control. Sizes of molecular weight markers are shown in kilodaltons. One representative experiment out of two is shown for panel B and C. (D) Representative regions of super-resolution images of HeLa cells expressing HIV-1 Δvpu and empty plasmid, mEosFP-tetherin or tetherin-Flag that were labeled by indirect immunofluorescence against tetherin or

Flag or left unlabeled (mEosFP-tetherin), scale bar 500 nm. E) Ripley's L analysis: normalized L(r)-r plots indicate clustering at distances r with positive L(r)-r values, F) Representative regions of super-resolution images of HeLa cells expressing HIV-1 Δvpu and indicated tetherin-HA or mutant constructs. The cells were labeled by indirect immunofluorescence with primary anti-HA and Alexa Fluor 647 secondary antibodies, scale bar 500 nm. G) Ripley's L analysis indicates higher degree of clustering of wt tetherin than tetherin mutants delTM and delGPI.
doi:10.1371/journal.ppat.1002456.g002

analyzed the distribution of tetherin mutants lacking one of the membrane anchors relative to HIV-1 budding sites by super-resolution microscopy and co cluster analysis using bivariant Ripley's L function. HeLa cells were transfected with HIV-1 Δvpu, Gag-mEosFP and tetherin-HA or its mutants delTM and delGPI and labeled by anti-HA immunofluorescence. Tetherin-HA and the delGPI mutant, but not delTM associated with Gag-mEosFP-containing budding sites (Figure 5), indicating that the tetherin transmembrane domain drives tetherin localization to HIV-1 budding sites.

Finally to test whether tetherin could associate with budding structures via lipid rafts, HeLa cells expressing HIV-1 Δvpu and Gag-mEosFP or mEosFP-tetherin, were fixed, stained for the lipid raft marker GM1 using Alexa Fluor 647 Cholera-toxin and analyzed by super-resolution microscopy and co cluster analysis using bivariant Ripley's L function. GM1 localized to clusters of variable sizes that showed minor coclustering with mEosFP-tetherin domains, but did not show significant overlap (Figure 6B and C), indicating that both proteins are found in distinct, but adjacent domains. In contrast, we could not detect significant coclustering of GM1 with Gag-mEosFP-containing HIV-1 budding sites (Figure 6A and C). As positive control for coclustering, we monitored mEosFP-tetherin and tetherin-HA at HIV-1 budding sites labeled by HIV-1 ENV and Gag-mEosFP, respectively (Figure 3D and 6C). In addition, the GPI anchor was not sufficient to mediate enrichment of tetherin-HA delTM at budding sites (Figure 5). We conclude that tetherin and GM1, although both were reported to associate with lipid rafts, localize to different but adjacent lipid domains and that GM1-containing lipid rafts and the tetherin GPI anchor are unlikely to drive tetherin to HIV-1 assembly sites.

## Quantification of tetherin molecules at HIV-1 assembly sites

Single-molecule imaging and localization of PAFP provides super-resolution images and was previously used to estimate

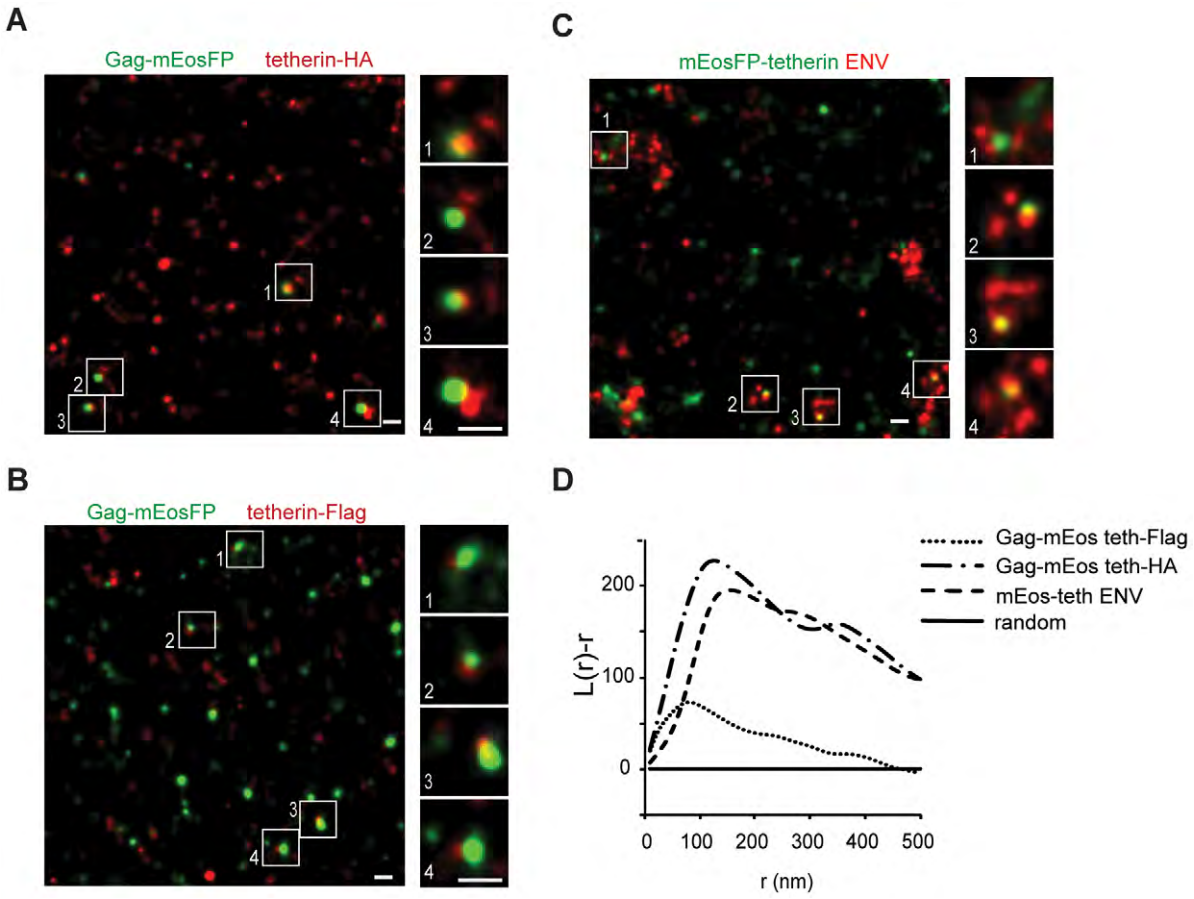


**Figure 3. Single tetherin domains cocluster with HIV-1 budding sites.** (A–C) Representative regions of super-resolution images of HeLa cells transfected with HIV-1 Δvpu and: (A) Gag-mEosFP and tetherin-HA; (B) Gag-mEosFP and tetherin-Flag and (C) mEosFP-tetherin. Tetherin-HA, tetherin-Flag and HIV-1 ENV were stained by indirect immunofluorescence for HA, Flag and ENV, respectively. (D) Bivariant Ripley's L analysis indicates coclustering of tetherin-HA, tetherin-Flag and mEosFP-tetherin with HIV-1 Gag-mEosFP and ENV, respectively. Images are representative of 5-10 cells from two independent transfections.
doi:10.1371/journal.ppat.1002456.g003

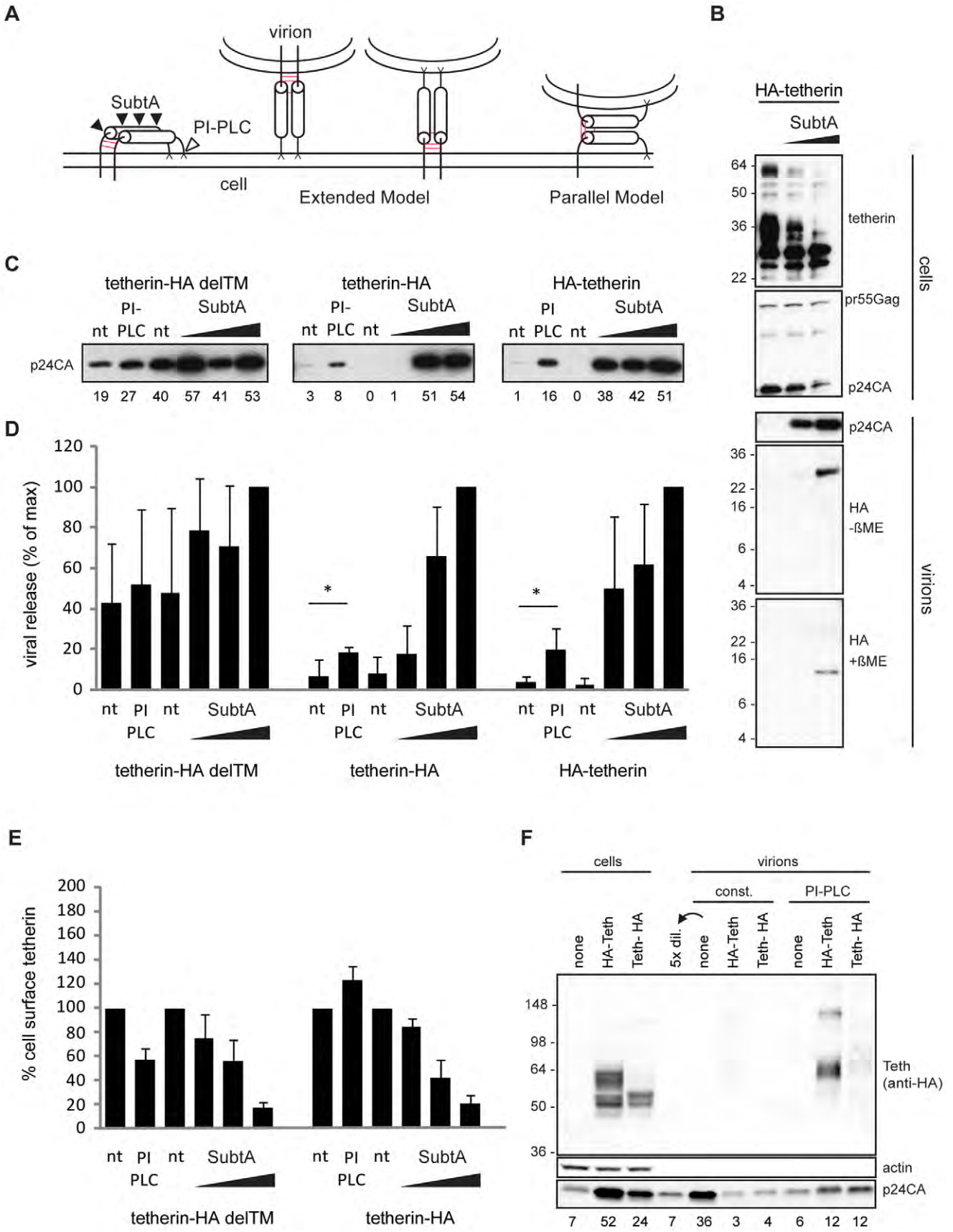
A
virion
SubtA
PI-PLC
cell
Extended Model
Parallel Model
B
HA-tetherin
SubtA
64
50
36
22
tetherin
pr55Gag
p24CA
cells
p24CA
36
22
16
6
4
HA
-ßME
HA
+ßME
virions
C
tetherin-HA delTM
tetherin-HA
HA-tetherin
PI-
PLC
nt
SubtA
PI
p24CA
19 27 40 57 41 53
3 8 0 1 51 54
1 16 0 38 42 51
D
viral release (% of max)
120
100
80
60
40
20
0
*
nt
PI
PLC
SubtA
tetherin-HA delTM
tetherin-HA
HA-tetherin
E
% cell surface tetherin
200
180
160
140
120
100
80
60
40
20
0
F
cells
virions
const.
PI-PLC
none
HA-Teth
Teth- HA
5x dil.
148
98
64
50
36
Teth
(anti-HA)
actin
p24CA
7 52 24 7 36 3 4 6 12 12

**Figure 4. Tetherin restricts HIV-1 release as extended dimers.** (A) Model of tetherin, enzymatic cleavage sites of subtilisin A (SubtA) and phosphatidyl-inositol-specific phospholipase C (PI-PLC) and possible orientations during restriction, disulfide bonds are represented in red. (B) Western blot analysis of subtilisin A stripped cells and virions. 293T cells transfected with HIV-1 Δvpu and HA-tetherin were treated with subtilisin A (0,5 or 50 μg/ML). Released Virions were pelleted through sucrose and analyzed under non-reducing (-βME) or reducing (+βME) SDS-PAGE/Western blot together with corresponding cell lysates (+βME). Data is representative of 2 experiments. (C) Western blot analysis (anti-p24CA) of purified virions released from non-treated (nt), PI-PLC (1 U/ML) or subtilisin A (0.2, 1 or 5 μg/ML) treated 293T cells transfected with HIV-1 Δvpu, GFP and either transmembrane-deficient tetherin-HA delTM, tetherin-HA or HA-tetherin, that contain either a C or N-termal HA-tag. Numbers below each lane indicate integrated densities in arbitrary units and are representative of 3 experiments. (D) Quantification of viral release from non-treated (nt), PI-PLC or subtilisin A treated cells 3-4 independent experiments as in B), maximal release by 5 μg/ML Subtilin A treatment was normalized to 100%. Error bars represent standard deviations and * indicates statistically significant difference with $p = 0.05$ (two-tailed paired Student's t-test). (E) Enzymatic removal of tetherin from cells in (C) was analyzed by Fluorescence-activated cell sorting (FACS). Shown are mean fluorescence intensities of anti-HA labeling in GFP-positive cells with non-treated cells set to 100%. Error bars represent standard deviations ($n = 3$). (F) Western blot analysis of PI-PLC stripped virions from 293T cells transfected with HIV-1 Δvpu and HA-tetherin or tetherin-HA. Virions that were constitutively released (const.) or released following incubation of cells with 1 U/ML PI-PLC were pelleted through sucrose. Virions and corresponding cell lysates were analyzed by Western blotting with anti-HA, anti-p24CA and anti-actin antibodies. Numbers below each lane indicate integrated densities of p24CA in arbitrary units. Sizes of molecular weight markers are shown in kilodaltons.
doi:10.1371/journal.ppat.1002456.g004

molecule numbers [37–39]. Detailed photophysical characterization of the irreversible photo-convertible mEos [40] revealed long-lived dark states of the photoactivated red form that could lead to clustering artifacts and significant overcounting [39,41]. Annibale *et al.* showed that continuous instead of pulsed photoactivation by 405 nm light and the introduction of dark times significantly reduced overcounting [41]. Following this methodology, fields of monodispersed mEosFP were used to determine appropriate imaging and analysis parameter including 561 nm excitation intensity [42], continuous 405 nm photoactivation and a dark time of 5 s. As a result, we found 1–2 reactivation events per single mEosFP molecule (25th–75th percentile range, Figure 7C and Figure S7), which may reflect the presence of a minor fraction of mEosFP multimers. Subsequently, using this optimized imaging and analysis parameters we estimated the number of mEosFP-tetherin molecules in free clusters and at HIV-1 budding sites (Figure 7A,B). At 550 assembly sites, we found 7–14 mEosFP-tetherin molecules (25th–75th percentile range, median is 10), corresponding to 4–7 tetherin dimers per budding site (Figure 7D). In contrast 400 mEosFP-tetherin clusters in the absence of HIV-1 contained 11-22 mEosFP-tetherin molecules (25th–75th Percentile range, median is 16), corresponding to 5–11 tetherin dimers (Figure 7D). The difference is significant ($p<0.001$, Student's t-test) and indicates that tetherin clusters can associate with HIV-1 budding sites. Approximately 70% of tetherin molecules within a cluster stay associated with budding virions and may participate in restricting HIV-1 release.

## Discussion

We have performed biochemical and super-resolution analysis to provide further understanding of the interactions between the restriction factor tetherin and HIV-1.

First, to achieve specific and high density labeling of HIV-1 for super-resolution microscopy, we tested different monomeric PAFP in HIV-1 Gag fusions, similar to Gag-GFP that showed budding at the plasma membrane [29,30]. Gag-Dronpa, Gag-mEosFP and Dronpa-Vpr were incorporated into full HIV-1 particles, minimally affected infectivity and enabled super-resolution microscopy analysis of virions. This confirmed the expected virion diameter of 100 nm. Of note is the fact that Gag, fused to 50 kDa dimeric Eos protein, produced larger virus-like particles of 100–200 nm in initial super-resolution studies [21,28]. For multicolor super-resolution, we labeled HIV-1/cellular proteins with Dronpa, mEosFP or antibodies coupled to the photoswitchable dye Alexa Fluor 647 [24,43]. Using simultaneous detection of two fluorescent markers and high-resolution registration mapping [32] we acquired two-color super-resolution images within few minutes and with a colocalization precision of 17 nm throughout a field of view. The precise localization of antibody-labeled viral proteins within Dronpa-Vpr virions was determined by super-resolution microscopy. In accordance with PALM and electron microscopy [33] structures labeled with CA or MA antibodies had sizes of 112 nm and 117 nm, respectively and colocalized with Dronpa-Vpr. In contrast, HIV-1 integrase localized to a structure with a characteristic size of 75 nm within Dronpa-Vpr containing cores. HIV-1 ENV was predominantly found in 1–2 peripheral clusters close to Dronpa-Vpr, consistent with their localization in the viral membrane. A clustered distribution of ENV on HIV-1 virions was observed in electron tomography images and could be functionally relevant during cell attachment and fusion [35,44].

HIV-1 assembly at the plasma membrane of HeLa cells was previously visualized using diffraction-limited microscopy [29,30,45]. Super-resolution microscopy of Gag-mEosFP and antibody-stained ENV on non-permeabilized cells revealed important structural features of budding sites. Gag-mEosFP clusters of varying sizes together with clustered ENV were found in the same TIRF imaging plane close to the coverslip, indicating assembly at the plasma membrane. As previously noted, ENV was found in distinct clusters [46] that incorporated into Gag-mEosFP assembly sites. Overall, our super-resolution microscopy analysis provides a detailed picture of HIV-1 virions and their assembly sites, which was previously exclusively obtained by electron microscopy.

We applied super-resolution microscopy for the HIV-1 cellular restriction factor, tetherin. Endogenous and overexpressed tetherin were previously identified in endosomal compartments and in clusters at the plasma membrane both by fluorescence microscopy [2,3,12,15] and electron microscopy [14,15,47]. The overall clustered distribution of tetherin was not influenced by HIV-1 particle formation, however localization of tetherin at budding sites was noted in some cases [2,3,14,15], but not all [18,48]. The size of the clusters could not be determined due to the diffraction-limited resolution of conventional fluorescence microscopy or low density labeling in immuno-electron microscopy.

Using different labeling approaches for super-resolution microscopy and calibrated size measurements we found that both endogenous and overexpressed tetherins are organized in 70–90 nm clusters at the plasma membrane of HeLa cells. Annibale *et al* recently reported that dark state recovery of mEos2 can cause clustering artifacts, due to repeated localization of single molecules [41]. Since we observe similar cluster sizes for all tetherin constructs and endogenous tetherin, consistent clustering of mEosFP-tetherin using comparable imaging parameter as [41] and a significant decrease in clustering of different mutant

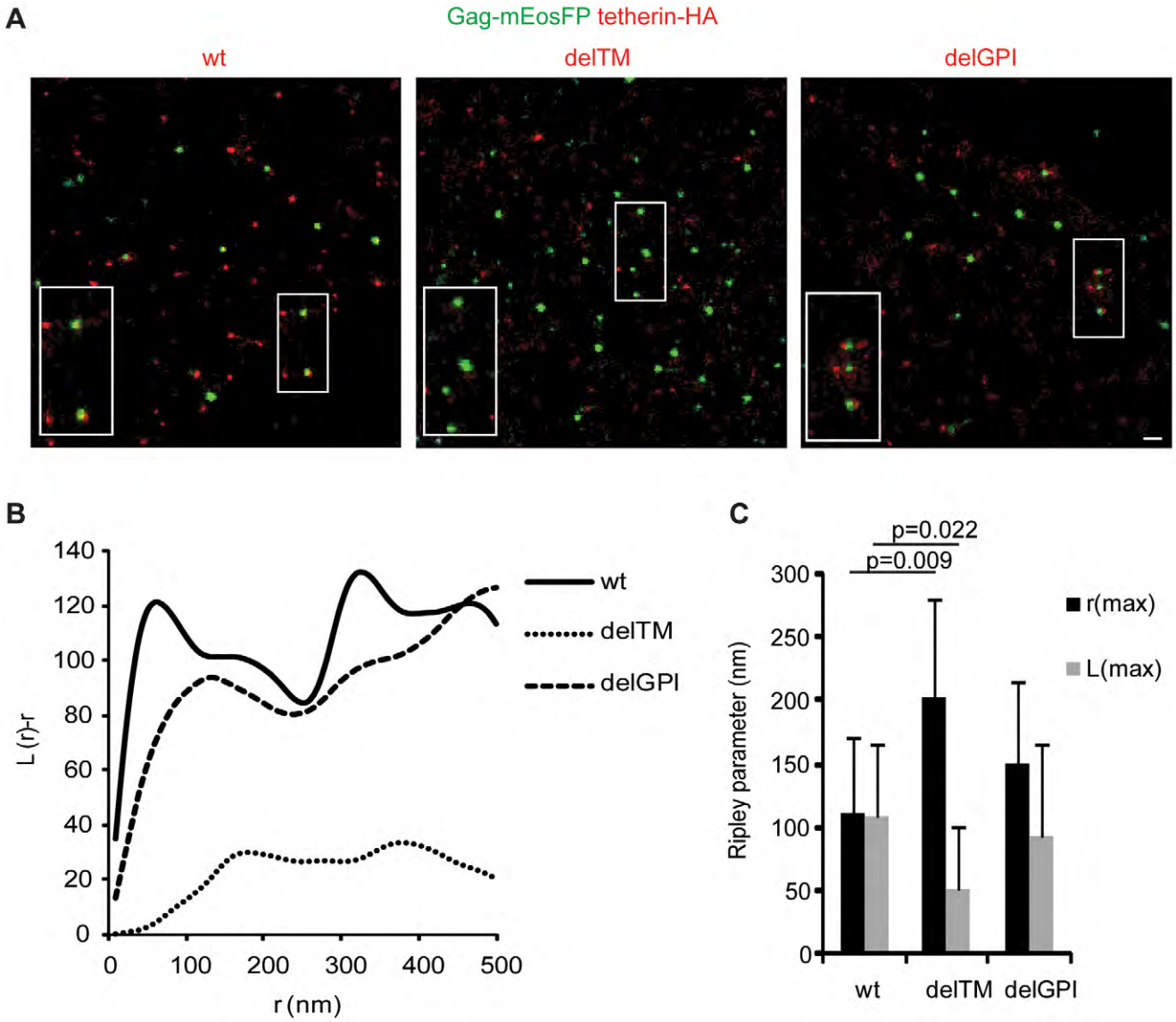


**Figure 5. Association of tetherin with HIV-1 budding sites depends on its transmembrane domain.** A) Representative regions of super-resolution images of HeLa cells transfected with HIV-1Δvpu, Gag-mEosFP and tetherin-HA wt, delTM or delGPI, scale bar 200 nm, B) bivariant Ripley's L analysis on fields shown in A), C) Multiple fields were analyzed by bivariant Ripley's L function and r(max) and L(max) determined, error bars represent standard deviations (9 fields from 3 cells per conditions), p values were determined by Student's t-test.
doi:10.1371/journal.ppat.1002456.g005

tetherins we report here a relevant localization of tetherin at the plasma membrane.

Notably, our increased resolution revealed that both membrane anchors of tetherin are required for clustering possibly through high order complexes between dimers [13], interaction of the cytoplasmic tail with the actin cytoskeleton [49] and lipid raft association via the GPI anchor [11].

Several models depicting the orientation of tetherin during the restriction on release of enveloped viruses have been proposed [6]. Here, we provide biochemical and microscopic evidence for HIV-1 restriction via an extended conformation of tetherin dimers. This model requires that pairs of membrane anchors incorporate into the cell membrane and the viral membrane and an extended coiled-coil domain spans the gap between both membranes (Figure 4). PI-PLC and subtilisin A treatment of 293T cells transfected with tetherin efficiently removed virions from the surface that contained dimeric tetherins. Of note, vpu-deficient HIV-1 virions were not released by PI-PLC treatment from HeLa cells, but efficient cleavage of the tetherin GPI anchor was not demonstrated [15,50]. Furthermore, slower enzymatic cleavage of the GPI anchor could occur in virion associated clusters of tetherin compared to efficient proteolytic cleavage by subtilisin A. In HeLa cells higher endocytosis rates could result in lower amounts of vpu-deficient virions bound to the cell surface compared to 293T cells [1]. Virus accumulation in biofilm-like extracellular assemblies [51] could further limit stripping efficiency by PI-PLC. Alternatively a fraction of tetherin that contains a second transmembrane domain instead a C-terminal GPI-anchor would be insensitive to PI-PLC treatment [50]. Since our results and previous reports indicate a C-terminal GPI-modification of rat and human tetherin [11,13,52] further biochemical analysis of tetherin C-terminal membrane anchor by mass spectroscopy is needed.

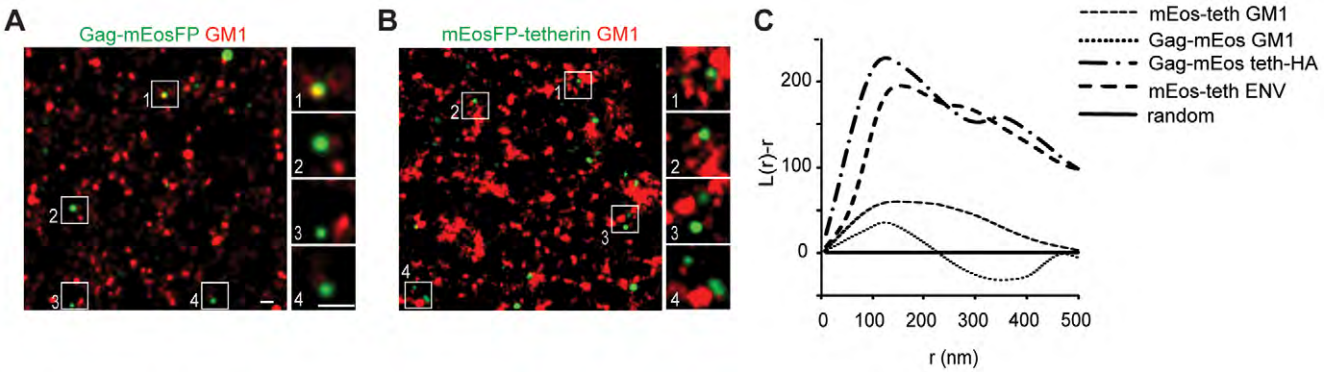


**Figure 6. Tetherin domains and HIV-1 budding sites do not overlap with GM1 containing lipid rafts.** (A,B) Representative regions of super-resolution images of HeLa cells transfected with HIV-1 Δvpu and Gag-mEosFP(A) or mEosFP-tetherin (B) that were fixed and stained for GM1 with Cholera toxin B Alexa Fluor 647, scale bars 200 nm (C) Bivariant Ripley's L analysis of panel A and B of this figure and Figure 3A and C Images and cocluster analysis shown is representative of multiple fields from 4–6 transfected cells from two independent transfections.
doi:10.1371/journal.ppat.1002456.g006

Of note, our biochemical analysis does not provide information on initial orientation of extended tetherin dimer at assembly sites since chains and clusters of tethered HIV-1 particles contain both of the possible orientations (Figure 4A) [13].

Therefore, we compared the incorporation of tetherin mutants lacking either the TM or GPI membrane anchor into single budding sites in HeLa cells by super-resolution microscopy. We found that the tetherin transmembrane domain stably associated with HIV-1 membranes during assembly.

Alternatively tetherin could also associate with HIV-1 budding sites via shared localization to lipid raft domains as both show some resistance to cold detergent extraction [1,11,53,54]. Both tetherin and Gag also cofractionated with the lipid raft marker caveolin [55]. Nevertheless cofractionation of proteins with raft markers does not prove their direct association or localization to similar lipid raft domains [56]. Indeed crosslinking antibodies against tetherin inhibited its antiviral effect but increased tetherin/Gag cofractionation [55].

Using super-resolution microscopy we found tetherin clusters in close association with GM1 lipid domains, but without significant overlap as previously noted for other raft proteins [57]. HIV-1 budding sites did not show significant association with GM1 lipid domains or with a tetherin mutant containing only the GPI membrane anchor. Recently HIV-1 Gag multimerization was shown to induce the coalescence of lipid raft markers and tetraspanins as visualized by antibody copatching, FRET analysis and single molecule tracking [58,59]. Both studies required copatching of raft markers (GM1, CD55 and HA–TM) and tetraspanins (CD9, CD81) to demonstrate their enrichment at HIV-1 budding sites due to the limited detection sensitivity of conventional fluorescence microscopy. Copatching could affect protein mobility and association with HIV-1 budding sites. GFP-GPI and unpatched CD55 failed to stably associate with viral assembly sites [45,59]. The later observations are consistent with our results obtained from unpatched GM-1 that was stained after fixation. Additionally the stable association of patched HA-TM and tetraspanins with viral assembly sites [58,59] is in line with our observation that clustered tetherin molecules stably associates with the viral membrane via their transmembrane domains.

Altogether the tetherin GPI modification and the association with GM1 lipid domains are not important for localization of tetherin to HIV-1 budding sites, but implicated in local concentration of tetherin (Figure 2) and maybe important for the endocytosis of retained virions. Alternatively tetherin could associate with HIV-1 assembly sites via other lipid rafts or tetraspanin-enriched domains. More efficient tetherin restriction could be obtained via late and stable incorporation into budding membranes within tetraspanin-enriched domains compared to early or transient association observed with raft markers [58,59].

At HIV-1 assembly sites, we found single tetherin clusters. mEosFP-tetherin showed a clustered plasma membrane distribution, restricted efficiently HIV-1 particle release in a Vpu-dependent manner (Figure 2A,B and Figure S6) and did not interfere with Gag assembly (Figure S6A). Therefore, the irreversible photoswitching properties of mEosFP allowed us to determine relevant mEosFP-tetherin quantities at HIV-1 assembly sites. Careful photo-physical characterization of purified mEosFP and the adjustment of imaging and analysis parameters enabled reliable single molecule counting of mEosFP.

We found 5–11 tetherin dimers in single clusters in the absence of HIV-1 and 4–7 tetherin dimers associated with HIV-1 budding sites, that represents a significant difference ($p<0.001$, Student's t-test). This indicates that about 70% of tetherin molecules within a cluster remain stably associated with budding sites possibly through incorporation of their TM domains into the viral membrane. Overall a low number of clustered tetherin dimers is sufficient to restrict the release of newly formed virions. Interestingly crosslinking antibodies against tetherin interfere with tethering function, reduce incorporation of tetherin into virions and affected the distribution of tetherin within membrane raft fractions [55]. Therefore it is possible that antibody crosslinking affects tetherin clustering, but cannot be detected by conventional diffraction limited microscopy [55]. We propose that the supramolecular organization of tetherin dimers in clusters could concentrate and position tetherin for optimal restriction and limit access to viral countermeasures. In summary, our biochemical and super-resolution analysis provided new insights into tetherin interaction with HIV-1 virions. We can propose the following mechanism for HIV-1 restriction by tetherin: Initially, tetherin locally concentrates in clusters containing 5–11 dimers and this involves both TM and GPI membrane anchors. In the absence of Vpu, tetherin N-termini associate with HIV-1 budding sites independently of GM1-enriched raft domains and become trapped during Gag-multimerization. Clusters containing 4 to 7 tetherin dimers remain associated with budding virions and can mediate restriction. Flexible coiled-coil interactions within dimers [12] are likely to enable retention of GPI anchors within the host cell membrane during budding and membrane scission. The final

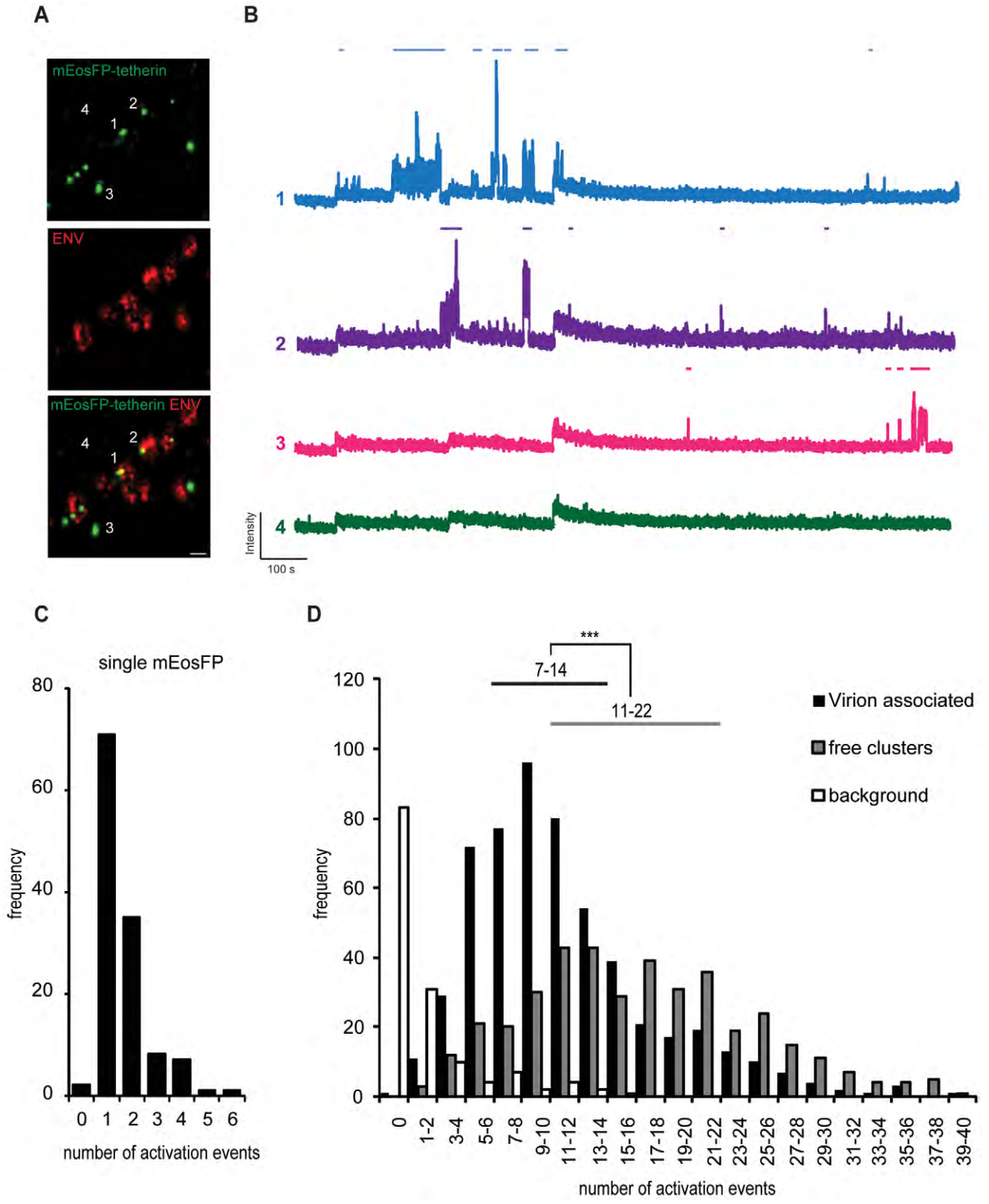


**Figure 7. Single fluorescent molecule quantification of mEosFP-tetherin at HIV-1 budding sites.** (A) Representative region of super-resolution images of HeLa cells transfected with HIV-1 Δvpu and mEosFP-tetherin and stained by indirect immunofluorescence for HIV-1 ENV. Acquisition was performed under alternating 561 and 644 nm excitation and continuous 405 nm photoactivation for 15 000 frames, scale bar 200 nm. (B) Intensity traces of single mEosFP-tetherin clusters as depicted in (A). Automated detection of activation events on top of each trace is depicted using a threshold of 10 standard deviations above background and a dark time of 5 s. (C) Histogram of number of activation events per single mEosFP molecules in 1% PVA (n = 125). (D) Histogram of number of activation events of mEosFP-tetherin molecules in free clusters (n = 400) or

clusters that are associated with HIV-1 budding sites (n = 550) in 5 cells. Background was selected in regions without clusters. Range indicates 25th–75th percentile. *** indicates statistically significant difference with $p<0.001$ (two-tailed paired Student's t-test).
doi:10.1371/journal.ppat.1002456.g007

predicted topology is that of extended tetherin dimers with N-termini inside newly formed virions.

Our study demonstrates that multicolor super-resolution imaging allows characterization of the interplay between viral and cellular structures with nanometer resolution. Quantitative analysis of single molecule localization in combination with biochemical analysis offers novel insights into the tetherin restriction mechanism and can be used to investigate virus-host interactions.

## Materials and Methods

### Cell lines

Human cell lines 293T, HeLa and HeLa-derived TZMbl were obtained through NIH AIDS Research and Reference Reagent Program and grown under standard conditions.

### Plasmids and reagents

The HIV-1 expression vectors pR9 INHA (kind gift of F.D. Bushman, University of Pennsylvania) and vpu-deficient pR9 Δvpu (HIV-1 Δvpu) are based on pR9 [60]. Plasmids coding for Gag-PAFP were obtained by replacing GFP from pGag-GFP [61] with Dronpa [62], mKikGR [63], mutant mKikGR15.1 containing K141E and V160I (kind gifts from A. Miyawaki, Riken Brain Science Institute, Japan), PS-CFP2, Dendra2 [64] (both from Evrogen), mEosFP [40] (pQE32 mEosFP was a kind gift of J.Wiedenmann, University of Southampton, U.K) or PAmCherry1 [65] (kind gift of V. Verkhusha, Albert Einstein College of Medicine, NY) by standard PCR cloning. The plasmid coding for Dronpa, (pCDNA3 Dronpa) and Dronpa-Vpr was generated by standard PCR cloning. ptetherin-Flag was constructed by inserting the Flag tag after the predicted coiled-coil domain (residue 154) by PCR cloning as previously described [3]. pmEosFP-tetherin contains mEosFP separated by a spacer peptide (*ggglyksglrsra*) from tetherin N-terminus. Plasmid coding for HA-tetherin was previously described in [19]. Details for primers and cloning can be provided upon request. Plasmids coding for tetherin-HA as well as mutants delTM and delGPI [13] were a kind gift from P. Bieniasz (Aaron Diamond AIDS Research Center, NY).

### Transfections, virus production and infectivity assay

293T cells were transfected using a standard calcium-phosphate-based technique. HeLa cells were transfected using Lipofectamine 2000 (Invitrogen) or Fugene HD (Roche), according to manufacturer instructions. Infectious HIV-1 particles were produced from 293T cells, filtered through a 0.45 μm filter and concentrated through 20% sucrose by centrifugation [6]. Viral titer was determined by applying limiting dilutions of filtered supernatants from producer cells on HeLa TZMbl indicator cells for 48h. Cells were fixed in 1% formaldehyde and stained for β-lactamase expression with 5-bromo-4-chloro-3-indolyl-b-D-galactoside (X-gal).

### Protein and immunofluorescence analysis

Enzymatic removal of surface virions was performed by incubating transfected 293T cells 36 h post transfection with 1 U/ML PI-PLC (Invitrogen) in DMEM or 0.2–50 μg/ML subtilisin A (Sigma-Aldrich) in stripping buffer [13] for 1 h at 37°C followed by filtration and concentration through 20% sucrose. Viral pellets and cellular lysates were lysed in RIPA with protease inhibitor (Sigma) and subjected to standard SDS Page/Western blot analysis. Proteins were detected by mouse monoclonal antibodies against Dronpa (Amalgaam), HIV-1 p24CA (183-H12-5C), mature HIV-1 p17MA (4C9, kind gift from M. Marsh), HA tag (Roche), GFP (Miltenyi biotec), PCNA (Oncogene Research Products) or rabbit polyclonal antibodies against tetherin and Vpu made by K. Strebel (obtained through NIH AIDS Research and Reference Reagent Program).

Recombinant mEosFP was purified from *E. coli* BL21 DE3 transformed with pQE32 mEosFP after 5 h culture at 37°C in presence of 100 μM IPTG as described in [40]. Purified protein was desalted using PD10 columns (GE Healthcare) and protein content was determined using BCA (Thermo Scientific) against known concentrations of bovine serum albumin. For single-molecule characterization 1 nM mEosFP was prepared in 1% PVA and spin-coated on clean coverslips for 2 min at 3000 rpm.

For immunofluorescence analysis, HeLa cells or viral particles on coverslips were fixed with 3% paraformaldehyde and incubated under standard conditions with mouse monoclonal antibodies against HA-tag (Covance), Flag-tag (Sigma), HIV-1 p24CA, mature HIV-1 p17MA, mouse polyclonal antibody against tetherin (kindly provided by Chugai Pharmaceutical Co., Ltd, Kanagawa, Japan) or human monoclonal antibody against HIV-1 gp120 (2G12, obtained through NIH AIDS Research and Reference Reagent Program). Alexa Fluor 647-conjugated secondary antibodies and Alexa Fluor 647-conjugated Cholera toxin subunit B were purchased from Invitrogen. Super-resolution microscopy was performed on cells and viruses in chambered coverglass (LabTek) with freshly prepared switching buffer [24].

### Super-resolution microscopy

Super-resolution microscopy was performed on an inverted microscope (Olympus IX-71) equipped with an TIRF oil objective (60x, NA 1.6, Olympus) and two simultaneously acquiring cooled Electron Multiplying-CCD (ImagEM, Hamamatsu). Dronpa was excited with 1–5 kW/cm$^2$ of 491 nm laser (Cobolt), mEosFP with 0.4 kW/cm$^2$ of 561 nm (Cobolt) and Alexa Fluor 647 with 0.3 kW/cm$^2$ of 644 nm (Spectra Physics) diode pumped solid state lasers. Photoactivation of photoactivatable proteins was performed with a 405 nm laser (Cube, coherent) using stroboscopic illumination [31] or continuous illumination with 0.2–1.8 W/cm$^2$ obtained with an optical acoustic modulator (AA Opto-Electronics). Alexa Fluor 647 was activated by 491 nm (Cobolt) or 532 nm (JP Uniphase) laser diode pumped solid state laser.

For the simultaneous measurement of Dronpa and Alexa Fluor 647, the laser lines (405, 491 and 64 nm) were combined using a 405 (zt405rdc, Chroma) and a 505 dichroic (505DCLP, Chroma) and further guided onto the sample through the same dichroic mirror (z488/633rdc, Chroma). When measuring mEosFP and Alexa Fluor 647 simultaneously, the laser lines (405, 532, 561 and 644 nm) were combined using a 405 (zt405rdc, Chroma), a 532 (z532rdc, Chroma) and a 561 dichroic (z561rdc, Chroma). The four laser lines were then guided onto the sample through the same dichroic mirror (z561/644rdc, Chroma).

Emission from TIRF illuminated sample was collected by the same objective and split by 650 long pass dichroic mirror (z650rdc, Chroma). Additional filters were used to remove excitation light and signal from other channels, namely 527/30 band pass for Dronpa (HQ527/30m, Chroma), 570 long pass and 607/67 band

pass for mEosFP (HQ570LP and HQ607/67, Chroma), 665 long pass and 700/71 band pass for Alexa Fluor 647 (HQ665LP and HQ700/71x, Chroma). The images were acquired with a final maximum field of view of ca. $41\times41$ $\mu m^2$ ($80\times80$ $nm^2$ per pixel) with a frame rate of 10–20 Hz. In order to reduce the background and the crosstalk between the two channels, the excitation of the two fluorophores and data acquisition were synchronized using 2 mechanical shutters (NewPort). No additional stabilization of the system was required. Analysis of image sequences was performed with a homemade MATLAB routine for single molecule localization [31].

Registration mapping for two-color imaging was performed by a homemade Matlab routine. Briefly, fields of 100–400 fluorescent beads (100 nm, Tetraspek, Invitrogen) were recorded as fiducial markers in both channels. Individual bead positions were determined by Gaussian fitting for both channels, assigned automatically and used to calculate a local weighted mean mapping as described in [32] and detailed in Figure S3.

## Cluster and cocluster analysis

For the determination of the cluster sizes, individual clusters were identified as discrete accumulations of 100 or more single molecule localizations within a fixed radius of 100–200 nm. The sizes were determined as 4 sigma of Gaussian function fitted to the distribution of localizations. Ripley's L function and bivariant Ripley's L function were determined from $4\times4$ $\mu m^2$ field of view as described [66].

## Counting of mEosFP molecules

For counting the number of mEosFP molecules per cluster images were acquired using continuous illumination with 0.4 kW/$cm^2$ of 561 nm to excite the red form of mEosFP and 0.5–1.8 W/$cm^2$ 405 nm laser light for photoactivation. Centers of individual clusters of mEosFP-tetherin within 100 nm from ENV staining were manually selected in two-color super-resolution images. The intensity of 9 pixels around the cluster position was measured and plotted against time for 15′000 frames. Single molecules were identified in intensity traces when intensity signals increased 10 standard deviations above background [38] using a homemade Matlab routine. Intensity increases within a dark time of 5 s were not considered to exclude blinking and recovery from long-lived dark states of activated mEosFP molecules.

Of note, the number of mEosFP-tetherin molecules represents a lower estimate since photoactivation prior to visualization, incomplete photoactivation during the experiment and missed detection of activated molecules may not be completely excluded.

## Accession numbers

The human tetherin clones used in this study correspond to Swiss-Prot entries Q10589.

# Supporting Information

**Figure S1 Screening photoactivatable fluorescent proteins (PAFP) for HIV-1 Gag labeling and PALM.** (A) Constructs used for PALM: HIV-1 Gag consisting of matrix (MA), capsid (CA), nucleocapsid (NC) and p6 was fused to different photoactivatable proteins, namely Dronpa, PS-CFP2, Dendra2, mKikGR, mEosFP and PAmCherry. Color code refers to standard emission color and gray indicates initial or photoinduced dark state. Numbers indicate wavelengths in nm used for photoactivation or excitation. (B) Western blot analysis (anti-p24CA) of cellular lysates and purified virions from 293T cells transfected with expression plasmids for HIV-1 together with indicated HIV-1 Gag-PAFP. (C) Infectivity of released virus as determined by single cycle replication assay in TZMBL cells and X-gal staining, "no PAFP" represents 100%. Error bars represent standard deviations ($n\geq4$), (D) Labeled virions analyzed by total internal reflection fluorescence microscopy (TIRF, top row) and PALM (bottom row) for comparison purposes, scale bar 200 nm.
(TIF)

**Figure S2 Setup and excitation/detection scheme used for super-resolution microscopy.** Setup, excitation and detection scheme used to measure Dronpa and Alexa Fluor 647 (A) or mEosFP and Alexa Fluor 647 fluorescence (B). Specific dicroic mirrors (DM1-4) and filters (BP1-2) are described in Material and Methods. OAM: acoustic optic modulator, MS1: mechanical shutter synchronized with CCD1, MS2: mechanical shutter synchronized with CCD2.
(TIF)

**Figure S3 Colocalization procedure for two-color super-resolution microscopy.** 100 nm fluorescent beads were used as fiducial markers to correct differences in alignment and chromatic aberrations of detection paths (A,B). Fields of 150–500 beads were imaged simultaneously in Dronpa channel (green) and Alexa Fluor 647 channel (red) and representative part of $2\times2$ μm is shown. Center positions of beads were determined from Gaussian fitting and corresponding pairs of positions assigned. Localization precision for beads was found 7.6 and 6.1 nm for Dronpa (green) and Alexa Fluor 647 (red) channel, respectively (C), Pairs of center positions were used to calculate a local weighted mean transformation needed to correct images (D,E). Colocalization precision of $17\pm20$ nm (mean $\pm$ StD, $n = 1857$) as measured from distances between bead positions after application of transformation (F).
(TIF)

**Figure S4 Incorporation of PAFP into HIV-1 virions and size histograms.** A) Immunofluorescence analysis (anti-CA, red) of HIV-1 virions containing indicated PAFP (green), scale bar 1 μm. B) Size distribution of Dronpa-Vpr, Gag-Dronpa and Gag-mEosFP in HIV-1 virions from super-resolution imaging and cluster analysis. C) Size distribution of integrase (IN), capsid (CA), matrix (MA) and Envelope (ENV) in HIV-1 virions from super-resolution imaging and cluster analysis.
(TIF)

**Figure S5 Calibration of cluster size analysis.** (A) Examples of simulated fields of 25 circular cluster of different sizes containing 100 random localizations, scale bar 1 μm, (B) Ripley's L analysis of simulated clusters: Note decrease of peaks and shift of maxima towards larger r at larger cluster sizes, (C) Sizes of simulated clusters were estimated using Cluster analysis or Ripley's L maxima, error bars represent StD from>6 fields. (D) Sizes of simulated clusters with varied number of localizations per cluster were estimated using cluster analysis. Error bars represent standard deviations from measurements on six fields. Note that there is no effect of number of localizations on mean cluster size
(TIF)

**Figure S6 Characterisation of tetherin mutants.** (A) 293T cells were transfected with HIV-1 Δvpu and either tetherin-HA, tetherin-HA delTM or tetherin-HA delGPI without or with Vpu as indicated and infectious output was determined on HeLa indicator cells. Error bars represent range of duplicate titrations. (B) Western blot analysis of cell lysates from A) was performed for pr55Gag, tetherin, Vpu, GFP as transfection control and PCNA as loading control. Note that data shown in panel A and B were obtained under identical conditions as Figure 2 B,C. (C) 293T cells

were transfected with HIV-1 Δvpu and either HA-tetherin or mEosFP-tetherin. Virions that were constitutively released (const.) or released following incubation of cells with subtilisin A (SubtA) were pelleted through sucrose. Virions and corresponding cell lysates were analyzed by quantitative Western blotting with anti-HA and anti-p24CA antibodies. Numbers below each lane indicate integrated densities of p24CA signal in arbitrary units. Sizes of molecular weight markers in B and C are shown in kilodaltons. (D) Histogram of number of mEosFP-tetherin clusters per HIV-1 budding site. Error bars represent standard deviations from quantification in 5 individual super-resolution images with a total of 550 tetherin-positive HIV-1 budding sites analyzed.
(TIF)

**Figure S7 Single molecule photo-physical characterization of mEosFP.** (A) SDS-PAGE and Coomassie staining of 1 or 4 μg of purified 6xHis-tagged mEosFP. Sizes of molecular weight markers are shown in kilodaltons. The predicted size of 6xHis mEosFP is 31 kDa and lower molecular weight bands represent mEosFP cleavage products associated with premature photoactivation. (B) Representative single molecule traces of mEosFP molecules in 1% PVA under 0.4 kW/cm$^2$ 561 nm excitation and pulsed (red) or continuous (black) photoactivation (PA) by 405 nm light (0.2–0.5 kW/cm$^2$). Traces comprise 15 000 frames acquired with 50 ms/frame. (C) Determination of dark times (td) of the photoactivated red form of mEosFP under continuous photoactivation. Number of reactivation events per single molecule trace of (total of 15000 frames with 50 ms/frame) were determined from 25–50 traces for different $t_d$ and 405 nm intensities. (D) Histogram of number of reactivation events per single molecule trace acquired under pulsed photoactivation (PA) or continuous PA using 405 nm light (0.5–1.8 W/cm$^2$) and analyzed using $t_d$ = or 5 s. (E) Effect of excitation light on quantification of single mEosFP molecules in 1% PVA. The red form of mEosFP was detected under continuous 561 nm excitation (0.4 kW/cm$^2$). Continuous photoactivation by 405 nm light (1.8 W/cm$^2$) was switched on after 20–500 s corresponding to usual acquisition times used. Representative regions of super-resolution images are shown. Scale bar 1 μm. (F) Cluster analysis revealed similar number of detected mEosFP molecules following different exposure intervals with 561 nm excitation light as in (E). Scale bar 1 μm
(TIF)

## Acknowledgments

We thank F. Leuba and A. Deres for technical assistance, F. D. Bushman, J. Wiedenmann, V. Verkhusha, A. Miyawaki and P. Bieniasz for the kind gift of reagents and Louise Kemp and Silvia Anghel for critical reading of the manuscript.

## Author Contributions

Conceived and designed the experiments: ML JH VP. Performed the experiments: ML SR BM FB HU. Analyzed the data: ML SR BM FB HU. Contributed reagents/materials/analysis tools: SR BM HU. Wrote the paper: ML VP. Build set-up: SR HU ML.

## References

1. Neil SJ, Eastman SW, Jouvenet N, Bieniasz PD (2006) HIV-1 Vpu promotes release and prevents endocytosis of nascent retrovirus particles from the plasma membrane. PLoS Pathog 2: e39.
2. Van Damme N, Goff D, Katsura C, Jorgenson RL, Mitchell R, et al. (2008) The interferon-induced protein BST-2 restricts HIV-1 release and is downregulated from the cell surface by the viral Vpu protein. Cell Host Microbe 3: 245–252.
3. Jouvenet N, Neil SJ, Zhadina M, Zang T, Kratovac Z, et al. (2009) Broad-spectrum inhibition of retroviral and filoviral particle release by tetherin. J Virol 83: 1837–1844.
4. Sakuma T, Noda T, Urata S, Kawaoka Y, Yasuda J (2009) Inhibition of Lassa and Marburg virus production by tetherin. J Virol 83: 2382–2385.
5. Mansouri M, Viswanathan K, Douglas JL, Hines J, Gustin J, et al. (2009) Molecular mechanism of BST2/tetherin downregulation by K5/MIR2 of Kaposi's sarcoma-associated herpesvirus. J Virol 83: 9672–9681.
6. Neil SJ, Zang T, Bieniasz PD (2008) Tetherin inhibits retrovirus release and is antagonized by HIV-1 Vpu. Nature 451: 425–430.
7. Jia B, Serra-Moreno R, Neidermyer W, Rahmberg A, Mackey J, et al. (2009) Species-specific activity of SIV Nef and HIV-1 Vpu in overcoming restriction by tetherin/BST2. PLoS Pathog 5: e1000429.
8. Sauter D, Schindler M, Specht A, Landford WN, Munch J, et al. (2009) Tetherin-driven adaptation of Vpu and Nef function and the evolution of pandemic and nonpandemic HIV-1 strains. Cell Host Microbe 6: 409–421.
9. Gupta RK, Mlcochova P, Pelchen-Matthews A, Petit SJ, Mattiuzzo G, et al. (2009) Simian immunodeficiency virus envelope glycoprotein counteracts tetherin/BST-2/CD317 by intracellular sequestration. Proc Natl Acad Sci U S A 106: 20889–20894.
10. Le Tortorec A, Neil SJ (2009) Antagonism to and intracellular sequestration of human tetherin by the human immunodeficiency virus type 2 envelope glycoprotein. J Virol 83: 11966–11978.
11. Kupzig S, Korolchuk V, Rollason R, Sugden A, Wilde A, et al. (2003) Bst-2/HM1.24 is a raft-associated apical membrane protein with an unusual topology. Traffic 4: 694–709.
12. Hinz A, Miguet N, Natrajan G, Usami Y, Yamanaka H, et al. (2010) Structural basis of HIV-1 tethering to membranes by the BST-2/tetherin ectodomain. Cell Host Microbe 7: 314–323.
13. Perez-Caballero D, Zang T, Ebrahimi A, McNatt MW, Gregory DA, et al. (2009) Tetherin inhibits HIV-1 release by directly tethering virions to cells. Cell 139: 499–511.
14. Hammonds J, Wang JJ, Yi H, Spearman P (2010) Immunoelectron microscopic evidence for Tetherin/BST2 as the physical bridge between HIV-1 virions and the plasma membrane. PLoS Pathog 6: e1000749.
15. Fitzpatrick K, Skasko M, Deerinck TJ, Crum J, Ellisman MH, et al. (2010) Direct restriction of virus release and incorporation of the interferon-induced protein BST-2 into HIV-1 particles. PLoS Pathog 6: e1000701.
16. McNatt MW, Zang T, Hatziioannou T, Bartlett M, Fofana IB, et al. (2009) Species-specific activity of HIV-1 Vpu and positive selection of tetherin transmembrane domain variants. PLoS Pathog 5: e1000300.
17. Mitchell RS, Katsura C, Skasko MA, Fitzpatrick K, Lau D, et al. (2009) Vpu antagonizes BST-2-mediated restriction of HIV-1 release via beta-TrCP and endo-lysosomal trafficking. PLoS Pathog 5: e1000450.
18. Goffinet C, Allespach I, Homann S, Tervo HM, Habermann A, et al. (2009) HIV-1 antagonism of CD317 is species specific and involves Vpu-mediated proteasomal degradation of the restriction factor. Cell Host Microbe 5: 285–297.
19. Mangeat B, Gers-Huber G, Lehmann M, Zufferey M, Luban J, et al. (2009) HIV-1 Vpu neutralizes the antiviral factor Tetherin/BST-2 by binding it and directing its beta-TrCP2-dependent degradation. PLoS Pathog 5: e1000574.
20. Bieniasz PD (2009) The cell biology of HIV-1 virion genesis. Cell Host Microbe 5: 550–558.
21. Betzig E, Patterson GH, Sougrat R, Lindwasser OW, Olenych S, et al. (2006) Imaging intracellular fluorescent proteins at nanometer resolution. Science 313: 1642–1645.
22. Hess ST, Girirajan TP, Mason MD (2006) Ultra-high resolution imaging by fluorescence photoactivation localization microscopy. Biophys J 91: 4258–4272.
23. Rust MJ, Bates M, Zhuang X (2006) Sub-diffraction-limit imaging by stochastic optical reconstruction microscopy (STORM). Nat Methods 3: 793–795.
24. Heilemann M, van de Linde S, Schuttpelz M, Kasper R, Seefeldt B, et al. (2008) Subdiffraction-resolution fluorescence imaging with conventional fluorescent probes. Angew Chem Int Ed Engl 47: 6172–6176.
25. Bates M, Huang B, Dempsey GT, Zhuang X (2007) Multicolor super-resolution imaging with photo-switchable fluorescent probes. Science 317: 1749–1753.
26. Shroff H, Galbraith CG, Galbraith JA, White H, Gillette J, et al. (2007) Dual-color superresolution imaging of genetically expressed probes within individual adhesion complexes. Proc Natl Acad Sci U S A 104: 20308–20313.
27. Huang B, Babcock H, Zhuang X (2010) Breaking the diffraction barrier: super-resolution imaging of cells. Cell 143: 1047–1058.
28. Manley S, Gillette JM, Patterson GH, Shroff H, Hess HF, et al. (2008) High-density mapping of single-molecule trajectories with photoactivated localization microscopy. Nat Methods 5: 155–157.
29. Larson DR, Johnson MC, Webb WW, Vogt VM (2005) Visualization of retrovirus budding with correlated light and electron microscopy. Proc Natl Acad Sci U S A 102: 15453–15458.
30. Jouvenet N, Bieniasz PD, Simon SM (2008) Imaging the biogenesis of individual HIV-1 virions in live cells. Nature 454: 236–240.
31. Flors C, Hotta J, Uji-i H, Dedecker P, Ando R, et al. (2007) A stroboscopic approach for fast photoactivation-localization microscopy with Dronpa mutants. J Am Chem Soc 129: 13970–13977.
32. Churchman LS, Okten Z, Rock RS, Dawson JF, Spudich JA (2005) Single molecule high-resolution colocalization of Cy3 and Cy5 attached to macromol-

ecules measures intramolecular distances through time. Proc Natl Acad Sci U S A 102: 1419–1423.
33. Briggs JA, Wilk T, Welker R, Krausslich HG, Fuller SD (2003) Structural organization of authentic, mature HIV-1 virions and cores. EMBO J 22: 1707–1715.
34. Carlson LA, de Marco A, Oberwinkler H, Habermann A, Briggs JA, et al. (2010) Cryo electron tomography of native HIV-1 budding sites. PLoS Pathog 6: e1001173.
35. Zhu P, Liu J, Bess J, Jr., Chertova E, Lifson JD, et al. (2006) Distribution and three-dimensional structure of AIDS virus envelope spikes. Nature 441: 847–852.
36. Hess ST, Gould TJ, Gudheti MV, Maas SA, Mills KD, et al. (2007) Dynamic clustered distribution of hemagglutinin resolved at 40 nm in living cell membranes discriminates between raft theories. Proc Natl Acad Sci U S A 104: 17370–17375.
37. Lillemeier BF, Mortelmaier MA, Forstner MB, Huppa JB, Groves JT, et al. (2009) TCR and Lat are expressed on separate protein islands on T cell membranes and concatenate during activation. Nat Immunol 11: 90–96.
38. Greenfield D, McEvoy AL, Shroff H, Crooks GE, Wingreen NS, et al. (2009) Self-organization of the Escherichia coli chemotaxis network imaged with super-resolution light microscopy. PLoS Biol 7: e1000137.
39. Annibale P, Vanni S, Scarselli M, Rothlisberger U, Radenovic A (2011) Quantitative photo activated localization microscopy: unraveling the effects of photoblinking. PLoS One 6: e22678.
40. Wiedenmann J, Ivanchenko S, Oswald F, Schmitt F, Rocker C, et al. (2004) EosFP, a fluorescent marker protein with UV-inducible green-to-red fluorescence conversion. Proc Natl Acad Sci U S A 101: 15905–15910.
41. Annibale P, Vanni S, Scarselli M, Rothlisberger U, Radenovic A (2011) Identification of clustering artifacts in photoactivated localization microscopy. Nat Methods 8: 527–528.
42. Jones SA, Shim SH, He J, Zhuang X (2011) Fast, three-dimensional super-resolution imaging of live cells. Nat Methods 8: 499–508.
43. Heilemann M, van de Linde S, Mukherjee A, Sauer M (2009) Super-resolution imaging with small organic fluorophores. Angew Chem Int Ed Engl 48: 6903–6908.
44. Sougrat R, Bartesaghi A, Lifson JD, Bennett AE, Bess JW, et al. (2007) Electron tomography of the contact between T cells and SIV/HIV-1: implications for viral entry. PLoS Pathog 3: e63.
45. Ivanchenko S, Godinez WJ, Lampe M, Krausslich HG, Eils R, et al. (2009) Dynamics of HIV-1 assembly and release. PLoS Pathog 5: e1000652.
46. Leung K, Kim JO, Ganesh L, Kabat J, Schwartz O, et al. (2008) HIV-1 assembly: viral glycoproteins segregate quantally to lipid rafts that associate individually with HIV-1 capsids and virions. Cell Host Microbe 3: 285–292.
47. Habermann A, Krijnse-Locker J, Oberwinkler H, Eckhardt M, Homann S, et al. (2010) CD317/tetherin is enriched in the HIV-1 envelope and downregulated from the plasma membrane upon virus infection. J Virol 84: 4646–4658.
48. Miyagi E, Andrew AJ, Kao S, Strebel K (2009) Vpu enhances HIV-1 virus release in the absence of Bst-2 cell surface down-modulation and intracellular depletion. Proc Natl Acad Sci U S A 106: 2868–2873.
49. Rollason R, Korolchuk V, Hamilton C, Jepson M, Banting G (2009) A CD317/tetherin-RICH2 complex plays a critical role in the organization of the subapical actin cytoskeleton in polarized epithelial cells. J Cell Biol 184: 721–736.
50. Andrew AJ, Kao S, Strebel K (2011) The C-terminal hydrophobic region in human BST-2/tetherin functions as a second transmembrane motif. J Biol Chem 286: 39967–39981.
51. Pais-Correia AM, Sachse M, Guadagnini S, Robbiati V, Lasserre R, et al. (2009) Biofilm-like extracellular viral assemblies mediate HTLV-1 cell-to-cell transmission at virological synapses. Nat Med 16: 83–89.
52. Masuyama N, Kuronita T, Tanaka R, Muto T, Hirota Y, et al. (2009) HM1.24 is internalized from lipid rafts by clathrin-mediated endocytosis through interaction with alpha-adaptin. J Biol Chem 284: 15927–15941.
53. Nguyen DH, Hildreth JE (2000) Evidence for budding of human immunodeficiency virus type 1 selectively from glycolipid-enriched membrane lipid rafts. J Virol 74: 3264–3272.
54. Ono A, Freed EO (2001) Plasma membrane rafts play a critical role in HIV-1 assembly and release. Proc Natl Acad Sci U S A 98: 13925–13930.
55. Miyagi E, Andrew A, Kao S, Yoshida T, Strebel K (2011) Antibody-mediated enhancement of HIV-1 and HIV-2 production from BST-2/tetherin+ cells. J Virol 85: 11981–11994.
56. Lingwood D, Simons K (2010) Lipid rafts as a membrane-organizing principle. Science 327: 46–50.
57. van Zanten TS, Gomez J, Manzo C, Cambi A, Buceta J, et al. (2010) Direct mapping of nanoscale compositional connectivity on intact cell membranes. Proc Natl Acad Sci U S A 107: 15437–15442.
58. Hogue IB, Grover JR, Soheilian F, Nagashima K, Ono A (2011) Gag Induces the Coalescence of Clustered Lipid Rafts and Tetraspanin-Enriched Microdomains at HIV-1 Assembly Sites on the Plasma Membrane. J Virol 85: 9749–9766.
59. Krementsov DN, Rassam P, Margeat E, Roy NH, Schneider-Schaulies J, et al. (2010) HIV-1 assembly differentially alters dynamics and partitioning of tetraspanins and raft components. Traffic 11: 1401–1414.
60. Naldini L, Blomer U, Gallay P, Ory D, Mulligan R, et al. (1996) In vivo gene delivery and stable transduction of nondividing cells by a lentiviral vector. Science 272: 263–267.
61. Schneider R, Campbell M, Nasioulas G, Felber BK, Pavlakis GN (1997) Inactivation of the human immunodeficiency virus type 1 inhibitory elements allows Rev-independent expression of Gag and Gag/protease and particle formation. J Virol 71: 4892–4903.
62. Ando R, Mizuno H, Miyawaki A (2004) Regulated fast nucleocytoplasmic shuttling observed by reversible protein highlighting. Science 306: 1370–1373.
63. Habuchi S, Tsutsui H, Kochaniak AB, Miyawaki A, van Oijen AM (2008) mKikGR, a monomeric photoswitchable fluorescent protein. PLoS One 3: e3944.
64. Chudakov DM, Lukyanov S, Lukyanov KA (2007) Tracking intracellular protein movements using photoswitchable fluorescent proteins PS-CFP2 and Dendra2. Nat Protoc 2: 2024–2032.
65. Subach FV, Malashkevich VN, Zencheck WD, Xiao H, Filonov GS, et al. (2009) Photoactivation mechanism of PAmCherry based on crystal structures of the protein in the dark and fluorescent states. Proc Natl Acad Sci U S A 106: 21097–21102.
66. Wendy L, Martinez ARM (2008) Computational Statistics Handbook with MATLAB. Chapman & Hall/CRC.

## Supporting Information: Figure S1

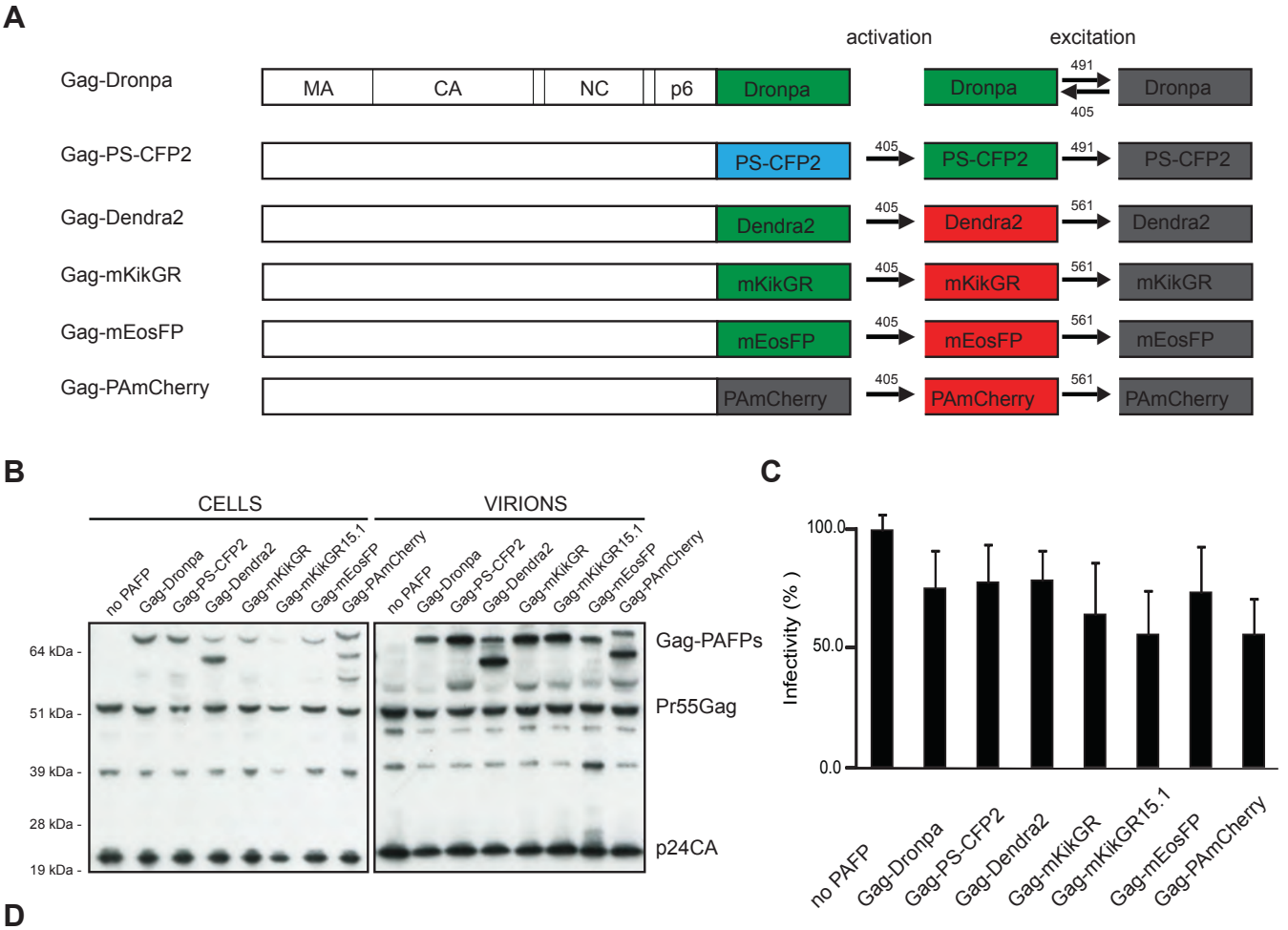

## Supporting Information: Figure S2

**A**

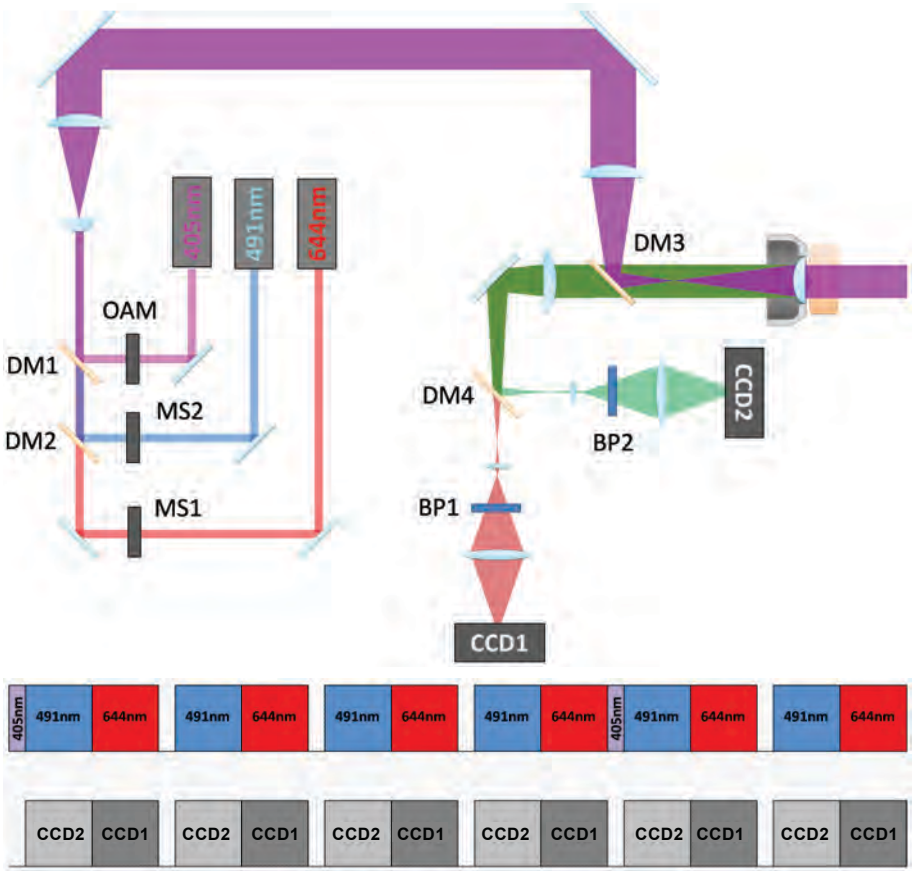


**B**

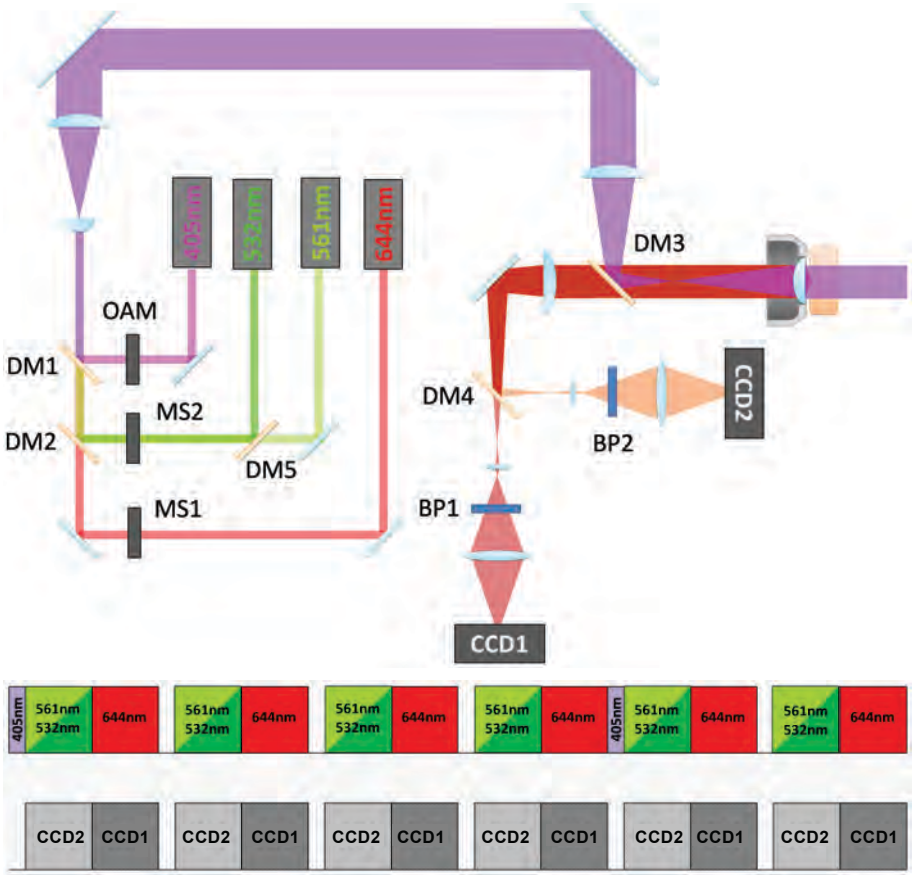

## Supporting Information: Figure S3

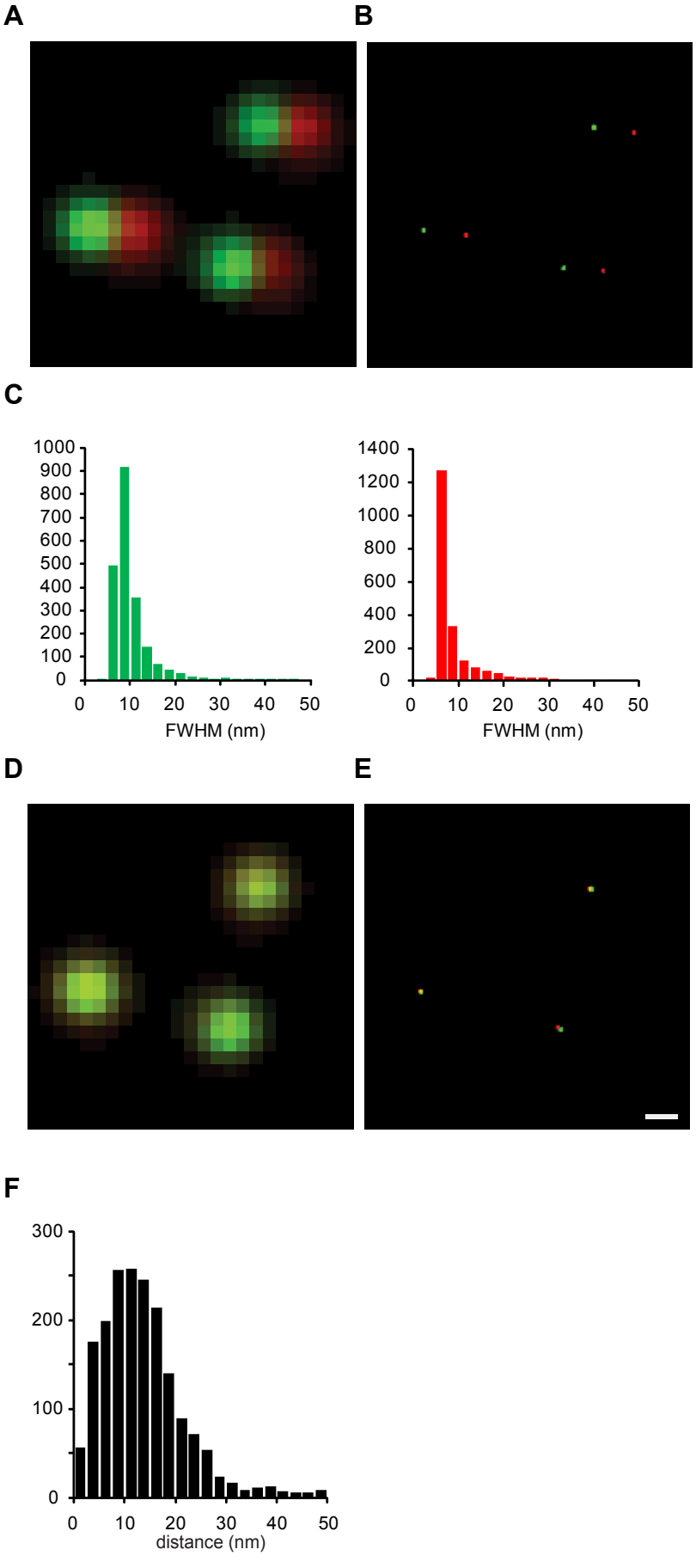

## Supporting Information: Figure S4

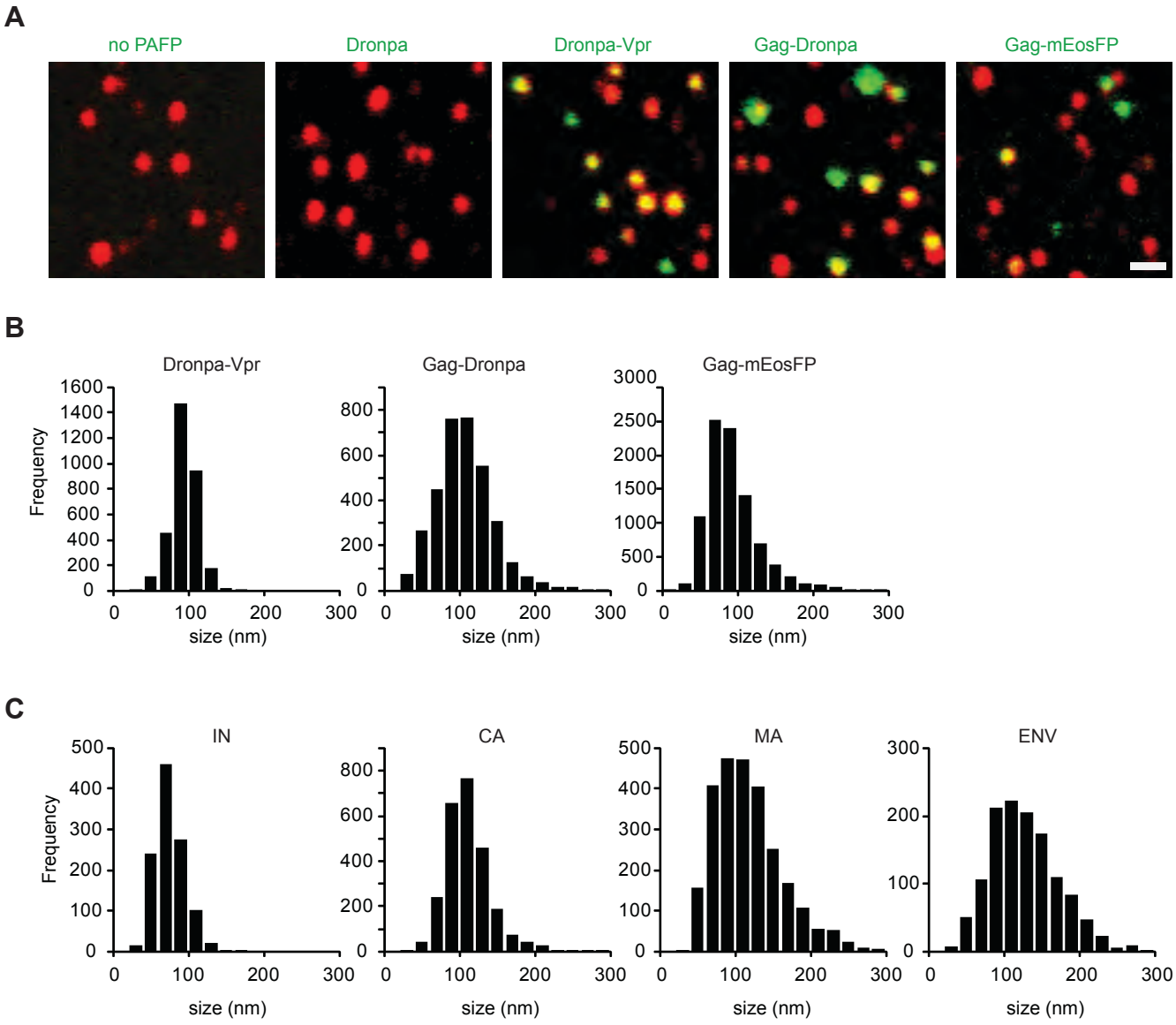

## Supporting Information: Figure S5

A

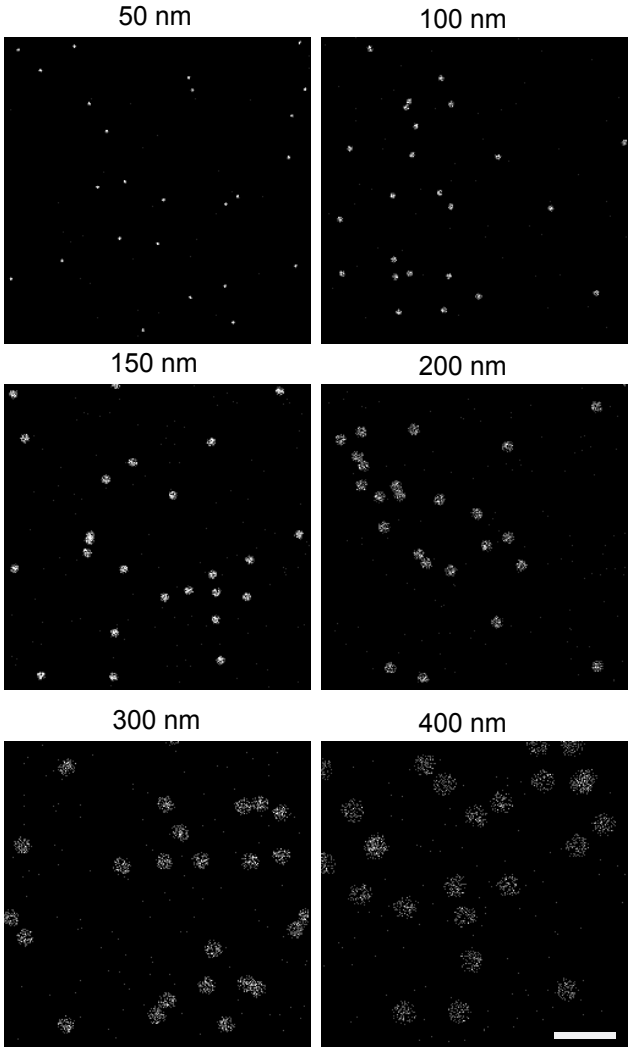


B

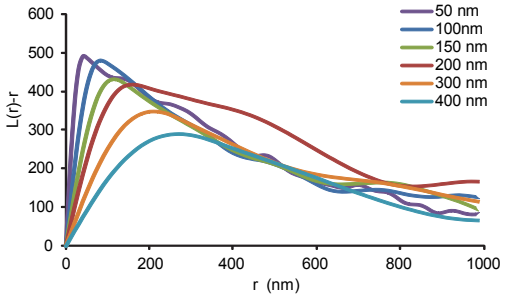


C

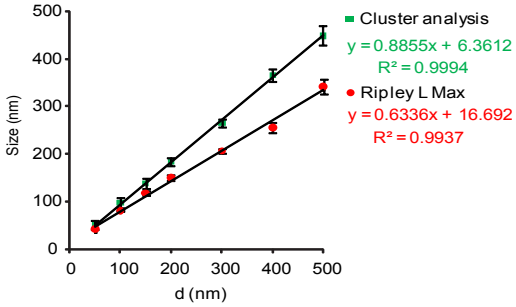


D

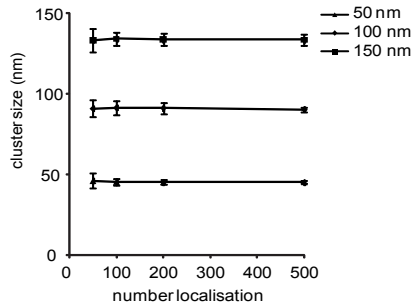

## Supporting Information: Figure S6

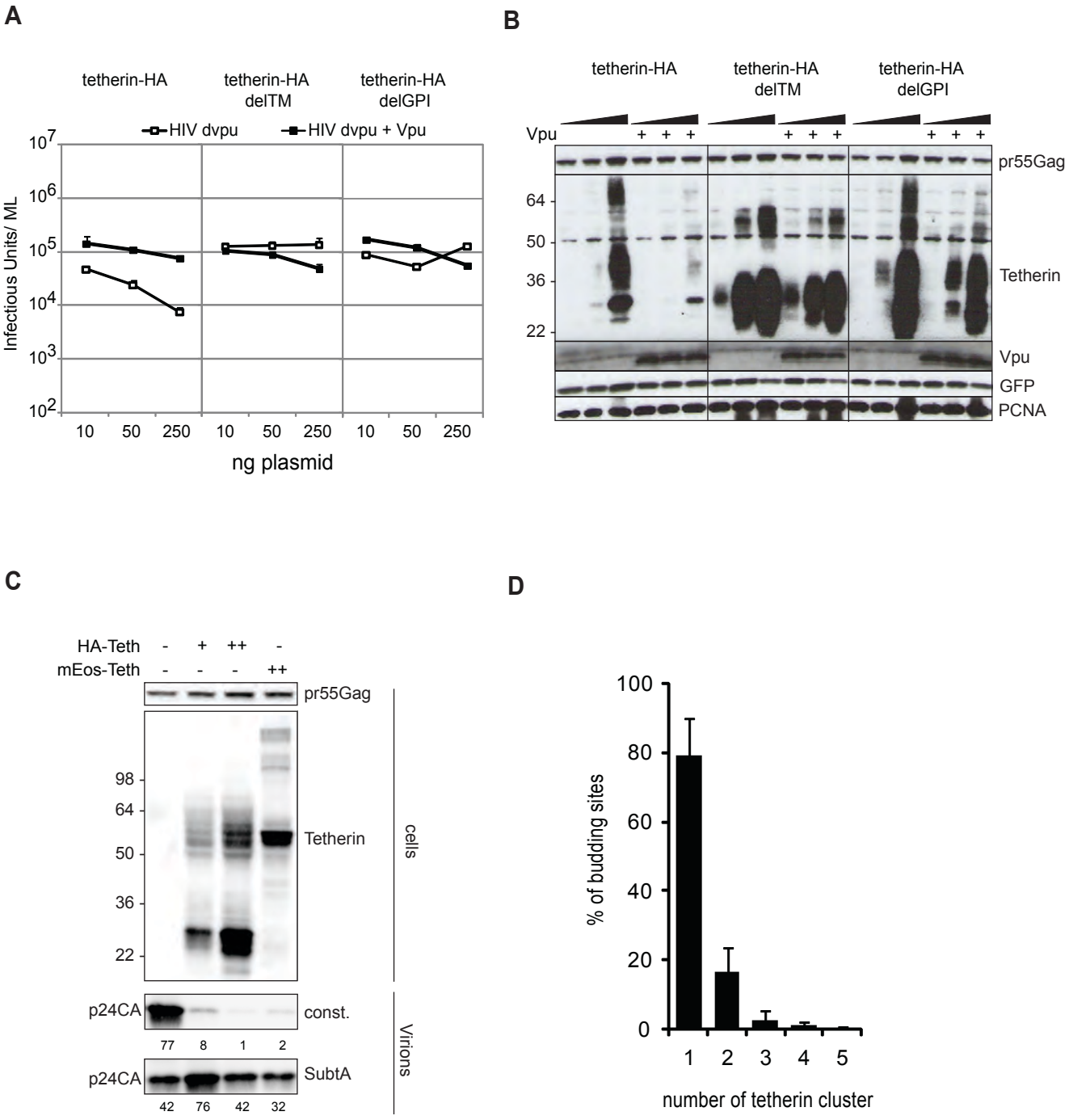

## Supporting Information: Figure S7

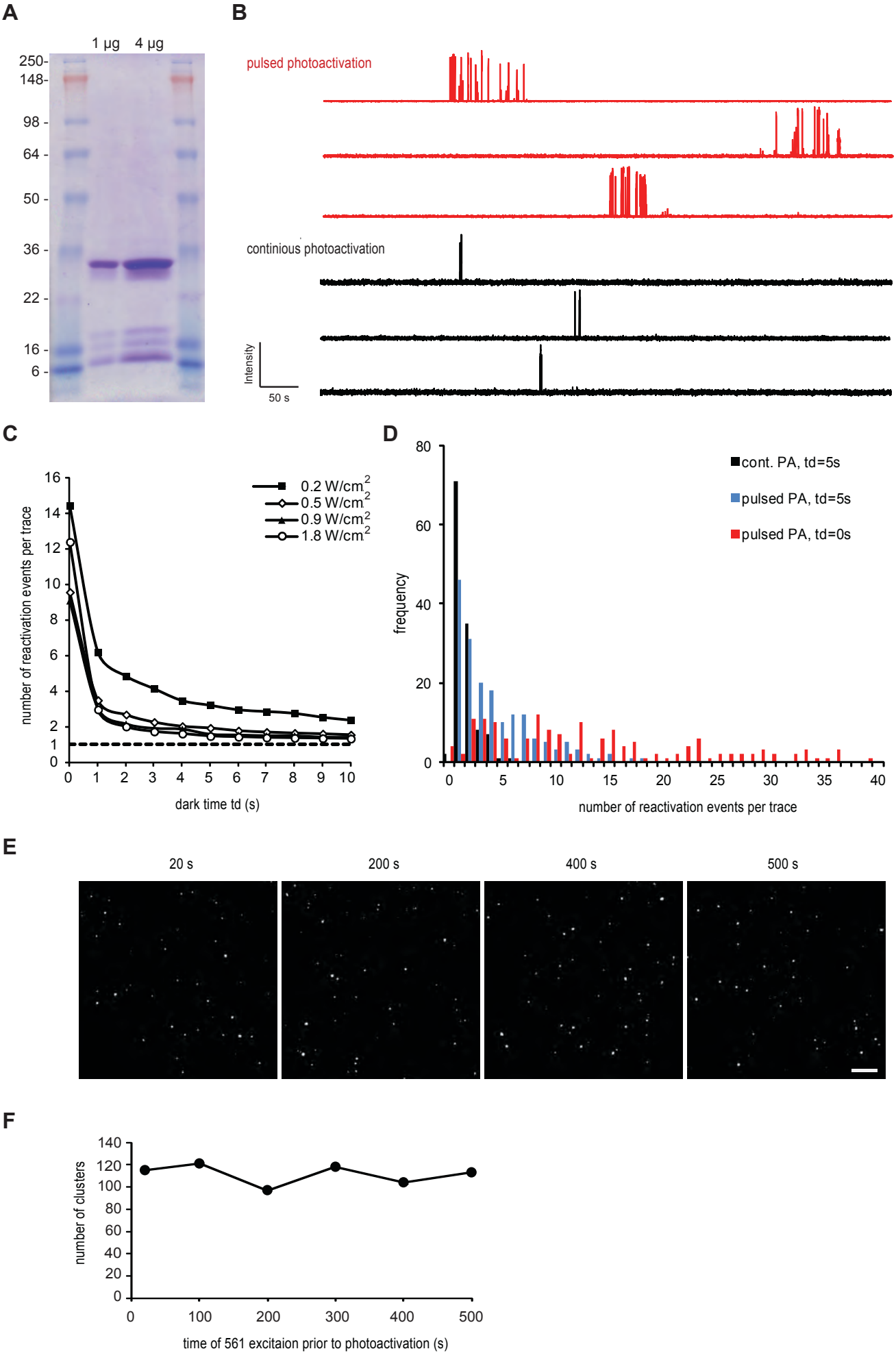

## Extended discussion and perspectives

We have performed biochemical and quantitative single molecule based super-resolution analysis to provide further understanding in the interactions between the restriction factor tetherin and HIV-1 virions.

**S**pecific and high density labeling of HIV-1 for super-resolution microscopy was achieved with Gag-Dronpa, Gag-mEosFP and Dronpa-Vpr. Similar to previously described Gag-GFP [65, 192], Gag-mEosFP and Gag-Dronpa showed budding at the plasma membrane and were incorporated into fully infectious HIV-1 particles. Gag-Dronpa, Gag-mEosFP and Dronpa-Vpr labeled virions were shown to have the expected diameter of 100nm by super-resolution microscopy. A previous PALM study found larger virus-like particles of up to 200nm as they were labeled with Gag-tandem Eos (Gag-tdEos), but without evaluating possible effects of tdEos on assembly and infectivity [163, 171]. Our results suggest that monomeric fluorescent proteins are better suited to follow assembly and budding of authentic HIV-1 in cells.

For multicolor super-resolution, we labeled HIV-1/cellular proteins with Dronpa, mEosFP or antibodies coupled to the photoswitchable dye Alexa 647 [166, 172]. PAFPs of different colors offer the possibility to genetically tag and observe different proteins and cellular structures in intact cells. PAFP are small (2-3nm) and can produce high density labeling when fusion constructs are overexpressed, but might still interfere with protein function. Compared to fluorescent dyes and quantum dots PAFP emit less photons and produces super-resolution of usually 20-50 nm.

Several groups have used Alexa 647, a bright, photostable and switchable organic dye that is commercial available in divers biological conjugates[166, 169] (www.invitrogen.com). Of note other small organic dyes from the Alexa, Atto and Cy families are also suited for single molecule super-resolution microscopy and are readily available as biological conjugates[174, 193]. A wide range of antibodies used in immunodetection of antigens like proteins, lipids and sugars can be labeled directly with this fluorophors or by similarly conjugated secondary antibodies. Antibody labeling often produces incomplete labeling due to limited affinity and access of epitopes within biological structures. In addition, antibodies have sizes between 7-10nm that must be taken into consideration when colocalisation needs to be analyzed in the range below 20nm.

Since the emission maxima of PAFP and Alexa 647 are separated by more than 100 nm, chromatic aberrations, imperfect optics and alignment need to be carefully corrected to

perform super-resolution colocalisation analysis of both fluorophors. We used high-resolution registration mapping based on fluorescent marker beads and achieved a colocalization precision of 17 nm throughout the field of view, that is comparable to results from previous two-color super-resolution studies[187, 194]. Additionally our registration procedure does not require sample incorporation of fluorescent or gold beads for local alignment.

In order to minimize possibilities for drift during image acquisition we detected emission of two fluorophors simultaneously on two independent EMCCD cameras (see Material and Methods of [191]). We could acquire two-color super-resolution images within few minutes without noticeable drift. Compared to ratio-based multicolor PALM and dSTORM imaging[188, 195], we were using the full field of view of each camera corresponding to 41x41 μm. This allowed us to image several HeLa cells at the same time and to improve statistical analysis.

We tested our two-color set-up and the colocalisation procedure on samples of Alexa 647 antibody-labeled viral proteins within Dronpa-Vpr virions. As for fluorescent beads very good colocalisation was observed for to viral capsid markers. Furthermore in accordance with electron microscopy[28] viral structures labeled with CA or MA antibodies had sizes of 112 nm and 117 nm. HIV-1 integrase localized to a structure with a characteristic size of 75nm within Dronpa-Vpr containing cores. This is to our knowledge the first time a non-structural viral protein could be localized within virions.

HIV-1 ENV was predominantly found in 1-2 peripheral clusters close to Dronpa-Vpr, consistent with their localization in the viral membrane. The clustered distribution of ENV was not induced by antibody-mediated cross-linking since the viral particles were fixed extensively with paraformaldehyde prior to immunofluorescence staining.

A clustered distribution of ENV on HIV-1 virions was observed by electron tomography previously and could be functionally relevant during cell attachment and fusion[**196, 197**]. Clustered ENV may result from incorporation of concentrated Env in lipid microdomains of producer cells and may facilitate CD4 and coreceptor recruitment that is required for signaling and fusion[39, 198].

HIV-1 assembles at the plasma membrane of HeLa cells within 10-15 min as previously visualized by diffraction-limited TIRF microscopy of Gag-GFP[65, 66]. We observed by super-resolution microscopy Gag-mEosFP clusters of varying sizes surrounded by ENV clusters. Coclustering appeared within the TIRF imaging plane that is 100-200nm above the coverslip. This indicates that budding events, but not endocytosed virions are visualized at the plasma membrane of HeLa cells. ENV was previously found in distinct clusters at assembly sites [198]. Overall, super-resolution microscopy analysis provides detailed images of HIV-1 proteins at

assembly sites and can be used to investigate cellular proteins interacting with budding virions.

We applied super-resolution microscopy for the HIV-1 cellular restriction factor, tetherin with the aim to investigate tetherin plasma membrane distribution, virus-tetherin interaction and orientation of tetherin molecules during restriction. Previous electron and conventional fluorescence microscopy found endogenous and overexpressed tetherin in endosomal compartments and in clusters at the plasma membrane[129-131]. The localization of tetherin at budding sites was noted in some cases [96, 117, 129, 130], but not all [100, 141]. The size of the clusters could not be determined due to the diffraction-limited resolution of conventional fluorescence microscopy or low density labeling in immuno-electron microscopy.

Using super-resolution microscopy and calibrated size measurements we found that both endogenous and overexpressed tetherins are organized in 70-90 nm clusters at the plasma membrane of HeLa cells.

Clustering of tetherin could be an artifact due to repeated localization of single molecules of mEos2 or Alexa 647 that repeatedly recover from dark into fluorescent states [199]. We observe similar cluster sizes of 70-90nm for all tetherin constructs and endogenous tetherin labeled with photoactivatable proteins and Alexa 647 antibodies. Repeated localization of single molecules would result in much smaller cluster sizes close to the resolution limit of 20-40nm[200]. Additionally the decrease in clustering of different mutant tetherins, that are all labeled with Alexa 647 antibodies points against a clustering artifact. Similarly antibody or GFP-labeled tetherin was recently found in 70-150 nm clusters in HeLa cells by structured illumination microscopy[201]. Overall several imaging techniques established the localization of tetherin in nanometer sized clusters at the plasma membrane.

Our super-resolution analysis revealed that both membrane anchors of tetherin are required for clustering possibly through high order complexes [103], interaction of the cytoplasmic tail with the actin cytoskeleton [113] and lipid raft association via the GPI anchor [98].

Several models depicting the orientation of tetherin during the restriction on release of HIV-1 (Figure 16A) and other enveloped viruses have been proposed[87]. Recent studies have shown that tetherin act alone and that no cofactor in the viral or cellular membrane is needed for inhibition of HIV-1 release[103]. Based on increased incorporation of GPI- deficient tetherin into virions with late-budding defects Perez-Caballero proposed that extended tetherin dimers inhibit HIV-1 release[103]. Our work provides biochemical and super-resolution microscopy evidence for HIV-1 restriction via an extended conformation of tetherin. This model requires that pairs of membrane anchors incorporate into the cell membrane and the viral membrane and an extended coiled-coil domain spans the gap between both membranes. PI-PLC and subtilisin A treatment efficiently removed tethered virions from the surface of 293T cells transfected with tetherin. Of note, in HeLa cells vpu-deficient HIV-1 virions were not released by PI-PLC treatment and few more virions were released by proteolytic digestions or mechanical sheering [104, 130]. Neither of these studies demonstrated cleavage of the tetherin GPI anchor in HeLa cells. We found that PIPLC indeed cleaves surface tetherin less efficiently than the protease Subtilisin A. Additionally HeLa cells have lower amounts of vpu-deficient virions bound to the cell surface compared to 293T cells [202]. Virus accumulation in biofilm-like extracellular assemblies as reported for HTLV could further limit stripping efficiency by PI-PLC[203]. Alternatively a fraction of tetherin that contains a second transmembrane domain instead a C-terminal GPI-anchor would be insensitive to PI-PLC treatment [104] but our results and previous reports indicate a C-terminal GPI-modification of rat and human tetherin [98, 102, 103] further biochemical analysis of tetherin C-terminal membrane anchor by mass spectroscopy is needed.

Our biochemical analysis established that extended tetherin dimers restrict HIV-1 release, but does not allow conclusions on the initial orientation of tetherin, since chains and clusters of tethered virions must contain both possible orientations of the extended tetherin dimers[103].

Using super-resolution microscopy and colocalisation analysis, we found that tetherin mutants lacking the TM failed to concentrate at HIV-1 assembly sites. This result indicates that the tetherin transmembrane domain stably associated with HIV-1 membranes.

Alternatively tetherin could also associate with HIV-1 budding sites via shared localization to lipid raft domains (Figure 16B) as both show some resistance to cold detergent extraction [55, 98, 202, 204]. Both tetherin and Gag also co fractionated with the lipid raft marker caveolin [205]. Nevertheless cofractionation of proteins with raft markers does not prove their direct

association or localization to similar lipid raft domains [206]. Indeed cross-linking antibodies against tetherin inhibited its antiviral effect but increased tetherin/Gag cofractionation [205].

Using super-resolution microscopy we found tetherin clusters in close association with GM1 lipid domains, but without significant overlap as previously noted for other raft proteins [207]. HIV-1 budding sites did not show significant association with GM1 lipid domains or with a tetherin mutant containing only the GPI membrane anchor. Recently HIV-1 Gag multimerization was shown to induce the coalescence of lipid raft markers and tetraspanins as visualized by antibody copatching, FRET analysis and single molecule tracking[58, 208]. Both studies required copatching of raft markers (GM1, CD55 and HA–TM) and tetraspanins (CD9, CD81) to demonstrate their enrichment at HIV-1 budding sites due to the limited detection sensitivity of conventional fluorescence microscopy. Copatching could affect protein mobility and association with HIV-1 budding sites.

GFP-GPI and unpatched CD55 failed to stably associate with viral assembly sites[58, 66]. The later observations are consistent with our results obtained from unpatched GM-1 that was stained after fixation. Additionally the stable association of patched HA-TM and tetraspanins with viral assembly sites [58, 208] is in line with our observation that clustered tetherin molecules stably associates with the viral membrane via their transmembrane domains.

Altogether, we found that the tetherin GPI modification and the association with GM1 lipid domains are not important for localization of tetherin to HIV-1 budding sites. Tetherin GPI anchors is implicated in local concentration of tetherin and maybe important for the endocytosis of retained virions.

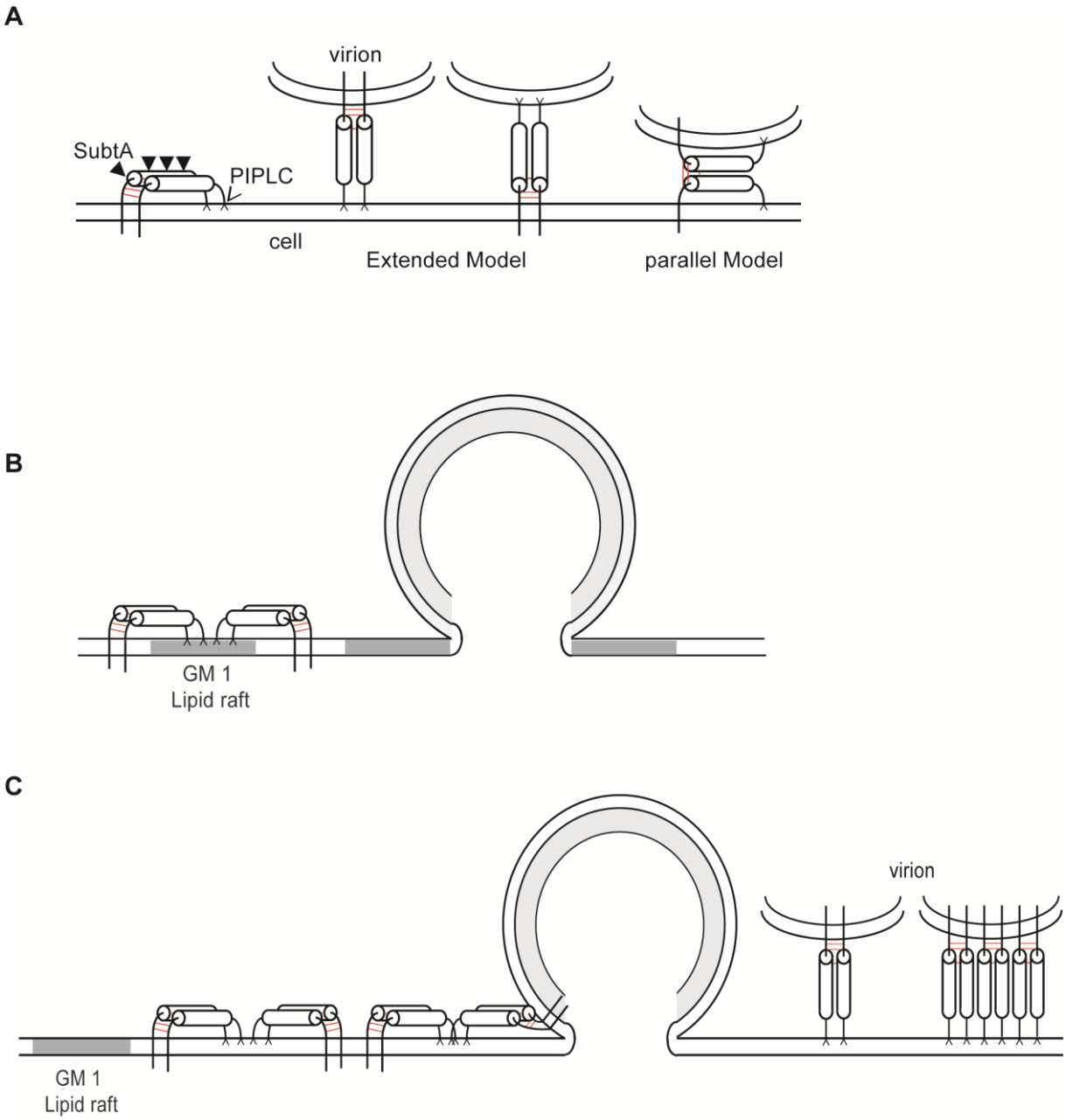


**Figure 16. Models for tetherin orientation and recruitment to HIV-1 budding sites**

*(A) Model of tetherin and possible orientations during restriction with potential enzymatic sites of Subtilisin A (SubtA) and PIPLC*

*(B) Hypothetic model for tetherin recruitment to HIV-1 budding sites via GM1 lipid raft domains*

*(C) Proposed model of tetherin restriction based on results from*[191]*. Tetherin concentrates in clusters containing 5-11 dimers independent of GM1 lipid rafts and stably incorporates their TMD into budding virions.4-7 tetherin dimers remain associated with budding sites.*

At HIV-1 assembly sites, we found single tetherin clusters and wanted to determine the number of tetherin molecules in these clusters. We constructed photoactivatable mEosFP-tetherin that showed a clustered plasma membrane distribution, efficient restriction of HIV-1 particle release and was counteracted by Vpu. After careful photo-physical characterization of purified mEosFP and the adjustment of imaging and analysis parameters to enabled reliable single molecule counting of mEosFP we determined mEosFP-tetherin quantities at HIV-1 assembly sites.

We found 5-11 tetherin dimers in single clusters in the absence of HIV-1 and 4-7 tetherin dimers associated with HIV-1 budding sites, that represents a significant difference ($p<0.001$, Student's t-test). This indicates that about 70% of tetherin molecules within a cluster remain stably associated with budding sites possibly through incorporation of their TM domains into the viral membrane. The exact number of tetherin molecules that restrict individual HIV-1 virions remains actually to be determined. Unfortunately, in our TIRF illumination field we were not able to image chains of attached virions. Thin-sections of 200-300 nm of cells expressing HIV-1 and mEosFP-tetherin could be analyzed by super-resolution microscopy[163]. mEosFP-tetherin could then be counting in viral clusters and chains allowing the estimation of tetherin molecules that restrict individual HIV-1.

Of note, a low number of clustered tetherin dimers are sufficient to restrict the release of newly formed virions. Crosslinking antibodies against tetherin interfere with tethering function, reduce incorporation of tetherin into virions and affected the distribution of tetherin within membrane raft fractions [205]. Similarly, mutations within the extracellular domain reduced tetherin clustering and impaired anti-viral activity[201].

We can propose the following mechanism for HIV-1 restriction by tetherin as depicted in Figure 16C:

Initially, tetherin locally concentrates in clusters containing 5-11 dimers and this involves both TM and GPI membrane anchors. The organization of tetherin dimers in clusters could concentrate and position tetherin for optimal restriction and limit access to viral countermeasures. In the absence of Vpu, tetherin N-termini associate with HIV-1 budding sites independently of GM1-enriched raft domains and become trapped during Gag-multimerization. Clusters containing 4-7 tetherin dimers remain associated with budding virions and can mediate restriction. Flexible coiled-coil interactions within dimers [107] are likely to enable retention of GPI anchors within the host cell membrane during budding and membrane scission. The final predicted topology is that of extended tetherin dimers with N-termini inside newly formed virions.

## Paper 2: HIV-1 activates Cdc42 and induces membrane extensions in immature dendritic cells to facilitate cell-to-cell virus propagation

Dendritic cells participate in early events of mucosal HIV-1 transmission through capture and subsequent transfer of virus to T-cells at infectious synapses[36]. HIV-1 spreads more than 100 fold more efficiently through direct cell-to-cell contacts than through the cell-free route [209]. Virions that are transferred at cell-to-cell contacts can avoid neutralizing antibodies and gain facilitated access to concentrated receptors at the contact zone [35, 210]. Infectious synapses and membrane extensions mediate HIV-1 cell-to-cell transfer between T-cells and depend on the actin cytoskeleton[61, 211, 212].

DC capture HIV-1 via binding to the c-type lectin DC-SIGN[32] and store virions in intracellular compartments, enriched in tetraspanins and actin[213, 214]. Previous work from our lab has established that DC-SIGN also plays an important role in HIV-1 infectious synapse formation (Figure 17) through an unclear mechanism[215, 216]. It is known that DC-SIGN engagement by HIV-1 Env activates Rho-GTPases and various signaling pathways involved in cellular migration, maturation and cytoskeleton remodeling that overall preserve an immature DC phenotype[217, 218]. The contribution of the cytoskeleton to the formation of infectious synapses, membrane extensions and viral transfer between HIV-1 pulsed immature DC and T-cells is of high physiological relevance to early HIV-1 dissemination and were therefore investigated here in detail.

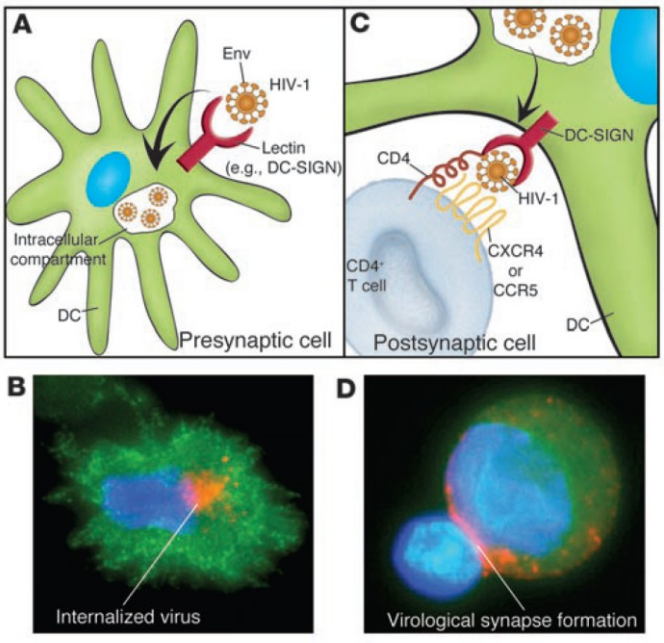


**Figure 17. Model of HIV-1 capture by dendritic cells and transfer to T-cells**

*(A,B) HIV-1 binds to C-type lectins (e.g. DC-SIGN) and is internalized into intracellular compartments inside the DC (green)*

*(C,D) When HIV-1 loaded DC encounter CD4$^+$ T-cells intracellular virions were redistributed to the contact zone and become transferred to the T-cell. In immunofluorescence images nuclei are blue, DC green and HIV-1 virions orange. Taken from* [219]

We used systematic siRNA knockdowns of cytoskeleton modulators like guanine-exchange factors, different Rho-GTPases and formins in immature DCs (iDC) to identify pathways required for HIV-1 trafficking and transfer at the infectious synapse.
Both X4 and R5 HIV-1 Env induced the formation of membrane-extensions in iDC through binding to DC-SIGN and Cdc42 signaling. Notably both genetic and pharmacological inhibition of the Rho-GTPase Cdc42 reduced the number of membrane extensions and decreased HIV-1 transfer to target T cells significantly. Fluorescently labeled HIV-1 particles were found on dynamic membrane extensions on iDC and within infectious synapses between iDC and target T-cells. Ion-abrasion scanning electron microscopy and live cell imaging revealed structural and dynamic properties of these sheet-like membrane extension, that are distinct from previously described filopodia and nanotubes[212, 220]. When contacts between iDCs and T cells were increased by promoting IS or at high T to DC cell ratio, as found typically in lymph nodes, most of the HIV-1 transfer was mediated by Cdc42-dependent membrane extensions. Therefore, HIV-1 induces membrane extensions in iDC via Env-DC-Sign-Cdc42 signaling to increase viral transfer at the infectious synapse as determined in this highly relevant primary cell model. The overall importance of the actin cytoskeleton, membrane extensions and cell-to-cell transfer between DC and T-cells within infected individuals remain to be determined. The better knowledge of early mucosal HIV-1 transmission can help to design effective microbicides[221].

I contributed to this work fluorescent labeling, biochemical characterization and dynamic visualization of HIV-1 particles (Figure S6). Specifically I imaged HIV-1 on membrane extensions on live immature dendritic cells and within infectious iDC-T- cell synapses using spinning disc confocal microscopy (Figure 5B-C and Supplemental movies 1-6).

The results of this publication, implications and relevant recent literature concerning HIV-1 and cytoskeleton remodeling are extensively discussed in a recently published accompanying review[39]:

## Review: How HIV-1 takes advantage of the cytoskeleton for replication and cell-to-cell transfer.

# HIV-1 activates Cdc42 and induces membrane extensions in immature dendritic cells to facilitate cell-to-cell virus propagation

Damjan S. Nikolic,[1] Martin Lehmann,[1] Richard Felts,[2] Eduardo Garcia,[1] Fabien P. Blanchet,[1,3] Sriram Subramaniam,[2] and Vincent Piguet[1,3]

[1]Departments of Dermatology and Venereology, Microbiology and Molecular Medicine, University Hospitals and Medical School of Geneva, Geneva, Switzerland; [2]Laboratory of Cell Biology, Center for Cancer Research, National Cancer Institute, National Institutes of Health, Bethesda, MD; and [3]Department of Dermatology and Wound Healing, Cardiff University School of Medicine and University Hospital of Wales, Cardiff, United Kingdom

**HIV-1 cell-to-cell transmission confers a strong advantage as it increases efficiency of transfer up to 100-fold compared with a cell-free route. Mechanisms of HIV-1 cell-to-cell transmission are still unclear and can in part be explained by the presence of actin-containing cellular protrusions. Such protrusions have been shown to facilitate cell-to-cell viral dissemination. Using fluorescence microscopy, electron tomography, and ion abrasion scanning electron microscopy we show that HIV-1 induces membrane extensions in immature dendritic cells through activation of Cdc42. We demonstrate that these extensions are induced after engagement of DC-SIGN by HIV-1$^{env}$ via a cascade that involves Src kinases, Cdc42, Pak1, and Wasp. Silencing of Cdc42 or treatment with a specific Cdc42 inhibitor, Secramine A, dramatically reduced the number of membrane protrusions visualized on the cell surface and decreased HIV-1 transfer via infectious synapses. Ion abrasion scanning electron microscopy of cell-cell contact regions showed that cellular extensions from immature dendritic cells that have the appearance of thin filopodia in thin section images are indeed extended membranous sheets with a narrow cross section. Our results demonstrate that HIV-1 binding on immature dendritic cells enhances the formation of membrane extensions that facilitate HIV-1 transfer to CD4$^+$ T lymphocytes. (*Blood*. 2011;118(18):4841-4852)**

## Introduction

Dendritic cells (DCs) are among the first potential targets for HIV-1 during mucosal transmission and participate in early dissemination of the virus.[1,2] One of the important steps for HIV-1 propagation is the transfer of virus at the infectious synapse between DCs and CD4$^+$ T cells.[3] This mode of cell-to-cell propagation of the pathogen across the DC-T cell infectious synapse may confer several advantages to the virus as it offers a faster propagation as well as some level of immune evasion.[4,5] Despite many advances in the understanding of transfer of HIV-1 infection from DCs to T cells,[2,3,6-12] not much is known yet about the structural and biochemical mechanisms that are responsible for viral transfer by cell-to-cell transmission.

It has been reported that binding of HIV-1 to the C-type lectin receptor DC-SIGN[7] on DC increases DC-T cell infectious synapse formation[6] and that DC-SIGN engagement by HIV-1 induces activation of Rho-GTPases via the guanidine exchange factor LARG,[8,9] which then presumably activates the kinase Raf-1.[12] Alternatively, gp120-mediated activation of Pyk2, p38 MAP kinase, and LSP1 has also recently been implicated in DC migration after HIV-1 binding.[10] Other signaling cascades in DCs, such as the Erk pathway[11,12] and the Src/Syk pathway,[15] might also be activated by HIV-1. These signaling programs triggered by DC-SIGN engagement suggest potential links between C-type lectin receptors activation on DCs and cytoskeletal remodeling. In addition to these mechanisms, Rho-GTPases are known to modulate cytoskeletal components and are required for a broad range of cellular functions, such as cell migration, trafficking, or cell polarity.[13] Several bacterial pathogens have developed strategies to activate host cell Rho-GTPases to facilitate propagation, such as Shigella, which induces Cdc42 activation to facilitate bacterial invasion.[14] Effector proteins of Salmonella can mimic functions of Rho-GTPases, thereby facilitating remodeling of actin cytoskeleton in host cells.[15] Similar findings have been reported with herpes simplex virus type 1 (HSV-1) and African swine fever virus, which appear to induce membrane projections on target cells.[16,17] The relative contribution of these actin-based protrusions during cell-to-cell transmission of HIV-1 is currently not fully established, although a recent study has attempted to tackle this question during T cell–T cell transmission of HIV-1,[18] and recent 3D electron microscopic studies of the virologic synapse formed between mature DCs and CD4$^+$ T cells have shown that there are extensive membrane extensions emanating from the DCs that wrap around the T cells.

Because DC-SIGN has previously been identified as a factor promoting DC-T cell infectious synapse formation,[6,25] we investigated whether HIV-1 could trigger a signaling program that induces actin-based protrusions at the surface of DCs, thereby facilitating an anterograde viral transfer from DCs to CD4$^+$ T cells across infectious synapses. Our results demonstrate a 2-step model for HIV-1 transfer from immature DCs to T cells that involves HIV-1$^{env}$ engagement of the DC-SIGN receptor, leading to Cdc42 activation and formation of membrane extensions, followed by the Cdc42-dependent transfer of virus to the T-cell.

Submitted September 1, 2010; accepted April 24, 2011. Prepublished online as *Blood* First Edition paper, May 11, 2011; DOI 10.1182/blood-2010-09-305417.

The online version of this article contains a data supplement.

The publication costs of this article were defrayed in part by page charge payment. Therefore, and solely to indicate this fact, this article is hereby marked "advertisement" in accordance with 18 USC section 1734.

## Methods

### Cells

Monocytes were purified after Ficoll gradient separation with CD14 MicroBeads (130-050-201; Miltenyi Biotec). $CD14^+$ cells were obtained at purities $> 95\%$. Human DCs were generated by incubating purified monocytes in complete Iscove modified Dulbecco medium supplemented with 500 IU/mL GM-CSF and 500 IU/mL IL-4 (both Strathman Biotec). DCs were harvested at day 6 and analyzed by flow cytometry. Resting autologous $CD4^+$ T lymphocytes were purified by negative selection with $CD4^+$ T Cell Isolation kit II (130-091-155; Miltenyi Biotec). Myeloid DCs (MyDCs) were purified by negative and positive selection with CD1c $(BDCA\text{-}1)^+$ Dendritic Cell Isolation Kit (130-090-506; Miltenyi Biotec), as recently described.[20] Jurkat (J77Cl.20) and resting autologous $CD4^+$ T lymphocytes were maintained in complete RPMI 1640. 293T human embryonic kidney cells, and HeLa P4-R5 (#3580; National Institutes of Health AIDS Research & Reference Reagent Program) cells were maintained in DMEM.

### Plasmids

The plasmids R9 and R9 INHA were provided by D. Trono (EPFL). S15 mCherry was a kind gift of T. Hope (Northwestern University, Chicago, IL). Enhanced green fluorescent protein (eGFP) *vpr* was generated by PCR cloning of *vpr* with primers 5′-TATACTGCAGGAATGGAACAAGCCCCAGAAGACC-3′ and 5′-TATAGGATCCGCTAGCTGGCCAGGATCGGT-3′ from pCMX.vpr96 and inserted into Pst1 and BamH1 sites of eGFP-C1 (Clontech). Full-length HIV-1–expressing F522Y-mutant HIV-1*gp41* was previously described.[21] pcDNA3-EGFP-Cdc42 (WT; 12599), pcDNA3-EGFP-Cdc42 (Q61L/ Constitutive Active; 12600), and pcDNA3-EGFP-Cdc42 (T17N/Dominant Negative; 12601) were from Addgene.

### DC nucleofection

A total of $2 \times 10^6$ immature DCs were nucleofected with 10 μg pcDNA of the different Cdc42 mutants with the Amaxa Nucleofector (AAD-1001) and the Human Dendritic Cell Nucleofector Kit I (VPA-1004). Cells were recovered in IMDM for 12 hours and subsequently analyzed for viability and eGFP expression by flow cytometry.

### DC sorting

Nucleofected DCs expressing eGFP-tagged Cdc42 mutants were sorted 12 hours after transfection with a FACSVantage SE sorter (BD Biosciences). Cells were subsequently analyzed for viability, fraction enrichment, and CD1a and DC-SIGN cell surface expression 2 to 4 hours after sorting. Sorted DCs were then used for confocal microscope analysis, coculture experiments with T lymphocytes, and fusion-assay experiments.

### Virus production

Virus stocks were produced by transient transfection of 293T cells with calcium-phosphate coprecipitated proviral plasmid pR9, which encodes for a full-length HIV-1×4 strain provirus. R9-eGFP*vpr*-S15mCherry was produced as described.[22] Infectious titers of viral stocks were evaluated by limiting dilution on HeLa P4-R5 cells. Physical titers were evaluated by quantification of HIV-1 $p24^{gag}$ by ELISA kit (Beckman Coulter).

### Drugs

All chemicals were obtained from Sigma-Aldrich unless stated otherwise. Puromycin 25 was used at 1μM. Cytochalasin D was diluted to 1, 2, or 10μM. Latrunculin A was used at 100nM or 1μM. Jasplakinolide (Calbiochem) was used at 100nM or 1μM. For transfer assays, indinavir (Merck) was used at 1 μg/mL and 50 μg/mL. Pronase (Roche Diagnostics) was diluted at concentrations ranging from 100 to 400 μg/mL. The specific Src kinase inhibitor 4-amino-5-(4-chlorophenyl)-7-(t-butyl)pyrazolo[3,4-d pyrimidine (PP2; Calbiochem) was used at a final concentration of 50μM. Secramine A was a kind gift from the Kirchhausen laboratory (Harvard Medical School) and the Hammond laboratory (University of Louisville) and was synthesized by Bo Xu and G. B. Hammond (University of Louisville).[23]

### Antibodies and reagents

Antibodies against LARG (N-14), actin (C-11), Dia1 (N-16), and Arp3 (A1) were from Santa Cruz Biotechnology. Antibodies against CD3 (UCHT-1) and Rac1 (23A8) were from Millipore. Antibody against Cdc42 was from BD Transduction Laboratories. Anti-Src (#2108), anti–Phospho-Src (#2101), anti-Pak1 (#2602), anti–Phospho-Pak1 (#2605), and anti-Wasp (#4860) were from Cell Signaling Technology. Anti–phospho-WASP (NB100-2307) was obtained from Novus Biologicals. Anti–HIV-1-$p24^{gag}$ (KC57) was from Beckman Coulter. Anti-dsRed was from Clontech. Human anti–HIV-1 was from Immunodiagnostic. Fluorescence-activated cell sorter antibodies were obtained from BD Transduction Laboratories. Phalloidin AlexaFluor-546 and AlexaFluor-647 were from Invitrogen. Superantigens were obtained from Toxin Technology.

### Infections and transfer assays

DCs ($2.5 \times 10^5$) were put in contact with 500 ng p24 HIV-1 overnight. Cells were then recovered, washed, and put in contact with $CD4^+$ T lymphocytes at different ratios (5:1; 1:1, 1:5) for 96 hours in the presence of the protease inhibitor indinavir. Drugs, when used, were added to cocultures for 30 minutes before washing. Conjugates were recovered and stained for CD3 and HIV-1p24. The fraction of CD3-positivie cells (T lymphocytes) was analyzed for HIV-1p24 coexpression, thus representing the HIV-1–infected fraction of $CD4^+$ T lymphocytes. Normalized HIV-1 transfer was defined as a comparison relative to nontreated condition artificially set at 100%.

### Cdc42 activation assay

Active Cdc42 bound to Pak1 was recovered following the manufacturer's instructions (BK034; Cytoskeleton). The activated fraction of the total pool of available Cdc42 bound to its downstream target Pak1 was recovered. Pak1 bound to Pak1 binding domain beads was recovered by centrifugation. Input and pull-down fractions were subsequently analyzed for Cdc42 protein expression. Pull-down efficiency was analyzed with glutathione S-transferase (71-7500; Zymed) detection.

### DC-T cell infectious synapses assay

Infectious synapse assays were performed as previously described.[6,24] DCs ($2.5 \times 10^5$) were put in contact with 500 ng p24 HIV-1 overnight. Cells were then recovered, washed, and put in contact with $CD4^+$ T lymphocytes at different ratios (5:1; 1:1, 1:5) for 30 minutes. Drugs, when used, were added to cocultures for 30 minutes before washing. Cells were then fixed with 3% paraformaldehyde for 20 minutes and processed for confocal microscopy. We defined an infectious synapse as a DC-T cell conjugate where the majority of HIV-1 ($> 50\%$) is focused at the zone of contact with the Jurkat/resting autologous $CD4^+$ T cells as previously described.[3,6]

### Transmission electron microscopy

Cells were harvested and fixed in 2% formaldehyde plus 1.5% glutaraldehyde in 0.2M sodium phosphate buffer, pH 7.4, at room temperature for 2 hours. Cells were then washed once in sodium phosphate buffer and prepared for epon sectioning. After ultramicrotome sectioning, sections were analyzed with a Philips CM10 transmission electron microscope (Philips).

### Electron tomography

Cells were fixed in glutaraldehyde, Epon-embedded, and stained with osmium tetroxide and uranyl acetate as described previously.[25] Sections with nominal thicknesses of 100 nm and 175 nm were prepared using a Leica Ultracut microtome and imaged in a Tecnai 12 electron microscope (FEI Company) operated at 120 kV, and equipped with a 4K × 4K Gatan charge-coupled device. For tomography, images were recorded over an angular range of ± 70 degrees, and reconstructed to obtain a 3D volume using weighted back projection as implemented in the image processing package IMOD.[26]

### Ion abrasion scanning electron microscopy

Cells were prepared using procedures identical to those used for the electron tomographic experiments. The resin blocks containing the cells were trimmed using a razor into a cube with approximate surface dimensions of 1 $mm^2$. The cube was secured to an aluminum SEM stub using silver paint. The sample was then coated with a 100-nm layer of gold using a sputter coater before coating with platinum/palladium to a thickness of ~ 1000 nm using the gas injector system of the microscope. The sample was imaged using a Nova 200 NanoLab dual-beam instrument (FEI) equipped with a Ga ion source for milling and a field emission gun scanning electron microscope with an in-lens secondary electron detector for imaging. Secondary electron scanning electron microscopy (SEM) images were typically recorded at an accelerating voltage of 3 kV, a magnification of 10 000×, and a beam current of 273 pA in the immersion lens mode, with a 5.0 mm working distance and a pixel size of 5.3 nm. Material was removed in step sizes of approximately 25 nm using the focused ion beam. Image segmentation was carried out using Amira (Visage Imaging).

### Fusion assay

For analysis of virus fusion, HIV-1 labeled with eGFP-*vpr* and S15-mCherry was spinoculated onto cells, washed, and fixed in 4% paraformaldehyde immediately or after 2 to 3 hours of incubation at 37°C. Fixed cells were quenched in 0.1M glycine, mounted in Mowiol, and analyzed by CLSM (Zeiss LSM 510 Meta). Colocalization analysis was performed with ImageJ (National Institutes of Health) on an overlapping pixel area basis.

### Live cell imaging

Cells were maintained at 37°C in a humidified-atmosphere cage incubator (Okolab). Image acquisition was performed using a 60× NA 1.4 oil objective (Nikon) on a spinning-disk confocal microscope (Ultraview; PerkinElmer Life and Analytical Sciences) upgraded with Andor Revolution, and controlled by the software Revolution iQ (Andor). Image sequences were processed and analyzed with ImageJ software (National Institutes of Health). Single particle trajectories were extracted from eGFP signals using a tracking algorithm and analyzed using Excel 2007 software (Microsoft).

### siRNA transfections

DCs or MyDCs were transfected with siCtrl (5′-AAATGAACGTGAATTGCTCAA-3); siRNA sequence specific for luciferase, siDia1 (5′-AAGCTGGTCAGAGCCATGGAT-3); siRNA sequence specific for Dia1, siLarg (5′-AAGAAACTCGTCGCATCTTCC-3); siRNA sequence specific for LARG, all from QIAGEN. Alternatively, the following siRNA mixes were purchased from Santa Cruz Biotechnology: siRac1 (sc-36351), siCdc42 (sc-29256), siArp3 (sc-29739), and siMoesin (sc-35955). Transfections were performed twice using HiPerFect Transfection Reagent (QIAGEN) according to the manufacturer's recommendations. Specific gene knockdowns were assessed by Western blot followed by densitometry analysis (Quantity One; Bio-Rad).

### Statistical analysis

Significant differences between groups were calculated using the Student *t* test. Only Student *t* test *P* values $< .05$ were considered significant. Unless stated otherwise, SDs are presented instead of SEM. Bonferroni test with an α-error value of 5% was applied to all panels with multiple comparisons.

## Results

### HIV-1 activates Cdc42 and induces membrane extensions in DCs

We first sought to determine the relative proportion of actin-containing structures at the surface of DCs with or without HIV-1 treatment. We refer to these as "membrane extensions" as the 3D electron microscopic studies presented in later figures provide more definitive insights into the nature of these membranous features. Incubation of HIV-1 for 1 hour with immature DCs leads to a measurable increase of the number of visible membrane extensions at the cell surface as determined by confocal microscopy (1.88-fold ± 0.19 increase; Figure 1A) and transmission electron microscopy (1.76-fold ± 0.34 increase; Figure 1B). Notably, this increase was found at the entire cell border of DCs, without obvious enrichment at infectious synapses with adjacent DCs or other sites of HIV-1 concentration. In addition, we also observed a relative increase in cortical actin density after contact with HIV-1. A similar increase in the number of membrane extensions on DC surface was observed with either a CXCR4-tropic (X4 HIV-1) or a CCR5-tropic HIV-1 (R5 HIV-1) (Figure 1A). No change in the number of membrane extensions was observed with envelope-deleted HIV-1 (HIV-1Δ*env*), suggesting that this process was dependent on HIV-$1^{env}$, independent of its tropism (Figure 1A). Incubation of immature DCs with HIV-$1^{env}$ (trimeric gp120IIIb; 2 μg/mL) or a DC-SIGN agonist antibody (H-200) also resulted in an increase in membrane extensions at the surface of DC (2.01-fold ± 0.2 and 1.65-fold ± 0.16 increase, respectively), suggesting a role for engagement of the DC-SIGN receptor by the viral envelope in this process.

To test whether Cdc42 may have a role in formation of membrane extensions, we pretreated DCs coincubated with HIV-1 for 30 minutes with the specific Cdc42 inhibitor secramine A and observed that it efficiently blocked induction of additional membrane extensions (Figure 1A). We then analyzed whether HIV-1 was able to induce Cdc42 activation in DCs. Incubation of DCs for 10 minutes with HIV-1, HIV-$1^{env}$ (trimeric gp120IIIb), a DC-SIGN agonist antibody (H-200), or tumor necrosis factor-α triggered Cdc42 activation as determined by a pull-down affinity assay detecting specifically activated Cdc42 bound to its partner Pak1 (Figure 1C). In contrast, envelope-deleted HIV-1 (HIV-1Δ*env*) was unable to induce Cdc42 activation. Cdc42 activation was also inhibited by the addition of the Cdc42 inhibitor secramine A (data not shown)

We next investigated potential signaling events that could link DC-SIGN engagement and Cdc42 activation. Pak1[27] and Wasp[28] have already been previously involved in membrane extensions formation, and Src kinases have been linked to DC-SIGN signaling in DCs[29] and Cdc42 activation in other cell types.[27] To analyze the relative activation of Src, Pak1, and WASP, we examined the proportion of phosphorylated proteins relative to their total cellular content. This allowed us to quantify their specific activation. We established that Src kinases Pak1 and Wasp were activated on incubation of DCs with wild type HIV-1, HIV-$1^{env}$ (trimeric gp120IIIb), a DC-SIGN agonist (antibody H-200), but not with HIV-1Δ*env* (Figure 1D). Interestingly, Cdc42 inhibition with secramine A or inhibition of Src kinases with PP2 indicated that Src activation on DC-SIGN engagement occurs upstream of Cdc42, Pak1, and Wasp activation (Figure 1D). These data suggest that Src kinases potentially provide a link between DC-SIGN engagement by HIV-1 envelope on DC surface and subsequent Cdc42, Pak1, and Wasp activation, thereby leading to an increase in membrane extensions at the DC surface.

### Cdc42 is required for efficient HIV-1 transfer of infection to T lymphocytes but not for DC-T lymphocyte infectious synapse formation

To dissect the role of key regulators of actin cytoskeleton in the transfer of HIV-1 infection from DCs to $CD4^+$ T cells, we performed a systematic knock-down of the Rho-GTPases Rac1 and Cdc42, the mammalian diaphanous-related formin Dia1, the actin

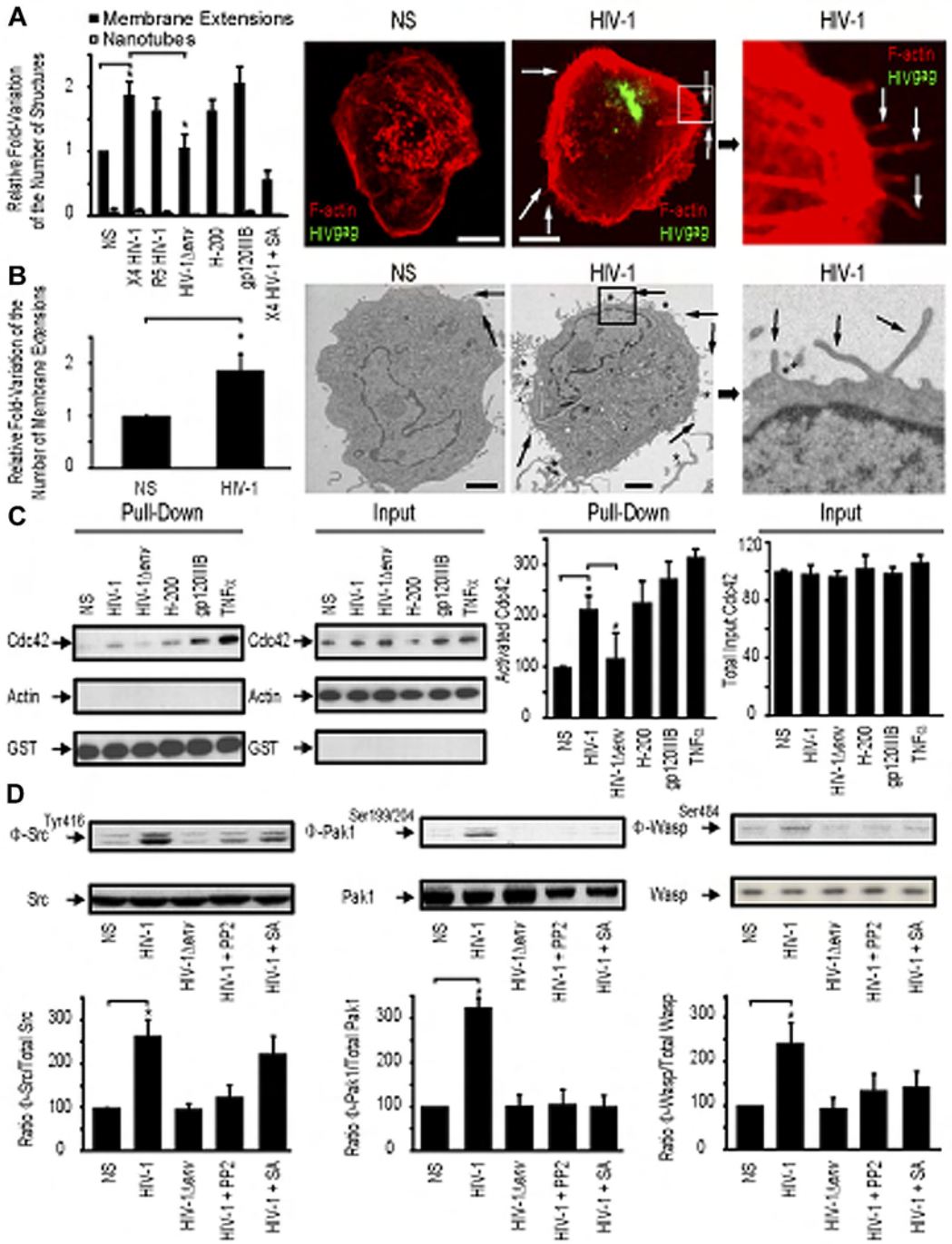


**Figure 1. HIV-1 induces membrane extensions and Cdc42 activation in DCs.** (A) Quantification by confocal microscopy of the number of membrane extensions or nanotubes in DCs either nonstimulated (NS) or stimulated with X4 HIV-1, R5 HIV-1, HIV-1Δ*env*, gp120IIIb, H-200, and X4 HIV-1 plus secramine A. Data are mean ± SD of 3 independent counts (left panel). Representative confocal images of DCs (right panel). Bar represents 5 μm. (B) Transmission electron microscopy images of HIV-1–treated DCs. Quantitation of the normalized number of membrane extensions on DCs after HIV-1 treatment. Data are mean ± SD of 2 independent counts (left panel) and corresponding representative images (right panel). Arrows indicate membrane extensions. *HIV-1 viral particles. Bar represents 2 μm. (C) Pull-down assay for activated Cdc42 in DC. Cdc42 expression by Western blot band quantitation. Data are mean ± SD of 3 independent pull-down experiments. (D) Western blot analysis for Phospho-Src (Φ-Src)/Src (left panel), Phospho-Pak1 (Φ-Pak1)/Pak1 (middle panel), and Phospho-Wasp (Φ-Wasp)/Wasp (right panel) detection in DCs. One representative Western blot per condition is represented. *$P < .05$ (Student *t* test).

nucleation complex Arp2/3, the guanidine-exchange factor Larg, and the ERM complex protein moesin. Two rounds of transfection of immature DCs with a mix of 3 different siRNA targeting these cellular proteins lead to an efficient down-regulation of 75% to 95% depending on the protein tested (supplemental Figure 1A-B, available on the *Blood* Web site; see the Supplemental Materials link at the top of the online article). RNA interference of immature DCs did not result in significant toxicity (supplemental Figure 1C) or phenotypic maturation of immature DCs, as determined by surface levels of CD83 or HLA-DR (supplemental Figure 1D). We first determined the impact of the silencing of each protein on the formation of infectious synapses. Infectious synapses were determined as conjugates (ie, close cell-to-cell contacts) of DCs and T lymphocytes in which > 50% of HIV-1 was concentrated on the

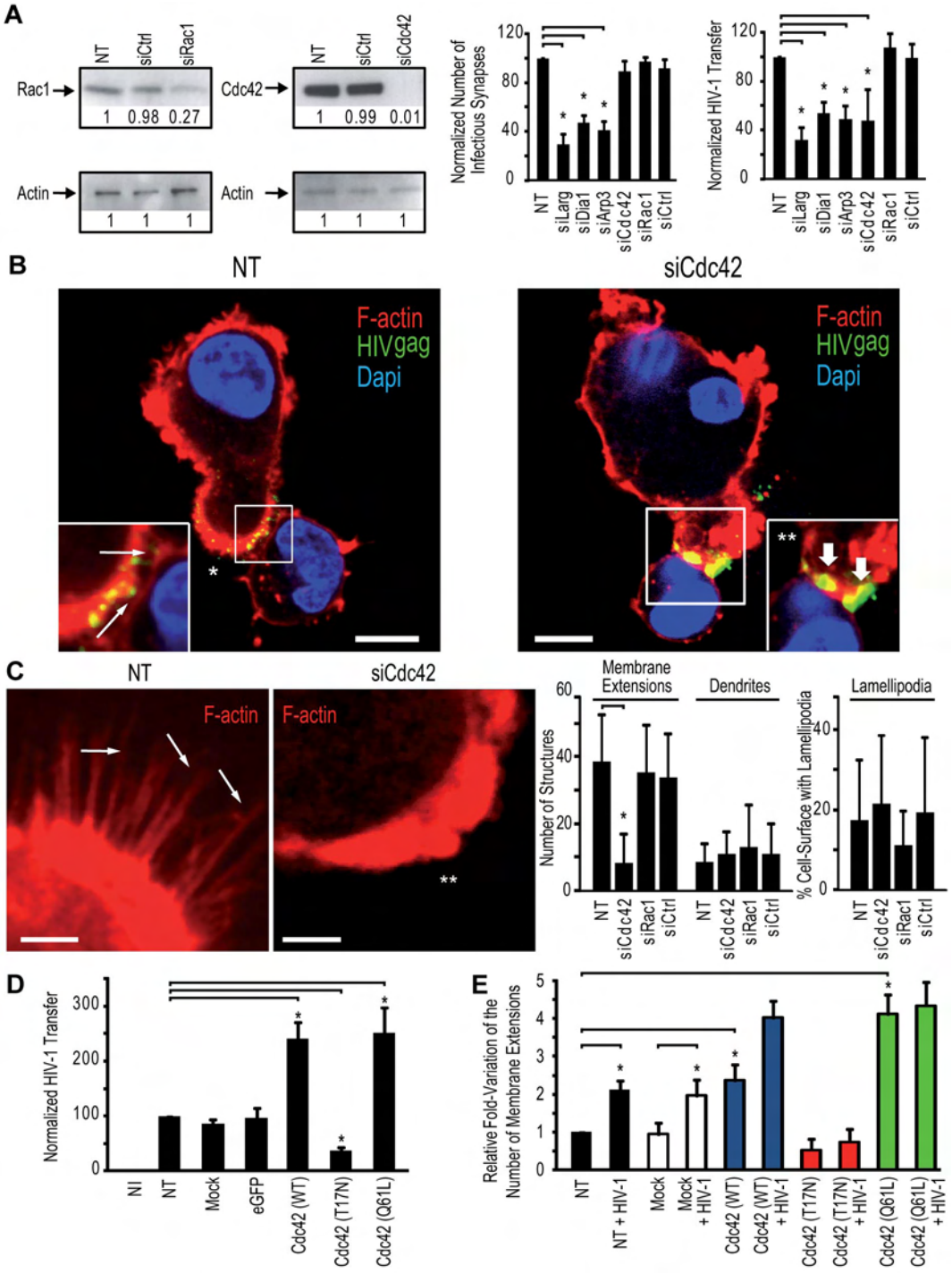


**Figure 2. Cdc42 is required for HIV-1 transfer across DC-CD4$^+$ T cell infectious synapses.** (A) Impact of silencing in DCs of cytoskeletal rearrangement proteins. (Left panel) Western blots for Cdc42 and Rac1 protein expression. (Middle panel). DC-CD4$^+$ T cell infectious synapses counts. (Right panel). HIV-1 infection transfer to Jurkat CD4$^+$ T cells. Data are mean ± SD of 5 independent experiments. (B) Confocal microscope images of DC-Jurkat CD4$^+$ T cell infectious synapses. White thin arrows indicate viral particles on membrane extensions. *"Hairy" appearance of the DC surface. Thick white arrows indicate the presence of viral aggregates at the infectious synapse. **Loss of membrane extensions at the surface of the Cdc42-depleted DCs. Bar represents 5 μm. (C) Quantitation of the number of thin membrane extensions, dendrites, and lamellipodia in DCs after Cdc42 and Rac1 silencing. White arrows point to membrane extensions; and double-white asterisks, the DC-surface devoid of membrane extensions. The plot at right shows quantitation of membrane extensions, dendrites, and cell surface covered with lamellipodia (right panel). Data are mean ± SD of 4 independent experiments. (D) Impact of Cdc42 mutant nucleofection in DCs on HIV-1 transfer to resting autologous CD4$^+$ T lymphocytes. Data are mean ± SD of 2 independent experiments. (E) Quantitation of the number of membrane extensions in DCs after Cdc42 mutant nucleofection. Data are mean ± SD of 3 independent experiments. *$P < .05$ (Student $t$ test). Bonferroni test with an $\alpha$-error value of 5% has been applied to all panels with multiple comparisons.

site of contact between the DCs and the T lymphocyte. Strikingly, silencing of Cdc42 exhibited a clearly different phenotype than Larg, Dia1, or Arp2/3 inhibition. Cdc42 knockdown in DCs had no impact on the number of DC-T cell infectious synapses (Figure 2A) but showed a clear decrease of transfer of HIV-1 infection to target Jurkat CD4$^+$ T lymphocytes a single infection round assay (Figure 2A). In contrast, Rac1 silencing in DCs neither impaired DC-T cell infectious synapses formation nor abrogated the transfer of HIV-1

infection to Jurkat CD4$^+$ T cells (Figure 2A; supplemental Figure 1E). Cdc42 and Rac1 knockdown in DC did not impair cell viability (supplemental Figure 1C) or HIV-1 capture (supplemental Figure 2). Imaging of the DC-T cell infectious synapse, 30 minutes after incubation of DCs with T cells, showed accumulation of HIV-1 particles at the zone of contact in the presence or absence of Cdc42, indicating that the mere concentration of virus at the DC-T cell infectious synapse was not sufficient to allow a complete transfer of HIV-1 infection to T cells and that this process of concentration appears to be independent of Cdc42 (Figure 2B). Taken together, these data demonstrate that HIV-1 transfer across DC-T cell infectious synapse requires Cdc42 but not Rac1. In contrast, Larg, Dia1, and Arp2/3 were required for infectious synapse formation (Figure 2A; supplemental Figure 1E). Silencing of these proteins in immature DCs did not reduce the number of DC-T cell conjugates (supplemental Figure 1F; with the exception of Arp2/3 complex), suggesting that loss of HIV-1 infection transfer was not the result of loss of contact between DCs and CD4$^+$ T lymphocytes. Similarly, reduction in HIV-1 transfer could not be explained by increase in mortality or decreased DC-associated HIV-1 content (supplemental Figure 2). Similar results as for Larg and Dia1 silencing were obtained on Rho inhibition in DCs with C3 transferase (data not shown). HIV-1 transfer across infectious synapse was also dependent on intact actin. The use of actin-disrupting drugs (supplemental Figure 3) inhibited both formation of DC-T cell infectious synapses and transfer of HIV-1 infection, in agreement with previous observations,[30] and Cdc42 silencing in DC resulted in a strong decrease in the number of visible membrane extensions (Figure 2C).

To extend our analysis on the role of Cdc42 and membrane extensions in HIV-1 transfer to CD4$^+$ T lymphocytes and to rule out off-target effects of RNA interference strategies, we transfected immature DCs with a wild-type (WT) Cdc42, a dominant-negative Cdc42 (T17N), and a constitutively active Cdc42 variant (Q61L). Transfection efficiencies before eGFP-positive cells sorting were $\sim$ 10% to 15% (supplemental Figure 4A). Sorting of eGFP-positive DCs increased the percentage of transfected cells to $\sim$ 90% to 95% (supplemental Figure 4B), without significant modification of cell-surface DC-SIGN expression (supplemental Figure 4B) or DC viability (supplemental Figure 4C). The morphology of DCs transfected with dominant negative Cdc42 (T17N) was altered, as we observed more round-shaped cells compared with other conditions. However, we did not observe a difference in numbers of conjugates formed between immature DCs and primary CD4$^+$ T cells, even after transfection with dominant negative Cdc42 (T17N), in agreement with our results obtained after Cdc42 silencing in DCs by RNAi (supplemental Figure 1). Interestingly, we observed a noticeable increase in HIV-1 transfer from immature DCs to primary CD4$^+$ in a single round infection assay when DCs were transfected with either a Cdc42 (WT) or constitutively activated Cdc42 (Q61L; 147.4% $\pm$ 26.4% increase; Figure 2D). In contrast, transfection of a dominant negative Cdc42 (T17N) inhibited transfer of HIV-1 infection from DCs to T cells (63.6% $\pm$ 5.9% decrease; Figure 2D). These results directly correlated with corresponding changes in the number of membrane extensions on DC surface, increasing with constitutively active Cdc42 (Q61L) or decreasing with dominant negative Cdc42 (T17N; Figure 2E; supplemental Figure 4D). Whereas transfection of immature DCs with WT Cdc42 resulted in a 2-fold increase in the number of membrane extensions, addition of HIV-1 led to a more than 4-fold increase, correlating with a strong activation of Cdc42 by the viral envelope after engagement of DC-SIGN. Treatment of DCs with the Cdc42 inhibitor secramine A or the Src kinases inhibitor PP2 also strongly reduced transfer of HIV-1 infection to primary CD4$^+$ T lymphocytes (81.4% $\pm$ 5.1% decrease and 83.5% $\pm$ 3.8% decrease, respectively; supplemental Figure 5).

### HIV-1 is present on membrane extensions at the DC- T lymphocyte infectious synapse

Next, we analyzed the ultrastructural features of contacts formed between T cells and immature DCs using electron microscopy and electron tomography. In the absence of virus, projection electron microscopic images showed that regions of contact between T cells and DCs were relatively smooth or had short membrane extensions from the DCs that were not localized just to regions of contact with the T cells (Figure 3A). In the presence of HIV-1, extensive membrane extensions were observed to originate from the DCs (Figure 3B) and were present in every zone of contact between T cells and DCs (n = 30). However, there was no obvious increase of these extensions at the site of the infectious synapse; rather, a global increase at the whole cell surface was observed. HIV-1 was present in abundance in the contact zones. To better establish the 3D localization of HIV-1 in the contact region, we carried out electron tomography. Tomographic slices show definitively that HIV-1 is located on the surfaces of these membrane extensions all along their length, both when the membrane extensions are far from the CD4$^+$ T cell (Figure 3D; supplemental Video 1) and when they are in close contact (Figure 3E-F; supplemental Video 2). These findings strongly suggest that the viruses might "surf" along the surfaces of the membrane extensions of the DCs, which are increased as a result of exposure to HIV-1. Treatment of DCs with the Cdc42 inhibitor secramine A largely abrogated these extensions (Figure 3C). HIV-1 localization on the membrane extensions was further supported with staining of the Ena/Vasp complex, which is present predominantly at tips of membrane extensions[31] (Figure 3G). To show actual transfer of HIV-1 to T lymphocytes, we used a viral fusion assay. Viral fusion events were measured by color separation of viral particles incorporating an S15-mCherry–tagged *env* and eGFP-tagged *vpr* as previously described.[22,32] HIV-1 harboring a mutation in gp41 (F522Y-HIV-1) abrogating fusogenic properties of the viral envelope did not show color separation in our assay (supplemental Figure 6). Transfection of DCs with Cdc42 (WT) and Cdc42 (Q61L) increased HIV-1 fusion in target CD4$^+$ lymphocytes (1.94 fold $\pm$ 0.37, respectively; 2.05-fold $\pm$ 0.18% increase; Figure 3H). Control experiments were performed using DCs transfected with dominant negative Cdc42 (T17N) and resulted in decreased HIV-1 fusion with CD4$^+$ T lymphocytes (61.7% $\pm$ 4.9% decrease; Figure 3H).

To obtain a better understanding of the structure of these membrane extensions, we analyzed the distribution of HIV-1 at the level of DC-T cell infectious synapses using ion-abrasion (IA) SEM[33] (Figure 4A-D). In contrast to electron tomography, IA-SEM allows imaging the entire depth of the synapse with the iterative use of a focused ion beam to remove material from the surface of the specimen and a scanning electron beam to image the newly exposed surface. Two important results emerge from the IA-SEM studies. First, the extensions observed in the tomographic slices (Figure 3D-E) and in the individual SEM images (Figure 4A-D) that have the appearance of filopodia are clearly seen to be sections through thin-walled membrane extensions originating from the DCs (Figure 4E-H). A cross-sectional image of the entire cell-cell contact region and the corresponding 3D rendering of the entire sheet-like extension are presented in Figure 4I and J, respectively.

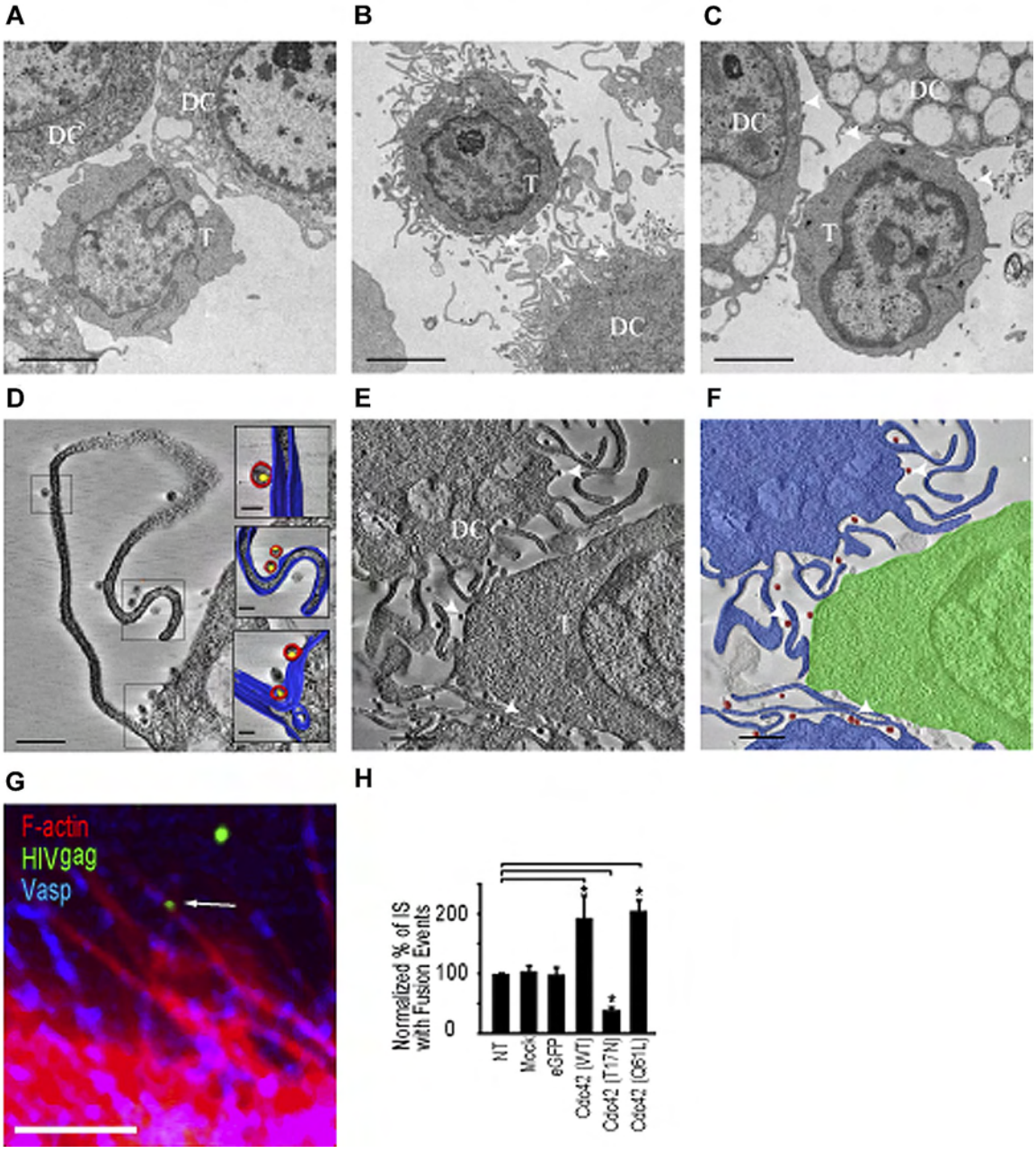


**Figure 3. HIV-1 is localized on membrane extensions at the DC-CD4$^+$ T cell infectious synapse.** Transmission electron microscopy of contacts between immature DC and T cells. (A-C) Projection electron microscopy images of a 100-nm-thick section from fixed, plastic-embedded cocultures of T cells and immature DCs either in the absence of added HIV-1 (A), after exposure to HIV-1 for 1 hour (B), and after treatment with the cdc42 inhibitor secramine A, followed by exposure to HIV-1 (C). (D-E) A 5-nm tomographic slice from a 3D image of a 175-nm-thick section prepared from fixed, plastic-embedded cocultures of T cells and DCs exposed to HIV-1 (as in B) showing viruses riding on the membrane extensions from the DCs. (F) Schematic rendering of tomographic slice in panel E highlighting contact between T cells (green) and immature DCs (blue) in the presence of HIV (red). Scale bars, original magnifications: (A-C) 2 μm; (D-E) 1 μm. (G) Representative image of membrane extensions on DCs with HIV-1 near extension tips. Bar represents 1 μm. (H) Quantification of fused HIV-1 viral particles in target CD4$^+$ T lymphocytes after nucleofection of Cdc42 mutants in DCs. All values are normalized to a 100% value assigned to the nontreated condition. Arrows indicate HIV-1 viral particles on membrane extensions on DCs. Data are mean ±SD of 3 independent experiments. *$P < .05$ (Student $t$ test). Bonferroni test with an $\alpha$-error value of 5% has been applied to all panels with multiple comparisons.

These results therefore show that these membrane extensions from the DC cell surface are best described as thin membranous sheets emanating from the DC membrane and are therefore similar in this respect to the findings recently reported from IA-SEM analysis of infectious synapses formed between CD4$^+$ T cells and mature DCs.[19] However, in contrast to the findings with the synapses formed by mature DCs, the membrane extensions in the synapses formed by immature DCs do not wrap around the T cells (Figure 4K-L). Thus, although the membrane extensions from both mature and immature DCs are sheet-like in nature, the major difference in the corresponding synapses is that there is no visible encasement of the T cells by these extensions in the case of the infectious synapses formed by the immature DCs.

Next, to evaluate whether we could observe transfer of infectious virions at the immature DC-T cell interface, we measured viral fusion events in the presence or absence or Cdc42. We observed a significant reduction of HIV-1 fusion in target Jurkat CD4$^+$ T lymphocytes (47.8% ± 6.8% decrease; supplemental

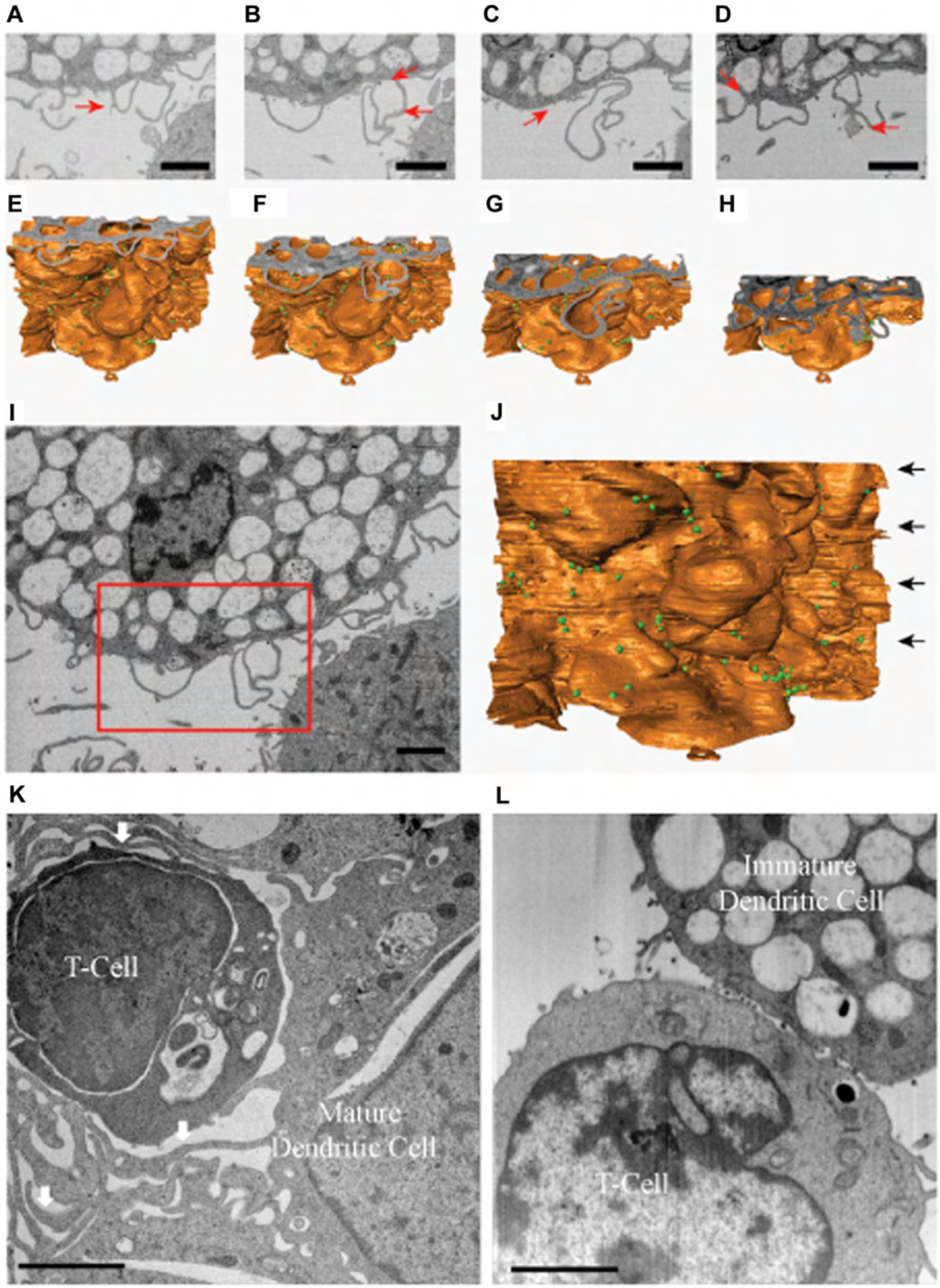


**Figure 4. Immature DCs do not form wrapping sheets around T lymphocytes in the context of the infectious synapse.** IA-SEM analysis of immature and mature DC-T cell infectious synapses. (A-D) 2D images of immature DC-T cell infectious synapses from the IA-SEM image stack corresponding to slices at progressively lower locations in the image stack. Red arrows point to some of the HIV-1 particles visible in the image. (E-H) Surface representations of the image stack with top surfaces corresponding to the images shown in panels A to D, respectively. (I-J) Top slice and front surface view of IA-SEM image stack showing the entire imaged area; the boxed region corresponds to the region highlighted in panels A to D. The green spheres represent the location of HIV-1. (K-L) Comparison of the infectious synapse between mature DCs (K) pulsed with HIV-1 and $CD4^+$ T cells and of immature DCs (I) pulsed with HIV-1 and $CD4^+$ T cells. (K) Arrows indicate the location of the sheet-like protrusions from the mature DCs that surround the T cells. Bar represents 2 μm.

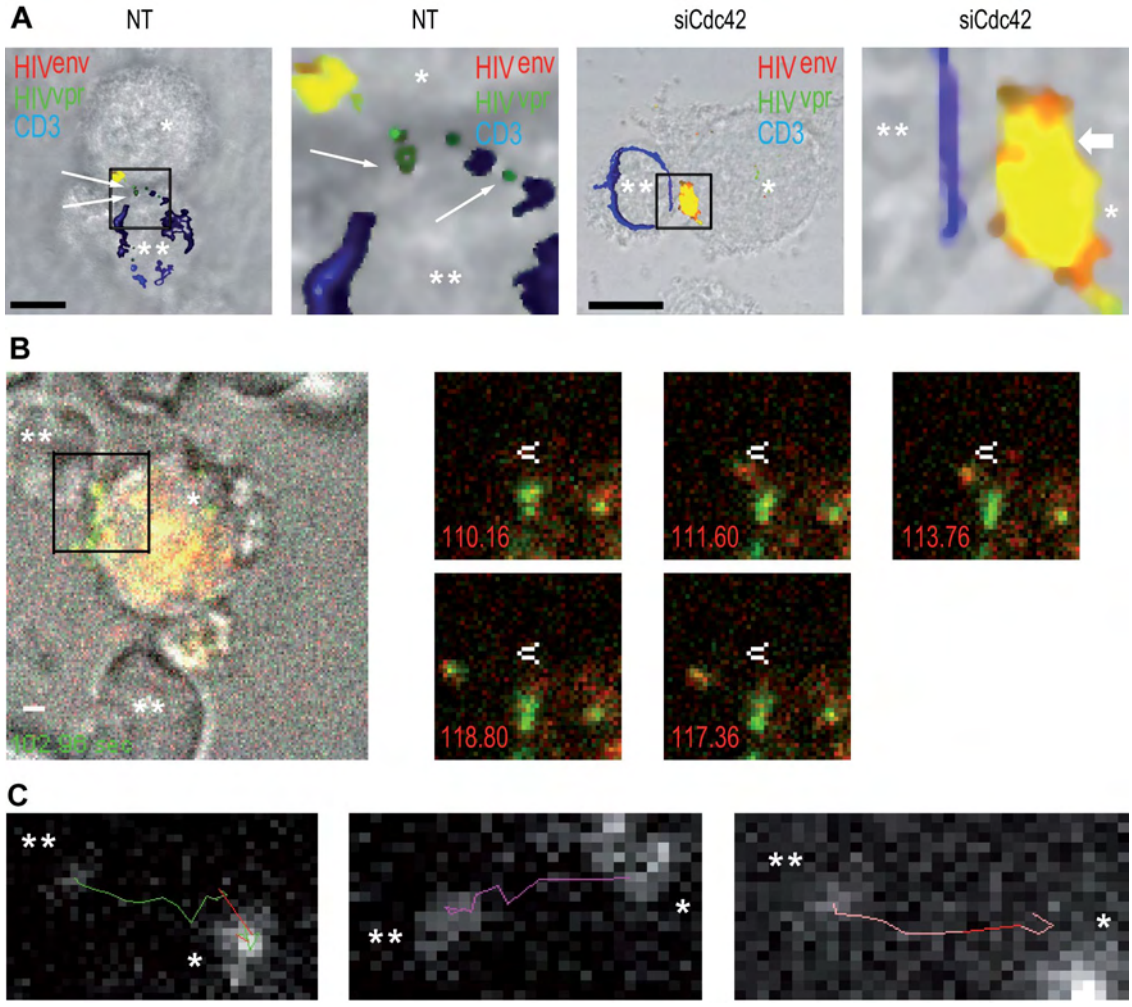


**Figure 5. Cdc42 silencing in DCs prevents HIV-1 fusion in target T lymphocytes.** (A) Confocal microscope analysis of HIV-1 fusion in target CD4$^+$ T lymphocytes. Nontreated (left panels) and siCdc42 (right panels) conditions are represented. Fused viral particles (green only) are shown by arrows. Bar represents 5 μm. (B) Live imaging analysis of HIV-1 transfer across DC-CD4$^+$ T cell infectious synapses. (Left panel) Infectious synapse analyzed in supplemental Video 1. *DCs. **CD4$^+$ T cells. Bar represents 2 μm. Right panel demonstrates time points during HIV-1 transfer across DC-CD4$^+$ T cell infectious synapse shown in supplemental Video 1. White arrow indicates a static point along HIV-1 transfer trajectory. (C) Different examples of HIV-1 transfer trajectories across DC-CD4$^+$ T cell infectious synapses. *DCs. **CD4$^+$ T cells. *$P < .05$ (Student *t* test).

Figure 7) after Cdc42 silencing in DCs, as assessed by confocal microscopy (Figure 5A). This indicates that the block of HIV-1 transfer across DC-CD4$^+$ T cells infectious synapses after Cdc42 silencing in DC occurs at the infectious synapse before fusion with target CD4$^+$ T lymphocytes. To further characterize the events occurring at the DC-T cell infectious synapse, we performed live confocal imaging analysis of the infectious synapse. We found that, as expected, HIV-1 viral particles were transferred from DCs to CD4$^+$ T lymphocytes on thin membrane extensions (Figure 5B; supplemental Videos 3-5). Then, we analyzed HIV-1 trajectories during viral transfers and established that they occurred in a very rapid and linear manner (Figure 5C). Average speed of trajectories was 0.40 ± 0.23 μm/s. Live imaging analysis of the DC-T cell infectious synapse after Cdc42 silencing in DCs was then performed. No HIV-1 transfer across the infectious synapse was observed in Cdc42-depleted DCs. Furthermore, HIV-1 movements at the DC surface were clearly reduced in Cdc42-knockdown conditions (supplemental Video 6). Together, these results show that membrane extensions that we have now characterized using light and electron microscopy are essential for the rapid movement of HIV-1 at the DC cell surface and for HIV-1 transfer across infectious synapses.

### Cdc42 and membrane extensions are essential for HIV-1 transfer across the DC-T cell infectious or immunologic synapse

To obtain a quantitative estimate of the contribution of the membrane extensions to HIV-1 transfer from immature DCs to resting autologous CD4$^+$ T lymphocytes, we set up an assay that allowed us to independently modulate either the number of infectious synapses or these membrane extensions. To force infectious synapse formation, we used a high number of infected DCs with a low number of resting autologous CD4$^+$ T cells (ratio 5:1) and added a cocktail of 3 superantigens (sAg), known to stabilize DC-T cell contacts at the infectious synapse and promote T-cell activation.[34] Cdc42 silencing resulted in a net decrease of transfer of HIV-1 infection (62.6% ± 12.1% inhibition; Figure 6A-B). These results are consistent with the idea that Cdc42-dependent membrane extensions are required for HIV-1 transfer to resting autologous CD4$^+$ T lymphocytes, even under conditions where a high number of stable DC-T cell immunologic synapses are formed. In parallel, we carried out similar experiments where the ratio of DC to T cells was reversed, with the T cells in 5-fold excess, conditions that are closer to those found in mucosal tissues

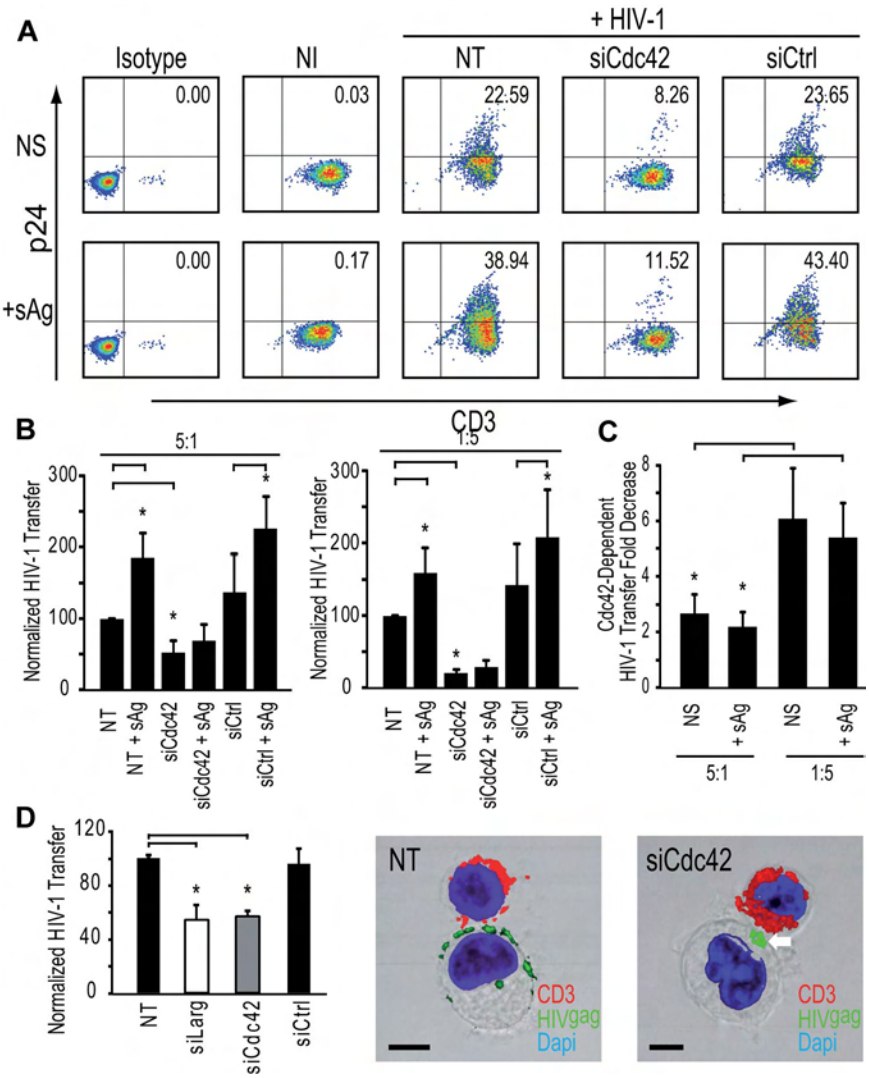


**Figure 6. Cdc42 is required for HIV-1 transfer from DCs to autologous resting CD4⁺ T cells in the presence of sAg.** (A) HIV-1 infection transfer to resting autologous CD4⁺ T lymphocytes after sAg stimulation. (B) HIV-1 infection transfer in DC-resting autologous CD4⁺ T lymphocyte cocultures. DC/T ratio 5:1 (left panel) and DC/T ratio 1:5 are shown (right panel). Data are mean ± SD of 3 independent experiments. (C) Fold decrease of HIV-1 transfer in DCs: resting autologous CD4⁺ T lymphocyte ratio conditions 5:1 (left panel) and 1:5 (right panel). Data are mean ± SD of 3 independent experiments. (D) Impact of Cdc42 or Larg silencing in MyDCs on HIV-1 transfer to Jurkat CD4⁺ T lymphocytes (left panel). Data are mean ± SD of 4 independent experiments. Two representative images of MyDCs-CD4⁺ T cell infectious synapses are shown (middle and right panels). Bar represents 5 μm. $*P < .05$ (Student *t* test). Bonferroni test with an α-error value of 5% has been applied to all panels with multiple comparisons.

or gut-associated lymphoid tissue, Interestingly, under these conditions, we found that most of HIV-1 infection transfer is dependent on Cdc42 both in the absence (84.0% ± 6.1% inhibition) and presence of sAg (81.4% ± 8.2% inhibition; Figure 6C). As a further verification of the physiologic relevance of these findings, we also extended our observations to primary blood derived-MyDCs. MyDCs are a major type of DCs in the bloodstream and are involved in HIV-1 transfer to CD4⁺ T lymphocytes.[35,37] Silencing of Cdc42 or Larg in immature MyDCs significantly reduced HIV-1 transfer (Figure 6D) with no impact on infectious synapse formation (Figure 6D) in agreement with results observed with immature monocyte-derived DCs. In conclusion, our results conclusively show that Cdc42-dependent membrane extensions are essential components of HIV-1 transmission at DC-CD4⁺ T-cell infectious synapses and account for most of the transfer of virus from DCs to CD4⁺ T cells.

## Discussion

Our data provide direct evidence that Cdc42 activation by HIV-1 facilitates its cell-to-cell spread at the infectious synapse formed between immature DCs and CD4⁺ T cells. We here show that DC-SIGN engagement by HIV-1 leads to Src kinase activation and that Cdc42, Pak1, and WASP activation occurs downstream of Src kinases, suggesting that a signaling cascade triggered by DC-SIGN engagement by the viral envelope leads ultimately to induction of the membrane extensions responsible for virus transmission. Our conclusion that HIV-1$^{env}$–dependent signaling cascade facilitates viral spread in this manner is supported by the finding that disruption of Cdc42 or Src kinase resulted in a strong inhibition of the process. Our results establish that the actin-rich cellular protrusions can confer up to 90% of transfer of HIV-1 infection HIV-1, even if immunologic synapses between DC and CD4⁺ T lymphocytes are induced via MHC-TCR engagement (Figure 4C). In summary, our observations establish that a 2-step process is initiated by HIV-1 for its delivery to the T cells. First, the virus becomes concentrated at the infectious synapse either by surfing on the cell surface[36,37] (supplemental Video 6) or after recycling from a tetraspanin-rich compartment.[24,32] The second step of transfer from the DC to the T-cell is mediated by Cdc42-dependent induction of membrane extensions that enable transfer from the DCs to the T cells. The crucial role of the extended membranous sheets for the transfer of HIV-1 infection across the DC-T cell infectious synapse is further exemplified in conditions where low numbers of DC are incubated with T cells. During the early events of HIV-1 infection, either in mucosal tissues or in the gut-associated lymphoid tissue, the number of CD4⁺ T cells far

exceeds DCs, suggesting that this mode of transfer of HIV-1 infection may be a critical component of HIV-1 transmission in vivo.[38] Despite the general similarities in the nature of the membrane extensions observed on immature and mature DCs, an interesting difference is that the envelopment of the T-cell seen in mature DCs is not observed with the immature DCs. This distinction between the more discreet "action-at-a-distance" mode for immature DC-T cell contact versus a more intimate "interdigitating" mode for mature DC-T cell contacts could be functionally relevant and consistent with DC physiology. However, it is clear that, in virologic synapses formed by both immature and mature DCs, virus delivery to the T cell is not passive, and there is a fundamental role for membrane extensions from the DCs in ensuring effective transfer of HIV-1 to T cells. In conclusion, our study identifies a novel mode of HIV-1 cell-to-cell transfer initiated by the virus itself, representing a potential paradigm for other viral diseases. In addition, mechanisms that disrupt formation of membrane extensions that enable virus transmission could represent a useful target for blocking virus propagation in the early events of HIV-1 infection.

## Acknowledgments

The authors thank Tom Hope, Olivier Schwartz, and Didier Trono for reagents; Jeremy Luban and Caterina Strambio De Castillia for discussions and technical assistance with live confocal microscopy studies; Gavin Murphy for assistance with segmentation of the IA-SEM data; Ralph Steinman and Didier Trono for critical reading of the manuscript; Mark Marsh for discussions; Florence Leuba and Pierre Carraux for technical help; and Romaine Stalder for assistance with the figures. Some of the samples used for electron microscopy were prepared with the help of the Pôle Facultaire de Microscopie Ultrastructurale at the Faculty of Medicine of the University of Geneva under the supervision of M. Foti. Flow cytometry analysis was performed with the support of the Flow Cytometry Core Facility of the Faculty of Medicine of the University of Geneva.

This work was supported by the Swiss National Science Foundation, the Human Science Frontier Program, and Cardiff University (V.P.), the National Cancer Institute (S.S.), an MD-PhD scholarship (D.S.N.), and the National Institute of General Medical Sciences (Pharmacology Research Associate Fellowship; R.F.).

## Authorship

Contribution: V.P., S.S., and D.S.N. designed the experiments and wrote the manuscript; and D.S.N., M.L., R.F., E.G., and F.P.B. performed experiments and analyzed data.

Conflict-of-interest disclosure: The authors declare no competing financial interests.

Correspondence: Vincent Piguet, Department of Dermatology and Wound Healing, Welsh Institute of Dermatology, 3rd Floor, Glamorgan House, Cardiff University and University Hospital of Wales, Heath Park, Cardiff, CF14 4XN, Wales, United Kingdom; e-mail: piguetv@cardiff.ac.uk.

## References

1. Piguet V, Steinman RM. The interaction of HIV with dendritic cells: outcomes and pathways. *Trends Immunol.* 2007;28(11):503-510.
2. Wu L, KewalRamani VN. Dendritic-cell interactions with HIV: infection and viral dissemination. *Nat Rev Immunol.* 2006;6(11):859-868.
3. McDonald D, Wu L, Bohks SM, KewalRamani VN, Unutmaz D, Hope TJ. Recruitment of HIV and its receptors to dendritic cell-T cell junctions. *Science.* 2003;300(5623):1295-1297.
4. Piguet V, Sattentau Q. Dangerous liaisons at the virological synapse. *J Clin Invest.* 2004;114(5):605-610.
5. Sattentau Q. Avoiding the void: cell-to-cell spread of human viruses. *Nat Rev Microbiol.* 2008;6(11):815-826.
6. Arrighi JF, Pion M, Garcia E, et al. DC-SIGN-mediated infectious synapse formation enhances X4 HIV-1 transmission from dendritic cells to T cells. *J Exp Med.* 2004;200(10):1279-1288.
7. Geijtenbeek TB, Kwon DS, Torensma R, et al. DC-SIGN, a dendritic cell-specific HIV-1-binding protein that enhances trans-infection of T cells. *Cell.* 2000;100(5):587-597.
8. Hodges A, Sharrocks K, Edelmann M, et al. Activation of the lectin DC-SIGN induces an immature dendritic cell phenotype triggering Rho-GTPase activity required for HIV-1 replication. *Nat Immunol.* 2007;8(6):569-577.
9. Gringhuis SI, den Dunnen J, Litjens M, van der Vlist M, Geijtenbeek TB. Carbohydrate-specific signaling through the DC-SIGN signalosome tailors immunity to Mycobacterium tuberculosis, HIV-1 and Helicobacter pylori. *Nat Immunol.* 2009;10(10):1081-1088.
10. Anand AR, Prasad A, Bradley RR, et al. HIV-1 gp120-induced migration of dendritic cells is regulated by a novel kinase cascade involving Pyk2, p38 MAP kinase and LSP1. *Blood.* 2009;114(17):3588-3600.
11. Caparros E, Munoz P, Sierra-Filardi E, et al. DC-SIGN ligation on dendritic cells results in ERK and PI3K activation and modulates cytokine production. *Blood.* 2006;107(10):3950-3958.
12. Gilbert C, Barat C, Cantin R, Tremblay MJ. Involvement of Src and Syk tyrosine kinases in HIV-1 transfer from dendritic cells to CD4+ T lymphocytes. *J Immunol.* 2007;178(5):2862-2871.
13. Heasman SJ, Ridley AJ. Mammalian Rho GTPases: new insights into their functions from in vivo studies. *Nat Rev Mol Cell Biol.* 2008;9(9):690-701.
14. Tran Van Nhieu G, Caron E, Hall A, Sansonetti PJ. IpaC induces actin polymerization and filopodia formation during Shigella entry into epithelial cells. *EMBO J.* 1999;18(12):3249-3262.
15. Alto NM, Shao F, Lazar CS, et al. Identification of a bacterial type III effector family with G protein mimicry functions. *Cell.* 2006;124(1):133-145.
16. Dixit R, Tiwari V, Shukla D. Herpes simplex virus type 1 induces filopodia in differentiated P19 neural cells to facilitate viral spread. *Neurosci Lett.* 2008;440(2):113-118.
17. Jouvenet N, Windsor M, Rietdorf J, et al. African swine fever virus induces filopodia-like projections at the plasma membrane. *Cell Microbiol.* 2006;8(11):1803-1811.
18. Rudnicka D, Feldmann J, Porrot F, et al. Simultaneous cell-to-cell transmission of human immunodeficiency virus to multiple targets through polysynapses. *J Virol.* 2009;83(12):6234-6246.
19. Felts RL, Narayan K, Estes JD, et al. 3D visualization of HIV transfer at the virological synapse between dendritic cells and T cells. *Proc Natl Acad Sci U S A.* 2010;107(30):13336-13341.
20. Blanchet FP, Moris A, Nikolic DS, et al. Human immunodeficiency virus-1 inhibition of immunoamphisomes in dendritic cells impairs early innate and adaptive immune responses. *Immunity.* 2010;32(5):654-669.
21. Bergeron L, Sullivan N, Sodroski J. Target cell-specific determinants of membrane fusion within the human immunodeficiency virus type 1 gp120 third variable region and gp41 amino terminus. *J Virol.* 1992;66(4):2389-2397.
22. Campbell EM, Perez O, Melar M, Hope TJ. Labeling HIV-1 virions with two fluorescent proteins allows identification of virions that have productively entered the target cell. *Virology.* 2007;360(2):286-293.
23. Xu B, Pelish H, Kirchhausen T, Hammond GB. Large scale synthesis of the Cdc42 inhibitor secramine A and its inhibition of cell spreading. *Org Biomol Chem.* 2006;4(22):4149-4157.
24. Garcia E, Nikolic DS, Piguet V. HIV-1 replication in dendritic cells occurs through a tetraspanin-containing compartment enriched in AP-3. *Traffic.* 2008;9(2):200-214.
25. Bennett AE, Narayan K, Shi D, et al. Ion-abrasion scanning electron microscopy reveals surface-connected tubular conduits in HIV-infected macrophages. *PLoS Pathog.* 2009;5(9):e1000591.
26. Kremer JR, Mastronarde DN, McIntoch JR. Computer visualization of three-dimensional image data using IMOD. *J Struct Biol.* 1996;116(1):71-76.
27. Faix J, Rottner K. The making of filopodia. *Curr Opin Cell Biol.* 2006;18(1):18-25.
28. Miki H, Sasaki T, Takai Y, Takenawa T. Induction of filopodium formation by a WASP-related actin-depolymerizing protein N-WASP. *Nature.* 1998;391(6662):93-96.
29. Gringhuis SI, den Dunnen J, Litjens M, van Het Hof B, van Kooyk Y, Geijtenbeek TB.

C-type lectin DC-SIGN modulates Toll-like receptor signaling via Raf-1 kinase-dependent acetylation of transcription factor NF-kappaB. *Immunity.* 2007;26(5):605-616.

30. Wang JH, Wells C, Wu L. Macropinocytosis and cytoskeleton contribute to dendritic cell-mediated HIV-1 transmission to CD4+ T cells. *Virology.* 2008;381(1):143-154.
31. Kwiatkowski AV, Gertler FB, Loureiro JJ. Function and regulation of Ena/VASP proteins. *Trends Cell Biol.* 2003;13(7):386-392.
32. Yu HJ, Reuter MA, McDonald D. HIV traffics through a specialized, surface-accessible intracellular compartment during trans-infection of T cells by mature dendritic cells. *PLoS Pathog.* 2008;4(8):e1000134.
33. Heymann JA, Shi D, Kim S, Bliss D, Milne JL, Subramaniam S. 3D imaging of mammalian cells with ion-abrasion scanning electron microscopy. *J Struct Biol.* 2009;166(1):1-7.
34. Bhardwaj N, Young JW, Nisanian AJ, Baggers J, Steinman RM. Small amounts of superantigen, when presented on dendritic cells, are sufficient to initiate T cell responses. *J Exp Med.* 1993; 178(2):633-642.
35. Lore K, Smed-Sorensen A, Vasudevan J, Mascola JR, Koup RA. Myeloid and plasmacytoid dendritic cells transfer HIV-1 preferentially to antigen-specific CD4+ T cells. *J Exp Med.* 2005; 201(12):2023-2033.
36. Sherer NM, Lehmann MJ, Jimenez-Soto LF, Horensavitz C, Pypaert M, Mothes W. Retroviruses can establish filopodial bridges for efficient cell-to-cell transmission. *Nat Cell Biol.* 2007;9(3): 310-315.
37. Cavrois M, Neidleman J, Kreisberg JF, Greene WC. In vitro derived dendritic cells trans-infect CD4 T cells primarily with surface-bound HIV-1 virions. *PLoS Pathog.* 2007;3(1):e4.
38. Haase AT. Perils at mucosal front lines for HIV and SIV and their hosts. *Nat Rev Immunol.* 2005; 5(10):783-792.

**Figure S1. Cytoskeleton organizer proteins are required for HIV-1 transfer across DC-CD4$^+$ T-cell infectious synapses**
(A) Western blot analysis of cytoskeleton organizer proteins expression in DC upon specific protein silencing. Values are normalized to NT conditions and actin protein content. (B) Quantification cytoskeleton organizer proteins expression in DC upon specific protein silencing. Values are normalized to NT conditions. (C) DC viability upon cytoskeleton organizer proteins silencing. Percentage of 7-AAD$^{low}$ cells is represented. (D) Maturation markers CD83 (left) and HLA-DR (right) expression levels in DC upon cytoskeleton organizer proteins silencing. (E) Confocal microscope analyses of DC-CD4$^+$ T-cell infectious synapses. Representative images are shown. HIV-1 p24$^{gag}$ is represented in green, F-actin in red and nuclei (Dapi) in blue. Bar = 5 μm. (F) Conjugates formed between DC and CD4$^+$ T cells were counted after processing for confocal microscopy. Values are normalized to NT condition. * indicates Student's Test *P* values < 0.05.

**Figure S2. DC-associated HIV-1 content upon cytoskeleton organizer proteins silencing**
(A,B) Western Blot analysis for HIV-1 p24$^{gag}$ and actin expression in DC. (A) Short exposure for HIV-1 p24$^{gag}$ expression. Lysates from non-infected (NI) DC are represented on the left and lysates from HIV-1–treated DC (+ HIV-1) on the right. (B) Longer exposure for HIV-1 p24$^{gag}$ expression (upper panel) and actin expression (lower panel).

**Figure S3. Actin filaments are required for DC–T-cell HIV-1 infectious synapses formation and transfer of HIV-1 infection to CD4$^+$ T lymphocytes**
(A) DC-CD4$^+$ T-cell infectious synapses counts. Data are mean +/− sd. of four independent experiments. (B) HIV-1 infection transfer to CD4$^+$ T cells (right panel). Data are mean +/− sd. of four independent experiments. (C) Representative confocal microscope image of a DC–T-cell HIV-1 infectious synapse. Bar = 5 μm. (D) Percentage of disrupted-like HIV-1–containing compartments as assessed by confocal microscopy. Data are mean +/− sd. of three independent experiments. (E) Relative percentage of DC–T-cell conjugates as assessed by confocal microscopy. Data are mean +/− sd. of three independent experiments. * indicates Student's Test *P* values < 0.05.

**Figure S4. Characterization of DC nucleofected with Cdc42 mutants**
(A) Pre-sort flow cytometry analysis of eGFP expression in nucleofected DC. (B) Post-sort (4h) flow cytometry analysis of eGFP and DC-SIGN expression in sorted nucelofected DC. (C) Post-sort (4h) cell viability analysis of sorted nucleofected DC. 7-AAD exclusion is represented as a marker of DC cell viability. (D) Representative confocal microscope images of nucleofected DC 6 hours after sorting of eGFP-positive DC. F-actin is represented in Red. Bar = 5 μm.

**Figure S5. Cdc42 or Src kinases inhibition prevents transfer of HIV-1 infection to CD4$^+$ T lymphocytes**
(A) HIV-1 infection transfer to CD4$^+$ T cells. All values are normalized to a 100% value assigned to the HIV-1 condition. Data are mean +/− sd. of three independent experiments. (B) Flow cytometry data corresponding to a representative experiment shown in **a.** AZT indicates treatment of DC-CD4$^+$ T lymphocytes co-cultures with the reverse transcriptase inhibitor zidovudine. PP2 is a specific Src kinases inhibitor. Secramine A (SA) is a specific Cdc42 inhibitor. * indicates Student's Test *P* values < 0.05.

**Figure S6. Generation of double-labeled HIV-1 virions for color-separation assay and visualization of HIV-1 fusion in target cells**
(A) Expression of p24gag, eGFP and S15-mCherry in 293T producing cells and in released virions (left panel). Infectivity of double-labeled HIV-1 virions (right panel). Data are mean +/− sd. of two independent experiments. (B) Visualization of viral fusion in P4-R5 HeLa cells at 0h (upper panel) and 3h (lower panel). Green dots, representing fused viral particles are shown (white arrows). Quantification of the number of particles (upper right panel) and of the total area (lower left panel) demonstrating co-localization between green and red. Data are mean +/− sd. of two independent experiments. * indicates Student's Test *P* values < 0.05.

**Figure S7. Impact of Cdc42 silencing in DC on HIV-1 fusion in target $CD4^+$ T lymphocytes**
Quantification of fused viral particles in target $CD4^+$ T cells and infectious synapses following Cdc42 silencing in DC is represented. Data are mean +/− sd. of three independent experiments. * indicates Student's Test *P* values < 0.05.

Figure S1

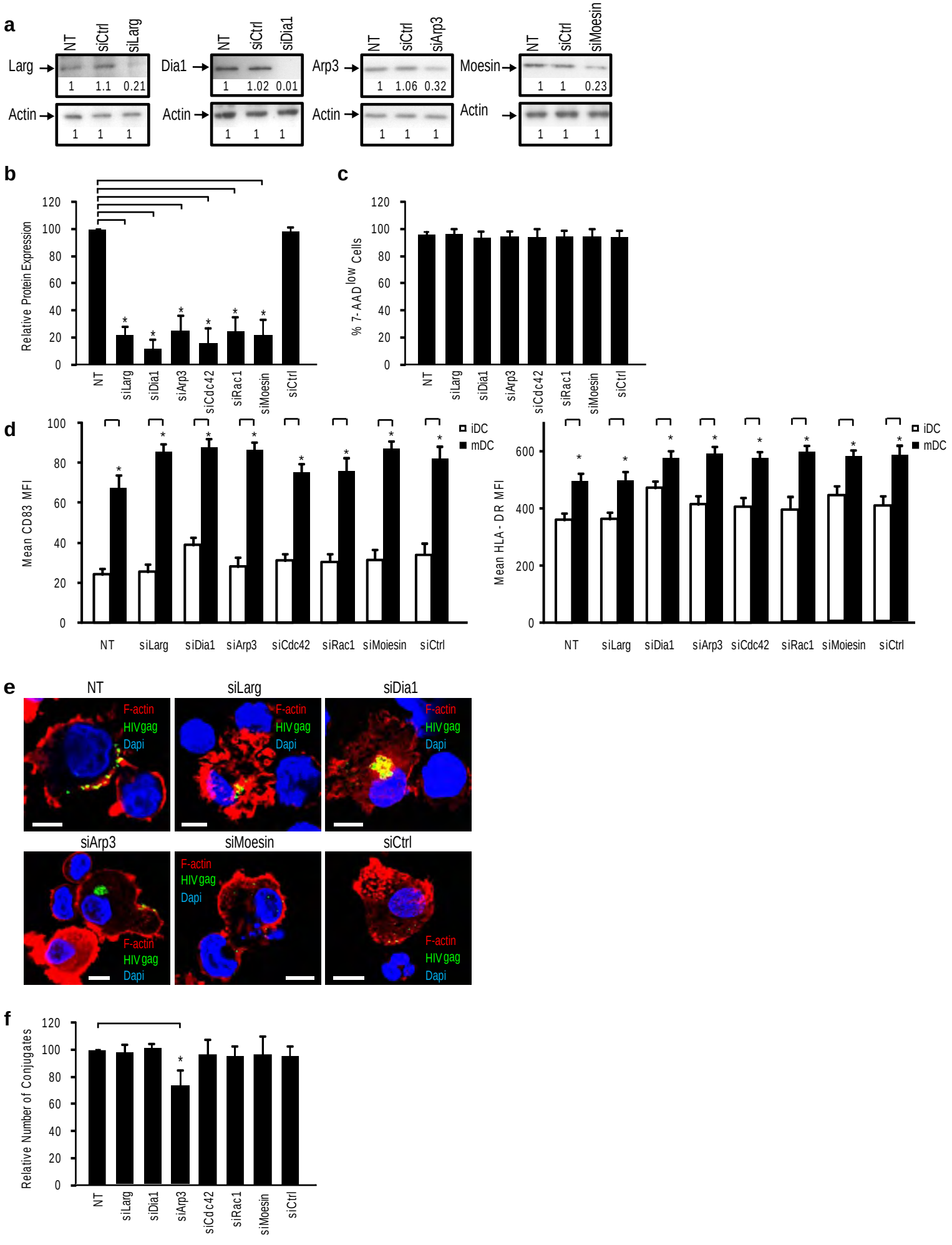
a
NT
siCtrl
siLarg
Larg
1 1.1 0.21
Actin
1 1 1
siDia1
Dia1
1 1.02 0.01
siArp3
Arp3
1 1.06 0.32
siMoesin
Moesin
1 1 0.23
b
Relative Protein Expression
NT
siLarg
siDia1
siArp3
siCdc42
siRac1
siMoesin
siCtrl
c
% 7-AAD low Cells
d
Mean CD83 MFI
Mean HLA - DR MFI
iDC
mDC
e
F-actin
HIV gag
Dapi
f
Relative Number of Conjugates

Figure S2

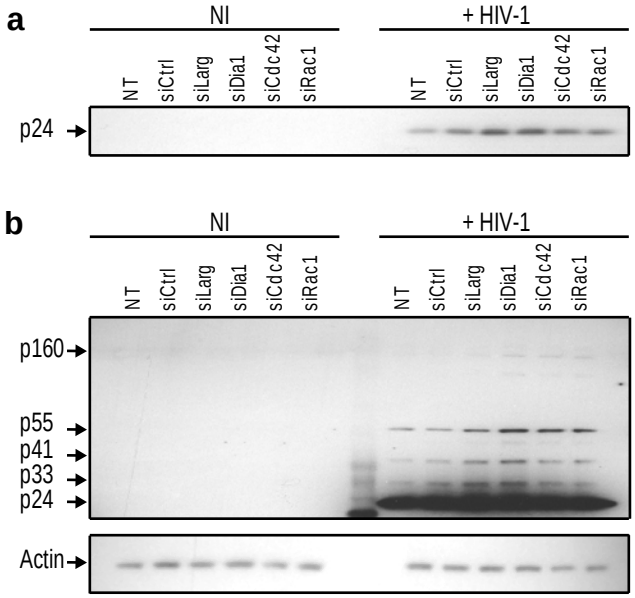
a
NI
+ HIV-1
NT
siCtrl
siLarg
siDia1
siCdc42
siRac1
p24
b
NI
+ HIV-1
NT
siCtrl
siLarg
siDia1
siCdc42
siRac1
p160
p55
p41
p33
p24
Actin

Figure S3

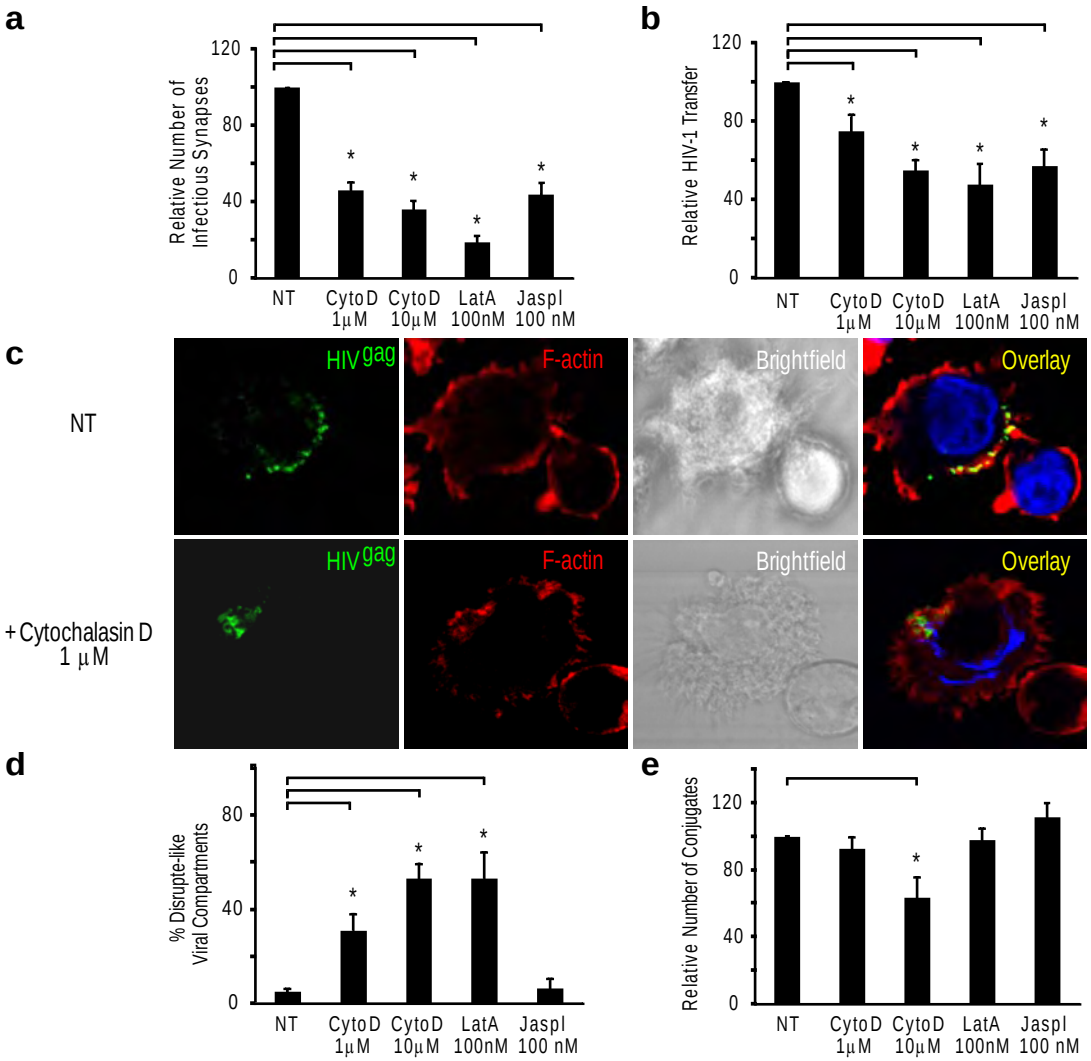
a
Relative Number of Infectious Synapses
120
80
40
0
NT
CytoD 1µM
CytoD 10µM
LatA 100nM
Jaspl 100 nM
b
Relative HIV-1 Transfer
c
NT
+ Cytochalasin D 1 µM
HIV gag
F-actin
Brightfield
Overlay
d
% Disrupte-like Viral Compartments
e
Relative Number of Conjugates

Figure S4

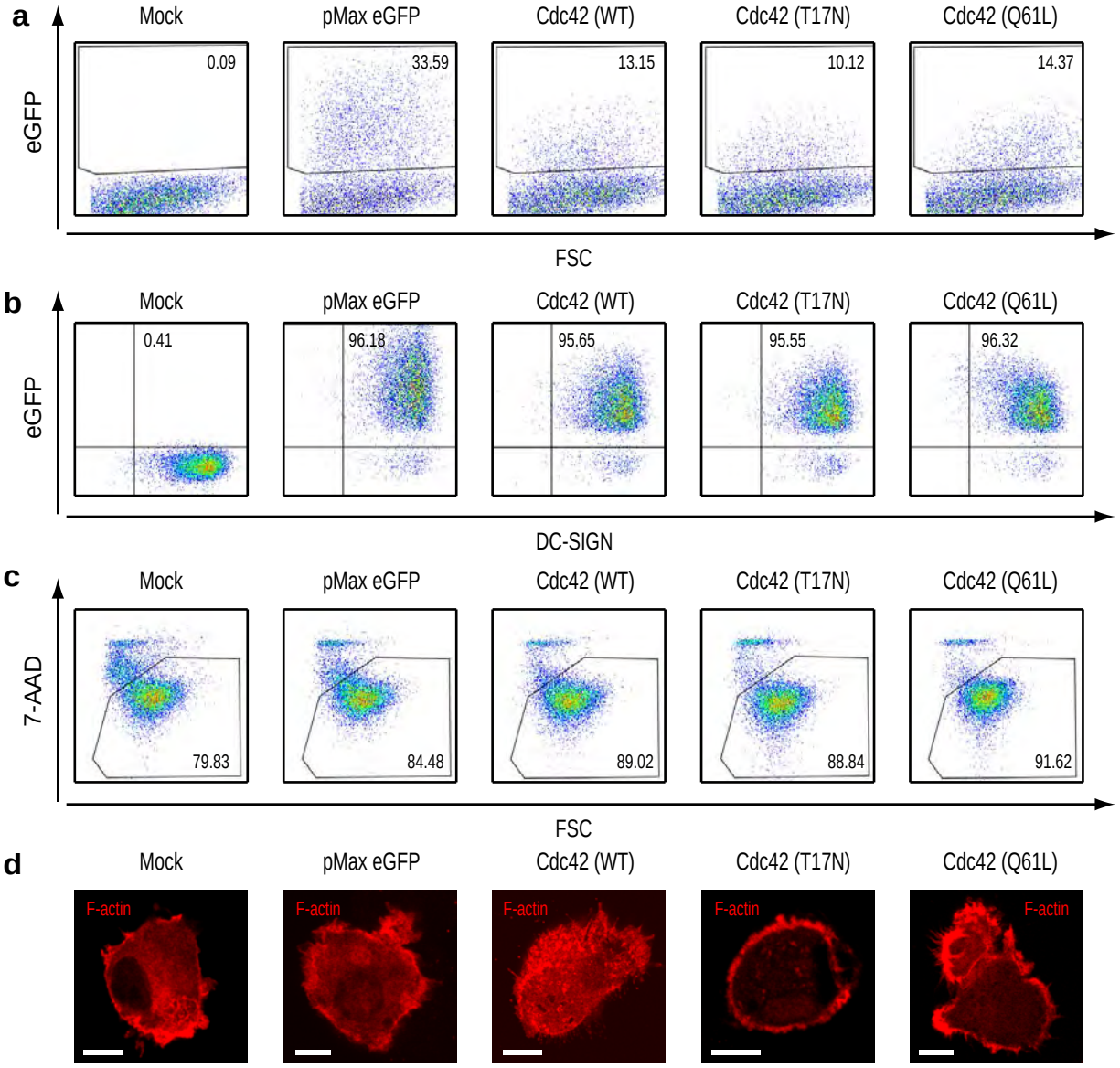
a
Mock
pMax eGFP
Cdc42 (WT)
Cdc42 (T17N)
Cdc42 (Q61L)
0.09
33.59
13.15
10.12
14.37
eGFP
FSC
b
Mock
pMax eGFP
Cdc42 (WT)
Cdc42 (T17N)
Cdc42 (Q61L)
0.41
96.18
95.65
95.55
96.32
eGFP
DC-SIGN
c
Mock
pMax eGFP
Cdc42 (WT)
Cdc42 (T17N)
Cdc42 (Q61L)
79.83
84.48
89.02
88.84
91.62
7-AAD
FSC
d
Mock
pMax eGFP
Cdc42 (WT)
Cdc42 (T17N)
Cdc42 (Q61L)
F-actin
F-actin
F-actin
F-actin
F-actin

Figure S5

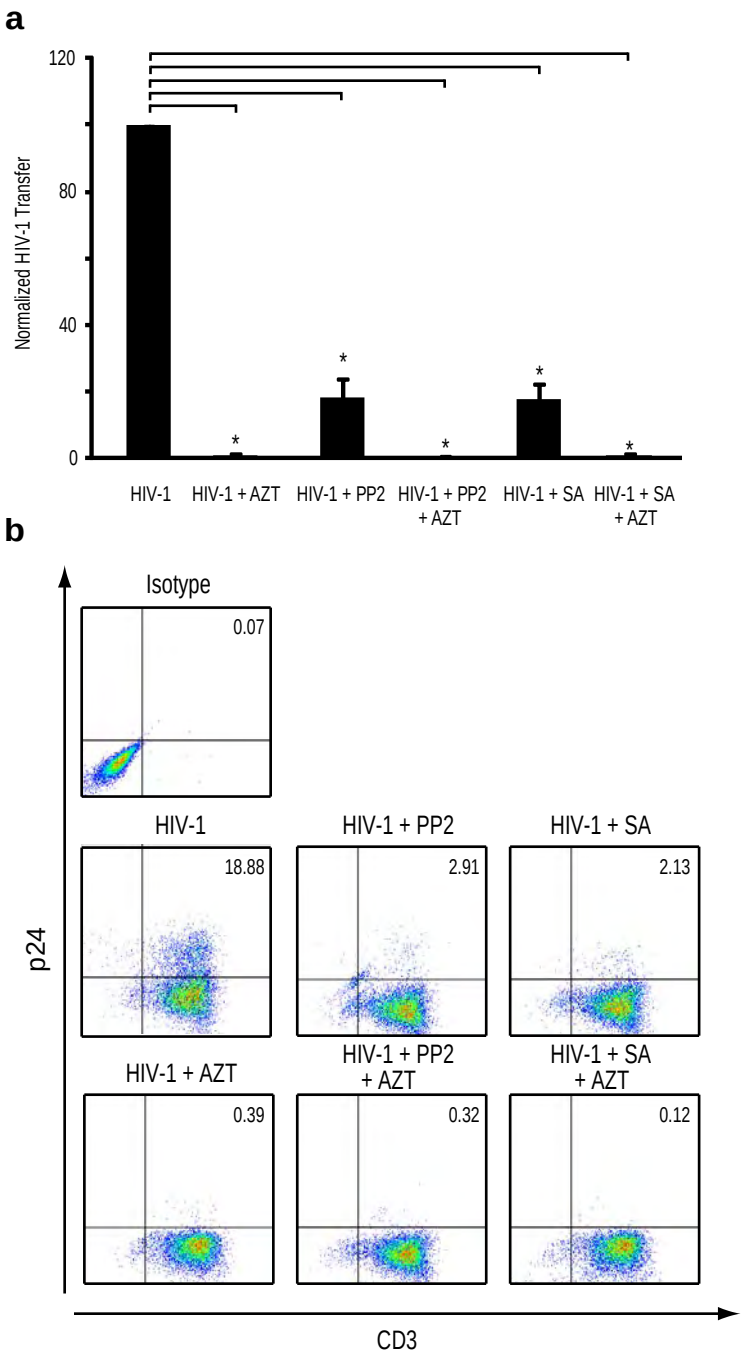
a
120
80
40
0
Normalized HIV-1 Transfer
HIV-1
HIV-1 + AZT
HIV-1 + PP2
HIV-1 + PP2 + AZT
HIV-1 + SA
HIV-1 + SA + AZT
b
Isotype
0.07
HIV-1
18.88
HIV-1 + PP2
2.91
HIV-1 + SA
2.13
HIV-1 + AZT
0.39
HIV-1 + PP2 + AZT
0.32
HIV-1 + SA + AZT
0.12
p24
CD3

Figure S6

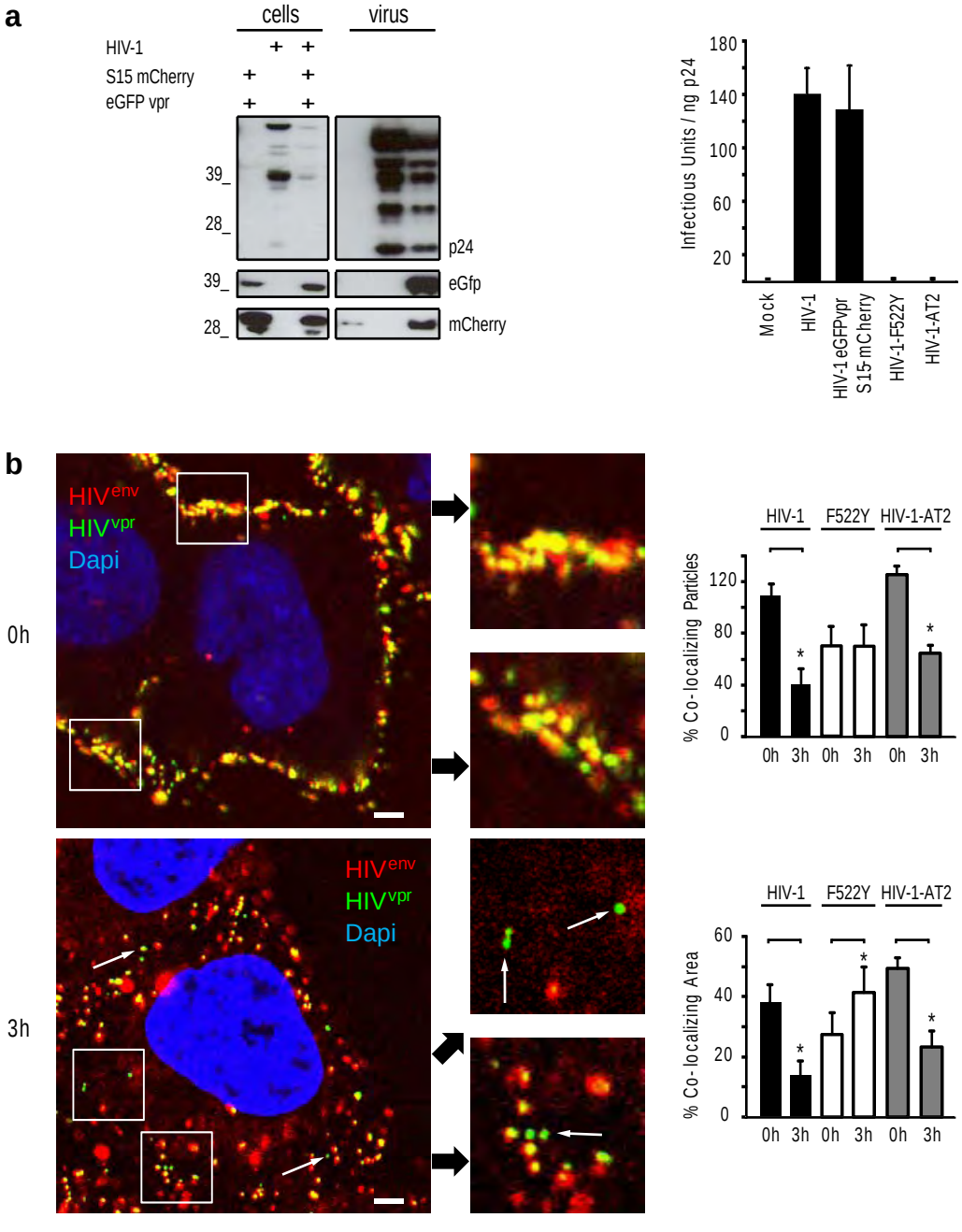
a
cells
virus
HIV-1
S15 mCherry
eGFP vpr
39_
28_
p24
39_
eGfp
28_
mCherry
Infectious Units / ng p24
180
140
100
60
20
Mock
HIV-1
HIV-1 eGFPvpr S15-mCherry
HIV-1-F522Y
HIV-1-AT2
b
0h
3h
HIV env
HIV vpr
Dapi
HIV-1
F522Y
HIV-1-AT2
% Co-localizing Particles
120
80
40
0
0h 3h 0h 3h 0h 3h
% Co-localizing Area
60
40
20
0

Figure S7

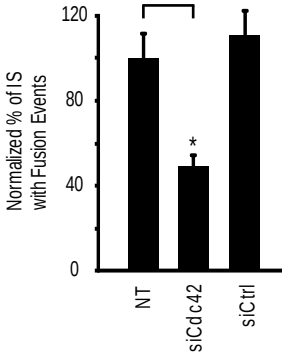
120
80
40
0
Normalized % of IS with Fusion Events
*
NT
siCdc42
siCtrl

*Viruses* **2011**, *3*, 1757-1776; doi:10.3390/v3091757

OPEN ACCESS

*viruses*

**ISSN 1999-4915**

www.mdpi.com/journal/viruses

*Review*

# How HIV-1 Takes Advantage of the Cytoskeleton during Replication and Cell-to-Cell Transmission

**Martin Lehmann [1,2], Damjan S. Nikolic [1,2] and Vincent Piguet [1,2,3,*]**

[1] Department of Microbiology and Molecular Medicine, University Hospital and Medical School of Geneva, Geneva 1211, Switzerland; E-Mails: martin.lehmann@unige.ch (M.L.); damjan.nikolic@hcuge.ch (D.S.N)

[2] Department of Dermatology and Venereology, University Hospital and Medical School of Geneva, Geneva 1211, Switzerland

[3] Department of Dermatology and Wound Healing, Cardiff University School of Medicine and University Hospital of Wales, Cardiff, Wales, CF144XN, UK

* Author to whom correspondence should be addressed; E-Mail: piguetv@cardiff.ac.uk; Tel.: +44-(0)-29-20-744721; Fax: +44-(0)-29-20-744312.

*Received: 8 July 2011; in revised form: 26 August 2011 / Accepted: 30 August 2011 / Published: 15 September 2011*

---

**Abstract:** Human immunodeficiency virus 1 (HIV-1) infects T cells, macrophages and dendritic cells and can manipulate their cytoskeleton structures at multiple steps during its replication cycle. Based on pharmacological and genetic targeting of cytoskeleton modulators, new imaging approaches and primary cell culture models, important roles for actin and microtubules during entry and cell-to-cell transfer have been established. Virological synapses and actin-containing membrane extensions can mediate HIV-1 transfer from dendritic cells or macrophage cells to T cells and between T cells. We will review the role of the cytoskeleton in HIV-1 entry, cellular trafficking and cell-to-cell transfer between primary cells.

**Keywords:** HIV-1; actin; microtubules; virological synapse; dendritic cells; cell-to-cell transfer

---

## 1. Introduction

The cytoskeleton supports mechanical stability of the cell, enables its movement, division and intracellular organelle transport by way of three types of filaments: intermediate filaments, actin and microtubules. Intermediate filaments form dynamic cellular networks that provide mechanical stability and position intracellular organelles [1]. Monomers of microtubules and actin assemble into polar filaments that can be used as tracks by plus and minus end motor proteins. Kinesins and dynein are microtubule motors that mediate long range outward and inward transport, respectively. On the other hand, short range transport at the cell periphery involves myosin motor proteins moving on actin filaments [2].

For viruses that enter the cytoplasm through fusion at the plasma membrane, the cytoskeleton can represent an additional mechanical barrier. Subsequent diffusion of subviral particles larger than 500 kDa is restricted in the cytoplasm, so host cytoskeleton-associated motor proteins can be used for active transport of the genome to the nucleus for replication [3]. Transport of Adenovirus and Herpes simplex virus genomes to the nucleus relies on active transport on microtubules [4]. To efficiently infect neurons, Herpes simplex virus uses kinesins and dynein to move along the microtubules within dendrites or axons and spread through neuronal synapses [3,5]. At late stages of infection, Vaccinia virus induces actin tails that efficiently propel enveloped viral particles towards uninfected cells [6]. Furthermore, viruses can use alternative mechanisms, such as actin-rich cell surface structures and cell-to-cell contacts, for efficient viral dissemination [7].

Human immunodeficiency virus 1 (HIV-1) infects cells of the immune system, namely CD4 T cells, macrophages and dendritic cells (DCs). In order to efficiently enter these cells, HIV-1 has to recruit its fusion receptors, overcome the cortical actin cytoskeleton and transport its genome to the nucleus. Immune cells are mobile and exchange information during antigen presentation via cellular contacts, notably immunological synapses. Similarly, HIV-1 can efficiently spread between immune cells using close cell-contacts called virological synapses (VS) [8].

Here we will discuss how HIV-1 manipulates the cytoskeleton during entry, replication and cell-to-cell transmission using VS and transfer on membrane extensions. Whenever possible we will focus on data from most relevant primary cells.

## 2. The Role of the Cytoskeleton in HIV-1 Replication

### *2.1. Entry*

To initiate viral membrane fusion the gp120 part of the HIV-1 envelope (Env) interacts sequentially with the primary receptor CD4 and coreceptor CXCR4 or CCR5, which leads to the exposure of the fusion promoting peptide of the gp41 part of Env [9]. Early studies indicated that the binding of HIV-1 Env to CD4 induces clustering of CD4 and CXCR4. CD4/CXCR4 clustering was dependent on actin polymerization and is required for entry and infection [10]. Similar dependency on the actin cytoskeleton was more recently described for CCR5 clustering [11]. Only recently it was shown that Env-dependent actin remodeling involves the actin-crosslinker Filamin-A, Rho-A and Rac guanosine-triphosphatases (GTPase) and actin-depolymerization factor cofilin (Figure 1). The actin-crosslinking protein Filamin-A binds the cytoplasmic tails of CD4 and CXCR4 and subsequent Env-dependent

signaling leads to the activation of Rho-A [11] and Rac1 [12]. Both Rho-A and Rac GTPase activate LIM domain kinase, which phosphorylates and inactivates cofilin. Inactive cofilin triggers early actin polymerization and receptor clustering [11,12]. In addition, Env-binding to CD4 activates moesin of the ezrin/radixin/moesin (ERM) complex that promotes CD4/CXCR4 clustering [13]. Active ERM complex tethers transmembrane and cytoplasmic proteins to filamentous actin (F-actin) and promotes its membrane recruitment.

While recruitment of sufficient receptor/coreceptor complexes through actin polymerization is required to initiate fusion, the cortical actin—although a highly dynamic network—could pose a barrier to fusion pore enlargement and the passage of the capsid into the cytoplasm [14–16]. Env binding to CXCR4 induces signaling and promotes actin remodeling critical for viral intracellular entry. Activation of cofilin, an actin depolymerization factor, is required to overcome the cortical actin barrier in resting T cells [14]. Furthermore, Env signaling through CXCR4 activates Rac1-GTPase, which promotes fusion pore formation and entry via Wave2 and the actin-nucleation factor Arp2/3 [16–18].

The precise recruitment and activation of the different actin remodeling factors upon Env signaling via CD4 and coreceptor remains to be determined. Likewise, Env signaling upstream of the Rho-A/ Rac-LIMK-cofilin pathway and the kinase that phosphorylates moesin in the ERM complex have still to be ascertained. Furthermore, it is not yet clear whether Env induced receptor clustering results from centripetal actin flow generated by myosin motors or reflects a simple diffusion-capture mechanism [19].

In order to follow Env-dependent signaling and actin remodeling dynamically *in vivo*, recently developed fluorescent probes such as Rho/Rac GTPase-biosensors [20] and the fluorescent actin-probe lifeact [21] could be useful. Super-resolution microscopy can resolve and track single molecules in living cells with 20–40 nm resolution [22] and could provide detailed insight into actin-remodeling upon single virus binding events.

HIV-1 Nef, a small myristoylated protein also affects early post-fusion steps leading to increased infectivity [23,24]. The defect in infectivity of Nef-deficient HIV-1 can be complemented by disruption of the actin cytoskeleton [15] or by pseudotyping virions with Vesicular Stomatitis Virus glycoprotein (VSV-G) that fuses in low pH endocytotic vesicles.

Dynamin-2 and clathrin, both regulators of vesicular trafficking, are required in producer cells to observe the effect of Nef on infectivity [25]. By affecting clathrin-dependent endocytosis Nef could change the lipid composition of virions [25] and/or specifically remove a host factor from virions that limits fusion pore enlargement and passage of the viral core through the cortical actin cytoskeleton.

Productive infection of CD4 T cells mainly occurs through fusion at the plasma membrane [9,26]. Alternatively, HIV-1 could enter and infect cells via endocytosis and subsequent fusion with endosomal membranes [27–32]. HIV-1 may take distinct endocytotic routes in different cell types.

Clathrin-mediated endocytosis of HIV-1 was observed in HeLa cells and in primary and transformed T cells [27,28,30]. HIV-1 pseudotyped with VSV-G allows CD4/coreceptor independent entry through endocytosis in various cell types, including transformed T cells. On the contrary, infection of resting primary CD4-T cells required HIV-1 Env but not VSV-G, indicating the importance of HIV-1 Env signaling and actin remodeling in relevant primary cells [33].

**Figure 1.** Simplified model of the role of the cytoskeleton in HIV-1 entry and release. (**a**) Binding of HIV-1 Env to CD4/CXCR4 and signaling leads to transient actin polymerization and receptor clustering through Filamin-A dependent crosslinking of CD4/CXCR4, activation of the ezrin/radixin/moesin (ERM) complex and inactivation of Cofilin. Subsequent actin depolymerization and fusion pore formation requires CXCR4 signaling to activate cofilin and Arp2/3. Viral cores can be transported on microtubules or actin towards the nucleus. Alternatively, HIV-1 enters through endocytosis and fuses with intracellular vesicles. (**b**) Usually HIV-1 assembles at the plasma membrane of non-polarized cells independently of the cytoskeleton. Note that transport of Env through the secretory pathway is not depicted. (**c**) Assembly of HIV-1 in polarized T cells occurs at actin rich pseudo-pod structures with a polarized microtubule organizing center (MTOC). (**d**) Assembly in chronically infected macrophages occurs at invaginated regions of the plasma membrane enriched in tetraspanins which are stabilized by the actin cytoskeleton.

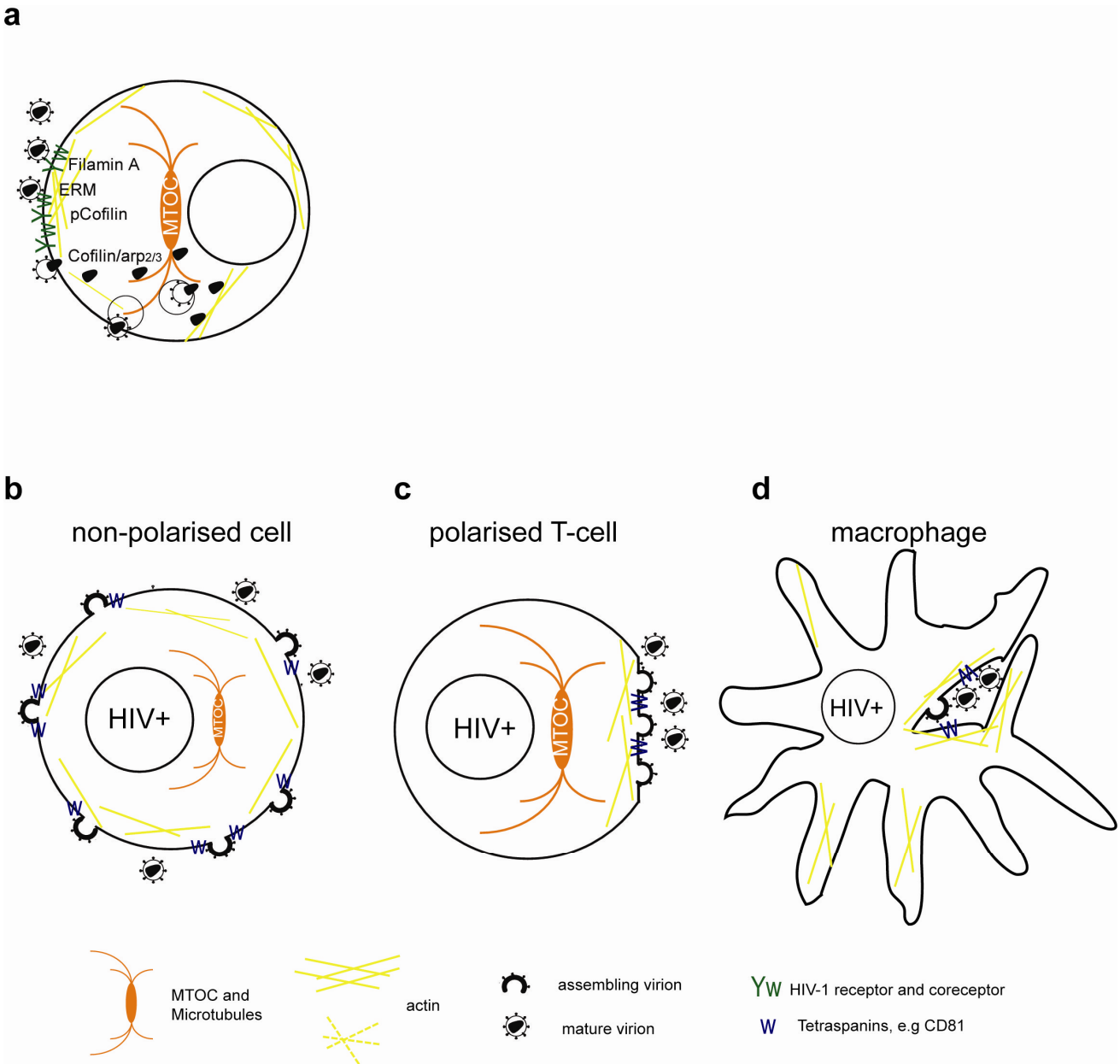

Uptake into DCs requires macropinocytosis, intact actin filaments and microtubules, but their role in productive infections has not been determined [34,35]. DCs capture HIV-1 through the C-type lectin DC-SIGN and preserve infectious virions inside internal compartments enriched in actin and tetraspanins [35,36]. Conversely Langerhans cells, an epidermal subtype of DCs, capture virions via the C-type lectin langerin and efficiently degrade HIV-1 [37].

HIV-1 enters and infects macrophages following dynamin-dependent macropinocytosis, which in contrast to classical macropinocytosis, does not require myosin II and vesicle acidification [29,31].

Entry pathways in primary cells have only been characterized using a few pharmacological inhibitors that may have possible non-specific effects. Thus, the role of endocytosis in productive infection should be confirmed by genetic strategies using RNAi or dominant negative constructs. Transduction of primary macrophages and DCs by HIV-1-derived lentiviral vectors is highly effective in the presence of vpx [38].

Overall, entry through endocytosis is advantageous for the virus as it minimizes its contact with neutralizing antibodies, enables passage through the cortical actin cytoskeleton and retrograde transport towards the nucleus. Nevertheless the virus has to escape lysosomal degradation, especially in professional phagocytotic cells, like macrophages and DCs. Therefore, as recently proposed, cell type specific entry receptor levels, Env fusion kinetics and endocytosis rates can determine whether fusion occurs at the plasma-membrane or from endosomes [39].

### *2.2. Intracellular Transport*

Cell fractionation has shown that the reverse transcription of viral RNA in the cytoplasm relies on interactions of the HIV-1 core with the actin cytoskeleton [40]. Live-cell microscopy revealed actin and microtubule-dependent movements of fluorescently-labeled HIV-1 [41,42]. Pharmacological inhibition of actin and microtubule polymerization arrested overall movements. Moreover, specific antibodies against dynein or genetic targeting of the dynein activator complex, dynactin, blocked minus-end transport of the particles towards the nucleus [41,42]. At the nuclear periphery, the pre-integration complex associates with perinuclear actin and eventually enters the nucleus [42]. Of note, both studies used adhered cells with a large cytoplasm and well defined microtubules. In contrast, in transformed and resting CD4 T cells microtubule integrity was not required for infection [43], indicating that short cytoplasmic distances in T cells can be overcome by actin-dependent transport. Nevertheless, microtubule-dependent transport might be necessary for the infection of adhered macrophages and dendritic cells.

Overall, it remains unclear how the viral genome is transported, uncoated and reverse transcribed and how these processes are coordinated. Notably, these steps in the HIV-1 life-cycle are sensitive to potent host restriction factors Apobec3G, TRIM5 and SAMHD1 [44–47] and their mechanisms should be better characterized.

### *2.3. Assembly and Budding*

The transport of newly synthesized viral proteins towards assembly sites occurs via the secretory pathway for HIV-1 Env and via diffusion for HIV-1 Gag [9,48].

During assembly, HIV-1 Gag binds F-actin via its nucleocapsid region [49,50]. Actin, myosin and actin-binding proteins were found at assembly sites and inside virions [51–53]. During HIV-1 budding star-shaped actin structures formed when the nucleocapsid region of Gag was present [54]. Despite the interaction of actin and HIV-1 Gag, pharmacological inhibitors of actin and microtubule assembly only slightly decreased or did not affect HIV-1 release from cell lines and primary cells [10,53,55,56]. Therefore, the cytoskeleton seems not to be required for HIV-1 assembly and release from the plasma membrane of infected cells.

In polarized T cells and monocytes, HIV-1 budding was observed at polarized caps or cell protrusions (Figure 1c) [57–59]. At this actin-rich uropod structure HIV-1 Env and Gag colocalize with GM1 lipid rafts, tetraspanins and adhesion molecules [55,60–62]. Gag localization to the uropod is Env independent, but requires an intact Gag nucleocapsid part. The uropod structures copolarized with the MTOC and polarized Gag was sensitive to inhibitors of actin, myosin and microtubules, indicating a possible role of the cytoskeleton in targeted secretion and polarized budding [55,62].

In HIV-1 infected macrophages and DCs, assembly was observed on internal compartments that were subsequently identified as tetraspanin-rich sequestered plasma membrane domains [63–67]. The disruption of the actin cytoskeleton in infected macrophages decreased intracellular accumulation of HIV-1, but had no effect on the overall release [56].

Therefore, despite interaction of HIV-1 Gag with actin, there is no direct functional role of the cytoskeleton in HIV-1 assembly. Nevertheless, polarized budding at T cell uropods and intracellular budding in macrophages both depend on the cytoskeleton. The local concentration of virus at the uropod or in an intracellular compartment could facilitate subsequent cell-to-cell spread of HIV-1.

## 3. Role of Cytoskeleton in Cell-to-Cell Transfer between T Cells

### *3.1. HIV-1 Transmission*

HIV-1 can spread between hosts through sexual transmission of cell-free or cell-associated virus. Major efforts are directed into the development of microbicides blocking the early steps of viral transmission at the mucosa [68]. Following entry, HIV-1 encounters potential target cells [69,70]. CD4 T cells can be directly infected in mucosal tissue [71]. Otherwise, HIV-1 can be taken up by APCs, such as dermal DCs, Langerhans cells (LC) and macrophages [69]. LC can transfer captured virus to resident T cells [71]. Alternatively, APCs can exit the mucosa and migrate to proximal lymph nodes, where captured and newly replicated virus can be transferred to T cells [70,72,73].

Cell-to-cell transfer can provide several advantages over cell free infection. (i) HIV-1 could escape detection by neutralizing antibodies, (ii) close contact limits diffusion time to a new target cell, and (iii) the VS concentrates virus and viral entry receptors to increase fusion efficiency. HIV-1 infection through cell-to-cell transfer was shown to be 100- to 18,000-times more effective than through cell-free virus [57,74]. Protection from neutralizing antibodies at the HIV-1 VS was initially observed [26,32,57], but recently challenged by another study [75]. Efficient HIV-1 cell-to-cell transfer takes place at cell-contacts called the VS, that was observed between: (i) HIV-1 pulsed DCs and T cells, (ii) infected and uninfected T cells, and (iii) infected macrophages and T cells [26,73,76,77]. Since

virological synapses are cell contacts formed between different types of immune cells, analogies to antigen presentation at the immunological synapses were proposed [26,76,78].

Immunological synapses (IS) are specialized cell contacts either between antigen-presenting cells (APCs) and T cells or between target cells and effector T cells (Figure 2a). APCs can activate T cells which upon clonal expansion can execute effector functions, such as cytokine release or directed cytolysis. Peptide-major histocompatibility complex (pMHC) on the APCs engage a specific T-cell receptor (TCR), CD4 and kinases into an actin-dependent microcluster. TCR microcluster converge towards the central supramolecular activation complex (cSMAC), where TCR signaling is terminated. The cSMAC is surrounded by a ring of adhesion molecules and is associated with talin and F-actin. This peripheral SMAC (pSMAC) stabilizes the IS. The duration of the IS can be transient or last for hours. Strong pMHC-TCR affinity and costimulatory signals lead to polarization of the MTOC towards the APC and full activation of the T-cell. Cytoskeleton remodeling during T-cell activation was extensively reviewed recently [79].

### *3.2. The Virological Synapse*

The structure of the VS and the mechanism of transfer are best characterized in the T cell context, but are similar in APC-T cell VS (Figure 2b).

Mobile monocytes and lymphocytes form membrane extensions at their rear, called uropods. The uropod is rich in cytoskeleton and adhesion molecules, can mediate cell-to-cell contacts and support polarized HIV-1 assembly [57–59,62]. Both polarized budding and cell-to-cell transfer depend on the actin and the microtubule cytoskeleton [26,32,55,80]. Therefore, the cytoskeleton could facilitate cell contacts, VS formation and cell-to-cell transfer through polarized budding.

The VS forms between a HIV-1 infected and uninfected cells via Env interactions with CD4 and CXCR4 or CCR5. Env and Gag concentrate on the infected cell, leading to polarized budding and transfer of virions across the VS [26,32]. On the target cell CD4 and coreceptor polarize towards the VS, thereby increasing the probability of virus fusion and the strength of the cell contact.

Additional stability to the virological synapse is conferred by adhesion molecules. Intercellular adhesion molecule 1 (ICAM-1) or ICAM-3 on the infected cell interact with the integrin lymphocyte function-associated antigen 1 (LFA-1) on the target cell [81]. Talin, an actin-bridging molecule, interacts with LFA-1 and thereby reorganizes F-actin in the target cell. Adhesion molecules, talin and F-actin form a stable ring-like structure, resembling the pSMAC [26,80,81]. Pharmacological inhibition of actin remodeling and myosin-dependent transport in target cells inhibited CD4, CXCR4 and Env clustering and transfer of infection at the VS [26,57].

Recently, live-cell imaging of CD4 T cells interacting with planar lipid bilayers containing HIV-1 Env and ICAM-1 provided a detailed structural and dynamic view of the VS [78,82,83]. Upon contact with CD4 T cells, Env forms an actin-dependent microcluster. The microclusters converge into the cSMAC and reorganize CD4 on the target cell. The CD4/Env containing cSMAC, surrounded by a ring of adhesion molecules and F-actin, transiently arrests T-cell migration [83]. Furthermore, Env induces partial TCR signaling that activates Lck and creates an F-actin depleted zone at the cSMAC [82]. Notably, some TCR recruitment and F-actin depletion from the center of the VS were also apparent in authentic T-cell contacts [26]. However, the absence of Zap70, the key mediator of

TCR signaling, in target T cells does not affect HIV-1 transfer [82]. Therefore, it remains unclear if TCR signaling is required for VS formation and how Lck activation leads to depletion of F-actin from the central zone of the VS.

Alternatively, actin remodeling during the formation of the VS could also implicate Filamin-A or Env-dependent activation of ERM, Arp2/3 and cofilin as discussed before [19]. Env expressing cells induce Filamin-A dependent clustering of CD4 and CXCR4/CCR5 on target cells [11]. The role of Filamin-A, Lck, ERM, Arp2/3 and cofilin in Env-dependent signaling and actin remodeling in authentic VS needs further detailed investigation. The simplified lipid-bilayer system of the VS combined with high-resolution live-cell microscopy [84] or super-resolution techniques [22,85] could answer these questions and reveal how actin is dynamically remodeled.

HIV-1 transfer through VS relies on intact microtubules [55,80]. During transfer the microtubule organizing centre (MTOC) in HIV-1 infected T cells, but not in target cells polarizes towards the VS [7,82,86]. As expected, in infected T cells that engage multiple target cells through polysynapses the MTOC polarizes only to an individual synapse [80]. Zap70, a key mediator of TCR signaling and MTOC polarization, is required for VS formation and HIV-1 transfer. HIV-1 infected donor cells lacking Zap70 show defects in MTOC polarization and VS formation, but release normal amounts of infectious virus and establish conjugates with uninfected cells [86]. Therefore, the microtubule network may be involved in targeted secretion of viral components, adhesion molecules, tetraspanins or specific lipids to the VS that favor directed budding towards the target cell [87]. Once a stable VS is formed, the MTOC could initiate additional cell contacts leading to polysynapses.

Alternatively, polarized budding at the VS could result from incorporation of locally concentrated Env in virus particles that depend on the cytoplasmic tail (CT) of HIV-1 Env [9]. HIV-1 Env lacking the CT increases cell-to-cell transfer, but is more neutralization-sensitive than full-length Env [57]. Mouse Leukemia virus (MLV) Env concentrates at the cell-to-cell contact through interaction with receptors, interacts with MLV Gag via its cytoplasmic tail (CT) and could initiate polarized budding [88,89]. How the cytoskeleton and HIV-1 Env polarization affects polarized budding at the VS remains an important question for the future.

Dynamic imaging of the T-cell VS revealed HIV-1 Gag in button-shaped discs or ring like structures with Gag patches migrating into the synapse and transfer of viral aggregates [32,80]. Therefore, VS can provide stable contacts lasting minutes to hours that would allow polarized budding at the contact and transfer of virus from distal assembly sites. The attachment factor and details of HIV-1 movement on infected cells prior to transfer remain to be determined [89,90].

### *3.3. Actin-Containing Membrane Protrusions*

Besides VS actin-containing membrane extensions, filopodial bridges, nanotubes and tunneling nanotubes have been implicated in cell-to-cell transfer of HIV-1 (Figure 2c) and other retroviruses [80,91–93]. Filopodial bridges extend from uninfected to infected epithelial cells, are stabilized through Env-receptor interaction and mediate viral transfer through retrograde actin flow towards the uninfected cell [91]. Nanotubes, on the other hand, are formed upon transient contact between T cells and connect cells over several cell lengths in curved paths. HIV-1 infection did not affect the frequency nor the direction of intercellular connections through nanotubes, but infection of

target cells occurred in a receptor-dependent manner [92]. Tunneling nanotubes, however, are induced by HIV-1 infection of macrophages and contain HIV-1 particles [93].

**Figure 2.** Simplified model of the immunological synapse and cell-to-cell transfer via the virological synapse or through membrane extensions (**a**) The antigen-presenting cell (APC)-T-cell immunological synapse (IS) is a stable contact. It is mediated by peptide-loaded-MHC II on the APC interacting with the TCR on the T-cell, in a central region called cSMAC, which is devoid of F-actin. Adhesion molecules ICAM1 on the APC and LFA1 on the T-cell surround and stabilize the cSMAC. In turn, talin and F-actin are organized into a peripheral ring like structure, the pSMAC. Note that costimulatory signaling through CD4/Lck, and TCR signaling leading to T-cell activation are not depicted for simplicity. (**b**) Transfer of HIV-1 between T cells occurs via the virological synapse (VS). HIV-1 Env–CD4 interactions result in clustering of CD4/CXCR4, adhesion molecules and talin at the cell contact zone, similar to the IS. HIV-1 Env signaling leads to partial T-cell activation and creates a central actin-depleted region. HIV-1 assembles directly at the VS or is transported to the contact prior to transfer. Fusion takes place directly at the target cell membrane or after endocytosis. The formation of the immunological and virological synapse are dependent on the actin and microtubule cytoskeleton (**c**) Alternatively, transfer of HIV-1 can take place on actin-containing membrane extensions: filopodial bridges or nanotubes. Filopodial bridges extend from uninfected to infected cells and transport receptor-bound virions through retrograde actin-flow. Nanotubes connect uninfected and infected cells and transport virions in an Env-independent manner.

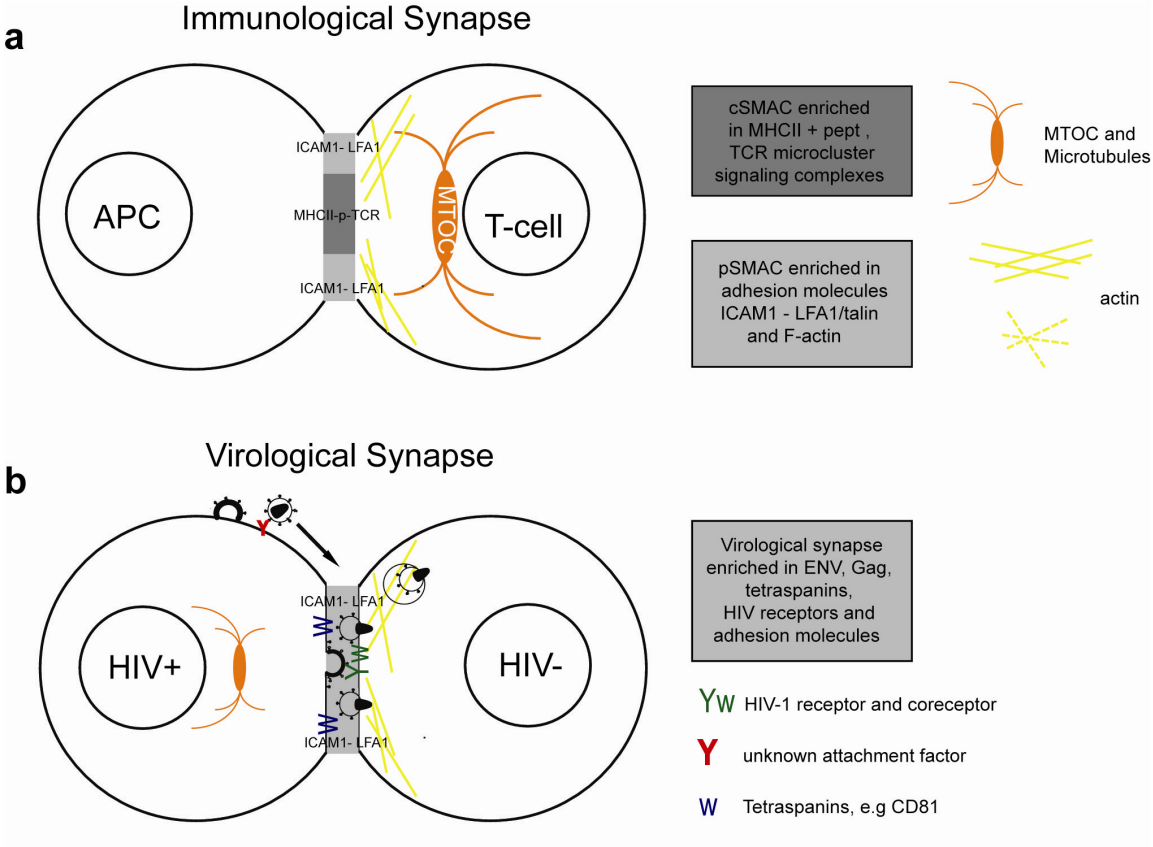

**Figure 2.** *Cont.*

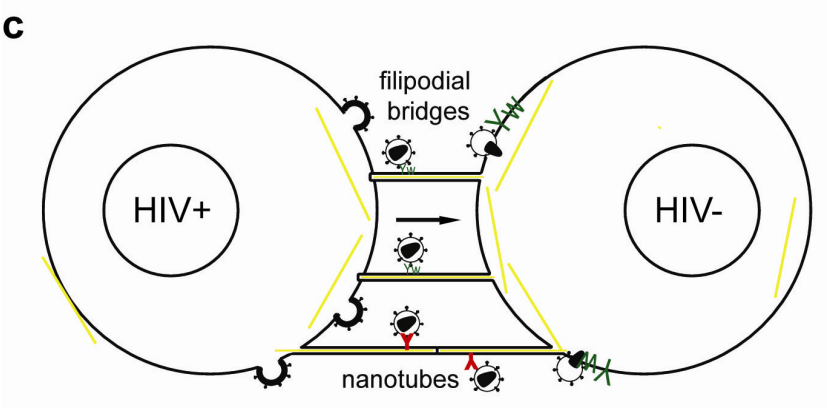


Recently, the relative contributions of virological synapses, nanotubes and filopodial bridges to HIV-1 transfer between T cells were quantified. The authors found less than 10% of transfer occurring on nanotubes or filopodia with main contributions to viral transfer made by virological synapses [80]. Another study found 30–50% of T cells connected through nanotubes and approximately half of these structures were associated with HIV-1 Gag [92].

Live-cell microscopy visualized transfer of viral particles on nanotubes occurred with 0.08 μm/s, on filopodial bridges with 0.01 μm/s and into VS with 0.1–0.25 μm/s [91,92]. The different movement of viral particles can reflect diffusion, drift, confinements or use of distinct motor proteins and interaction with the underlying cytoskeleton in different cells [90]. Alternatively, the proximity of filopodia bridges to the glass surface and 3D matrix used to stabilize nanotubes may affect the viral movements. Therefore, the relative contributions of different cell-to-cell transfer mechanisms should be carefully examined under *in vivo* conditions in lymphatic tissue. Of note, clusters of SIV-positive cells were found in vaginal and lymph node tissue of macaques, indicating effective transfer between T cells, albeit the sensitivity and resolution of this technique limit detailed interpretation [80].

HIV-1 Nef was shown to remodel the actin cytoskeleton in infected lymphocytes leading to impaired migration in response to cytokines, inhibition of membrane ruffles and induction of filopodia-like protrusions [94,95] and reviewed in [96]. Overall reduced mobility and protrusions could enhance cell-to-cell transfer. Conversely, HIV-1 Nef modestly increased cell-to-cell transfer in lymphocytes without affecting actin remodeling in virological synapses and nanotubes [97]. Increased cell-to-cell transfer was attributed to a positive effect of Nef on infectivity [97].

Similarly, infected macrophages formed Nef-dependent long range intercellular protrusions with B cells that induced antibody class switching, leading to decreased virus-specific antibody responses [98]. The effects of Nef on cell mobility and communication between immune cells are discussed in a review by Stolp and Fackler in this issue [96].

## 4. Role of the Cytoskeleton in Virological Synapses between DCs and T Cells

DCs participate in the early HIV-1 dissemination in mucosal and lymphatic tissue [69,70,99]. Immature DCs bind, internalize and degrade extracellular material into peptides that can be presented on MHC complexes. Potential pathogens, like viruses and bacteria are recognized by pattern recognition receptors and can lead to DC maturation. During maturation DCs decrease endocytosis and upregulate chemokine-receptors and co-stimulatory proteins (CD80, CD83 and CD86). While maturating, DCs migrate to lymph nodes, where they present antigens to T cells and B cells. HIV-1 exposure does not lead to DC maturation [67,100], except when high doses of virus are used or when high infection rates are achieved in the presence of SIV vpx [101,102].

The initial maturation state of DCs upon contact has significant impact on HIV-1 infection and transfer [70,99]

While both immature DCs (iDCs) and mature DCs (mDCs) efficiently capture HIV-1, mDCs transfer virions more efficiently to T cells [73,76,103]. Alternatively, HIV-1 can infect iDCs more efficiently than mDCs and transfer newly replicated virus to T cells [70,72]. Overall, cell-to-cell transfer from DCs to T cells occurs in two phases, first transfer of captured virus occurs within 24 h after exposure and later newly replicated virus is transferred [73].

Following capture, HIV-1 alters endolysosomal trafficking of DCs and localizes to surface accessible compartments that contain tetraspanins and actin, but lack MHCII (Figure 3) [35,36,67,104,105]. Upon contact with CD4 T cells a VS is formed: viral proteins and tetraspanins polarize on the DC side, while CD4, CXCR4/CCR5 and LFA-1 concentrate on the target T-cell [36,76]. Subsequent live cell imaging of the transfer from DCs and macrophages revealed dynamic translocation of HIV-1 containing compartments towards the contact zone and transfer of individual virions toward T cells [35,106,107].

Inhibition of actin remodeling in DCs pulsed with HIV-1 inhibited VS formation and transfer to T cells [34,104,107]. Therefore, actin remodeling could control trafficking of internal compartments and/or cell surface structures involved in HIV-1 DC T cell transfer.

Recent ultra-structural work revealed that HIV-1 pulsed mDCs form extensive actin-containing membrane sheets around T cells. HIV-1 localizes to internal compartments in mDCs and on membrane protrusions of T cells that reach into the virus containing compartments [104].

This analysis suggests that efficient viral transfer at the highly secluded mDC-T cell virological synapse depends on actin-containing membrane extensions. The molecular mechanisms of VS formation and actin remodeling in mDC T-cell transfer remain to be discovered.

DC-SIGN specifically binds HIV-1 through Env, localizes to the VS and is required for targeting of HIV-1 from an internal compartment to the VS and for transfer of infection [76,108].

DC-SIGN engagement with antibodies induces signaling in DC: Both ERK and Rho-GTPase, but not Rac-GTPase become activated and modulate DC maturation, cytokine release and T-cell contacts [109,110]. Specifically, HIV-1 binding to DC-SIGN activates the Rho Guanine Exchange Factor (GEF) Larg that is required for VS formation and transfer [110]. Rho-GTPases control actin-dynamics during cell migration, IS formation and were proposed to affect dendrite formation in DCs [79,110].

**Figure 3.** (**a**) Dendritic cells (DCs) interact with HIV-1 via DC-SIGN and capture infectious virus inside endosome-like compartments and surface accessible pockets in an actin and microtubule dependent manner. (**b**) Interaction of HIV-1 Env with DC-SIGN (i) activates Larg/Rho signaling to establish DC T-cell contacts, (ii) activates Cdc42 to induce membrane extensions, and (iii) preserves an immature DC phenotype. (**c**, **d**) Transfer of HIV-1 at DC-T cell VS occurs at cell contact zones enriched in HIV-1 receptor/coreceptor, adhesion molecules, tetraspanins and actin. (**c**) Specifically transfer from iDCs occurs on actin containing and Cdc42 dependent membrane extensions, (**d**) conversely, mDCs wrap large membrane sheets around T cells forming the virological synapse. HIV-1 was found on mDC membrane sheets and on thin membrane extensions from the T cells reaching into virus containing compartments.

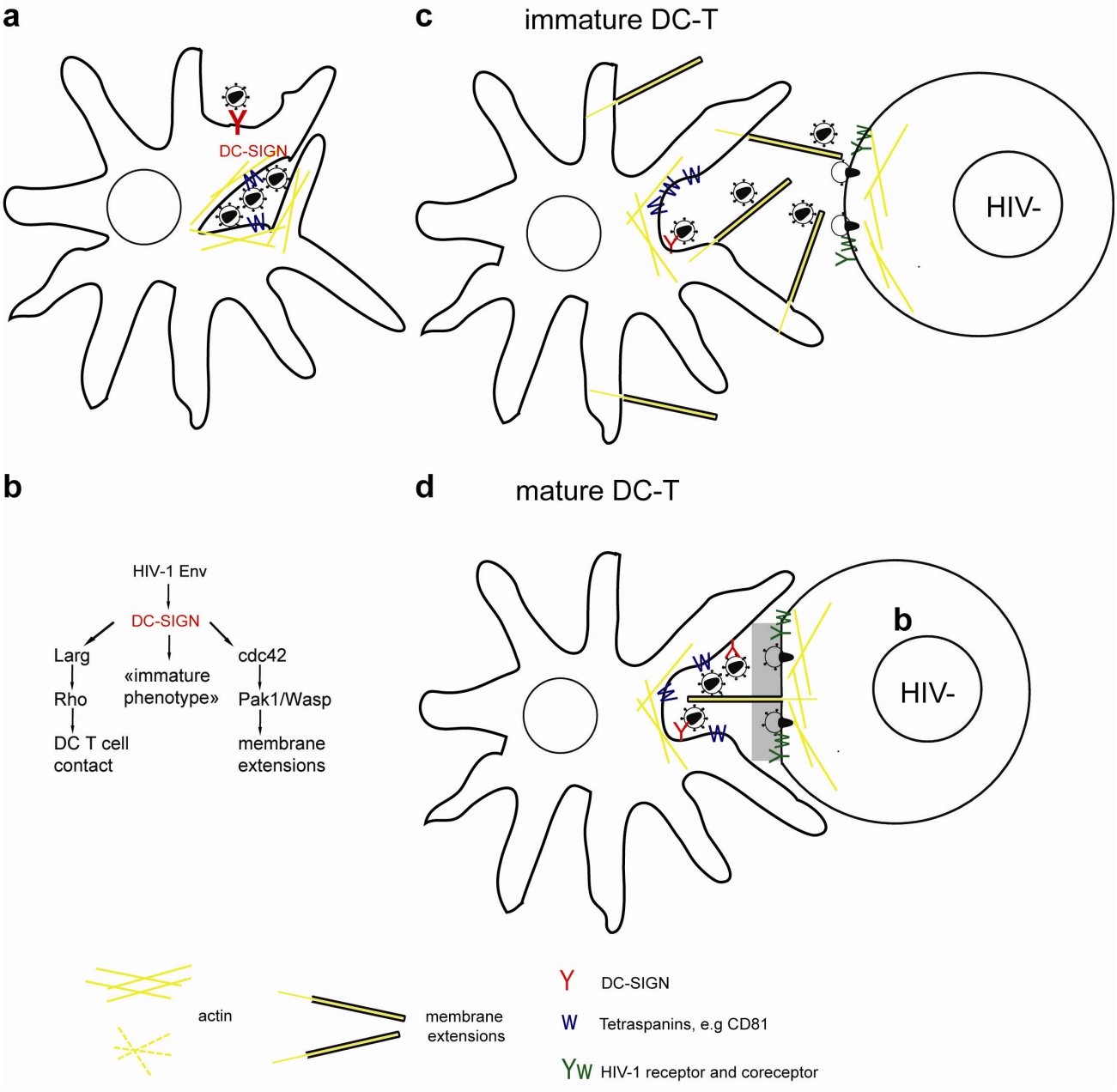

Recently, we used systematic siRNA knockdowns of cytoskeleton modulators like GEF, Rho-GTPases and formins in iDCs to identify pathways required for HIV-1 uptake, trafficking and transfer at the iDC-T-cell VS [107]. HIV-1 induced the formation of membrane-extensions in iDCs through Env binding to DC-SIGN and subsequent activation of the Rho GTPase Cdc42. Notably both CXCR4 and the CCR5 Env protein that mediates infection of macrophages and DCs activate Cdc42 and induce membrane extensions in iDCs. Knockdown, pharmacological inhibition and dominant-negative constructs targeting Cdc42 reduced the number of membrane extensions and HIV-1 transfer to target T cells. In iDCs fluorescent HIV-1 particles were found on dynamic membrane extensions involved in transfer across VS. Notably, when contacts between iDCs and T cells were increased by promoting IS or at high T to DC cell ratio, as found in lymph nodes, we observed that most of the HIV-1 transfer was mediated by Cdc42-dependent membrane extensions.

HIV-1 infected iDCs showed polarized budding and transfer of viral particles on dendrites towards target cells [67]. How HIV-1 infection of DCs affects actin remodeling, membrane extension and VS formation in detail remains to be determined.

## 5. Conclusions and Perspectives

During its replication cycle, HIV-1 remodels cytoskeleton structures using different viral proteins. Upon binding to cells, HIV-1 Env induces actin remodeling to concentrate receptor/coreceptors, initiate fusion and overcome the plasma membrane cortical actin network. HIV-1 entry through endocytosis and transport of its genome on actin or microtubules largely depends on the cell type. Polarized budding and cell-to-cell transfer in primary cells, but not HIV-1 assembly and release, depend on the cytoskeleton. HIV-1 uses different actin-containing structures to spread efficiently between T cells and from APCs to T cells: virological synapses, filopodial bridges, nanotubes, tunneling nanotubes and membrane extensions. A detailed mechanism for Env-induced actin remodeling at the VS is still missing. HIV-1 binding to DC-SIGN affects DC maturation, actin remodeling and induction of membrane extension in the context of DC-T cell VS.

How virological synapses and different actin-containing cell surface structures contribute to *in vivo* spread of HIV-1 remains a challenging question for the future.

## Acknowledgements

We thank Louise Kemp and Silvia Anghel for critical reading of the manuscript. Our work was supported by grants from the Swiss National Science Foundation and the Human Science Frontier Program to V.P. The authors have no conflicting financial interests.

## References and Notes

1. Toivola, D.M.; Strnad, P.; Habtezion, A.; Omary, M.B. Intermediate filaments take the heat as stress proteins. *Trends Cell Biol.* **2010**, *20*, 79–91.
2. Vale, R.D. The molecular motor toolbox for intracellular transport. *Cell* **2003**, *112*, 467–480.
3. Dohner, K.; Sodeik, B. The role of the cytoskeleton during viral infection. *Curr. Top. Microbiol. Immunol.* **2005**, *285*, 67–108.

4. Mabit, H.; Nakano, M.Y.; Prank, U.; Saam, B.; Dohner, K.; Sodeik, B.; Greber, U.F. Intact microtubules support adenovirus and herpes simplex virus infections. *J. Virol.* **2002**, *76*, 9962–9971.
5. Smith, G.A.; Gross, S.P.; Enquist, L.W. Herpesviruses use bidirectional fast-axonal transport to spread in sensory neurons. *Proc. Natl. Acad. Sci. U. S. A.* **2001**, *98*, 3466–3470.
6. Cudmore, S.; Cossart, P.; Griffiths, G.; Way, M. Actin-based motility of vaccinia virus. *Nature* **1995**, *378*, 636–638.
7. Sattentau, Q. Avoiding the void: Cell-to-cell spread of human viruses. *Nat. Rev. Microbiol.* **2008**, *6*, 815–826.
8. Piguet, V.; Sattentau, Q. Dangerous liaisons at the virological synapse. *J. Clin. Invest.* **2004**, *114*, 605–610.
9. Freed, E.O. HIV-1 replication. *Somat. Cell Mol. Genet.* **2001**, *26*, 13–33.
10. Iyengar, S.; Hildreth, J.E.; Schwartz, D.H. Actin-dependent receptor colocalization required for human immunodeficiency virus entry into host cells. *J. Virol.* **1998**, *72*, 5251–5255.
11. Jimenez-Baranda, S.; Gomez-Mouton, C.; Rojas, A.; Martinez-Prats, L.; Mira, E.; Ana Lacalle, R.; Valencia, A.; Dimitrov, D.S.; Viola, A.; Delgado, R.; *et al*. Filamin-a regulates actin-dependent clustering of hiv receptors. *Nat. Cell Biol.* **2007**, *9*, 838–846.
12. Vorster, P.J.; Guo, J.; Yoder, A.; Wang, W.; Zheng, Y.; Xu, X.; Yu, D.; Spear, M.; Wu, Y. Lim kinase 1 modulates cortical actin and CXCR4 cycling and is activated by HIV-1 to initiate viral infection. *J. Biol. Chem.* **2011**, *286*, 12554–12564.
13. Barrero-Villar, M.; Cabrero, J.R.; Gordon-Alonso, M.; Barroso-Gonzalez, J.; Alvarez-Losada, S.; Munoz-Fernandez, M.A.; Sanchez-Madrid, F.; Valenzuela-Fernandez, A. Moesin is required for HIV-1-induced CD4-CXCR4 interaction, F-actin redistribution, membrane fusion and viral infection in lymphocytes. *J. Cell Sci.* **2009**, *122*, 103–113.
14. Yoder, A.; Yu, D.; Dong, L.; Iyer, S.R.; Xu, X.; Kelly, J.; Liu, J.; Wang, W.; Vorster, P.J.; Agulto, L.; *et al.* Hiv envelope-CXCR4 signaling activates cofilin to overcome cortical actin restriction in resting CD4 T cells. *Cell* **2008**, *134*, 782–792.
15. Campbell, E.M.; Nunez, R.; Hope, T.J. Disruption of the actin cytoskeleton can complement the ability of nef to enhance human immunodeficiency virus type 1 infectivity. *J. Virol.* **2004**, *78*, 5745–5755.
16. Pontow, S.E.; Heyden, N.V.; Wei, S.; Ratner, L. Actin cytoskeletal reorganizations and coreceptor-mediated activation of rac during human immunodeficiency virus-induced cell fusion. *J. Virol.* **2004**, *78*, 7138–7147.
17. Harmon, B.; Campbell, N.; Ratner, L. Role of abl kinase and the Wave2 signaling complex in HIV-1 entry at a post-hemifusion step. *PLoS Pathog.* **2010**, *6*, e1000956.
18. Komano, J.; Miyauchi, K.; Matsuda, Z.; Yamamoto, N. Inhibiting the Arp2/3 complex limits infection of both intracellular mature vaccinia virus and primate lentiviruses. *Mol. Biol. Cell* **2004**, *15*, 5197–5207.
19. Liu, Y.; Belkina, N.V.; Shaw, S. HIV infection of t cells: Actin-in and actin-out. *Sci. Signal* **2009**, *2*, pe23.

20. Machacek, M.; Hodgson, L.; Welch, C.; Elliott, H.; Pertz, O.; Nalbant, P.; Abell, A.; Johnson, G.L.; Hahn, K.M.; Danuser, G. Coordination of Rho GTPase activities during cell protrusion. *Nature* **2009**, *461*, 99–103.
21. Riedl, J.; Crevenna, A.H.; Kessenbrock, K.; Yu, J.H.; Neukirchen, D.; Bista, M.; Bradke, F.; Jenne, D.; Holak, T.A.; Werb, Z.; *et al.* Lifeact: A versatile marker to visualize F-actin. *Nat. Methods* **2008**, *5*, 605–607.
22. Manley, S.; Gillette, J.M.; Patterson, G.H.; Shroff, H.; Hess, H.F.; Betzig, E.; Lippincott-Schwartz, J. High-density mapping of single-molecule trajectories with photoactivated localization microscopy. *Nat. Methods* **2008**, *5*, 155–157.
23. Cavrois, M.; Neidleman, J.; Yonemoto, W.; Fenard, D.; Greene, W.C. HIV-1 virion fusion assay: Uncoating not required and no effect of Nef on fusion. *Virology* **2004**, *328*, 36–44.
24. Aiken, C.; Trono, D. Nef stimulates human immunodeficiency virus type 1 proviral DNA synthesis. *J. Virol.* **1995**, *69*, 5048–5056.
25. Pizzato, M.; Helander, A.; Popova, E.; Calistri, A.; Zamborlini, A.; Palu, G.; Gottlinger, H.G. Dynamin 2 is required for the enhancement of HIV-1 infectivity by Nef. *Proc. Natl. Acad. Sci. U. S. A.* **2007**, *104*, 6812–6817.
26. Jolly, C.; Kashefi, K.; Hollinshead, M.; Sattentau, Q.J. HIV-1 cell to cell transfer across an env-induced, actin-dependent synapse. *J. Exp. Med.* **2004**, *199*, 283–293.
27. Daecke, J.; Fackler, O.T.; Dittmar, M.T.; Krausslich, H.G. Involvement of clathrin-mediated endocytosis in human immunodeficiency virus type 1 entry. *J. Virol.* **2005**, *79*, 1581–1594.
28. Miyauchi, K.; Kim, Y.; Latinovic, O.; Morozov, V.; Melikyan, G.B. HIV enters cells via endocytosis and dynamin-dependent fusion with endosomes. *Cell* **2009**, *137*, 433–444.
29. Carter, G.C.; Bernstone, L.; Baskaran, D.; James, W. HIV-1 infects macrophages by exploiting an endocytic route dependent on dynamin, Rac1 and Pak1. *Virology 409*, 234–250.
30. Bosch, B.; Grigorov, B.; Senserrich, J.; Clotet, B.; Darlix, J.L.; Muriaux, D.; Este, J.A. A clathrin-dynamin-dependent endocytic pathway for the uptake of HIV-1 by direct T cell-T cell transmission. *Antivir. Res.* **2008**, *80*, 185–193.
31. Marechal, V.; Prevost, M.C.; Petit, C.; Perret, E.; Heard, J.M.; Schwartz, O. Human immunodeficiency virus type 1 entry into macrophages mediated by macropinocytosis. *J. Virol.* **2001**, *75*, 11166–11177.
32. Hubner, W.; McNerney, G.P.; Chen, P.; Dale, B.M.; Gordon, R.E.; Chuang, F.Y.; Li, X.D.; Asmuth, D.M.; Huser, T.; Chen, B.K. Quantitative 3D video microscopy of HIV transfer across T cell virological synapses. *Science* **2009**, *323*, 1743–1747.
33. Yu, D.; Wang, W.; Yoder, A.; Spear, M.; Wu, Y. The HIV envelope but not vsv glycoprotein is capable of mediating HIV latent infection of resting CD4 T cells. *PLoS Pathog.* **2009**, *5*, e1000633.
34. Chen, H.L.; Lin, S.R.; Liu, H.F.; King, C.C.; Hsieh, S.C.; Wang, W.K. Evolution of dengue virus type 2 during two consecutive outbreaks with an increase in severity in southern taiwan in 2001–2002. *Am. J. Trop. Med. Hyg.* **2008**, *79*, 495–505.
35. Yu, H.J.; Reuter, M.A.; McDonald, D. HIV traffics through a specialized, surface-accessible intracellular compartment during *trans*-infection of T cells by mature dendritic cells. *PLoS Pathog.* **2008**, *4*, e1000134.

36. Garcia, E.; Pion, M.; Pelchen-Matthews, A.; Collinson, L.; Arrighi, J.F.; Blot, G.; Leuba, F.; Escola, J.M.; Demaurex, N.; Marsh, M.; *et al.* HIV-1 trafficking to the dendritic cell-T-cell infectious synapse uses a pathway of tetraspanin sorting to the immunological synapse. *Traffic* **2005**, *6*, 488–501.
37. de Witte, L.; Nabatov, A.; Pion, M.; Fluitsma, D.; de Jong, M.A.; de Gruijl, T.; Piguet, V.; van Kooyk, Y.; Geijtenbeek, T.B. Langerin is a natural barrier to HIV-1 transmission by langerhans cells. *Nat. Med.* **2007**, *13*, 367–371.
38. Berger, G.; Durand, S.; Goujon, C.; Nguyen, X.N.; Cordeil, S.; Darlix, J.L.; Cimarelli, A. A simple, versatile and efficient method to genetically modify human monocyte-derived dendritic cells with HIV-1-derived lentiviral vectors. *Nat. Protoc.* **2011**, *6*, 806–816.
39. Permanyer, M.; Ballana, E.; Este, J.A. Endocytosis of HIV: Anything goes. *Trends Microbiol.* **2010**, *18*, 543–551.
40. Bukrinskaya, A.; Brichacek, B.; Mann, A.; Stevenson, M. Establishment of a functional human immunodeficiency virus type 1 (HIV-1) reverse transcription complex involves the cytoskeleton. *J. Exp. Med.* **1998**, *188*, 2113–2125.
41. McDonald, D.; Vodicka, M.A.; Lucero, G.; Svitkina, T.M.; Borisy, G.G.; Emerman, M.; Hope, T.J. Visualization of the intracellular behavior of HIV in living cells. *J. Cell Biol.* **2002**, *159*, 441–452.
42. Arhel, N.; Genovesio, A.; Kim, K.A.; Miko, S.; Perret, E.; Olivo-Marin, J.C.; Shorte, S.; Charneau, P. Quantitative four-dimensional tracking of cytoplasmic and nuclear HIV-1 complexes. *Nat. Methods* **2006**, *3*, 817–824.
43. Yoder, A.; Guo, J.; Yu, D.; Cui, Z.; Zhang, X.E.; Wu, Y. Effects of microtubule modulators on HIV-1 infection of transformed and resting CD4 T cells. *J. Virol.* **2011**, *85*, 3020–3024.
44. Stremlau, M.; Owens, C.M.; Perron, M.J.; Kiessling, M.; Autissier, P.; Sodroski, J. The cytoplasmic body component Trim5alpha restricts HIV-1 infection in old world monkeys. *Nature* **2004**, *427*, 848–853.
45. Laguette, N.; Sobhian, B.; Casartelli, N.; Ringeard, M.; Chable-Bessia, C.; Segeral, E.; Yatim, A.; Emiliani, S.; Schwartz, O.; Benkirane, M. SAMHD1 is the dendritic- and myeloid-cell-specific HIV-1 restriction factor counteracted by Vpx. *Nature* **2011**, *474*, 654–657.
46. Sheehy, A.M.; Gaddis, N.C.; Choi, J.D.; Malim, M.H. Isolation of a human gene that inhibits HIV-1 infection and is suppressed by the viral Vif protein. *Nature* **2002**, *418*, 646–650.
47. Bishop, K.N.; Verma, M.; Kim, E.Y.; Wolinsky, S.M.; Malim, M.H. APOBEC3G inhibits elongation of HIV-1 reverse transcripts. *PLoS Pathog.* **2008**, *4*, e1000231.
48. Ono, A. HIV-1 assembly at the plasma membrane: Gag trafficking and localization. *Future Virol.* **2009**, *4*, 241–257.
49. Wilk, T.; Gowen, B.; Fuller, S.D. Actin associates with the nucleocapsid domain of the human immunodeficiency virus gag polyprotein. *J. Virol.* **1999**, *73*, 1931–1940.
50. Liu, B.; Dai, R.; Tian, C.J.; Dawson, L.; Gorelick, R.; Yu, X.F. Interaction of the human immunodeficiency virus type 1 nucleocapsid with actin. *J. Virol.* **1999**, *73*, 2901–2908.
51. Ott, D.E.; Coren, L.V.; Kane, B.P.; Busch, L.K.; Johnson, D.G.; Sowder, R.C., 2nd; Chertova, E.N.; Arthur, L.O.; Henderson, L.E. Cytoskeletal proteins inside human immunodeficiency virus type 1 virions. *J. Virol.* **1996**, *70*, 7734–7743.

52. Ott, D.E.; Coren, L.V.; Johnson, D.G.; Kane, B.P.; Sowder, R.C., 2nd; Kim, Y.D.; Fisher, R.J.; Zhou, X.Z.; Lu, K.P.; Henderson, L.E. Actin-binding cellular proteins inside human immunodeficiency virus type 1. *Virology* **2000**, *266*, 42–51.
53. Sasaki, H.; Nakamura, M.; Ohno, T.; Matsuda, Y.; Yuda, Y.; Nonomura, Y. Myosin-actin interaction plays an important role in human immunodeficiency virus type 1 release from host cells. *Proc. Natl. Acad. Sci. U. S. A.* **1995**, *92*, 2026–2030.
54. Gladnikoff, M.; Shimoni, E.; Gov, N.S.; Rousso, I. Retroviral assembly and budding occur through an actin-driven mechanism. *Biophys. J.* **2009**, *97*, 2419–2428.
55. Jolly, C.; Mitar, I.; Sattentau, Q.J. Requirement for an intact T-cell actin and tubulin cytoskeleton for efficient assembly and spread of human immunodeficiency virus type 1. *J. Virol.* **2007**, *81*, 5547–5560.
56. Jouvenet, N.; Neil, S.J.; Bess, C.; Johnson, M.C.; Virgen, C.A.; Simon, S.M.; Bieniasz, P.D. Plasma membrane is the site of productive HIV-1 particle assembly. *PLoS Biol.* **2006**, *4*, e435.
57. Chen, P.; Hubner, W.; Spinelli, M.A.; Chen, B.K. Predominant mode of human immunodeficiency virus transfer between t cells is mediated by sustained Env-dependent neutralization-resistant virological synapses. *J. Virol.* **2007**, *81*, 12582–12595.
58. Pearce-Pratt, R.; Malamud, D.; Phillips, D.M. Role of the cytoskeleton in cell-to-cell transmission of human immunodeficiency virus. *J. Virol.* **1994**, *68*, 2898–2905.
59. Perotti, M.E.; Tan, X.; Phillips, D.M. Directional budding of human immunodeficiency virus from monocytes. *J. Virol.* **1996**, *70*, 5916–5921.
60. Jolly, C.; Sattentau, Q.J. Human immunodeficiency virus type 1 virological synapse formation in T cells requires lipid raft integrity. *J. Virol.* **2005**, *79*, 12088–12094.
61. Jolly, C.; Sattentau, Q.J. Human immunodeficiency virus type 1 assembly, budding, and cell-cell spread in T cells take place in tetraspanin-enriched plasma membrane domains. *J. Virol.* **2007**, *81*, 7873–7884.
62. Llewellyn, G.N.; Hogue, I.B.; Grover, J.R.; Ono, A. Nucleocapsid promotes localization of HIV-1 Gag to uropods that participate in virological synapses between T cells. *PLoS Pathog.* **2010**, *6*, e1001167.
63. Garcia, E.; Nikolic, D.S.; Piguet, V. HIV-1 replication in dendritic cells occurs through a tetraspanin-containing compartment enriched in AP-3. *Traffic* **2008**, *9*, 200–214.
64. Deneka, M.; Pelchen-Matthews, A.; Byland, R.; Ruiz-Mateos, E.; Marsh, M. In macrophages, HIV-1 assembles into an intracellular plasma membrane domain containing the tetraspanins CD81, CD9, and CD53. *J. Cell Biol.* **2007**, *177*, 329–341.
65. Welsch, S.; Keppler, O.T.; Habermann, A.; Allespach, I.; Krijnse-Locker, J.; Krausslich, H.G. HIV-1 buds predominantly at the plasma membrane of primary human macrophages. *PLoS Pathog.* **2007**, *3*, e36.
66. Bennett, A.E.; Narayan, K.; Shi, D.; Hartnell, L.M.; Gousset, K.; He, H.; Lowekamp, B.C.; Yoo, T.S.; Bliss, D.; Freed, E.O.; *et al.* Ion-abrasion scanning electron microscopy reveals surface-connected tubular conduits in HIV-infected macrophages. *PLoS Pathog.* **2009**, *5*, e1000591.
67. Turville, S.G.; Aravantinou, M.; Stossel, H.; Romani, N.; Robbiani, M. Resolution of de novo HIV production and trafficking in immature dendritic cells. *Nat. Methods* **2008**, *5*, 75–85.

68. Nikolic, D.S.; Piguet, V. Vaccines and microbicides preventing HIV-1, HSV-2, and HPV mucosal transmission. *J. Invest. Dermatol.* **2009**, *130*, 352–361.
69. Hladik, F.; McElrath, M.J. Setting the stage: Host invasion by HIV. *Nat. Rev. Immunol.* **2008**, *8*, 447–457.
70. Piguet, V.; Steinman, R.M. The interaction of hiv with dendritic cells: Outcomes and pathways. *Trends Immunol.* **2007**, *28*, 503–510.
71. Hladik, F.; Sakchalathorn, P.; Ballweber, L.; Lentz, G.; Fialkow, M.; Eschenbach, D.; McElrath, M.J. Initial events in establishing vaginal entry and infection by human immunodeficiency virus type-1. *Immunity* **2007**, *26*, 257–270.
72. Pope, M.; Betjes, M.G.; Romani, N.; Hirmand, H.; Cameron, P.U.; Hoffman, L.; Gezelter, S.; Schuler, G.; Steinman, R.M. Conjugates of dendritic cells and memory T lymphocytes from skin facilitate productive infection with HIV-1. *Cell* **1994**, *78*, 389–398.
73. Turville, S.G.; Santos, J.J.; Frank, I.; Cameron, P.U.; Wilkinson, J.; Miranda-Saksena, M.; Dable, J.; Stossel, H.; Romani, N.; Piatak, M., Jr.; *et al.* Immunodeficiency virus uptake, turnover, and 2-phase transfer in human dendritic cells. *Blood* **2004**, *103*, 2170–2179.
74. Sourisseau, M.; Sol-Foulon, N.; Porrot, F.; Blanchet, F.; Schwartz, O. Inefficient human immunodeficiency virus replication in mobile lymphocytes. *J. Virol.* **2007**, *81*, 1000–1012.
75. Martin, N.; Welsch, S.; Jolly, C.; Briggs, J.A.; Vaux, D.; Sattentau, Q.J. Virological synapse-mediated spread of human immunodeficiency virus type 1 between T cells is sensitive to entry inhibition. *J. Virol.* **2010**, *84*, 3516–3527.
76. McDonald, D.; Wu, L.; Bohks, S.M.; KewalRamani, V.N.; Unutmaz, D.; Hope, T.J. Recruitment of HIV and its receptors to dendritic cell-T cell junctions. *Science* **2003**, *300*, 1295–1297.
77. Groot, F.; Welsch, S.; Sattentau, Q.J. Efficient HIV-1 transmission from macrophages to T cells across transient virological synapses. *Blood* **2008**, *111*, 4660–4663.
78. Vasiliver-Shamis, G.; Dustin, M.L.; Hioe, C.E. HIV-1 virological synapse is not simply a copycat of the immunological synapse. *Viruses* **2010**, *2*, 1239–1260.
79. Burkhardt, J.K.; Carrizosa, E.; Shaffer, M.H. The actin cytoskeleton in t cell activation. *Ann. Rev. Immunol.* **2008**, *26*, 233–259.
80. Rudnicka, D.; Feldmann, J.; Porrot, F.; Wietgrefe, S.; Guadagnini, S.; Prevost, M.C.; Estaquier, J.; Haase, A.T.; Sol-Foulon, N.; Schwartz, O. Simultaneous cell-to-cell transmission of human immunodeficiency virus to multiple targets through polysynapses. *J. Virol.* **2009**, *83*, 6234–6246.
81. Jolly, C.; Mitar, I.; Sattentau, Q.J. Adhesion molecule interactions facilitate human immunodeficiency virus type 1-induced virological synapse formation between T cells. *J. Virol.* **2007**, *81*, 13916–13921.
82. Vasiliver-Shamis, G.; Cho, M.W.; Hioe, C.E.; Dustin, M.L. Human immunodeficiency virus type 1 envelope Gp120-induced partial T-cell receptor signaling creates an F-actin-depleted zone in the virological synapse. *J. Virol.* **2009**, *83*, 11341–11355.
83. Vasiliver-Shamis, G.; Tuen, M.; Wu, T.W.; Starr, T.; Cameron, T.O.; Thomson, R.; Kaur, G.; Liu, J.; Visciano, M.L.; Li, H.; *et al.* Human immunodeficiency virus type 1 envelope gp120 induces a stop signal and virological synapse formation in noninfected CD4+T cells. *J. Virol.* **2008**, *82*, 9445–9457.

84. Jouvenet, N.; Bieniasz, P.D.; Simon, S.M. Imaging the biogenesis of individual HIV-1 virions in live cells. *Nature* **2008**, *454*, 236–240.
85. Kanchanawong, P.; Shtengel, G.; Pasapera, A.M.; Ramko, E.B.; Davidson, M.W.; Hess, H.F.; Waterman, C.M. Nanoscale architecture of integrin-based cell adhesions. *Nature* **2010**, *468*, 580–584.
86. Sol-Foulon, N.; Sourisseau, M.; Porrot, F.; Thoulouze, M.I.; Trouillet, C.; Nobile, C.; Blanchet, F.; di Bartolo, V.; Noraz, N.; Taylor, N.; *et al.* Zap-70 kinase regulates HIV cell-to-cell spread and virological synapse formation. *EMBO J.* **2007**, *26*, 516–526.
87. Jolly, C.; Sattentau, Q.J. Regulated secretion from CD4+ T cells. *Trends Immunol.* **2007**, *28*, 474–481.
88. Jin, J.; Sherer, N.M.; Heidecker, G.; Derse, D.; Mothes, W. Assembly of the murine leukemia virus is directed towards sites of cell-cell contact. *PLoS Biol.* **2009**, *7*, e1000163.
89. Mothes, W.; Sherer, N.M.; Jin, J.; Zhong, P. Virus cell-to-cell transmission. *J. Virol.* **2010**, *84*, 8360–8368.
90. Burckhardt, C.J.; Greber, U.F. Virus movements on the plasma membrane support infection and transmission between cells. *PLoS Pathog.* **2009**, *5*, e1000621.
91. Sherer, N.M.; Lehmann, M.J.; Jimenez-Soto, L.F.; Horensavitz, C.; Pypaert, M.; Mothes, W. Retroviruses can establish filopodial bridges for efficient cell-to-cell transmission. *Nat. Cell Biol.* **2007**, *9*, 310–315.
92. Sowinski, S.; Jolly, C.; Berninghausen, O.; Purbhoo, M.A.; Chauveau, A.; Kohler, K.; Oddos, S.; Eissmann, P.; Brodsky, F.M.; Hopkins, C.; *et al.* Membrane nanotubes physically connect T cells over long distances presenting a novel route for HIV-1 transmission. *Nat. Cell Biol.* **2008**, *10*, 211–219.
93. Eugenin, E.A.; Gaskill, P.J.; Berman, J.W. Tunneling nanotubes (tnt) are induced by HIV-infection of macrophages: A potential mechanism for intercellular HIV trafficking. *Cell. Immunol.* **2009**, *254*, 142–148.
94. Nobile, C.; Rudnicka, D.; Hasan, M.; Aulner, N.; Porrot, F.; Machu, C.; Renaud, O.; Prevost, M.C.; Hivroz, C.; Schwartz, O.; *et al.* HIV-1 Nef inhibits ruffles, induces filopodia and modulates migration of infected lymphocytes. *J. Virol.* **2009**, *84*, 2282–2293.
95. Stolp, B.; Reichman-Fried, M.; Abraham, L.; Pan, X.; Giese, S.I.; Hannemann, S.; Goulimari, P.; Raz, E.; Grosse, R.; Fackler, O.T. HIV-1 Nef interferes with host cell motility by deregulation of cofilin. *Cell Host Microbe* **2009**, *6*, 174–186.
96. B.Stolp; O.Fackler. How HIV takes advantage of the cytoskeleton in entry and replication. *Viruses* **2011**, *3*, 293–311.
97. Haller, C.; Tibroni, N.; Rudolph, J.M.; Grosse, R.; Fackler, O.T. Nef does not inhibit F-actin remodelling and HIV-1 cell-cell transmission at the T lymphocyte virological synapse. *Eur. J. Cell Biol.* **2010**, doi:10.1016/j.ejcb.2010.09.010.
98. Xu, W.; Santini, P.A.; Sullivan, J.S.; He, B.; Shan, M.; Ball, S.C.; Dyer, W.B.; Ketas, T.J.; Chadburn, A.; Cohen-Gould, L.; *et al.* HIV-1 evades virus-specific IgG2 and IgA responses by targeting systemic and intestinal B cells via long-range intercellular conduits. *Nat. Immunol.* **2009**, *10*, 1008–1017.
99. McDonald, D. Dendritic cells and HIV-1 trans-infection. *Viruses* **2010**, *2*, 1704–1717.

100. Granelli-Piperno, A.; Golebiowska, A.; Trumpfheller, C.; Siegal, F.P.; Steinman, R.M. HIV-1-infected monocyte-derived dendritic cells do not undergo maturation but can elicit IL-10 production and t cell regulation. *Proc. Natl. Acad. Sci. U. S. A.* **2004**, *101*, 7669–7674.
101. Harman, A.N.; Wilkinson, J.; Bye, C.R.; Bosnjak, L.; Stern, J.L.; Nicholle, M.; Lai, J.; Cunningham, A.L. HIV induces maturation of monocyte-derived dendritic cells and langerhans cells. *J. Immunol.* **2006**, *177*, 7103–7113.
102. Manel, N.; Hogstad, B.; Wang, Y.; Levy, D.E.; Unutmaz, D.; Littman, D.R. A cryptic sensor for HIV-1 activates antiviral innate immunity in dendritic cells. *Nature* **2010**, *467*, 214–217.
103. Geijtenbeek, T.B.; Kwon, D.S.; Torensma, R.; van Vliet, S.J.; van Duijnhoven, G.C.; Middel, J.; Cornelissen, I.L.; Nottet, H.S.; KewalRamani, V.N.; Littman, D.R.; *et al.* DC-SIGN, a dendritic cell-specific HIV-1-binding protein that enhances trans-infection of T cells. *Cell* **2000**, *100*, 587–597.
104. Felts, R.L.; Narayan, K.; Estes, J.D.; Shi, D.; Trubey, C.M.; Fu, J.; Hartnell, L.M.; Ruthel, G.T.; Schneider, D.K.; Nagashima, K.; *et al.* 3D visualization of HIV transfer at the virological synapse between dendritic cells and T cells. *Proc. Natl. Acad. Sci. U. S. A.* **2010**, *107*, 13336–13341.
105. Cavrois, M.; Neidleman, J.; Kreisberg, J.F.; Greene, W.C. *In vitro* derived dendritic cells trans-infect CD4 T cells primarily with surface-bound HIV-1 virions. *PLoS Pathog.* **2007**, *3*, e4.
106. Gousset, K.; Ablan, S.D.; Coren, L.V.; Ono, A.; Soheilian, F.; Nagashima, K.; Ott, D.E.; Freed, E.O. Real-time visualization of HIV-1 gag trafficking in infected macrophages. *PLoS Pathog.* **2008**, *4*, e1000015.
107. Nikolic, D.S.; Lehmann, M.; Felts, R.; Garcia, E.; Blanchet, F.P.; Subramaniam, S.; Piguet, V. HIV-1 activates Cdc42 and induces membrane extensions in immature dendritic cells to facilitate cell-to-cell virus propagation. *Blood* **2011**, doi:10.1182/blood-2010-09-305417.
108. Arrighi, J.F.; Pion, M.; Garcia, E.; Escola, J.M.; van Kooyk, Y.; Geijtenbeek, T.B.; Piguet, V. DC-SIGN-mediated infectious synapse formation enhances X4 HIV-1 transmission from dendritic cells to T cells. *J. Exp. Med.* **2004**, *200*, 1279–1288.
109. Caparros, E.; Munoz, P.; Sierra-Filardi, E.; Serrano-Gomez, D.; Puig-Kroger, A.; Rodriguez-Fernandez, J.L.; Mellado, M.; Sancho, J.; Zubiaur, M.; Corbi, A.L. DC-SIGN ligation on dendritic cells results in ERK and PI3K activation and modulates cytokine production. *Blood* **2006**, *107*, 3950–3958.
110. Hodges, A.; Sharrocks, K.; Edelmann, M.; Baban, D.; Moris, A.; Schwartz, O.; Drakesmith, H.; Davies, K.; Kessler, B.; McMichael, A.; *et al.* Activation of the lectin DC-SIGN induces an immature dendritic cell phenotype triggering Rho-GTPasease activity required for HIV-1 replication. *Nat. Immunol.* **2007**, *8*, 569–577.

## Paper 3: The inability to disrupt the immunological synapse between infected human T cells and APCs distinguishes HIV-1 from most other primate lentiviruses

Pathogenic HIV-1 infections, in contrast to non-pathogenic SIV infections in natural hosts are characterized by high levels of immune activation, accelerated T-cell turnover and apoptosis[15]. Recently SIVcpz infections lead to AIDS-like symptoms in chimpanzees most other natural SIV infections are non-pathogenic or significantly less pathogenic like HIV-2 infections in humans[25]. Host factors and accessory viral proteins, notably Nef, influence the different outcomes of HIV and SIV infections[27].

All primate lentiviruses code for Nef proteins that increase viral infectivity, viral loads and accelerates disease progression in humans[222]. Nef reduces surface levels of cellular receptors CD4, MHC-I and less potently CD28 to protect infected cells from superinfection and cytotoxic T-cell mediated killing. HIV-1 Nef increases the responsiveness of infected T-cells to TCR-mediated activation that favors proviral transcription. HIV-1 Nef interferes with various signaling pathways and increasing transcription of cytokines and activation markers.

Additionally Nefs from SIVs and HIV-2 downmodulate CD3 and were shown to prevent T-cell activation, apoptosis and $CD4^+$ T-cell loss in-vivo[223, 224]. In contrast HIV-1, SIVcpz and some closely related Cercopithecus viruses selectively lost this Nef function, but code for a vpu gene for unknown reasons[27].

CD3 is the key component of T-cell receptor (TCR) that interacts with APC's peptide-loaded MHC-II molecules within immunological synapses during T-cell priming. CD3 -MHC interactions are also required during effector T-cell and natural killer cell functions.

In general, immunological synapses (IS) are transient cellular contacts. The IS is highly structured into different supramolecular activation clusters (SMACs). The central cluster contains TCR-MHC-I signaling complexes and is stabilized by adhesion molecules (e.g. LFA-1), talin and cortical actin cytoskeleton forming a ring-like peripheral SMAC[225].

Since primate Nef proteins differentially affect T-cell activation and pathogenesis we wanted to investigate their effects on IS formation and early TCR- signaling.

We found that Nef alleles from HIV-2, SIVmac and SIVblu that downmodulate CD3 prevented infected primary T-cells from forming conjugates with super antigen-pulsed APCs that are macrophages and DC. Importantly typical IS marker CD3, Lck, CD43 and Talin were mostly absent from remaining T-cell-APC conjugates formed by T-cells expressing the Nef alleles that downmodulate CD3. In these cells Nef-dependent defect in IS formation was paralleled by perturbation in early and late TCR signaling as assessed by ZAP-70 kinase phosphorylation and IL2 production, respectively. In contrast, different Nef alleles from HIV-1 and SIVcpz did not affect IS formation and TCR signaling. Notably Nef mutant that are impaired in CD3 downmodulation shows phenotypes similar to HIV-1 confirming the importance of CD3 downmodulation in IS disruption. Therefore, the inability to disrupt the immunological synapse between infected human T cells and APCs distinguishes HIV-1 from most other primate lentiviruses.

As contributions to this work I isolated and infected primary $CD4^+$ T-cells with HIV-1 constructs that contained different HIV and SIV nef alleles. I determined how different Nef alleles interfered with the formation of immunological synapses of infected T-cells with autologous dendritic cells. The presence of various immunological synapse markers (CD3, Lck, Talin and LFA-1) was quantitatively analyzed by high-resolution confocal laser scanning microscopy (Figure 2-4, Supplementary Figure 5 and Table S2).

# The inability to disrupt the immunological synapse between infected human T cells and APCs distinguishes HIV-1 from most other primate lentiviruses

Nathalie Arhel,[1] Martin Lehmann,[2] Karen Clauß,[3] G. Ulrich Nienhaus,[3,4] Vincent Piguet,[2] and Frank Kirchhoff[1]

[1]Institute of Molecular Virology, University of Ulm, Ulm, Germany. [2]Department of Dermatology and Venereology and Department of Microbiology and Molecular Medicine, Geneva University Hospitals and University of Geneva, Geneva, Switzerland. [3]Institute of Biophysics, University of Ulm, Ulm, Germany. [4]Institute of Applied Physics and Center for Functional Nanostructures, University of Karlsruhe, Karlsruhe, Germany.

**Viruses that infect T cells, including those of the lentivirus genus, such as HIV-1, modulate the responsiveness of infected T cells to stimulation by interacting APCs in a manner that renders the T cells more permissive for viral replication. HIV-1 and other primate lentiviruses use their Nef proteins to manipulate the T cell/APC contact zone, the immunological synapse (IS). It is known that primate lentiviral Nef proteins differ substantially in their ability to modulate cell surface expression of the TCR-CD3 and CD28 receptors critical for the formation and function of the IS. However, the impact of these differences in Nef function on the interaction and communication between virally infected T cells and primary APCs has not been investigated. Here we have used primary human cells to show that Nef proteins encoded by HIV-2 and most SIVs, which downmodulate cell surface expression of TCR-CD3, disrupt formation of the IS between infected T cells and Ag-presenting macrophages or DCs. In contrast, *nef* alleles from HIV-1 and its simian precursor SIVcpz failed to suppress synapse formation and events downstream of TCR signaling. Our data suggest that most primate lentiviruses disrupt communication between virally infected CD4$^+$ Th cells and APCs, whereas HIV-1 and its SIV precursor have largely lost this capability. The resulting differences in the levels of T cell activation and apoptosis may play a role in the pathogenesis of AIDS.**

## Introduction

The interaction and communication of T cells and APCs via a contact zone known as immunological synapse (IS) is a key event of the adaptive immune response (1, 2). Synapse formation is a highly ordered process initiated by the binding of the TCR-CD3 complex on T cells to the peptide-MHC complex on the surface of APCs, such as DCs or macrophages (3). This interaction leads to the local clustering of various surface receptors, adhesion molecules, signaling factors, and cytoskeleton components into a well-organized supramolecular spatial structure. Besides TCR-CD3/peptide-MHC binding, a functional activating IS also requires the interaction between costimulatory molecules, such as CD28 on CD4$^+$ T cells and CD80 or CD86 on professional APCs (3, 4). The CD4 molecule on T cells, which is the primary receptor for HIV/SIV entry, is involved in the clustering process and may boost recognition of the MHC-peptide ligand by the TCR (5, 6). Deregulation of T cell/APC communication leads to immunological malfunctions, such as autoimmunity or tolerance (7).

Given that the IS is crucial for the initiation and regulation of adaptive immune responses, it is not surprising that various viruses manipulate it to suppress specific antiviral immune responses and hence to facilitate viral immune evasion (8–11). Lymphotropic viruses also modulate the responsiveness of virally infected T cells to stimulation by interacting APCs in a manner that renders them more permissive for viral replication (12–14). HIV-1 and other primate lentiviruses manipulate the function of the IS and T cell activation mainly by means of the accessory multifunctional Nef protein, which also impairs MHC Ag presentation and enhances viral infectivity and replication (14–16). Most importantly, Nef is required for efficient viral replication in vivo and greatly accelerates disease progression in HIV-1–infected individuals (17, 18). The HIV-1 Nef protein perturbs the interaction of virally infected T cells with APCs by downmodulating CD4 and (weakly) CD28 from the cell surface (19–21) and was reported to alter TCR trafficking and signaling, as well as the actin rearrangements induced by TCR triggering (11). It has been suggested that these Nef effects could be advantageous for HIV-1 because they reduce TCR-mediated T cell activation to levels sufficient for effective viral replication, but low enough to prevent exaggerated activation and premature activation–induced death of HIV-1–infected T cells (13, 14). Contrary to this suggestion, however, other studies have shown that Nef substantially enhances the responsiveness of T cells to stimulation and proposed that the hyperactivated phenotype of HIV-1–infected T cells may contribute to the high levels of chronic immune activation and apoptosis that are associated with progression to AIDS (22–26).

While it remains debatable whether HIV-1 Nefs reduce or enhance the responsiveness of virally infected T cells to stimulation, it is clear that the effects of most primate lentiviral Nef proteins on TCR signaling and potentially also on the formation of the IS are much more severe than those of HIV-1 Nef proteins, because they

**Authorship note:** Martin Lehmann and Karen Clauß contributed equally to this work.

**Conflict of interest:** The authors have declared that no conflict of interest exists.

**Citation for this article:** *J. Clin. Invest.* doi:10.1172/JCI38994.

also downmodulate TCR-CD3 and are substantially more effective in removing CD28 from the cell surface (20, 21, 27–30). Notably, the ability of Nef to downmodulate TCR-CD3 was specifically lost in the primate lentiviral lineage that gave rise to HIV-1: SIVcpz, its direct precursor from chimpanzees and some closely related SIVs from *Cercopithecus* monkeys (30). HIV-2 or SIV *nef* alleles that downmodulate CD3 block the responsiveness of virally infected primary T cells to TCR-mediated activation, whereas those of HIV-1 and its simian precursors fail to suppress T cell activation and programmed cell death (30). Besides host factors, these differences in Nef function may explain why high levels of chronic immune activation, associated with accelerated T cell turnover rates and apoptosis, are a hallmark of pathogenic HIV-1 infection but are absent in natural nonpathogenic SIV infections (15, 31).

The differential effects of HIV-1 and other primate lentiviruses on TCR-mediated stimulation of virally infected T cells by APCs may play an important role in the infection-associated levels of immune activation that drive the exhaustion of the immune system. Despite the possible importance of these processes in the pathogenesis of AIDS, however, the influence of various primate lentiviral Nef proteins on the formation and function of the IS between primary virally infected T cells and professional APCs has not been investigated. In the present study, we examined the effect of *nef* alleles from HIV-1 and other primate lentiviruses on the interaction of primary virally infected T lymphocytes with DCs — which are professional APCs and especially potent activators of $CD4^+$ helper T cells — and macrophages. We found that HIV-2 and SIV Nefs that downmodulate TCR-CD3 disrupted the formation of T cell/APC conjugates. The few interactions observed did not represent a functional IS. In contrast, Nef proteins of HIV-1 and its simian counterpart, SIVcpz, neither significantly reduced the capacity of virally infected T lymphocytes to form an IS nor prevented T cell activation by APCs. These differences in the ability of Nef to modulate the formation of the IS and TCR signaling may have important consequences for the antiviral immune response and the pathogenic outcome of primate lentiviral infections.

## Results

*Nef alleles from HIV-2 and SIVmac — but not those of HIV-1 and SIVcpz — prevent the formation of conjugates between virally infected T cells and APCs.* Our previous analysis of a large number of primate lentiviral Nefs showed that they can be divided into those that are unable and those that are able to downmodulate TCR-CD3 (groups 1 and 2, respectively; ref. 30). To examine possible differences in their effect on the IS, we selected 3 representative *nef* alleles from each group (see Supplemental Table 1; supplemental material available online with this article; doi:10.1172/JCI38994DS1). The alleles of group 1 were the HIV-1 NA7 *nef* allele, derived from an AIDS patient (32), the *nef* gene of the NL4-3 molecular clone, and the SIVcpz GAB2 *nef*, obtained from a wild-captured chimpanzee of the *Pan troglodytes troglodytes* subspecies in Gabon (33). The group 2 *nef*s were derived from HIV-2 BEN, the SIVmac239 molecular clone, and SIVblu from a Blue monkey (*Cercopithecus mitis*). All 6 *nef* alleles have been characterized in previous studies (29, 30, 34, 35) and were chosen because they are functionally active and represent the 2 human AIDS viruses (HIV-1 and HIV-2), their simian counterparts (SIVcpz and SIVmac), and a naturally SIV-infected small monkey species (SIVblu). The SIVmac239 and SIVblu Nefs were also selected because of the availability of specific mutants that are selectively active (mac tNef) or defective (SIVblu RR-AA; also referred to as bluRR) in TCR-CD3 modulation (30, 36).

To examine the effect on the IS, we cocultivated primary PBLs infected with proviral HIV-1 constructs coexpressing eGFP and Nef from bicistronic RNAs (30, 34) with autologous monocyte-derived macrophages (MDMs) or DCs pulsed with the superantigen (sAg) SEE and labeled with the aliphatic red dye PKH26. Notably, the proviral HIV-1 constructs differ only in their *nef* coding region and coexpress Nef and eGFP at correlating levels (30, 34). We used replication-competent VSV-G–pseudotyped viruses for infection because this allowed us to bypass the effect of Nef on virion infectivity (37) and excluded the possibility that lack of Env expression may bias the results. Prior to all interaction studies, we verified that comparably high numbers of cells were infected by all HIV-1 constructs (example shown in Supplemental Figure 1). The differential capability of the HIV-1 and SIV *nef* alleles to downmodulate TCR-CD3 was verified for virally infected $CD4^+$ T cells (Supplemental Table 2) as well as PBLs, and the phenotype of the DC and MDM preparations was verified by flow cytometric analysis (example shown in Supplemental Figure 2).

First, we assessed the proportion of HIV-1–infected ($eGFP^+$) PBLs contacting APCs by standard fluorescence microscopy (Figure 1A). Examination of $eGFP^+$ PBLs from randomly selected areas of the cocultures demonstrated that the HIV-1 NA7 *nef* allele (33) did not significantly reduce the frequency of contacts with Ag-presenting MDMs or DCs compared with the *nef*-defective control (Figure 1A). In both cases, the number of T cell/APC conjugates was similar to that observed between noninfected CFSE-labeled PBLs and autologous SEE-pulsed APCs (data not shown). Similar results were obtained with the NL4-3 and GAB2 Nefs (Figure 1A). In contrast, expression of the SIVmac239, SIVblu, and HIV-2 BEN Nefs reduced the number of conjugates between virally infected lymphocytes and APCs about 4-fold (Figure 1A), down to the background levels obtained with medium-pulsed APCs (data not shown). To verify this finding, we also determined the frequency of HIV-1–infected PBLs engaged in contacts with APCs by flow cytometry for cells in the MDM and DC gate that were positive for both eGFP and PKH26 (Figure 1B). In agreement with the results of the microscopic examination, HIV-2 and SIVmac Nefs, but not HIV-1 and SIVcpz Nefs, significantly impaired the capability of virally infected T cells to interact with APCs (Figure 1B). These data demonstrated that, in strict contrast to group 1 Nefs, those of group 2 viruses did not disrupt the formation of conjugates between primary T cells and APCs (summarized in Supplemental Table 2).

*Nef-mediated downmodulation of TCR-CD3 plays a key role in the disruption of the IS.* To assess a possible causal relationship between Nef-mediated TCR-CD3 downmodulation and the disruption of the IS, we used previously described mutant Nefs that are selectively active or disrupted in this function (Supplemental Table 1 and ref. 30). Microscopic examination and flow cytometric analysis showed that a truncated form of the SIVmac239 *nef* gene, tNef, which downmodulates TCR-CD3 but is otherwise defective (30, 36), was still capable of reducing the number of contacts between virally infected lymphocytes and Ag-presenting MDMs and DCs (Figure 1). Conversely, 2 point mutations of RR/AA in the SIVblu Nef that specifically abrogate downmodulation of TCR-CD3 also reduced its ability to prevent the interaction between HIV-1–infected PBLs and Ag-presenting MDMs or DCs (Figure 1). However, the potency

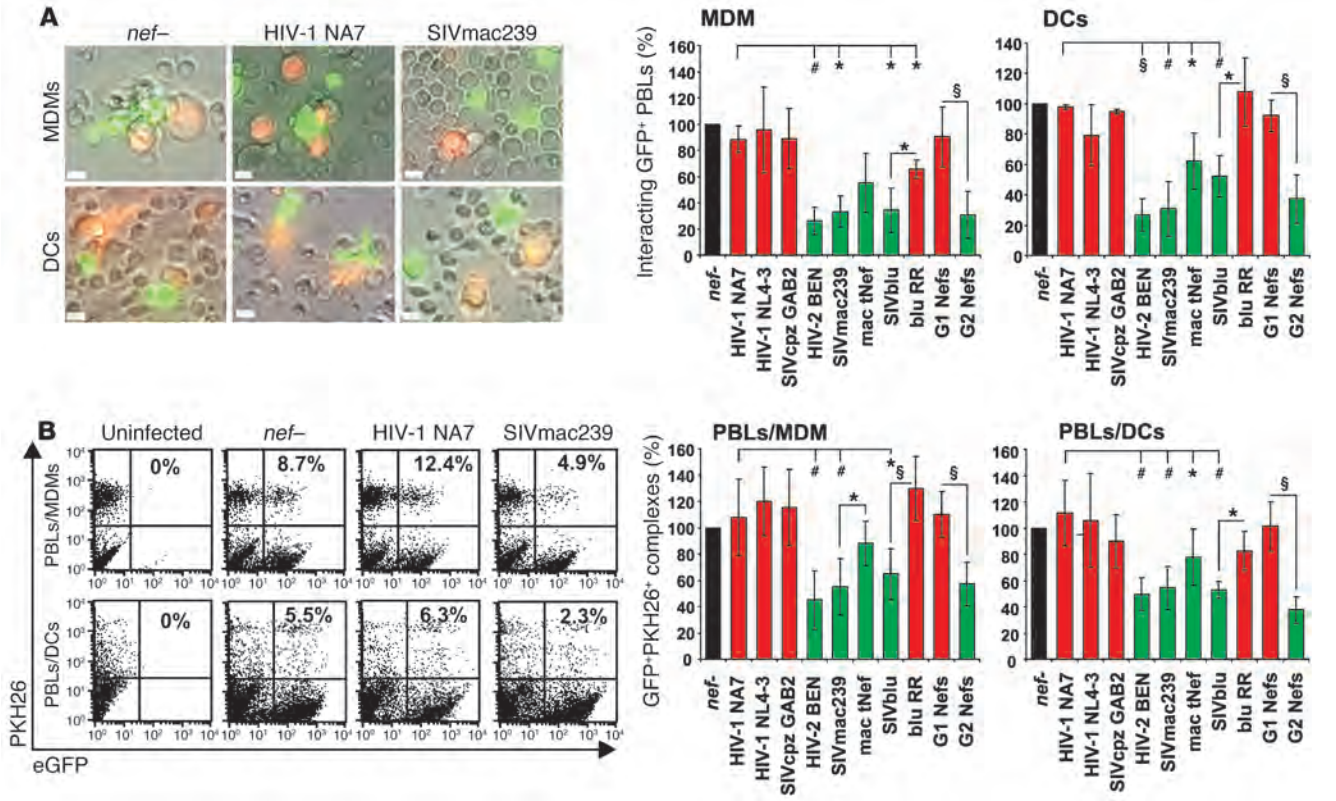


**Figure 1**

*Nef* alleles that downmodulate TCR-CD3 impair the ability of virally infected primary T cells to form complexes with APCs. (**A** and **B**) PBLs were infected with NL4-3–IRES–eGFP viruses encoding different Nefs, and complex formation with autologous SEE-pulsed DCs and MDMs was assessed 4 days after infection by fluorescence microscopy (**A**) and flow cytometry (**B**). (**A**) Representative acquisition frames of cocultures between infected PBLs and MDMs or DCs, with phase-contrast (Nomarski), eGFP, and PKH26 superimposed. Scale bars: 10 μm. The proportion of infected (eGFP$^+$) cells contacting labeled autologous MDMs or DCs was scored randomly by single-blind method with $n = 60$ per sample per experiment. Results are mean ± SD of 4–5 independent experiments. In all experiments, 25%–55% of PBLs infected with the *nef*-defective control HIV-1 construct (*nef*–) formed complexes with autologous APCs; *nef*– values are set as 100%. (**B**) Representative flow cytometry acquisitions for complex formation between infected PBLs and MDMs or DCs. Percentages denote the number of eGFP$^+$ cells in the DC gating that are PKH26$^+$ (as a percentage of all eGFP$^+$ cells). Graphs show mean ± SD of 3 and 4 experiments in DCs and MDMs, respectively. In all experiments, 3%–13% of PBLs infected with *nef*– formed complexes with autologous APCs; *nef*– values are set as 100%. Red and green bars denote *nef* alleles of group 1 and group 2, respectively. Combined results for group 1 (G1) and group 2 (G2) Nefs represent average values ± SD. $^*P < 0.05$; $^\#P < 0.01$; $^\S P < 0.001$.

of the tNef in disrupting the IS was slightly reduced compared with the wild-type SIVmac239 Nef, and the SIVblu RR-AA Nef frequently showed a phenotype intermediate between the HIV-1 and the parental SIVblu Nefs. This observation may be explained by the fact that, in contrast to wild-type mac239 Nef, the truncated tNef did not downmodulate CD28, and that SIVblu RR-AA Nef was more active than HIV-1 NA7 Nef in removing this costimulatory factor from the cell surface (Supplemental Table 1). Although CD28 is not required to initiate the contact between T cells and APCs, its presence at the cell surface may affect the strength and duration of this interaction (3, 4). Correlation analyses showed that all Nefs had similar disruptive effects on the interaction of infected PBLs with MDMs or DCs and verified that microscopic examination and flow cytometric analyses yielded similar results (Supplemental Figure 3). The reduction of conjugate formation between virally infected PBLs and APCs correlated with the efficiency of Nef-mediated downmodulation of TCR-CD3 (Supplemental Figure 4). Together, these data showed that Nef-induced TCR-CD3 downmodulation was required and sufficient to disrupt synapse formation, but further suggested that the effect of Nef on CD28 also affects the functional interaction between virally infected T cells and APCs.

*Only Nef alleles that do not downmodulate TCR-CD3 allow the formation of actual ISs.* The formation of an intact IS is associated with the clustering of surface receptors into focal points of supramolecular interacting signaling platforms, referred to as SMACs (1–4). Some molecules — such as TCR-CD3 and the tyrosine kinase Lck, which becomes transiently activated after TCR engagement — are recruited to the central SMAC, whereas others — like the adhesion factor LFA-1 and the cytoskeletal protein talin — are enriched in the peripheral SMAC. Finally, some factors, such as the large sialoprotein CD43, are actively excluded from a functional IS (38). To assess whether the conjugates between HIV-1–infected PBLs expressing various *nef* alleles and APCs represent real ISs, we labeled cocultures of purified CD4$^+$ T cells infected with various HIV-1 IRES-eGFP *nef* constructs and autologous sAg-pulsed DCs with CD3, Lck, talin, or LFA-1 and examined them by scanning confocal laser microscopy. These analyses confirmed that T cells expressing the HIV-2 BEN,

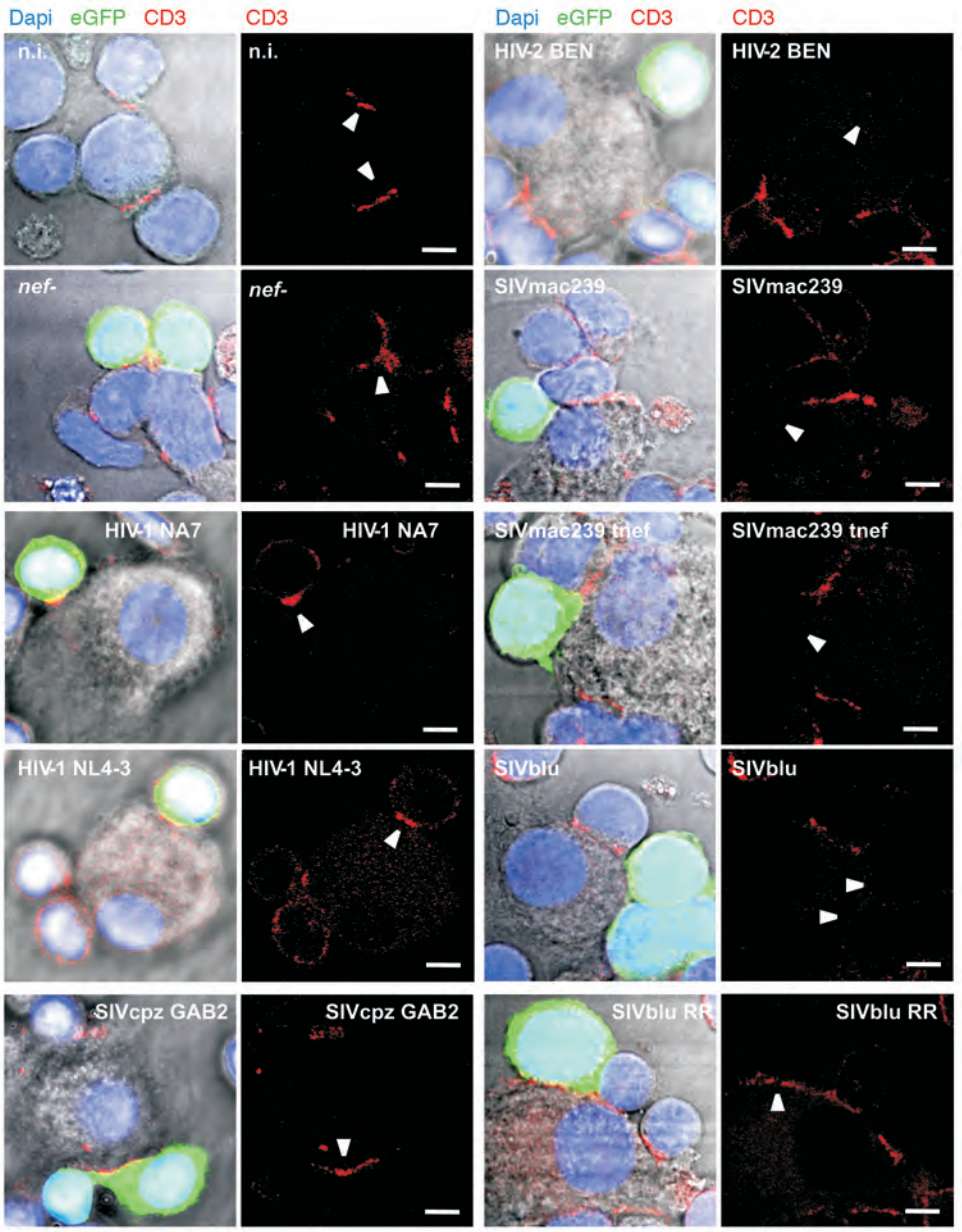


**Figure 2**
Effect of primate lentiviral Nefs on TCR-CD3 cell surface expression and clustering at the IS. Primary $CD4^+$ T cells were not infected (n.i.) or were infected with HIV-1 constructs expressing the indicated *nef* alleles. At 3 days after infection, the T cells were incubated with autologous sAg-pulsed DCs, fixed, and stained with anti-CD3. Images show representative confocal acquisitions from cocultures between infected $CD4^+$ T cells and autologous sAg-pulsed DCs labeled with DAPI. Shown are CD3 Ab labeling alone and merged images of eGFP, DAPI, and CD3. Arrowheads point to zones of close contact between infected T cells and DCs. Close contact was rarely observed in T cell/APC cultures infected with viral constructs expressing group 1 Nefs, and these cells did not express CD3 at their surface. Scale bars: 5 μm.

SIVmac239, tNef, and SIVblu Nefs did not express CD3 at the cell surface or at the IS (Figure 2). In comparison, we observed the typical clustering of CD3 at the contact zones between virally infected T cells and APCs for Nefs unable to downmodulate TCR-CD3 (Figure 2). Furthermore, only PBLs expressing HIV-1 or SIVcpz *nef* alleles showed normal frequencies of Lck polarization at the zone of contact with APCs (Figure 3). Thus, the group 2 Nefs affected the targeting of Lck to the IS much more severely than did those of group 1, although we noted that cells infected with virus constructs expressing HIV-1 or SIVcpz Nefs showed a moderate decrease of Lck at the IS and higher quantities of Lck in intracellular compartments than uninfected cells (Figure 3A). Next, we examined the effect of the various Nef alleles on the localization of talin, a large cytoskeletal adaptor protein that is a ubiquitously expressed and thought to be critical for the activation of integrins (39). We found that only *nef* alleles that downmodulate TCR-CD3 prevented the polarization of talin at the zone of contact between virally infected T cells and APCs (Figure 4). The differences in the effect of group 1 and group 2 Nefs on Lck or talin recruitment to the synapse were highly significant (Figure 3B and Figure 4B). Notably, none of the *nef* alleles had a marked impact on the number of T cell/APC conjugates showing polarization of LFA-1 (Supplemental Figure 5). LFA-1 functions as an adhesion molecule by binding to ICAM-1 on APCs (40) and may not be affected because it is involved in mediating the initial contact rather than the formation of a mature IS. Finally, we found that only conjugates between T cells infected with HIV-1 constructs incapable of downmodulating CD3 and autologous DCs showed CD43 exclusion (Figure 5). These analyses showed that HIV-1–infected PBLs expressing *nef* alleles unable to downmodulate TCR-CD3 were generally capable of forming ISs with APCs, as demonstrated by CD3, Lck, and talin polarization to the zone of contract, as well as by CD43 exclusion. In striking

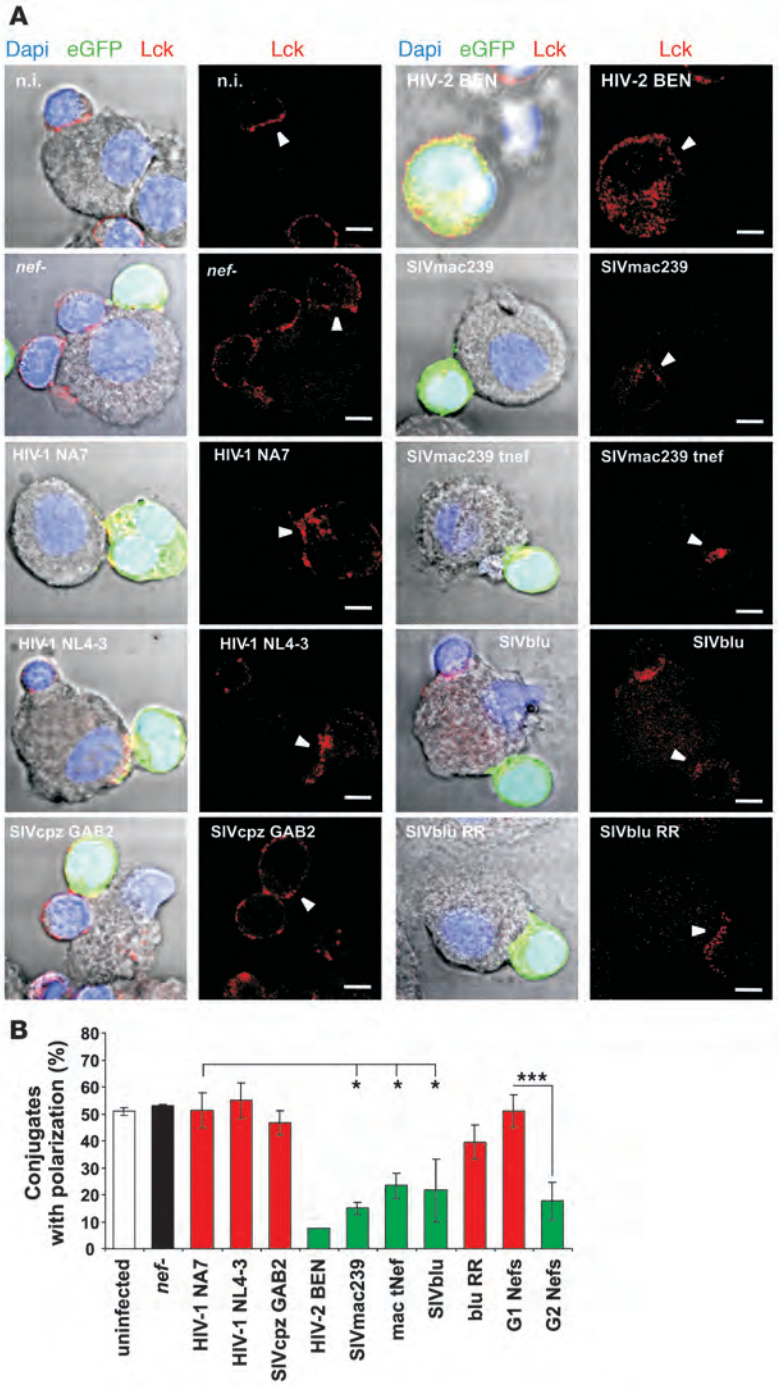


**Figure 3**
Nef-mediated downmodulation of TCR-CD3 prevents Lck polarization at the IS. (**A**) CD4+ T cells infected with HIV-1 constructs expressing the indicated *nef* alleles were incubated with autologous sAg-pulsed DCs, fixed, and stained with anti-Lck. Images show representative confocal acquisitions from cocultures between infected CD4+ T cells and autologous sAg-pulsed DCs labeled with DAPI. Shown are Lck Ab labeling alone and merged images of eGFP, DAPI, and Lck. Arrowheads point to zones of close contact between infected T cells and DCs. Scale bars: 5 μm. (**B**) Number of HIV-1–infected eGFP+ T cells engaged in complex formation with APCs, showing accumulation of Lck at the IS. Results are mean ± SD of 2 independent experiments. $^{*}P < 0.05$; $^{***}P < 0.001$.

contrast, conjugates between T cells infected with viral constructs capable of downmodulating CD3 and autologous DCs did not usually show an accumulation of synapse markers at the site of contact. Thus, even the few T cell/APC conjugates that were detected by microscopy and FACS analysis (Figure 1) did not represent real ISs. Our finding that tNef was sufficient to impair the clustering of Lck and talin or the exclusion of CD43 at the T cell/APC contact zone and that the RR-AA mutation severely reduced the disruptive effect of the SIVblu Nef, as well as correlation analyses (Supplemental Figure 4), support a key role of Nef-mediated downmodulation of CD3 in the disruption of ISs.

*The HIV-1 Nef lost its ability to block early TCR-CD3 signaling events*. It was previously reported that the primary target cells of HIV and SIV infection in vivo are memory CD4+ T cells that are phenotypically resting but represent a recently activated cell population (41, 42). To mimic this phenotype in vitro, we infected PHA-stimulated PBLs with HIV-1 Nef-IRES-eGFP constructs and incubated them in the absence of exogenous stimuli until they expressed low levels of activation markers and eGFP (data not shown). Thereafter, we exposed the cells for 15 minutes to anti-CD3/CD28 beads, which crosslink the TCR with CD28 (43) and hence resemble stimulation by APCs. To assess the ability of virally infected T cells to respond to stimulation, we measured the phosphorylation of the signaling molecule ZAP-70, which occurs within seconds to minutes of T cell/APC interaction and TCR triggering (44). We used an antibody that recognizes ZAP-70 phosphorylated at position Tyr493, previously reported to represent the primary site of TCR-induced tyrosine phosphorylation by Lck (45). Flow cytometric analysis showed that ZAP-70 phosphorylation was prevented by HIV-2, SIVmac, and SIVblu Nef proteins, whereas PBLs infected with viral constructs expressing HIV-1 or SIVcpz Nefs showed levels of ZAP-70 phosphorylation similar to those infected with the *nef*-defective control HIV-1 construct (Figure 6A). The SIVmac tNef and SIVblu RR-AA Nef alleles were usually both poorly active in inhibiting the induction of ZAP-70 phosphorylation. Thus, Nef-mediated downmodulation of both TCR-CD3 and CD28 was required to efficiently disrupt early TCR signaling events, at least upon high-affinity TCR ligation by anti-CD3/CD28 beads. Kinetic analyses showed that Nef alleles that downmodulate CD3 did not exhibit delayed ZAP-70 phosphorylation (Figure 6B). These results support that the group 2 Nefs prevent, not just delay, early TCR-CD3 signaling events.

*Efficient Nef-mediated downmodulation of TCR-CD3 and CD28 suppresses late TCR-CD3 signaling events*. The activating signaling cascades initiated by IS formation ultimately lead to the activation of transcription factors that drive cytokine expression. To test the effect of various Nef alleles on these late signaling events, we cocultivated HIV-1–infected T cells with autologous primary DCs

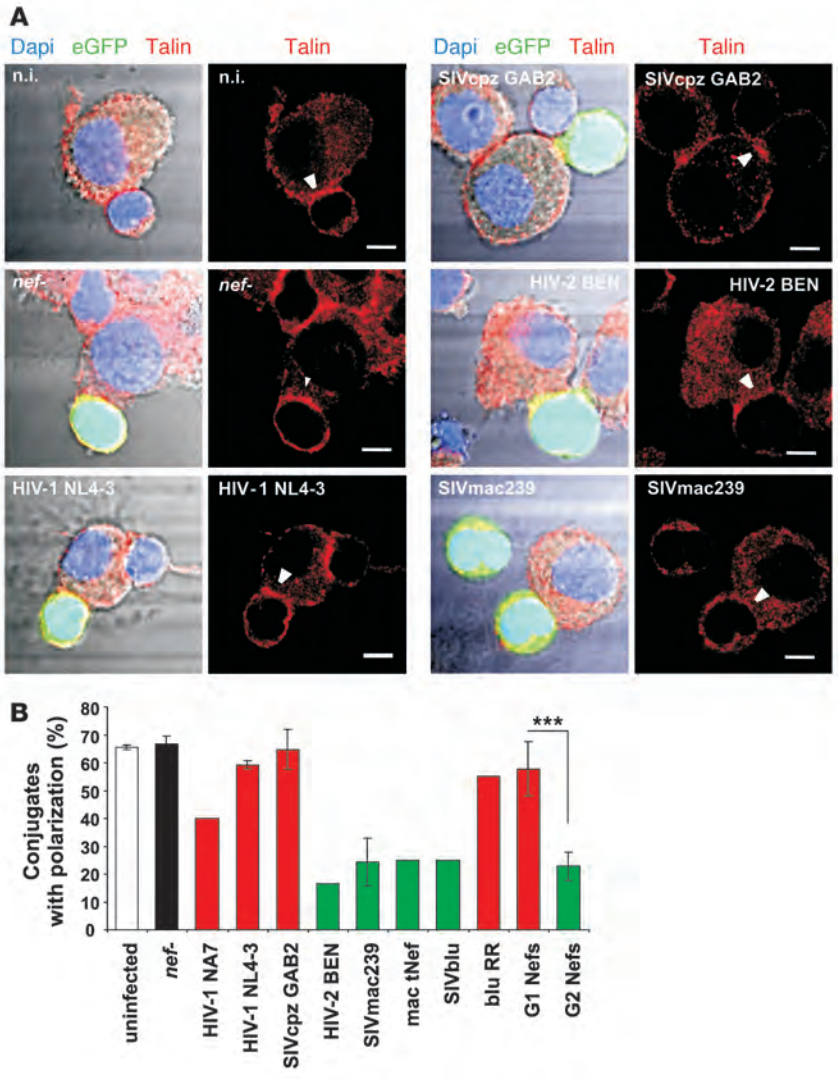


**Figure 4**
*Nef* alleles that downmodulate CD3 inhibit talin clustering at the IS. (**A**) CD4+ T cells infected with HIV-1 constructs expressing the indicated *nef* alleles were incubated with autologous sAg-pulsed DCs, fixed, and stained with anti-talin. Images show representative confocal acquisitions from cocultures between infected CD4+ T cells and autologous sAg-pulsed DCs labeled with DAPI. Shown are talin Ab labeling alone and merged images of eGFP, DAPI, and talin. Arrowheads point to zones of close contact between infected T cells and DCs. Scale bars: 5 μm. (**B**) Number of HIV-1–infected eGFP+ T cells engaged in complex formation with APCs, showing polarization of talin at the zone of contact. Results are mean ± SD of 2 independent experiments (except for NA7, tNef, and SIVblu Nefs, which were derived from a single experiment). ***$P < 0.001$.

or MDMs and measured the frequency of virally infected T cells that subsequently showed increased levels of intracellular IL-2 by flow cytometric analysis. We focused on IL-2 because it is one of the best-characterized cytokines and known to play a crucial role in regulating immune activation and homeostasis (46). We found that HIV-1 and SIVcpz Nef expression resulted in unaltered or slightly increased numbers of IL-2–expressing HIV-1–infected T cells after cocultivation with DCs or MDMs (Figure 7). In contrast, expression of HIV-2 and SIVmac239 Nefs was associated with decreased numbers of IL-2+ virally infected T cells compared with the *nef*-defective control. The difference between group 1 and group 2 Nefs was highly significant in both PBL/DC and PBL/MDM cocultures (Figure 7). Our set of *nef* alleles also allowed us to assess the role of Nef-mediated downmodulation of TCR-CD3 and CD28 in late TCR signaling events. The tNef, which downmodulates CD3 but not CD28 (Supplemental Table 1), suppressed the induction of IL-2 production as efficiently as the parental SIVmac239 Nef (Figure 7). The SIVblu RR-AA Nef, which shows essentially the opposite functional properties because it does not affect CD3 but efficiently removes CD28 from the cell surface, also suppressed IL-2 expression (Figure 7). This was expected, because costimulatory signaling through CD28 is known to play an essential role in TCR-mediated IL-2 production through activation of NF-κB (47, 48). The disruptive effect of the SIVblu RR-AA Nef was particularly pronounced in PBL/DC cocultures, possibly because IS of T lymphocytes with DCs and macrophages differ in their dynamics and signaling intensity (49). Notably, the efficient induction of IL-2 in virally infected T cells expressing HIV-1 and SIVcpz Nefs shows that the relatively modest downmodulation of CD28 by these Nef alleles is insufficient to suppress late TCR-signaling events. Taken together, our results showed that efficient Nef-mediated downmodulation of both TCR-CD3 and CD28 was sufficient to impair late TCR-signaling events. The differential levels of induction and secretion of IL-2 and other cytokines may impact uninfected bystander cells and thus the overall levels of infection-associated immune activation.

## Discussion

In the present study, we demonstrate that HIV-2, SIVmac, and SIVblu Nefs, but not those of HIV-1 and its simian precursor SIVcpz, strongly disrupted the formation and function of the IS. The availability of Nef mutants that are selectively active or defective in TCR-CD3 downmodulation revealed that this Nef function was sufficient and required to eliminate the capability of virally

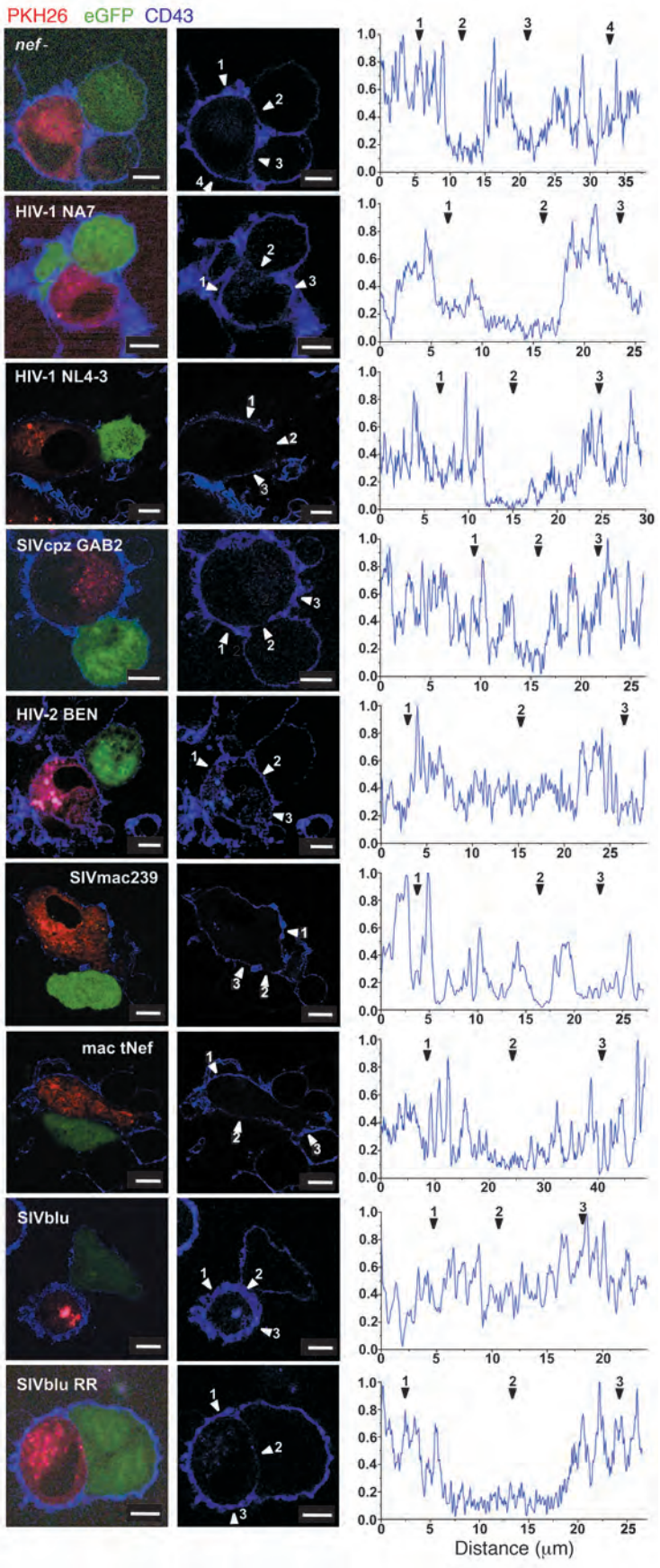


**Figure 5**
Nef alleles that downmodulate TCR-CD3 impair CD43 exclusion at the IS. Images show representative confocal acquisitions from cocultures between infected PBLs and autologous SEE-pulsed DCs. Shown are CD43 Ab labeling alone and merged images of eGFP, PKH26, and CD43. Scale bars: 5 μm. Close contact was rarely observed in PBL/APC cultures infected with viral constructs expressing HIV-2 BEN or SIVblu Nefs, and occasional cell-cell complexes did not show CD43 exclusion, as determined by microscopic examination and analysis of the CD43 signal intensity along the plane of the cell-cell interface. The *x* axis represents distance along the contact zone; the *y* axis denotes pixel intensity. The location of 3–4 representative points per construct, and their corresponding intensities, are shown by the numbered arrowheads.

infected T lymphocytes to form functional synapses with APCs. It has been shown previously that Nef-mediated downmodulation of TCR-CD3 function was specifically lost in the primate lentiviral lineage that gave rise to HIV-1 (30). Taken together, these results clearly suggest that the inability to suppress TCR-mediated activation and programmed death of virally infected T cells by disrupting their interaction with APCs distinguishes HIV-1 and its simian precursors from most other primate lentiviruses.

It remains to be clarified why the primate lentiviral lineage that gave rise to HIV-1 evolved to become much less effective in disrupting the communication between infected helper $CD4^+$ T cells and APCs. Of note, primate lentiviruses containing *nef* alleles that are unable to downmodulate TCR-CD3 usually contain a *vpu* gene: HIV-1; its simian precursor, SIVcpz; and some closely related *Cercopithecus* viruses, whose ancestor recombined with that of SIVrcm in chimpanzees to become SIVcpz (30). The fact that CD3 downmodulation by Nef was actually lost twice during primate lentiviral evolution when the virus acquired a *vpu* gene (30) suggests that Vpu reduces the selective pressure for effective disruption of the IS and hence suppression of TCR-mediated T cell activation. Recently, it was shown that Vpu counteracts a host restriction factor, tetherin, that tethers nascent virions at the cell surface and is induced by IFN-α (50). Thus, we previously proposed that HIV-1 and its simian precursors could possibly afford to cause higher levels of T cell activation, and hence more effective transcription of the proviral genome, because the acquisition of *vpu* allowed efficient viral spread in a more inflammatory environment (51). Notably, recent data show that some SIVs that do not contain a *vpu* gene use Nef to antagonize tetherin (52, 53).

The observed disruption of interactions between infected T cells and APCs is concordant with the previously reported downmodulation of surface CD3 and CD28 by HIV-2 and SIV (27–30). Still, although HIV-1 Nef does not reduce TCR-CD3 surface expression (27–30) and is only poorly effective in downmodulating CD28 (20, 21), a previous study suggested that it also impairs IS formation (11). Thoulouze and coworkers reported that the HIV-1 Nef causes a 2- to 3-fold reduction of conjugate formation between HIV-1–infected T lymphocytes and sAg-pulsed Raji B cells, resulting in reduced TCR signaling (11). In comparison, we found that HIV-1 Nefs did not impair the

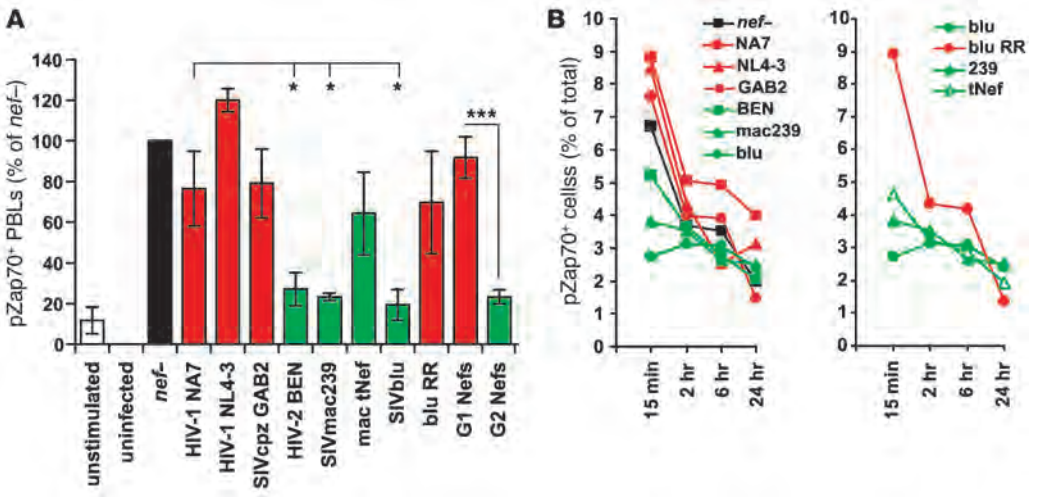


**Figure 6**
Downmodulation of IS formation perturbs early TCR-CD3 signaling events after coculture with APCs. PBLs were allowed to return to a less-activated state after infection by removal of all cytokines in the growth medium for 3 days. PBLs were stimulated with CD3/CD28 beads for the indicated times or left unstimulated, and then labeled for intracellular phospho–ZAP-70 kinase. (**A**) Percentage of pZAP-70+ infected cells, shown as mean ± SD of 3 independent experiments. In all experiments, 5%–20% of PBLs infected with *nef*– were pZAP-70+ after 15 minutes' stimulation with CD3/CD28 beads; *nef*– values are set as 100%. **P* < 0.05; ****P* < 0.001. (**B**) Kinetic of ZAP-70 phosphorylation in PBL cultures infected with HIV-1 constructs expressing the indicated *nef* alleles. Values represent percent ZAP-70+ cells and are representative of 2 independent experiments performed.

ability of virally infected T cells to form functional ISs with primary sAg-pulsed APCs. In part, this discrepancy may result from the use of different types of APCs: Raji B cells in the previous study (11) compared with primary DCs and macrophages in the present study. Although HIV-1 Nefs do not affect synapse formation, they certainly deregulate the communication between virally infected T cells and APCs by changing TCR-induced actin dynamics (13, 14) and by modulating downstream TCR signaling pathways (54, 55). Notably, we confirmed the previous finding (11) that HIV-1 Nef expression increased Lck accumulation in intracellular compartments (Figure 3). Whether HIV-1 Nefs reduce or increase the responsiveness of virally infected T cells to stimulation is a matter of debate (11–15, 22–26). We found that HIV-1 Nef expression in infected PBLs did not alter or even slightly enhance late signaling events, as measured by IL-2 production upon stimulation. Notably, we assessed this effect for the first time to our knowledge in the cell types that are most relevant for viral replication and Ag presentation in vivo and found that Nef proteins of other primate lentiviruses efficiently blocked the responsiveness of virally infected T cells to stimulation.

Because HIV/SIV gene expression and replication are dependent on the activation state of the infected T cells (56), our finding that most primate lentiviruses may prevent IS formation and TCR-mediated activation is at first surprising. Indeed, some primate lentiviruses that suppress rather than promote T cell activation may show lower replication rates in vivo. For instance, HIV-2–infected people show lower plasma viral RNA levels, but similar proviral loads, compared with those infected with HIV-1 (57). However, SIVagm and SIVsmm, which downmodulate TCR-CD3 and CD28 (30), achieve high viral loads and efficient replication in their natural monkey hosts (58), which indicates that the infected T cells express the factors required for effective proviral transcription. Thus, these viruses are capable of inducing levels of T cell activation that render infected host cells permissive for viral repli-

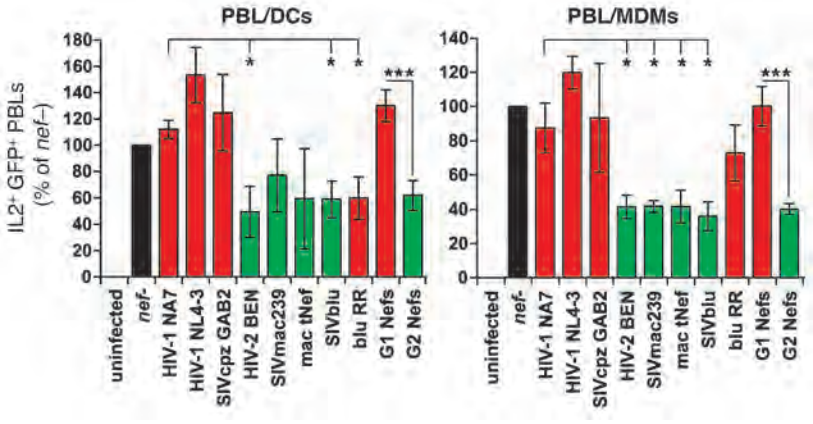


**Figure 7**
TCR-CD3 downmodulation leads to decreased IL-2 production after dynamic synapse interaction with primary APCs. Infected PBLs were cocultured with autologous SEE-pulsed DCs or MDMs for 16 hours and then labeled for intracellular IL-2. Shown is the percentage of IL-2+ cells in the infected PBL population; results are mean ± SD of 3 independent experiments. In all experiments, 2%–7% of PBLs infected with *nef*– stained positive for intracellular IL-2; *nef*– values are set as 100%. **P* < 0.05; ****P* < 0.001.

cation, independently of their interaction with APCs. Our current knowledge suggests several mechanisms by which SIVsmm and SIVagm may achieve this. First, these viruses replicate mainly in $CCR5^+$ memory $CD4^+$ T cells, which have had previous encounters with APCs and are thus at least partly activated. Second, Nef sensitizes infected T cells to stimulation by cytokines, such as IL-2 (59, 60). Thirdly, HIV and SIV Nefs themselves can trigger T cell signaling pathways reminiscent of TCR-mediated T cell activation (61, 62). Furthermore, other viral factors may stimulate key transcription factors; for example, it was previously shown that the viral transactivator Tat induces the expression of NF-κB, which binds to the core enhancer element in the HIV and SIV LTRs and plays an important role in viral gene expression (23). We also observed that Nef-mediated downmodulation of TCR-CD3 did not affect the levels of NF-κB expression in virally infected T cells (data not shown). Thus, uncoupling the stimulation of T cells from their interaction with APCs may allow some primate lentiviruses to more specifically activate the viral promoter. Finally, the disruption of the IS may be advantageous for the virus because it dampens the antiviral immune response and prolongs the period of virus production by delaying activation-induced death of infected T cells (14).

Some of the predicted consequences of IS disruption by primate lentiviruses — such as decelerated death of infected $CD4^+$ T cells, reduced expression of cytokines and death receptors, and muted immune response — should not only be advantageous for the virus, but may also help the infected host to prevent the escalation of immune activation to harmfully high levels. In agreement with this hypothesis, SIVagm and SIVsmm, which downmodulate TCR-CD3 and CD28 (30), replicate efficiently in their natural monkey hosts without causing high-level immune activation or disease (31, 58). In contrast, SIVcpz, which has lost the ability to modulate CD3 (30) and to disrupt the IS, causes an AIDS-like immunopathology in naturally infected chimpanzees (63). It is noteworthy that inefficient CD3 downmodulation by Nef is associated with loss of $CD4^+$ T cells even in naturally SIVsmm-infected sooty mangabeys (64). Thus, accumulating evidence supports that Nef-mediated downmodulation of surface TCR-CD3 and thus the impairment of IS formation contributes to the nonpathogenic phenotype of natural SIV infections and the attenuated pathogenicity of HIV-2. However, Nef-mediated suppression of T cell activation is clearly only one of several factors affecting the clinical outcome of infection. This is most obvious from the fact that effective downmodulation of TCR-CD3 and CD28 by Nef is insufficient to prevent disease in experimentally infected macaques that react with much higher levels of immune activation and T cell activation to SIV infection than the natural sooty mangabey host (65, 66).

In summary, our data show that primate lentiviruses exhibit striking differences in their capability to interfere with the formation and function of the IS and to alter the responsiveness of the infected T cells to TCR stimulation. Further studies are required to elucidate the importance of these distinct viral properties for the overall levels of immune activation and the associated high rates of T cell apoptosis and turnover that drive the progression to AIDS. Notably, most Nef functions that interfere with the formation and function of the IS — such as downmodulation of CXCR4, to inhibit the migration of T cells to APCs (67); of CD3, to prevent ligation and signaling (30); of CD28, to prevent costimulatory signals (20, 21); and of CD4, to limit signal transduction following TCR ligation (5, 6) — are all genetically separable. This separability may not only allow viruses to fine-tune their interaction with the host immune system, but also provide a means to study the role of these Nef activities in viral immune evasion and pathogenicity in appropriate animal models.

## Methods

*Virus stocks and transductions.* To generate viral stocks, 293T cells were cotransfected with pBR–NL4-3–IRES–eGFP plasmids encoding various Nef alleles and a plasmid expressing the VSG-G, as described previously (30). The latter was used to achieve comparably high infection levels for functional analysis independently of Nef (37). Viral supernatants were collected 48 hours after transduction and used either immediately or within 24 hours of storage at 4°C to infect PBLs, or concentrated by ultracentrifugation through 20% (w/v) sucrose and stored at –80°C. For transduction, $1 \times 10^6$ prestimulated PBLs were infected with virus stocks containing 50 ng p24 capsid Ag, quantified using a capture assay provided by the NIH AIDS Research and Reference Reagent Program. After 2 or 3 days, infected cells were fixed, and the frequency and phenotype of HIV-1–infected $GFP^+$ cells was determined by flow cytometry following staining with PE-conjugated CD3, PE-conjugated CD8, allophycocyanin-conjugated CD2, and PE-conjugated CD21 antibodies (all from BD Biosciences — Pharmingen) or with allophycocyanin-conjugated anti-CD4 (13B8.2, Immunotech).

*Primary cell preparation.* Citrate human blood was obtained from healthy donors at the Blood Donation Center of the University of Ulm. The study was reviewed and approved by the University of Ulm Institutional Review Board, and individuals provided informed consent prior to donating blood. Monocytes and PBLs were separated using adherence on plastic (45 minutes) after Ficoll gradient. PBLs were activated for 3 days with 1 μg/ml PHA and 10 ng/ml IL-2 prior to infection. Monocytes were differentiated to immature DCs by incubation for 5–7 days with 50 ng/ml recombinant human GM-CSF and 20 ng/ml IL-4 (Immunotools). Alternatively, monocytes were differentiated to macrophages by incubation for 7–10 days with 50 ng/ml GM-CSF alone. Phenotypic characterization prior to infection was carried out by flow cytometry. DCs were $CD14^-CD1a^+CD80^{lo}CD86^{lo}$, and macrophages were $CD14^+CD1a^{lo}$. For analysis of CD3, Lck, talin, and LFA-1 localization, buffy coats were obtained according to institutional guidelines of the ethical committee of the University of Geneva. Monocytes were purified after Ficoll gradient separation with CD14 MicroBeads (Miltenyi Biotec), and autologous $CD4^+$ T lymphocytes were purified by negative selection with $CD4^+$ T Cell Isolation kit II (Miltenyi Biotec). Purified autologous $CD4^+$ T lymphocytes were greater than 95% $CD3^+$ and greater than 95% $CD4^+$. Before infection, medium was replaced by RPMI without PHA and IL-2. All primary cells used in the present study were of human origin.

*Complex formation between PBLs and APCs.* PBLs were infected with NL4-3–IRES–eGFP viruses encoding different *nef* alleles. At 4 days after infection, autologous macrophages or DCs were labeled with the red lipophilic dye PKH26 (Sigma-Aldrich), according to the manufacturer's instructions. Labeled cells were then pulsed with 10 μg/ml SEE sAg (Toxin Technology) or medium for 15 minutes at 37°C. For microscopy studies, APCs were then seeded onto poly-L-lysine–treated (Sigma-Aldrich) culture wells or coverslips for 15 minutes at 37°C. Infected PBLs were added onto adherent APCs at a 1:1 ratio, and cocultures were fixed after 40 minutes by adding an equal volume of 2% PFA. Noninfected PBLs were stained with CFSE (Invitrogen) according to the manufacturer's guidelines. Complexes were observed either by standard epifluorescence microscopy using a Zeiss Axiovert microscope (×40 objective) or by confocal fluorescence microscopy using a Leica TCS 4Pi scanning confocal laser microscope (×100 objective).

*Polarization of CD3, Lck, talin, and LFA-1.* For microscopy studies, immature DCs were pulsed with a sAg cocktail (SEE, SEA, SED, SEC3, and TSST, all 1 μg/ml; Toxin Technology) for 15 minutes, washed, and mixed with

infected CD4+ T cells at a 1:1 ratio and seeded onto poly-L-lysine–treated (Sigma-Aldrich) coverslips at 37°C. Cells were fixed after 30–45 minutes by adding an equal volume of 3% PFA. Fixed cells were stained for CD3 (UCHT1; Chemicon) or LFA-1 (HI111; BD Biosciences) under nonpermeabilizing conditions, or for Lck (3A5; Santa Cruz Biotechnology Inc.) or talin (8D4; Sigma-Aldrich) in the presence of 0.05% saponin, followed by secondary antibodies Alexa Fluor 568–conjugated goat anti-mouse (Invitrogen) or rhodamine-conjugated donkey anti-mouse (Jackson Immunoresearch). Nuclei were labeled by DAPI (Roche). All confocal laser scanning microscopy was performed with a LSM 510 Meta microscope using a ×60 Plan Apochromat NA 1.4 DIC objective (Zeiss). Single section images were acquired as 512 pixels by 512 pixels and then processed using NIH ImageJ software (http://rsbweb.nih.gov/ij/). Polarization of Lck, LFA-1, and talin was defined as an immediately obvious enrichment (greater than 50% total staining) of IS markers at the immature DC/T cell contact. Quantification of polarization was carried out on a total of 20–60 conjugates for each condition for 2 different donors.

*CD43 exclusion*. For studies of CD43 exclusion from the IS, fixed cells were stained for CD43 (mouse anti-CD43; BD Biosciences — Pharmingen; and Alexa Fluor 647–conjugated anti-mouse; Invitrogen) prior to observation. The CD43 signal intensity along the plane of the cell-cell interface was quantified using ImageJ Plot Profile analysis, which displays the intensities of pixels along a line as a 2-dimensional graph.

*Effector pathways of IS formation*. Virally infected PBLs were treated with PHA and IL-2 as described above and subsequently washed and resuspended in RPMI without cytokines. A resting phenotype (as assessed by morphology, e.g., loss of cell aggregation and small cell size), lack of expression of activation markers, and loss of eGFP expression were observed after a further 3–4 days. For early IS signaling pathways, PBLs were then restimulated with CD3/CD28 beads (Invitrogen) at a 1:1 ratio for 15 minutes, 2 hours, 6 hours, or 24 hours or were left unstimulated. At the given time points, cells were fixed in 2% PFA, permeabilized, and immediately labeled with rabbit anti-pZap70 Tyr493 (0.5 μg/sample; Santa Cruz Biotechnology Inc.) and Alexa Fluor 647–conjugated anti-rabbit (0.5 μg/sample; Invitrogen). Alternatively, for late IS signaling, PBLs were stimulated with autologous MDMs or DCs for 16–24 hours and labeled for intracellular IL-2 using an allophycocyanin-conjugated IL-2 antibody (BD Biosciences — Pharmingen).

*Statistics*. All statistical calculations were performed with a 2-tailed unpaired Student's *t* test using Graph Pad Prism version 5.0. *P* values less than 0.05 were considered significant. Correlations were calculated with the linear regression module.

## Acknowledgments

We thank Thomas Mertens for support; Nicola Bailer, Martha Mayer, Daniela Krnavek, and Kerstin Regensburger for technical assistance; Fabien Blanchet for helpful discussion; and Ingrid Bennett for critical reading of the manuscript. This work was supported by the Swiss National Science Foundation, the Center for Functional Nanostructures (CFN), and the Deutsche Forschungsgemeinschaft (DFG).

Received for publication February 20, 2009, and accepted in revised form July 22, 2009.

Address correspondence to: Frank Kirchhoff, Institute of Virology, University of Ulm, Albert-Einstein-Allee 11, 89081 Ulm, Germany. Phone: 49-731-50065109; Fax: 49-731-50065131; E-mail: frank.kirchhoff@uniklinik-ulm.de.

1. Monks, C.R., Freiberg, B.A., Kupfer, H., Sciaky, N., and Kupfer, A. 1998. Three-dimensional segregation of supramolecular activation clusters in T cells. *Nature.* **395**:82–86.
2. Grakoui, A., et al. 1999. The immunological synapse: a molecular machine controlling T cell activation. *Science.* **285**:221–227.
3. Dustin, M.L. 2005. A dynamic view of the immunological synapse. *Semin. Immunol.* **17**:400–410.
4. Krummel, M.F., and Davis, M.M. 2002.Dynamics of the immunological synapse: finding, establishing and solidifying a connection. *Curr. Opin. Immunol.* **14**:66–74.
5. Krummel, M.F., Sjaastad, M.D., Wulfing, C., and Davis, M.M. 2000. Differential clustering of CD4 and CD3ζ during T cell recognition. *Science.* **289**:1349–1352.
6. Li, Q.J., et al. 2004. CD4 enhances T cell sensitivity to antigen by coordinating Lck accumulation at the immunological synapse. *Nat. Immunol.* **5**:791–799.
7. Banchereau, J., and Steinman, R.M. 1998. Dendritic cells and the control of immunity. *Nature.* **392**:245–252.
8. Müller, N., et al. 2006. Measles virus contact with T cells impedes cytoskeletal remodeling associated with spreading, polarization, and CD3 clustering. *Traffic.* **7**:849–858.
9. Cho, N.H., et al. 2004. Inhibition of T cell receptor signal transduction by tyrosine kinase-interacting protein of *Herpesvirus saimiri*. *J. Exp. Med.* **200**:681–687.
10. González, P.A., et al. 2008. Respiratory syncytial virus impairs T cell activation by preventing synapse assembly with dendritic cells. *Proc. Natl. Acad. Sci. U. S. A.* **105**:14999–15004.
11. Thoulouze, M.I., et al. 2006. Human immunodeficiency virus type-1 infection impairs the formation of the immunological synapse. *Immunity.* **24**:547–561.
12. Jerome, K.R. 2008. Viral Modulation of T-cell receptor signaling. *J. Virol.* **82**:4194–4204.
13. Haller, C., and Fackler, O.T. 2008. HIV-1 at the immunological and T-lymphocytic virological synapse. *Biol. Chem.* **389**:1253–1260.
14. Fackler, O.T., Alcover, A., and Schwartz, O. 2007. Modulation of the immunological synapse: a key to HIV-1 pathogenesis? *Nat. Rev. Immunol.* **7**:310–317.
15. Kirchhoff, F., Schindler, M., Specht, A., Arhel, N., and Munch, J. 2008. Role of Nef in primate lentiviral immunopathogenesis. *Cell Mol. Life Sci.* **65**:2621–2636.
16. Ariën, K.K., and Verhasselt, B. 2008. HIV Nef: role in pathogenesis and viral fitness. *Curr. HIV Res.* **6**:200–208.
17. Deacon, N.J., et al. 1995. Genomic structure of an attenuated quasi species of HIV-1 from a blood transfusion donor and recipients. *Science.* **270**:988–991.
18. Kirchhoff, F., Greenough, T.C., Brettler, D.B., Sullivan, J.L., and Desrosiers, R.C. 1995. Brief report: absence of intact nef sequences in a long-term survivor with nonprogressive HIV-1 infection. *N. Engl. J. Med.* **332**:228–232.
19. Garcia, J.V., and Miller, A.D. 1991. Serine phosphorylation-independent downregulation of cell-surface CD4 by nef. *Nature.* **350**:508–511.
20. Swigut, T., Shody, N., and Skowronski, J. 2001. Mechanism for downregulation of CD28 by Nef. *EMBO J.* **20**:1593–1604.
21. Bell, I., Schaefer, T.M., Trible, R.P., Amedee, A., and Reinhart, T.A. 2001. Downmodulation of the costimulatory molecule, CD28, is a conserved activity of multiple SIV Nefs and is dependent on histidine 196 of Nef. *Virology.* **283**:148–158.
22. Fenard, D., et al. 2005. Nef is physically recruited into the immunological synapse and potentiates T cell activation early after TCR engagement. *J. Immunol.* **175**:6050–6057.
23. Fortin, J., Barat, C., Beausejour, Y., Barbeau, B., and Tremblay, M.J. 2004. Hyper-responsiveness to stimulation of human immunodeficiency virus-infected CD4+ T cells requires Nef and Tat virus gene products and results from higher NFAT, NF-kappaB, and AP-1 induction. *J. Biol. Chem.* **279**:39520–39531.
24. Manninen, A., Huotari, P., Hiipakka, M., Renkema, G.H., and Saksela, K. 2001. Activation of NFAT-dependent gene expression by Nef: conservation among divergent Nef alleles, dependence on SH3 binding and membrane association, and cooperation with protein kinase C-theta. *J. Virol.* **75**:3034–3037.
25. Schrager, J., and Marsh, J. 1999. HIV-1 Nef increases T cell activation in a stimulus-dependent manner. *Proc. Natl. Acad. Sci. U. S. A.* **96**:8167–8172.
26. Wang, J., Kiyokawa, E., Verdin, E., and Trono, D. 2000. The Nef protein of HIV-1 associates with rafts and primes T cells for activation. *Proc. Natl. Acad. Sci. U. S. A.* **97**:394–399.
27. Bell, I., et al. 1998. Association of SIV Nef with the T cell receptor (TCR) zeta chain leads to TCR down modulation. *J. Gen. Virol.* **79**:2717–2727.
28. Howe, A.Y., Jung, J.U., and Desrosiers, R.C. 1998. Zeta chain of the T cell receptor interacts with nef of SIV and HIV-2. *J. Virol.* **72**:9827–9834
29. Münch, J., et al. 2005. Primary sooty mangabey simian immunodeficiency virus and human immunodeficiency virus type 2 nef alleles modulate cell surface expression of various human receptors and enhance viral infectivity and replication. *J. Virol.* **79**:10547–10560.
30. Schindler, M., et al. 2006. Nef-mediated suppression of T cell activation was lost in a lentiviral lineage that gave rise to HIV-1. *Cell.* **125**:1055–1067.
31. Silvestri, G. 2009. Immunity in natural SIV infections. *J. Intern. Med.* **265**:97–109.
32. Mariani, R., and Skowronski, J. 1993. CD4 down-regulation by nef alleles isolated from human immunodeficiency virus type 1-infected individuals. *Proc. Natl. Acad. Sci. U. S. A.* **90**:5549–5553.
33. Bibollet-Ruche, F., et al. 2004. Complete genome

analysis of one of the earliest SIVcpzPtt strains from Gabon (SIVcpzGAB2). *AIDS Res. Hum. Retroviruses.* **20**:1377–1381.
34. Schindler, M., et al. 2003. Downmodulation of mature major histocompatibility complex class II and up-regulation of invariant chain cell surface expression are well-conserved functions of human and simian immunodeficiency virus nef alleles. *J. Virol.* **77**:10548–10556.
35. Münch, J., et al. 2007. Nef-mediated enhancement of virion infectivity and stimulation of viral replication are fundamental properties of primate lentiviruses. *J. Virol.* **81**:13852–13864.
36. Münch, J., et al. 2002. T cell receptor:CD3 downregulation is a selected in vivo function of SIV Nef but is not sufficient for effective viral replication in rhesus macaques. *J. Virol.* **76**:12360–12364.
37. Aiken, C. 1997. Pseudotyping human immunodeficiency virus type 1 (HIV-1) by the glycoprotein of vesicular stomatitis virus targets HIV-1 entry to an endocytic pathway and suppresses both the requirement for Nef and the sensitivity to cyclosporin A. *J. Virol.* **71**:5871–5877.
38. Delon, J., Kaibuchi, K., and Germain, R.N. 2001. Exclusion of CD43 from the immunological synapse is mediated by phosphorylation-regulated relocation of the cytoskeletal adaptor moesin. *Immunity.* **15**:691–701.
39. Sampath, R., Gallagher, P.J., and Pavalko, F.M. 1998. Cytoskeletal interactions with the leukocyte integrin beta2 cytoplasmic tail. Activation-dependent regulation of associations with talin and alpha-actinin. *J. Biol. Chem.* **273**:33588–33594.
40. Dustin, M.L., and Cooper, J.A. 2000. The immunological synapse and the actin cytoskeleton: molecular hardware for T cell signaling. *Nat. Immunol.* **1**:23–29.
41. Li, Q., et al. 2005. Peak SIV replication in resting memory CD4(+) T cells depletes gut lamina propria CD4(+) T cells. *Nature.* **434**:1148–1152.
42. Mattapallil, J.J., et al. 2005. Massive infection and loss of memory CD4+ T cells in multiple tissues during acute SIV infection. *Nature.* **434**:1093–1097.
43. Trickett, A., and Kwan, Y.L. 2003. T cell stimulation and expansion using anti-CD3/CD28 beads. *J. Immunol. Methods.* **275**:251–255.
44. Béné, M.C. 2006. What is ZAP-70? *Cytometry B. Clin. Cytom.* **70**:204–208.
45. Chan, A.C., et al. 1995. Activation of ZAP-70 kinase activity by phosphorylation of tyrosine 493 is required for lymphocyte antigen receptor function. *EMBO J.* **14**:2499–2508.
46. Gaffen, S.L., and Liu, K.D. 2004. Overview of interleukin-2 function, production and clinical applications. *Cytokine.* **28**:109–123.
47. Riley, J.L., and June, C.H. 2005. The CD28 family: a T-cell rheostat for therapeutic control of T-cell activation. *Blood.* **105**:13–21.
48. Sansom, D.M., and Walker, L.S. 2006. The role of CD28 and cytotoxic T-lymphocyte antigen-4 (CTLA-4) in regulatory T-cell biology. *Immunol. Rev.* **212**:131–148.
49. Friedl, P., den Boer, A.T., and Gunzer, M. 2005. Tuning immune responses: diversity and adaptation of the immunological synapse. *Nat. Rev. Immunol.* **5**:532–545.
50. Neil, S.J., Zang, T., and Bieniasz, P.D. 2008. Tetherin inhibits retrovirus release and is antagonized by HIV-1 Vpu. *Nature.* **451**:425–430.
51. Kirchhoff, F. 2009. Is the high virulence of HIV-1 an unfortunate coincidence of primate lentiviral evolution? *Nat. Rev. Microbiol.* **7**:467–476.
52. Jia, B., et al. 2009. Species-specific activity of SIV Nef and HIV-1 Vpu in overcoming restriction by tetherin/BST2. *PLoS Pathog.* **5**:e1000429.
53. Zhang, F., et al. 2009. Nef proteins from simian immunodeficiency viruses are tetherin antagonists. *Cell Host Microbe.* **6**:54–67.
54. Greenway, A.L., et al. 2003. HIV-1 Nef control of cell signalling molecules: multiple strategies to promote virus replication. *J. Biosci.* **28**:323–335.
55. Renkema, G.H., and Saksela, K. 2000. Interactions of HIV-1 NEF with cellular signal transducing proteins. *Front. Biosci.* **5**:D268–D283.
56. Stevenson, M. 2003. HIV-1 pathogenesis. *Nat. Med.* **9**:853–860.
57. Popper, S.J., et al. 2000. Low plasma human immunodeficiency virus type 2 viral load is independent of proviral load: low virus production in vivo. *J. Virol.* **74**:1554–1557.
58. Pandrea, I., Sodora, D.L., Silvestri, G., and Apetrei, C. 2008. Into the wild: simian immunodeficiency virus (SIV) infection in natural hosts. *Trends Immunol.* **29**:419–428.
59. Glushakova, S., et al. 1999. Nef enhances human immunodeficiency virus replication and responsiveness to interleukin-2 in human lymphoid tissue ex vivo. *J. Virol.* **73**:3968–3974.
60. Alexander, L., Du, Z., Rosenzweig, M., Jung, J.U., and Desrosiers, R.C. 1997. A role for natural simian immunodeficiency virus and human immunodeficiency virus type 1 nef alleles in lymphocyte activation. *J. Virol.* **71**:6094–6099.
61. Simmons, A., Aluvihare, V., and McMichael, A. 2001. Nef triggers a transcriptional program in T cells imitating single-signal T cell activation and inducing HIV virulence mediators. *Immunity.* **14**:763–777.
62. Ndolo, T., George, M., Nguyen, H., and Dandekar, S. 2006. Expression of simian immunodeficiency virus Nef protein in CD4+ T cells leads to a molecular profile of viral persistence and immune evasion. *Virology.* **353**:374–387.
63. Keele, B.F., et al. 2009. Increased mortality and AIDS-like immunopathology in wild chimpanzees infected with SIVcpz. *Nature.* **460**:515–519.
64. Schindler, M., et al. 2008. Inefficient Nef-mediated downmodulation of CD3 and MHC-I correlates with loss of CD4+T cells in natural SIV infection. *PLoS Pathog.* **4**:e1000107.
65. Kaur, A., et al. 1998. Diverse host responses and outcomes following SIVmac239 infection in sooty mangabeys and rhesus macaques. *J. Virol.* **72**:9597–9611.
66. Silvestri, G., et al. 2005. Divergent host responses during primary simian immunodeficiency virus SIVsm infection of natural sooty mangabey and nonnatural rhesus macaque hosts. *J. Virol.* **79**:4043–4054.
67. Hrecka, K., Swigut, T., Schindler, M., Kirchhoff, F., and Skowronski, J. 2005. Nef proteins from diverse groups of primate lentiviruses downmodulate CXCR4 to inhibit migration to SDF-1 chemokine. *J. Virol.* **79**:10650–10659.

# Supplemental Data

## The Inability to Disrupt the Immunological Synapse distinguishes HIV-1 from most other Primate Lentiviruses

**Nathalie Arhel, Martin Lehmann, Karen Clauß, G. Ulrich Nienhaus, Vincent Piguet, and Frank Kirchhoff**

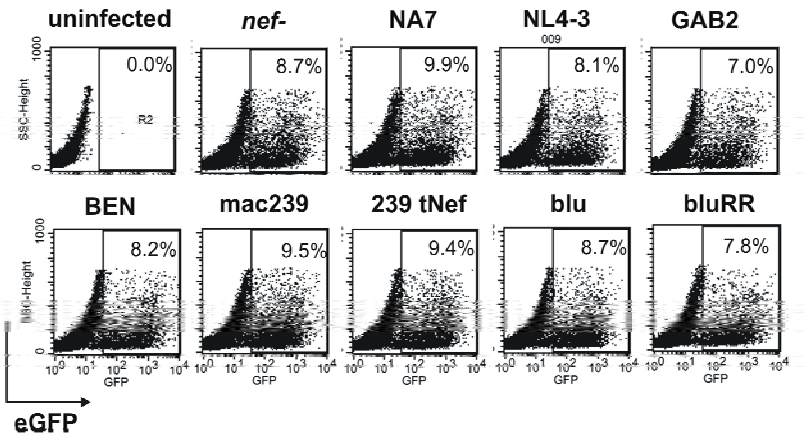


**Supplementary Figure 1:** Quantification of HIV-1 infection efficiencies. PBLs were infected with VSV-G pseudotyped HIV-1 particles containing normalized quantities of p24 (50 ng) and analyzed by flow cytometry 3d later. The numbers give the percentages of $eGFP^+$ (HIV-1-infected) PBLs of the total number of cells analyzed.

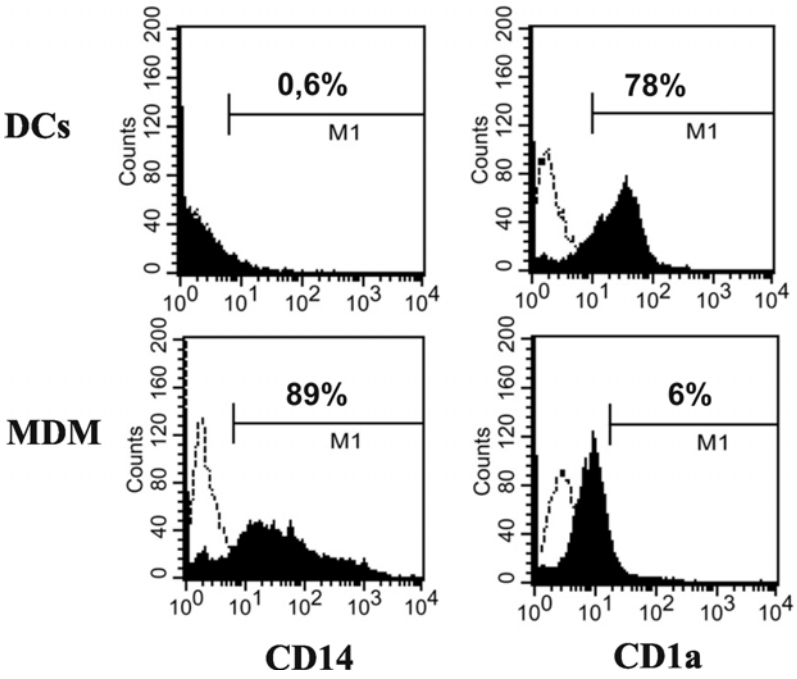


**Supplementary Figure 2:** Phenotypic characterization of primary DCs and MDMs. Flow cytometry analysis was performed on monocyte-derived DCs and MDMs at 5 and 7d post-differentiation, respectively. Dotted lines show isotype controls.

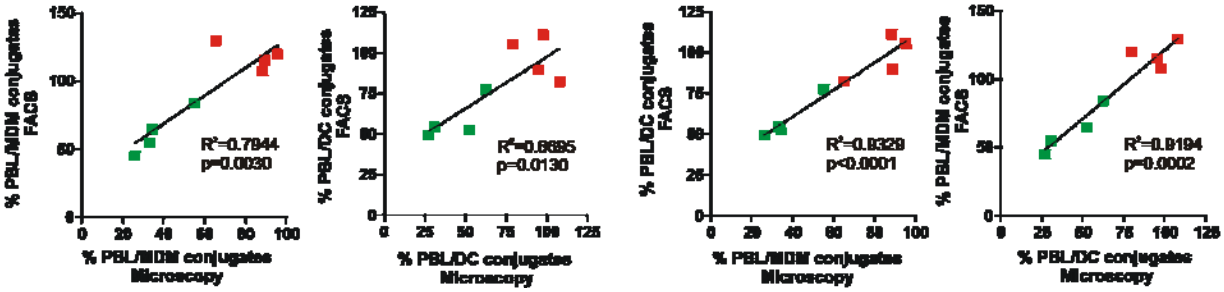


**Supplementary Figure 3:** Correlation of results from microscopy examination (Figure 1A) and flow cytometry analyses (Figure 1B) to assess complex formation between infected PBLs and autologous MDMs or DCs. The values used for the calculations are summarized in Table S2 and give the percentages of HIV-1-infected PBLs that formed complexes with autologous SEE-pulsed MDMs or DCs relative to those infected with the *nef*-defective control virus (100%) in the graphs. Results obtained using viral constructs expressing *nef* alleles that downmodulate TCR-CD3 are indicated by green and those that do not by red symbols.

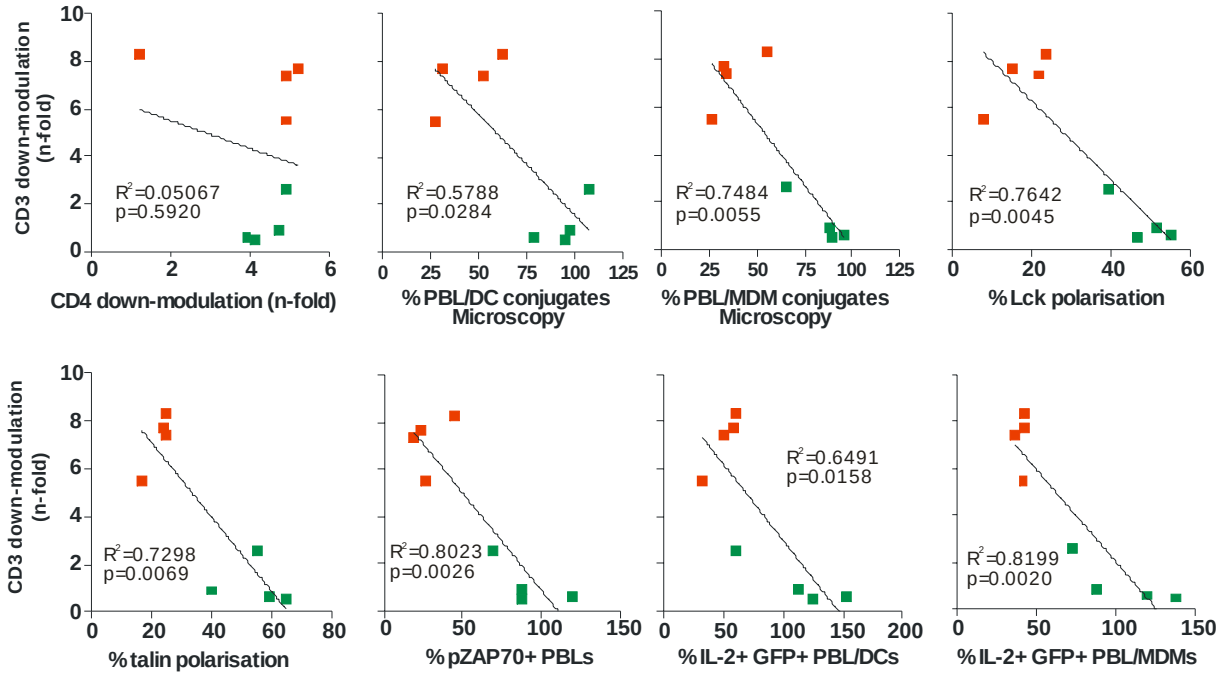


**Supplementary Figure 4:** Correlation between the efficiency of Nef-mediated down-modulation of TCR-CD3 and the modulation of CD4 cell surface expression, the formation of conjugates between virally infected PBLs and DCs or MDMs, the polarization of Lck and talin towards the contact zone, ZAP70 phosphorylation and IL-2 induction. All values used for linear regression analysis are provided in Table S2.

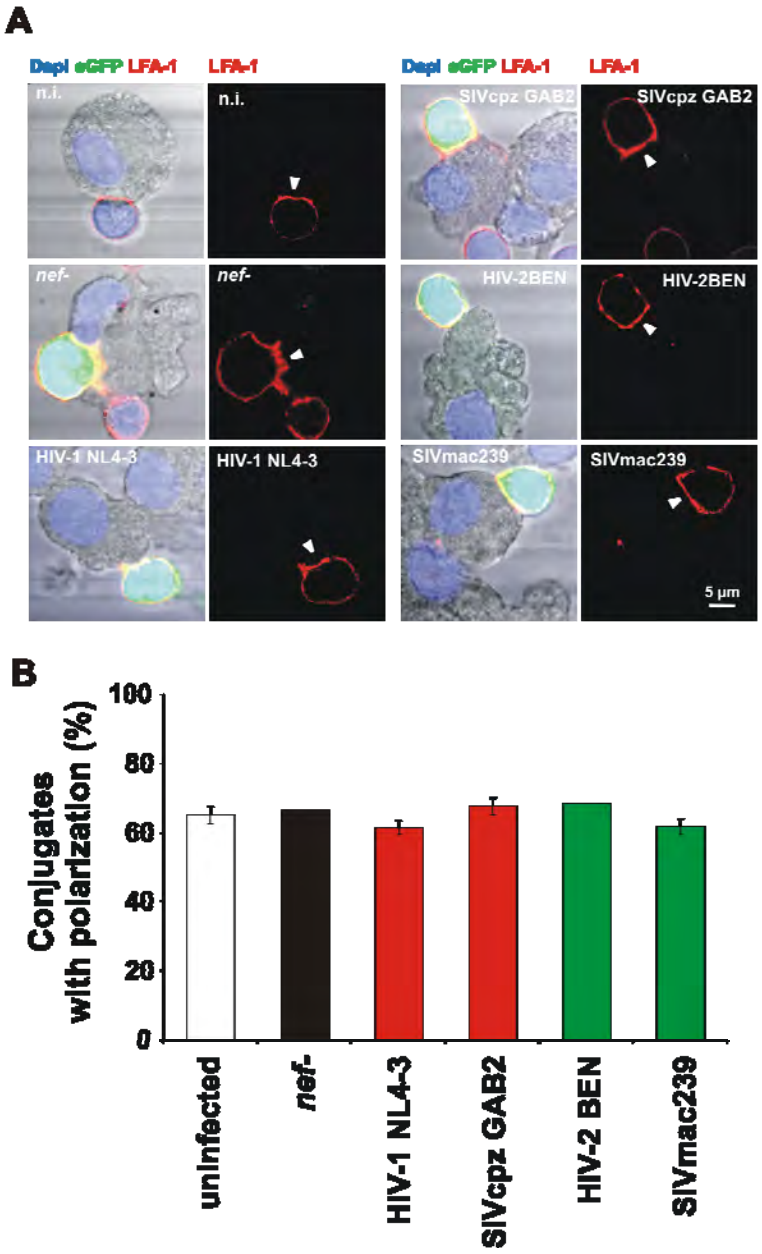


**Supplementary Figure 5:** Nef does not impair polarization of LFA-1 at the immune synapse. (A) $CD4^+$ T cells infected with HIV-1 constructs expressing the indicated *nef* alleles were incubated with autologous sAg-pulsed DCs, fixed and stained with anti-LFA-1. The right panels show LFA-1 antibody labeling and left panels a merge of eGFP, Dapi and LFA-1. (B) Number of HIV-1 infected $eGFP^+$ T cells engaged in complex formation with APCs showing a polarization of LFA-1 at the zone of contact. The graphs show the mean of two independent experiments +/- standard error of the mean, except for HIV-2 BEN which represents a single experiment.

**Table S1.** Modulation of cell surface receptors by HIV and SIV *nef* alleles

| | | GenBank | | down-modulation (n-fold) of: | | | | |
|---|---|---|---|---|---|---|---|---|
| Lineage | Clone | Accession # | Species/subspecies | CD4 | MHC-I | CD3 | CD28 | Group |
| HIV-1/M | NA7 | DQ242535 | Human (*Homo sapiens*) | 7.2 | 10.4 | 1.0 | 5.4 | 1 |
| HIV-1/M | NL4-3 | M19921 | Human (*Homo sapiens*) | 6.6 | 12.1 | 1.0 | 2.6 | 1 |
| SIVcpz*Ptt* | GAB2 | AF382828 | Central chimpanzee (*Pan t. troglodytes*) | 7.3 | 8.6 | 0.8 | 5.8 | 1 |
| HIV-2 | BEN | M30502 | Human (*Homo sapiens*) | 4.8 | 5.9 | 16.7 | 7.9 | 2 |
| SIVmac | 239 | M33262 | Rhesus macaque (*Maccaca mulatta*) | 7.0 | 9.1 | 16.4 | 16.9 | 2 |
| SIVmac | 239 tNef | n.a. | n.a. | 1.2 | 1.13 | 12.4 | 1.9 | 2 |
| SIVblu | KE31 | DQ222474 | Blue monkey (*Cercopithecus mitis*) | 6.9 | 11.0 | 18.0 | 20.0 | 2 |
| SIVblu | RR-AA | n.a. | n.a. | 5.8 | 7.3 | 1.8 | 14.3 | 2 |

The Nef-mediated *n*-fold down-modulation of CD4, MHC-I, TCR-CD3 and CD28 on HIV-1-infected PBMCs was calculated as the mean fluorescence intensity (MFI) in cells infected with HIV-1 constructs coexpressing Nef and eGFP relative to cells infected with a *nef*-deficient HIV-1. The results were derived from Ref. 30. Group 1 and 2 Nefs indicate Nefs that do not and do down-regulate TCR-CD3, respectively.

**Table S2.** Effect of HIV and SIV *nef* alleles on the interaction between virally infected T cells and APCs

| | | modulation of[1] | | Infected PBLs interacting with[2] | | | | polarisation of [3] | | | PBLs staining positive for[4] | | |
|---|---|---|---|---|---|---|---|---|---|---|---|---|---|
| Lineage | Clone | CD3 | CD4 | DC-F | MDM-F | DC-M | MDM-M | Lck | Talin | LFA-1 | Zap70$^+$ | IL-2 DCs | IL-2 MDM |
| HIV-1/M | NA7 | 0,6 | 3,9 | 88,4 | 97,7 | 107,8 | 111,3 | 51,3 | 40,0 | n.d. | 87,0 | 112,0 | 87,4 |
| HIV-1/M | NL4-3 | 0,9 | 4,7 | 95,4 | 79,4 | 120,0 | 105,7 | 55,0 | 59,3 | 61,3 | 120,0 | 153,4 | 119,8 |
| SIVcpz*Ptt* | GAB2 | 0,5 | 4,1 | 89,0 | 95,0 | 115,6 | 89,8 | 46,7 | 64,8 | 67,4 | 88,1 | 124,7 | 138,7 |
| HIV-2 | BEN | 5,5 | 4,9 | 25,9 | 26,9 | 45,0 | 49,4 | 7,5 | 16,7 | 68,4 | 27,2 | 32,8 | 41,4 |
| SIVmac | 239 | 7,7 | 5,2 | 33,2 | 30,8 | 55,0 | 54,4 | 15,0 | 24,4 | 61,7 | 23,3 | 58,0 | 41,6 |
| SIVmac | tNef | 8,3 | 1,2 | 55,2 | 62,3 | 84,2 | 77,5 | 23,3 | 25,0 | n.d. | 45,2 | 59,4 | 41,5 |
| SIVblu | KE31 | 7,4 | 4,9 | 34,1 | 52,3 | 64,8 | 52,7 | 21,7 | 25,0 | n.d. | 19,4 | 49,3 | 35,9 |
| SIVblu | RR-Nef | 2,6 | 4,9 | 65,4 | 108,0 | 129,8 | 82,5 | 39,5 | 55,0 | n.d. | 69,7 | 59,7 | 72,8 |

[1]CD3 and CD4 surface downmodulation in infected primary CD4$^+$ T cells was determined at 2 days post-infection. Numbers give the ratio between the MFI of cells infected with the *nef*- control construct and HIV-1 constructs containing intact *nef* alleles. Shown are average values derived from three independent experiments.

[2-4] The values were derived from Figures 1 ([2]), 3 to 5 ([3]) and 6 or 7 ([4]).

Abbreviations: n.d., not determined; -F, flow cytometry; -M, microscopy.

## References


1. Barre-Sinoussi, F. *et al.* Isolation of a T-lymphotropic retrovirus from a patient at risk for acquired immune deficiency syndrome (AIDS). *Science* **220**, 868-871 (1983).
2. Popovic, M. *et al.* Isolation and transmission of human retrovirus (human t-cell leukemia virus). *Science* **219**, 856-859 (1983).
3. Alizon, M. *et al.* Molecular cloning of lymphadenopathy-associated virus. *Nature* **312**, 757-760 (1984).
4. Wain-Hobson, S., Sonigo, P., Danos, O., Cole, S. & Alizon, M. Nucleotide sequence of the AIDS virus, LAV. *Cell* **40**, 9-17 (1985).
5. Ratner, L., Gallo, R.C. & Wong-Staal, F. HTLV-III, LAV, ARV are variants of same AIDS virus. *Nature* **313**, 636-637 (1985).
6. Clavel, F. *et al.* Molecular cloning and polymorphism of the human immune deficiency virus type 2. *Nature* **324**, 691-695 (1986).
7. Cohen, J. The emerging race to cure HIV infections. *Science* **332**, 784-785, 787-789 (2011).
8. Cohen, O.J. & Fauci, A.S. Chapter 60: Pathogenesis and Medical Aspects of HIV-1 Infection, in *Fields' virology*, Edn. 4th. (eds. B.N. Fields, D.M. Knipe, P.M. Howley & D.E. Griffin) (Lippincott Williams & Wilkins, Philadelphia; 2001).
9. Brenchley, J.M. *et al.* CD4+ T cell depletion during all stages of HIV disease occurs predominantly in the gastrointestinal tract. *J Exp Med* **200**, 749-759 (2004).
10. Homann, S., Smith, D., Little, S., Richman, D. & Guatelli, J. Upregulation of BST-2/Tetherin by HIV infection in vivo. *J Virol* **85**, 10659-10668 (2011).
11. Schmitz, J.E. *et al.* Control of viremia in simian immunodeficiency virus infection by CD8+ lymphocytes. *Science* **283**, 857-860 (1999).
12. Mellors, J.W. *et al.* Prognosis in HIV-1 infection predicted by the quantity of virus in plasma. *Science* **272**, 1167-1170 (1996).
13. Moris, A. *et al.* Dendritic cells and HIV-specific CD4+ T cells: HIV antigen presentation, T-cell activation, and viral transfer. *Blood* **108**, 1643-1651 (2006).
14. Ryan, M.D. & Flint, M. Virus-encoded proteinases of the picornavirus super-group. *J Gen Virol* **78 ( Pt 4)**, 699-723 (1997).
15. Stevenson, M. HIV-1 pathogenesis. *Nat Med* **9**, 853-860 (2003).
16. Finzi, D. *et al.* Latent infection of CD4+ T cells provides a mechanism for lifelong persistence of HIV-1, even in patients on effective combination therapy. *Nat Med* **5**, 512-517 (1999).
17. Little, S.J. *et al.* Antiretroviral-drug resistance among patients recently infected with HIV. *N Engl J Med* **347**, 385-394 (2002).
18. Sarkar, I., Hauber, I., Hauber, J. & Buchholz, F. HIV-1 proviral DNA excision using an evolved recombinase. *Science* **316**, 1912-1915 (2007).
19. Korber, B. & Gnanakaran, S. AIDS/HIV. Converging on an HIV vaccine. *Science* **333**, 1589-1590 (2011).
20. Malim, M.H. & Emerman, M. HIV-1 accessory proteins--ensuring viral survival in a hostile environment. *Cell Host Microbe* **3**, 388-398 (2008).
21. Gao, F. *et al.* Origin of HIV-1 in the chimpanzee Pan troglodytes troglodytes. *Nature* **397**, 436-441 (1999).
22. Sharp, P.M., Shaw, G.M. & Hahn, B.H. Simian immunodeficiency virus infection of chimpanzees. *J Virol* **79**, 3891-3902 (2005).
23. Hahn, B.H., Shaw, G.M., De Cock, K.M. & Sharp, P.M. AIDS as a zoonosis: scientific and public health implications. *Science* **287**, 607-614 (2000).

24. Worobey, M. *et al.* Direct evidence of extensive diversity of HIV-1 in Kinshasa by 1960. *Nature* **455**, 661-664 (2008).
25. Keele, B.F. *et al.* Increased mortality and AIDS-like immunopathology in wild chimpanzees infected with SIVcpz. *Nature* **460**, 515-519 (2009).
26. Kestler, H.W., 3rd *et al.* Importance of the nef gene for maintenance of high virus loads and for development of AIDS. *Cell* **65**, 651-662 (1991).
27. Kirchhoff, F. Is the high virulence of HIV-1 an unfortunate coincidence of primate lentiviral evolution? *Nat Rev Microbiol* **7**, 467-476 (2009).
28. Briggs, J.A., Wilk, T., Welker, R., Krausslich, H.G. & Fuller, S.D. Structural organization of authentic, mature HIV-1 virions and cores. *EMBO J* **22**, 1707-1715 (2003).
29. Freed, E.O. HIV-1 replication. *Somat Cell Mol Genet* **26**, 13-33 (2001).
30. Carlson, L.A. *et al.* Cryo electron tomography of native HIV-1 budding sites. *PLoS Pathog* **6**, e1001173 (2010).
31. Hladik, F. & McElrath, M.J. Setting the stage: host invasion by HIV. *Nat Rev Immunol* **8**, 447-457 (2008).
32. Geijtenbeek, T.B. *et al.* DC-SIGN, a dendritic cell-specific HIV-1-binding protein that enhances trans-infection of T cells. *Cell* **100**, 587-597 (2000).
33. Pope, M. *et al.* Conjugates of dendritic cells and memory T lymphocytes from skin facilitate productive infection with HIV-1. *Cell* **78**, 389-398 (1994).
34. Steinman, R.M. *et al.* The interaction of immunodeficiency viruses with dendritic cells. *Curr Top Microbiol Immunol* **276**, 1-30 (2003).
35. McDonald, D. *et al.* Recruitment of HIV and its receptors to dendritic cell-T cell junctions. *Science* **300**, 1295-1297 (2003).
36. Piguet, V. & Steinman, R.M. The interaction of HIV with dendritic cells: outcomes and pathways. *Trends Immunol* **28**, 503-510 (2007).
37. Liu, Y., Belkina, N.V. & Shaw, S. HIV infection of T cells: actin-in and actin-out. *Sci Signal* **2**, pe23 (2009).
38. B.Stolp & O.Fackler How HIV Takes Advantage of the Cytoskeleton in Entry and Replication. *Viruses* **3**, 293-311 (2011).
39. Lehmann, M., Nikolic, D.S. & Piguet, V. How HIV-1 Takes Advantage of the Cytoskeleton during Replication and Cell-to-Cell Transmission. *Viruses* **3**, 1757-1776 (2011).
40. Miyauchi, K., Kim, Y., Latinovic, O., Morozov, V. & Melikyan, G.B. HIV enters cells via endocytosis and dynamin-dependent fusion with endosomes. *Cell* **137**, 433-444 (2009).
41. Bukrinskaya, A., Brichacek, B., Mann, A. & Stevenson, M. Establishment of a functional human immunodeficiency virus type 1 (HIV-1) reverse transcription complex involves the cytoskeleton. *J Exp Med* **188**, 2113-2125 (1998).
42. McDonald, D. *et al.* Visualization of the intracellular behavior of HIV in living cells. *J Cell Biol* **159**, 441-452 (2002).
43. Arhel, N. *et al.* Quantitative four-dimensional tracking of cytoplasmic and nuclear HIV-1 complexes. *Nat Methods* **3**, 817-824 (2006).
44. Bieniasz, P.D. The cell biology of HIV-1 virion genesis. *Cell Host Microbe* **5**, 550-558 (2009).
45. Bukrinsky, M.I. *et al.* Association of integrase, matrix, and reverse transcriptase antigens of human immunodeficiency virus type 1 with viral nucleic acids following acute infection. *Proc Natl Acad Sci U S A* **90**, 6125-6129. (1993).
46. Fassati, A. & Goff, S.P. Characterization of intracellular reverse transcription complexes of human immunodeficiency virus type 1. *J Virol* **75**, 3626-3635. (2001).

47. Brass, A.L. *et al.* Identification of host proteins required for HIV infection through a functional genomic screen. *Science* **319**, 921-926 (2008).
48. Konig, R. *et al.* Global analysis of host-pathogen interactions that regulate early-stage HIV-1 replication. *Cell* **135**, 49-60 (2008).
49. Schroder, A.R. *et al.* HIV-1 integration in the human genome favors active genes and local hotspots. *Cell* **110**, 521-529 (2002).
50. Jordan, A., Bisgrove, D. & Verdin, E. HIV reproducibly establishes a latent infection after acute infection of T cells in vitro. *Embo J* **22**, 1868-1877 (2003).
51. Freed, E.O. & Martin, M.A. Chapter 59: HIVs and their replication, in *Fields' virology*, Edn. 4th. (eds. B.N. Fields, D.M. Knipe, P.M. Howley & D.E. Griffin) (Lippincott Williams & Wilkins, Philadelphia; 2001).
52. Freed, E.O. HIV-1 gag proteins: diverse functions in the virus life cycle. *Virology* **251**, 1-15. (1998).
53. Ono, A. HIV-1 Assembly at the Plasma Membrane: Gag Trafficking and Localization. *Future Virol* **4**, 241-257 (2009).
54. Martin-Serrano, J. & Neil, S.J. Host factors involved in retroviral budding and release. *Nat Rev Microbiol* **9**, 519-531 (2011).
55. Ono, A. & Freed, E.O. Plasma membrane rafts play a critical role in HIV-1 assembly and release. *Proc Natl Acad Sci U S A* **98**, 13925-13930 (2001).
56. Brugger, B. *et al.* The HIV lipidome: a raft with an unusual composition. *Proc Natl Acad Sci U S A* **103**, 2641-2646 (2006).
57. Ott, D.E. *et al.* Cytoskeletal proteins inside human immunodeficiency virus type 1 virions. *J Virol* **70**, 7734-7743 (1996).
58. Krementsov, D.N. *et al.* HIV-1 assembly differentially alters dynamics and partitioning of tetraspanins and raft components. *Traffic* **11**, 1401-1414 (2010).
59. Deneka, M., Pelchen-Matthews, A., Byland, R., Ruiz-Mateos, E. & Marsh, M. In macrophages, HIV-1 assembles into an intracellular plasma membrane domain containing the tetraspanins CD81, CD9, and CD53. *J Cell Biol* **177**, 329-341 (2007).
60. Sherer, N.M. *et al.* Visualization of retroviral replication in living cells reveals budding into multivesicular bodies. *Traffic* **4**, 785-801 (2003).
61. Sattentau, Q. Avoiding the void: cell-to-cell spread of human viruses. *Nat Rev Microbiol* **6**, 815-826 (2008).
62. Welsch, S. *et al.* HIV-1 buds predominantly at the plasma membrane of primary human macrophages. *PLoS Pathog* **3**, e36 (2007).
63. Jouvenet, N. *et al.* Plasma membrane is the site of productive HIV-1 particle assembly. *PLoS Biol* **4**, e435 (2006).
64. Felts, R.L. *et al.* 3D visualization of HIV transfer at the virological synapse between dendritic cells and T cells. *Proc Natl Acad Sci U S A* **107**, 13336-13341 (2010).
65. Jouvenet, N., Bieniasz, P.D. & Simon, S.M. Imaging the biogenesis of individual HIV-1 virions in live cells. *Nature* **454**, 236-240 (2008).
66. Ivanchenko, S. *et al.* Dynamics of HIV-1 assembly and release. *PLoS Pathog* **5**, e1000652 (2009).
67. Peterlin, B.M. & Trono, D. Hide, shield and strike back: how HIV-infected cells avoid immune eradication. *Nat Rev Immunol* **3**, 97-107 (2003).
68. Kondo, E. & Gottlinger, H.G. A conserved LXXLF sequence is the major determinant in p6gag required for the incorporation of human immunodeficiency virus type 1 Vpr. *J Virol* **70**, 159-164 (1996).
69. He, J. *et al.* Human immunodeficiency virus type 1 viral protein R (Vpr) arrests cells in the G2 phase of the cell cycle by inhibiting p34cdc2 activity. *J Virol* **69**, 6705-6711 (1995).

70. Belzile, J.P. *et al.* HIV-1 Vpr-mediated G2 arrest involves the DDB1-CUL4AVPRBP E3 ubiquitin ligase. *PLoS Pathog* **3**, e85 (2007).
71. Connor, R.I., Chen, B.K., Choe, S. & Landau, N.R. Vpr is required for efficient replication of human immunodeficiency virus type-1 in mononuclear phagocytes. *Virology* **206**, 935-944 (1995).
72. Lang, S.M. *et al.* Importance of vpr for infection of rhesus monkeys with simian immunodeficiency virus. *J Virol* **67**, 902-912 (1993).
73. Laguette, N. *et al.* SAMHD1 is the dendritic- and myeloid-cell-specific HIV-1 restriction factor counteracted by Vpx. *Nature* (2011).
74. Malim, M.H. APOBEC proteins and intrinsic resistance to HIV-1 infection. *Philos Trans R Soc Lond B Biol Sci* **364**, 675-687 (2009).
75. Lecossier, D., Bouchonnet, F., Clavel, F. & Hance, A.J. Hypermutation of HIV-1 DNA in the absence of the Vif protein. *Science* **300**, 1112 (2003).
76. Mangeat, B. *et al.* Broad antiretroviral defence by human APOBEC3G through lethal editing of nascent reverse transcripts. *Nature* **424**, 99-103 (2003).
77. Deacon, N.J. *et al.* Genomic structure of an attenuated quasi species of HIV-1 from a blood transfusion donor and recipients. *Science* **270**, 988-991 (1995).
78. Piguet, V. *et al.* Nef-induced CD4 degradation: a diacidic-based motif in Nef functions as a lysosomal targeting signal through the binding of beta-COP in endosomes. *Cell* **97**, 63-73. (1999).
79. Lama, J., Mangasarian, A. & Trono, D. Cell-surface expression of CD4 reduces HIV-1 infectivity by blocking Env incorporation in a Nef- and Vpu-inhibitable manner. *Curr Biol* **9**, 622-631. (1999).
80. Ross, T.M., Oran, A.E. & Cullen, B.R. Inhibition of HIV-1 progeny virion release by cell-surface CD4 is relieved by expression of the viral Nef protein. *Curr Biol* **9**, 613-621 (1999).
81. Collins, K.L. & Baltimore, D. HIV's evasion of the cellular immune response. *Immunol Rev* **168**, 65-74 (1999).
82. Kirchhoff, F. Immune evasion and counteraction of restriction factors by HIV-1 and other primate lentiviruses. *Cell Host Microbe* **8**, 55-67 (2010).
83. Xu, W. *et al.* HIV-1 evades virus-specific IgG2 and IgA responses by targeting systemic and intestinal B cells via long-range intercellular conduits. *Nat Immunol* **10**, 1008-1017 (2009).
84. Nobile, C. *et al.* HIV-1 Nef inhibits ruffles, induces filopodia and modulates migration of infected lymphocytes. *J Virol* (2009).
85. Pizzato, M. *et al.* Dynamin 2 is required for the enhancement of HIV-1 infectivity by Nef. *Proc Natl Acad Sci U S A* **104**, 6812-6817 (2007).
86. Campbell, E.M., Nunez, R. & Hope, T.J. Disruption of the actin cytoskeleton can complement the ability of Nef to enhance human immunodeficiency virus type 1 infectivity. *J Virol* **78**, 5745-5755 (2004).
87. Neil, S.J., Zang, T. & Bieniasz, P.D. Tetherin inhibits retrovirus release and is antagonized by HIV-1 Vpu. *Nature* **451**, 425-430 (2008).
88. Bolduan, S. *et al.* Ion channel activity of HIV-1 Vpu is dispensable for counteraction of CD317. *Virology* **416**, 75-85 (2011).
89. Goto, T. *et al.* A novel membrane antigen selectively expressed on terminally differentiated human B cells. *Blood* **84**, 1922-1930 (1994).
90. Ozaki, S. *et al.* Immunotherapy of multiple myeloma with a monoclonal antibody directed against a plasma cell-specific antigen, HM1.24. *Blood* **90**, 3179-3186 (1997).
91. Kawai, S. *et al.* Antitumor activity of humanized monoclonal antibody against HM1.24 antigen in human myeloma xenograft models. *Oncol Rep* **15**, 361-367 (2006).

92. Jalili, A. *et al.* Induction of HM1.24 peptide-specific cytotoxic T lymphocytes by using peripheral-blood stem-cell harvests in patients with multiple myeloma. *Blood* **106**, 3538-3545 (2005).
93. Blasius, A.L. *et al.* Bone marrow stromal cell antigen 2 is a specific marker of type I IFN-producing cells in the naive mouse, but a promiscuous cell surface antigen following IFN stimulation. *J Immunol* **177**, 3260-3265 (2006).
94. Liberatore, R.A. & Bieniasz, P.D. Tetherin is a key effector of the antiretroviral activity of type I interferon in vitro and in vivo. *Proc Natl Acad Sci U S A*.
95. Erikson, E. *et al.* In vivo expression profile of the antiviral restriction factor and tumor-targeting antigen CD317/BST-2/HM1.24/tetherin in humans. *Proc Natl Acad Sci U S A* **108**, 13688-13693 (2011).
96. Van Damme, N. *et al.* The interferon-induced protein BST-2 restricts HIV-1 release and is downregulated from the cell surface by the viral Vpu protein. *Cell Host Microbe* **3**, 245-252 (2008).
97. Aad, G. *et al.* Search for new particles in two-jet final states in 7 TeV proton-proton collisions with the ATLAS detector at the LHC. *Physical review letters* **105**, 161801 (2010).
98. Kupzig, S. *et al.* Bst-2/HM1.24 is a raft-associated apical membrane protein with an unusual topology. *Traffic* **4**, 694-709 (2003).
99. Ishikawa, J. *et al.* Molecular cloning and chromosomal mapping of a bone marrow stromal cell surface gene, BST2, that may be involved in pre-B-cell growth. *Genomics* **26**, 527-534 (1995).
100. Goffinet, C. *et al.* HIV-1 antagonism of CD317 is species specific and involves Vpu-mediated proteasomal degradation of the restriction factor. *Cell Host Microbe* **5**, 285-297 (2009).
101. Rollason, R., Korolchuk, V., Hamilton, C., Schu, P. & Banting, G. Clathrin-mediated endocytosis of a lipid-raft-associated protein is mediated through a dual tyrosine motif. *J Cell Sci* **120**, 3850-3858 (2007).
102. Masuyama, N. *et al.* HM1.24 is internalized from lipid rafts by clathrin-mediated endocytosis through interaction with alpha-adaptin. *J Biol Chem* **284**, 15927-15941 (2009).
103. Perez-Caballero, D. *et al.* Tetherin inhibits HIV-1 release by directly tethering virions to cells. *Cell* **139**, 499-511 (2009).
104. Andrew, A.J., Kao, S. & Strebel, K. The C-terminal hydrophobic region in human BST-2/tetherin functions as a second transmembrane motif. *J Biol Chem* **286**, 39967-39981 (2011).
105. Andrew, A.J., Miyagi, E., Kao, S. & Strebel, K. The formation of cysteine-linked dimers of BST-2/tetherin is important for inhibition of HIV-1 virus release but not for sensitivity to Vpu. *Retrovirology* **6**, 80 (2009).
106. Ohtomo, T. *et al.* Molecular cloning and characterization of a surface antigen preferentially overexpressed on multiple myeloma cells. *Biochem Biophys Res Commun* **258**, 583-591 (1999).
107. Hinz, A. *et al.* Structural basis of HIV-1 tethering to membranes by the BST-2/tetherin ectodomain. *Cell Host Microbe* **7**, 314-323 (2010).
108. Schubert, H.L. *et al.* Structural and functional studies on the extracellular domain of BST2/tetherin in reduced and oxidized conformations. *Proc Natl Acad Sci U S A* **107**, 17951-17956 (2010).
109. Yang, H. *et al.* Structural insight into the mechanisms of enveloped virus tethering by tetherin. *Proc Natl Acad Sci U S A* **107**, 18428-18432 (2010).

110. Hammonds, J. & Spearman, P. An imperfect rule for the particle roost. *Cell Host Microbe* **7**, 261-263 (2010).
111. Larkin, M.A. *et al.* Clustal W and Clustal X version 2.0. *Bioinformatics* **23**, 2947-2948 (2007).
112. Mitchell, R.S. *et al.* Vpu antagonizes BST-2-mediated restriction of HIV-1 release via beta-TrCP and endo-lysosomal trafficking. *PLoS Pathog* **5**, e1000450 (2009).
113. Rollason, R., Korolchuk, V., Hamilton, C., Jepson, M. & Banting, G. A CD317/tetherin-RICH2 complex plays a critical role in the organization of the subapical actin cytoskeleton in polarized epithelial cells. *J Cell Biol* **184**, 721-736 (2009).
114. Yoo, H., Park, S.H., Ye, S.K. & Kim, M. IFN-gamma-induced BST2 mediates monocyte adhesion to human endothelial cells. *Cell Immunol* **267**, 23-29 (2011).
115. Cao, W. *et al.* Regulation of TLR7/9 responses in plasmacytoid dendritic cells by BST2 and ILT7 receptor interaction. *J Exp Med* **206**, 1603-1614 (2009).
116. Cao, W. & Bover, L. Signaling and ligand interaction of ILT7: receptor-mediated regulatory mechanisms for plasmacytoid dendritic cells. *Immunol Rev* **234**, 163-176 (2010).
117. Jouvenet, N. *et al.* Broad-spectrum inhibition of retroviral and filoviral particle release by tetherin. *J Virol* **83**, 1837-1844 (2009).
118. Jia, B. *et al.* Species-specific activity of SIV Nef and HIV-1 Vpu in overcoming restriction by tetherin/BST2. *PLoS Pathog* **5**, e1000429 (2009).
119. Xu, F. *et al.* Tetherin inhibits prototypic foamy virus release. *Virol J* **8**, 198 (2011).
120. Sakuma, T., Noda, T., Urata, S., Kawaoka, Y. & Yasuda, J. Inhibition of Lassa and Marburg virus production by tetherin. *J Virol* **83**, 2382-2385 (2009).
121. Kaletsky, R.L., Francica, J.R., Agrawal-Gamse, C. & Bates, P. Tetherin-mediated restriction of filovirus budding is antagonized by the Ebola glycoprotein. *Proc Natl Acad Sci U S A* **106**, 2886-2891 (2009).
122. Weidner, J.M. *et al.* Interferon-induced cell membrane proteins, IFITM3 and tetherin, inhibit vesicular stomatitis virus infection via distinct mechanisms. *J Virol* **84**, 12646-12657 (2010).
123. Mansouri, M. *et al.* Molecular mechanism of BST2/tetherin downregulation by K5/MIR2 of Kaposi's sarcoma-associated herpesvirus. *J Virol* **83**, 9672-9681 (2009).
124. Watanabe, R., Leser, G.P. & Lamb, R.A. Influenza virus is not restricted by tetherin whereas influenza VLP production is restricted by tetherin. *Virology* **417**, 50-56 (2011).
125. Sliva, K. *et al.* The Cellular Anti-viral Restriction Factor Tetherin Does Not Inhibit Poxviral Replication. *J Virol* (2011).
126. Ye, L. *et al.* Tetherin has negligible activity in restricting hepatitis C virus in hepatocytes. *Innate immunity* (2011).
127. Gupta, R.K. *et al.* Mutation of a single residue renders human tetherin resistant to HIV-1 Vpu-mediated depletion. *PLoS Pathog* **5**, e1000443 (2009).
128. McNatt, M.W. *et al.* Species-specific activity of HIV-1 Vpu and positive selection of tetherin transmembrane domain variants. *PLoS Pathog* **5**, e1000300 (2009).
129. Hammonds, J., Wang, J.J., Yi, H. & Spearman, P. Immunoelectron microscopic evidence for Tetherin/BST2 as the physical bridge between HIV-1 virions and the plasma membrane. *PLoS Pathog* **6**, e1000749 (2010).
130. Fitzpatrick, K. *et al.* Direct restriction of virus release and incorporation of the interferon-induced protein BST-2 into HIV-1 particles. *PLoS Pathog* **6**, e1000701 (2010).

131. Habermann, A. *et al.* CD317/tetherin is enriched in the HIV-1 envelope and downregulated from the plasma membrane upon virus infection. *J Virol* **84**, 4646-4658 (2010).
132. Sato, K. *et al.* Comparative study on the effect of human BST-2/Tetherin on HIV-1 release in cells of various species. *Retrovirology* **6**, 53 (2009).
133. Miyakawa, K. *et al.* BCA2/Rabring7 promotes tetherin-dependent HIV-1 restriction. *PLoS Pathog* **5**, e1000700 (2009).
134. Skasko, M. *et al.* HIV-1 Vpu Protein Antagonizes Innate Restriction Factor BST-2 via Lipid-embedded Helix-Helix Interactions. *J Biol Chem* **287**, 58-67 (2012).
135. Vigan, R. & Neil, S.J. Separable determinants of subcellular localization and interaction account for the inability of group O HIV-1 Vpu to counteract tetherin. *J Virol* **85**, 9737-9748 (2011).
136. Bartee, E., McCormack, A. & Fruh, K. Quantitative membrane proteomics reveals new cellular targets of viral immune modulators. *PLoS Pathog* **2**, e107 (2006).
137. Mangeat, B. *et al.* HIV-1 Vpu neutralizes the antiviral factor Tetherin/BST-2 by binding it and directing its beta-TrCP2-dependent degradation. *PLoS Pathog* **5**, e1000574 (2009).
138. Schindler, M. *et al.* Vpu serine 52 dependent counteraction of tetherin is required for HIV-1 replication in macrophages, but not in ex vivo human lymphoid tissue. *Retrovirology* **7**, 1 (2010).
139. Douglas, J.L. *et al.* Vpu directs the degradation of the human immunodeficiency virus restriction factor BST-2/Tetherin via a {beta}TrCP-dependent mechanism. *J Virol* **83**, 7931-7947 (2009).
140. Dube, M. *et al.* Antagonism of tetherin restriction of HIV-1 release by Vpu involves binding and sequestration of the restriction factor in a perinuclear compartment. *PLoS Pathog* **6**, e1000856 (2010).
141. Miyagi, E., Andrew, A.J., Kao, S. & Strebel, K. Vpu enhances HIV-1 virus release in the absence of Bst-2 cell surface down-modulation and intracellular depletion. *Proc Natl Acad Sci U S A* **106**, 2868-2873 (2009).
142. Le Tortorec, A. & Neil, S.J. Antagonism to and intracellular sequestration of human tetherin by the human immunodeficiency virus type 2 envelope glycoprotein. *J Virol* **83**, 11966-11978 (2009).
143. Gupta, R.K. *et al.* Simian immunodeficiency virus envelope glycoprotein counteracts tetherin/BST-2/CD317 by intracellular sequestration. *Proc Natl Acad Sci U S A* **106**, 20889-20894 (2009).
144. Lopez, L.A. *et al.* Ebola virus glycoprotein counteracts BST-2/Tetherin restriction in a sequence-independent manner that does not require tetherin surface removal. *J Virol* **84**, 7243-7255 (2010).
145. Zhang, F. *et al.* Nef proteins from simian immunodeficiency viruses are tetherin antagonists. *Cell Host Microbe* **6**, 54-67 (2009).
146. Zhang, F. *et al.* SIV Nef proteins recruit the AP-2 complex to antagonize Tetherin and facilitate virion release. *PLoS Pathog* **7**, e1002039 (2011).
147. Serra-Moreno, R., Jia, B., Breed, M., Alvarez, X. & Evans, D.T. Compensatory changes in the cytoplasmic tail of gp41 confer resistance to tetherin/BST-2 in a pathogenic nef-deleted SIV. *Cell Host Microbe* **9**, 46-57 (2011).
148. Wolff, T. & Ludwig, S. Influenza viruses control the vertebrate type I interferon system: factors, mechanisms, and consequences. *J Interferon Cytokine Res* **29**, 549-557 (2009).
149. Fernandez-Suarez, M. & Ting, A.Y. Fluorescent probes for super-resolution imaging in living cells. *Nat Rev Mol Cell Biol* **9**, 929-943 (2008).

150. Keller, P.J., Schmidt, A.D., Wittbrodt, J. & Stelzer, E.H. Reconstruction of zebrafish early embryonic development by scanned light sheet microscopy. *Science* **322**, 1065-1069 (2008).
151. Hell, S.W., Stelzer, E.H., Lindek, S. & Cremer, C. Confocal microscopy with an increased detection aperture: type-B 4Pi confocal microscopy. *Optics letters* **19**, 222 (1994).
152. Hell, S.W. Toward fluorescence nanoscopy. *Nat Biotechnol* **21**, 1347-1355 (2003).
153. Betzig, E. & Trautman, J.K. Near-field optics: microscopy, spectroscopy, and surface modification beyond the diffraction limit. *Science* **257**, 189-195 (1992).
154. Schermelleh, L. *et al.* Subdiffraction multicolor imaging of the nuclear periphery with 3D structured illumination microscopy. *Science* **320**, 1332-1336 (2008).
155. Carlton, P.M. *et al.* Fast live simultaneous multiwavelength four-dimensional optical microscopy. *Proc Natl Acad Sci U S A* **107**, 16016-16022 (2010).
156. Kner, P., Chhun, B.B., Griffis, E.R., Winoto, L. & Gustafsson, M.G. Super-resolution video microscopy of live cells by structured illumination. *Nat Methods* **6**, 339-342 (2009).
157. Rego, E.H. *et al.* Nonlinear structured-illumination microscopy with a photoswitchable protein reveals cellular structures at 50-nm resolution. *Proc Natl Acad Sci U S A* (2011).
158. Donnert, G. *et al.* Macromolecular-scale resolution in biological fluorescence microscopy. *Proc Natl Acad Sci U S A* **103**, 11440-11445 (2006).
159. Sieber, J.J. *et al.* Anatomy and dynamics of a supramolecular membrane protein cluster. *Science* **317**, 1072-1076 (2007).
160. Donnert, G. *et al.* Two-color far-field fluorescence nanoscopy. *Biophys J* **92**, L67-69 (2007).
161. Willig, K.I. *et al.* Nanoscale resolution in GFP-based microscopy. *Nat Methods* **3**, 721-723 (2006).
162. Westphal, V. *et al.* Video-rate far-field optical nanoscopy dissects synaptic vesicle movement. *Science* **320**, 246-249 (2008).
163. Betzig, E. *et al.* Imaging intracellular fluorescent proteins at nanometer resolution. *Science* **313**, 1642-1645 (2006).
164. Hess, S.T., Girirajan, T.P. & Mason, M.D. Ultra-high resolution imaging by fluorescence photoactivation localization microscopy. *Biophys J* **91**, 4258-4272 (2006).
165. Rust, M.J., Bates, M. & Zhuang, X. Sub-diffraction-limit imaging by stochastic optical reconstruction microscopy (STORM). *Nat Methods* **3**, 793-795 (2006).
166. Heilemann, M. *et al.* Subdiffraction-resolution fluorescence imaging with conventional fluorescent probes. *Angew Chem Int Ed Engl* **47**, 6172-6176 (2008).
167. Folling, J. *et al.* Fluorescence nanoscopy by ground-state depletion and single-molecule return. *Nat Methods* **5**, 943-945 (2008).
168. Shroff, H., Galbraith, C.G., Galbraith, J.A. & Betzig, E. Live-cell photoactivated localization microscopy of nanoscale adhesion dynamics. *Nat Methods* **5**, 417-423 (2008).
169. Jones, S.A., Shim, S.H., He, J. & Zhuang, X. Fast, three-dimensional super-resolution imaging of live cells. *Nat Methods* **8**, 499-508 (2011).
170. Hess, S.T. *et al.* Dynamic clustered distribution of hemagglutinin resolved at 40 nm in living cell membranes discriminates between raft theories. *Proc Natl Acad Sci U S A* **104**, 17370-17375 (2007).
171. Manley, S. *et al.* High-density mapping of single-molecule trajectories with photoactivated localization microscopy. *Nat Methods* **5**, 155-157 (2008).

172. Bates, M., Huang, B., Dempsey, G.T. & Zhuang, X. Multicolor super-resolution imaging with photo-switchable fluorescent probes. *Science* **317**, 1749-1753 (2007).
173. Huang, B., Wang, W., Bates, M. & Zhuang, X. Three-dimensional super-resolution imaging by stochastic optical reconstruction microscopy. *Science* **319**, 810-813 (2008).
174. Heilemann, M., van de Linde, S., Mukherjee, A. & Sauer, M. Super-resolution imaging with small organic fluorophores. *Angew Chem Int Ed Engl* **48**, 6903-6908 (2009).
175. Wombacher, R. *et al.* Live-cell super-resolution imaging with trimethoprim conjugates. *Nat Methods* (2010).
176. Sengupta, P. *et al.* Probing protein heterogeneity in the plasma membrane using PALM and pair correlation analysis. *Nat Methods* (2011).
177. Subach, F.V. *et al.* Photoactivation mechanism of PAmCherry based on crystal structures of the protein in the dark and fluorescent states. *Proc Natl Acad Sci U S A* **106**, 21097-21102 (2009).
178. Wiedenmann, J. *et al.* EosFP, a fluorescent marker protein with UV-inducible green-to-red fluorescence conversion. *Proc Natl Acad Sci U S A* **101**, 15905-15910 (2004).
179. Habuchi, S., Tsutsui, H., Kochaniak, A.B., Miyawaki, A. & van Oijen, A.M. mKikGR, a monomeric photoswitchable fluorescent protein. *PLoS One* **3**, e3944 (2008).
180. Chudakov, D.M., Lukyanov, S. & Lukyanov, K.A. Tracking intracellular protein movements using photoswitchable fluorescent proteins PS-CFP2 and Dendra2. *Nature protocols* **2**, 2024-2032 (2007).
181. Subach, O.M. *et al.* A photoswitchable orange-to-far-red fluorescent protein, PSmOrange. *Nat Methods* **8**, 771-777 (2011).
182. McKinney, S.A., Murphy, C.S., Hazelwood, K.L., Davidson, M.W. & Looger, L.L. A bright and photostable photoconvertible fluorescent protein. *Nat Methods* **6**, 131-133 (2009).
183. Kanchanawong, P. *et al.* Nanoscale architecture of integrin-based cell adhesions. *Nature* **468**, 580-584 (2010).
184. Ando, R., Mizuno, H. & Miyawaki, A. Regulated fast nucleocytoplasmic shuttling observed by reversible protein highlighting. *Science* **306**, 1370-1373 (2004).
185. Andresen, M. *et al.* Photoswitchable fluorescent proteins enable monochromatic multilabel imaging and dual color fluorescence nanoscopy. *Nat Biotechnol* **26**, 1035-1040 (2008).
186. Stiel, A.C. *et al.* Generation of monomeric reversibly switchable red fluorescent proteins for far-field fluorescence nanoscopy. *Biophys J* **95**, 2989-2997 (2008).
187. Shroff, H. *et al.* Dual-color superresolution imaging of genetically expressed probes within individual adhesion complexes. *Proc Natl Acad Sci U S A* **104**, 20308-20313 (2007).
188. Gunewardene, M.S. *et al.* Superresolution imaging of multiple fluorescent proteins with highly overlapping emission spectra in living cells. *Biophys J* **101**, 1522-1528 (2011).
189. Hoyer, P., Staudt, T., Engelhardt, J. & Hell, S.W. Quantum Dot Blueing and Blinking Enables Fluorescence Nanoscopy. *Nano letters* (2010).
190. Gould, T.J., Verkhusha, V.V. & Hess, S.T. Imaging biological structures with fluorescence photoactivation localization microscopy. *Nature protocols* **4**, 291-308 (2009).
191. Lehmann, M. *et al.* Quantitative Multicolor Super-Resolution Microscopy Reveals Tetherin HIV-1 Interaction. *PLoS Pathog* **7**, e1002456 (2011).

192. Larson, D.R., Johnson, M.C., Webb, W.W. & Vogt, V.M. Visualization of retrovirus budding with correlated light and electron microscopy. *Proc Natl Acad Sci U S A* **102**, 15453-15458 (2005).
193. Dempsey, G.T., Vaughan, J.C., Chen, K.H., Bates, M. & Zhuang, X. Evaluation of fluorophores for optimal performance in localization-based super-resolution imaging. *Nat Methods* **8**, 1027-1036 (2011).
194. Bates, M., Dempsey, G.T., Chen, K.H. & Zhuang, X. Multicolor Super-Resolution Fluorescence Imaging via Multi-Parameter Fluorophore Detection. *Chemphyschem : a European journal of chemical physics and physical chemistry* **13**, 99-107 (2012).
195. Lampe, A., Haucke, V., Sigrist, S.J., Heilemann, M. & Schmoranzer, J. Multi-Color Direct STORM with Red Emitting Carbocyanines. *Biol Cell* (2011).
196. Sougrat, R. *et al.* Electron tomography of the contact between T cells and SIV/HIV-1: implications for viral entry. *PLoS Pathog* **3**, e63 (2007).
197. Zhu, P. *et al.* Distribution and three-dimensional structure of AIDS virus envelope spikes. *Nature* **441**, 847-852 (2006).
198. Leung, K. *et al.* HIV-1 assembly: viral glycoproteins segregate quantally to lipid rafts that associate individually with HIV-1 capsids and virions. *Cell Host Microbe* **3**, 285-292 (2008).
199. Annibale, P., Vanni, S., Scarselli, M., Rothlisberger, U. & Radenovic, A. Identification of clustering artifacts in photoactivated localization microscopy. *Nat Methods* **8**, 527-528.
200. Flors, C. *et al.* A stroboscopic approach for fast photoactivation-localization microscopy with Dronpa mutants. *Journal of the American Chemical Society* **129**, 13970-13977 (2007).
201. Hammonds, J. *et al.* The Tetherin/BST-2 Coiled-Coil Ectodomain Mediates Plasma Membrane Microdomain Localization and Restriction of Particle Release. *J Virol* (2011).
202. Neil, S.J., Eastman, S.W., Jouvenet, N. & Bieniasz, P.D. HIV-1 Vpu promotes release and prevents endocytosis of nascent retrovirus particles from the plasma membrane. *PLoS Pathog* **2**, e39 (2006).
203. Pais-Correia, A.M. *et al.* Biofilm-like extracellular viral assemblies mediate HTLV-1 cell-to-cell transmission at virological synapses. *Nat Med* **16**, 83-89 (2009).
204. Nguyen, D.H. & Hildreth, J.E. Evidence for budding of human immunodeficiency virus type 1 selectively from glycolipid-enriched membrane lipid rafts. *J Virol* **74**, 3264-3272 (2000).
205. Miyagi, E., Andrew, A., Kao, S., Yoshida, T. & Strebel, K. Antibody-mediated enhancement of HIV-1 and HIV-2 production from BST-2/tetherin+ cells. *J Virol* **85**, 11981-11994 (2011).
206. Lingwood, D. & Simons, K. Lipid rafts as a membrane-organizing principle. *Science* **327**, 46-50 (2010).
207. van Zanten, T.S. *et al.* Direct mapping of nanoscale compositional connectivity on intact cell membranes. *Proc Natl Acad Sci U S A* **107**, 15437-15442 (2010).
208. Hogue, I.B., Grover, J.R., Soheilian, F., Nagashima, K. & Ono, A. Gag Induces the Coalescence of Clustered Lipid Rafts and Tetraspanin-Enriched Microdomains at HIV-1 Assembly Sites on the Plasma Membrane. *J Virol* **85**, 9749-9766 (2011).
209. Chen, P., Hubner, W., Spinelli, M.A. & Chen, B.K. Predominant mode of human immunodeficiency virus transfer between T cells is mediated by sustained Env-dependent neutralization-resistant virological synapses. *J Virol* **81**, 12582-12595 (2007).

210. Jolly, C., Kashefi, K., Hollinshead, M. & Sattentau, Q.J. HIV-1 cell to cell transfer across an Env-induced, actin-dependent synapse. *J Exp Med* **199**, 283-293 (2004).
211. Jolly, C., Mitar, I. & Sattentau, Q.J. Requirement for an intact T-cell actin and tubulin cytoskeleton for efficient assembly and spread of human immunodeficiency virus type 1. *J Virol* **81**, 5547-5560 (2007).
212. Sowinski, S. *et al.* Membrane nanotubes physically connect T cells over long distances presenting a novel route for HIV-1 transmission. *Nat Cell Biol* **10**, 211-219 (2008).
213. Garcia, E. *et al.* HIV-1 trafficking to the dendritic cell-T-cell infectious synapse uses a pathway of tetraspanin sorting to the immunological synapse. *Traffic* **6**, 488-501 (2005).
214. Yu, H.J., Reuter, M.A. & McDonald, D. HIV traffics through a specialized, surface-accessible intracellular compartment during trans-infection of T cells by mature dendritic cells. *PLoS Pathog* **4**, e1000134 (2008).
215. Arrighi, J.F. *et al.* DC-SIGN-mediated infectious synapse formation enhances X4 HIV-1 transmission from dendritic cells to T cells. *J Exp Med* **200**, 1279-1288 (2004).
216. Arrighi, J.F. *et al.* Lentivirus-mediated RNA interference of DC-SIGN expression inhibits human immunodeficiency virus transmission from dendritic cells to T cells. *J Virol* **78**, 10848-10855 (2004).
217. Hodges, A. *et al.* Activation of the lectin DC-SIGN induces an immature dendritic cell phenotype triggering Rho-GTPase activity required for HIV-1 replication. *Nat Immunol* **8**, 569-577 (2007).
218. Gilbert, C., Barat, C., Cantin, R. & Tremblay, M.J. Involvement of Src and Syk tyrosine kinases in HIV-1 transfer from dendritic cells to CD4+ T lymphocytes. *J Immunol* **178**, 2862-2871 (2007).
219. Piguet, V. & Sattentau, Q. Dangerous liaisons at the virological synapse. *J Clin Invest* **114**, 605-610 (2004).
220. Sherer, N.M. *et al.* Retroviruses can establish filopodial bridges for efficient cell-to-cell transmission. *Nat Cell Biol* **9**, 310-315 (2007).
221. Nikolic, D.S. & Piguet, V. Vaccines and microbicides preventing HIV-1, HSV-2, and HPV mucosal transmission. *J Invest Dermatol* **130**, 352-361 (2009).
222. Kirchhoff, F., Greenough, T.C., Brettler, D.B., Sullivan, J.L. & Desrosiers, R.C. Brief report: absence of intact nef sequences in a long-term survivor with nonprogressive HIV-1 infection. *N Engl J Med* **332**, 228-232 (1995).
223. Schindler, M. *et al.* Nef-mediated suppression of T cell activation was lost in a lentiviral lineage that gave rise to HIV-1. *Cell* **125**, 1055-1067 (2006).
224. Schindler, M. *et al.* Inefficient Nef-mediated downmodulation of CD3 and MHC-I correlates with loss of CD4+T cells in natural SIV infection. *PLoS Pathog* **4**, e1000107 (2008).
225. Vasiliver-Shamis, G., Dustin, M.L. & Hioe, C.E. HIV-1 Virological Synapse is not Simply a Copycat of the Immunological Synapse. *Viruses* **2**, 1239-1260 (2010).

# Remerciements

Je remercie chaleureusement mon épouse Sherley Belley et ma famille pour son immense support durant mes recherches de doctorat et durant la rédaction de ce manuscrit. Je remercie Vincent Piguet pour son soutien et son aide, ainsi que les autres membres du Piguetlab, notamment Bastien Mangeat, Fabien Blanchet et Florence Leuba pour leur patience, leur enthousiasme et leurs enseignements. Je remercie Susana Rocha, Hiroshi Uji-i and Johan Hofkens pour leur aide avec la microscopie de super-résolution et la programmation MatLab, ainsi que le service de bioimaging pour le support excellent concernant la microscopie confocale.
Mes remerciements vont aussi aux professeurs Jean Gruenberg et Urs Greber, qui ont accepté le rôle de juré de thèse. En outre, je m'excuse pour les chercheurs et chercheuses dont les publications n'ont pas été mentionnées dans ce manuscrit. Mes recherches dans le laboratoire de Vincent Piguet etaient soutenue par le Fonds national suisse de la recherche et par le Human Science Frontier Program.